



SCRAMJET ISOLATOR MODELING AND CONTROL

DISSERTATION

John Robert Hutzal, Major, USAF

AFIT/DS/ENY/11-19

DEPARTMENT OF THE AIR FORCE
AIR UNIVERSITY

AIR FORCE INSTITUTE OF TECHNOLOGY

Wright-Patterson Air Force Base, Ohio

APPROVED FOR PUBLIC RELEASE; DISTRIBUTION UNLIMITED

The views expressed in this document are those of the author and do not reflect the official policy or position of the United States Air Force, the United States Department of Defense or the United States Government. This material is declared a work of the U.S. Government and is not subject to copyright protection in the United States.

AFIT/DS/ENY/11-19

SCRAMJET ISOLATOR MODELING AND CONTROL

DISSERTATION

Presented to the Faculty
Graduate School of Engineering and Management
Air Force Institute of Technology
Air University
Air Education and Training Command
In Partial Fulfillment of the Requirements for the
Degree of Doctor of Philosophy

John Robert Hutzal, B.S., M.S.
Major, USAF

December 2011

APPROVED FOR PUBLIC RELEASE; DISTRIBUTION UNLIMITED

SCRAMJET ISOLATOR MODELING AND CONTROL

John Robert Hutzal, B.S., M.S.

Major, USAF

Approved:

Douglas D. Decker (Chairman)

date

Richard G. Cobb (Member)

date

Jeffrey M. Donbar (Member)

date

Paul I. King (Member)

date

Michael J. Veth (Member)

date

Accepted:

M. U. THOMAS

Date

Dean, Graduate School of Engineering and Management

Abstract

The scramjet isolator is a duct in which pressure increases from the inlet to the combustor via a shock train. The shock train leading edge (LE) location must be controlled in an operational scramjet. A LE location measurement algorithm, dynamic model, and control algorithm were developed and validated with 500 frame per second (FPS) shadowgraph images in this research. The test apparatus consisted of a direct connect cold-flow high-speed wind tunnel with an adjustable ramp mounted in the tunnel floor. Ramp adjustments changed the tunnel cross-sectional area which changed the tunnel back pressure and LE location. Wall-mounted pressure transducers and a high-speed camera were used for data collection. The LE location measurement algorithm is the first with results validated using 500 FPS shadowgraph images to measure the LE location with root mean square (RMS) errors less than 20% of a duct height, D , although the transducers were separated by 50% of D . The developed and validated dynamic model is the first with error RMS values less than 24% of D . Finally, the first control algorithm capable of controlling the LE location within 50% of D was developed and validated.

Acknowledgements

I would like to thank my advisor, Dr. Doug Decker, for your guidance throughout the PhD process. Without your guidance I would have never made this accomplishment. I thank my committee for guiding me in your respective areas of specialty. This effort involved both aerodynamics and controls, two areas I could have not have learned without your help. Thank you to the AFIT laboratory technicians, particularly Jay Anderson and John Hixenbaugh. Without your help, I would not have been able to keep the laboratory running. I thank AFRL's Propulsion Directorate for funding this research. Also, I thank my fellow students who were always there to answer crazy questions and keep me sane.

Finally, I thank my wife and family. I realize the sacrifice you made and will always be grateful. I feel blessed for every day I get to spend with you.

John Robert Hutzal

Table of Contents

	Page
Abstract	iv
Acknowledgements	v
List of Figures	ix
List of Tables	xiv
List of Symbols	xvi
List of Abbreviations	xxii
 I. Introduction	 1
1.1 Major Scramjet Components	1
1.2 The Scramjet Isolator	2
1.3 Hypothesis	4
1.4 Motivation	5
1.5 Test Apparatus	6
1.6 Accomplished Research	6
1.6.1 Validate a Shock Train Location Measurement Algorithm	6
1.6.2 Develop a Dynamic Model of x_s Within a Duct	8
1.6.3 Develop and Validate an Automatic Feedback Con- troller for x_s	9
1.7 Contributions of This Research	9
 II. Literature Review	 11
2.1 System Dynamics	11
2.2 Pressure Rise	12
2.3 Leading Edge Detection	14
2.4 Current Modeling	17
2.4.1 Linearized Models	17
2.4.2 Engine Models Developed to Support Hypersonic Vehicle Models	18
2.5 Controls	19
2.5.1 Proportional Controllers	20
2.5.2 Optimal Controllers	21
2.5.3 “Smooth” Controller	21
2.5.4 Gain Scheduling	22
2.6 Literature Review Conclusion	22

	Page
III. Methodology	24
3.1 Test Apparatus	24
3.2 Operating Conditions and Experimental Procedure . . .	29
3.2.1 Test Procedure	29
3.2.2 Test Section Shock Waves	30
3.2.3 Choke Points	31
3.3 Ramp Actuator Dynamics	33
IV. Shock Train Leading Edge Location Measurement Techniques . .	36
4.1 Method Descriptions Along with Results and Analysis .	37
4.1.1 Pressure Ratio Method	39
4.1.2 Pressure Increase Method	42
4.1.3 Standard Deviation Method	45
4.1.4 Shock Train Location from Frequency Content .	49
4.1.5 Static Pressure Summation Method	54
4.1.6 Back Pressure Method	56
4.2 Complex Input Run	58
4.3 Real-Time Implementation	64
4.4 Summary and Conclusion	65
V. Shock Train Location Modeling	67
5.1 Static Polynomial Model	73
5.2 Continuous Linear Model with Static Polynomial Input .	75
5.3 ARX Models with Static Polynomial Input	79
5.4 NARX Models with Static Polynomial Input	82
5.4.1 Real-Time Experimental Results	87
5.4.2 Non-Dimensionalized Model	92
5.4.3 Increased Transducer Spacing	94
5.5 Ramp Angle to Location Modeling	96
5.5.1 Static Nonlinear Models	96
5.5.2 Static Nonlinearity Inversion	98
5.5.3 Dynamic Model Development	100
5.6 Modeling Conclusion	104
VI. Control	105
6.1 Deadbeat Controller Design	107
6.2 Observer Design	112
6.3 Integral Control	114
6.4 Controller Optical vs Measurement Algorithm Comparison	115
6.5 Controller Performance	119

	Page
6.6 Observer Performance	123
6.7 Disturbance Rejection	128
6.7.1 Disturbance I - Test Section Hole	128
6.7.2 Disturbance II - Decrease P_0	132
6.8 Control Conclusion	134
VII. Conclusion	135
Appendix A. Reynolds Number Calculation	138
Appendix B. Interpolation and Power Spectral Density Calculation .	140
B.1 Linear Interpolation Method	140
B.2 Power Spectral Density Calculation	141
Appendix C. Traditional System Identification	143
C.1 Linear System Identification Models	143
C.2 Nonlinear System Identification Models	146
Appendix D. Pseudo Random Binary Sequence Creation	148
Appendix E. Shadowgraph Leading Edge Location Measurement Tech- nique	150
E.1 Transformation Creation	150
E.2 Determining Shock Train Leading Edge Location	152
Appendix F. Laboratory Equipment Pictures	153
Appendix G. Transducer Calibrations	165
Appendix H. Matlab® Analysis Codes	169
H.1 Pressure Ratio Method	170
H.2 Pressure Method	173
H.3 Standard Deviation Method	176
H.4 Frequency Content Method	180
H.5 Static Pressure Summation Method	184
H.6 Back Pressure Method	185
H.7 ARX Model Maker	186
H.8 NARX Model Maker	190
Bibliography	193
Vita	199

List of Figures

Figure		Page
1.1.	Scramjet major components [1]	2
1.2.	Normal and oblique shock trains [2]	3
1.3.	Supersonic tongue after a bifurcated normal shock [3]	4
1.4.	Schematic of the overall controller	7
1.5.	Schematic of dynamic modeling	8
2.1.	Integrated hypersonic engine flowpath [4]	18
3.1.	A drawing of the air flow path (not to scale)	25
3.2.	A drawing of the test section and transducer mounting locations (not to scale)	25
3.3.	A drawing of the Mach 1.8 nozzle used throughout this research	26
3.4.	A picture of the ramps contracted and extended	28
3.5.	(a) Data collection phases and high-frequency pressure measure- ments (b) Ramp deployment angles	30
3.6.	(a) The test section static pressures on the floor and ceiling (b) A shadowgraph of the entire test section ($Re = 4.9 \times 10^6/\text{ft.}$) .	32
3.7.	(a) The test section static pressures on the floor and ceiling (b) A shadowgraph of the entire test section ($Re = 7.3 \times 10^6/\text{ft.}$) .	32
3.8.	A photo of the nozzle exit and test section entrance	33
3.9.	Transfer function of ramp input/measured output angle	35
4.1.	Illustration of pressure ratio measurement method	40
4.2.	Pressure ratio method measurement and error plots	41
4.3.	Illustration of pressure increase method	42
4.4.	Pressure increase method measurement and error plots	44
4.5.	Standard deviation measurement throughout run 4.9 measured at 9.7 in.	45
4.6.	Diagram of the standard deviation method implementation . .	47

Figure		Page
4.7.	Shock train LE location and error using standard deviation method	49
4.8.	PSD for two transducers with LE between them	50
4.9.	Illustration of the PSD method	52
4.10.	Frequency content method measurement and error plots	53
4.11.	Illustration of the pressure sum method data and static model .	55
4.12.	Sum of pressures correlation method measurement and error plots	56
4.13.	Diagram of the back pressure method data and static model . .	57
4.14.	Back pressure correlation method measurement and error plots	58
4.15.	A plot of the ramp angle for run 4.10	60
4.16.	Complex input stream run results for ratio and summation meth- ods	61
4.17.	Complex input stream run results for ratio and PSD methods .	62
4.18.	50% pressure rise method measurement and error plots with transducers separated by 95% of D	63
4.19.	Real time pressure increase method location and error plots across Reynolds numbers ($\xi = 50\%$)	65
5.1.	A schematic of the data flowing into the static and dynamic model for simulation	70
5.2.	A schematic of the data flowing into the static and dynamic model for real-time shock train location prediction	71
5.3.	P_{BP} to u_{NL} static models at three Reynolds numbers	75
5.4.	The Hammerstein model as implemented in this research . . .	76
5.5.	Step response for model three from Table 5.2	77
5.6.	u_{NL} commands for model three from Table 5.2	77
5.7.	Continuous model simulation location and error plot for run 4.11 validation	78
5.8.	ARX model simulation location and error plot	81
5.9.	NARX model simulation location and error plot	87
5.10.	Continuous, ARX, and NARX modeling real-time results . . .	89

Figure		Page
5.11.	Real-time results for static nonlinear and ARX models	91
5.12.	P_{BP}/P_0 to u_{NL}/D static model and data at three different Reynolds numbers	92
5.13.	Location and error results using the non-dimensionalized model	93
5.14.	ARX modeling simulation location and error plots with increased transducer spacing	96
5.15.	Multiple step input and x_{Meas} output plots for run 5.3	97
5.16.	Real-time results for static nonlinear and ARX models	98
5.17.	Plot of the measured ramp angle to dynamic model input nonlinearities	99
5.18.	Plot of the dynamic model input to measured ramp angle non-linearity inversions	100
5.19.	Ramp input PSD plots for runs 5.9-5.20	101
5.20.	ϕ_{Meas} -based Hammerstein model simulation results	102
5.21.	ϕ_{Meas} -based Hammerstein model real-time results	103
6.1.	Schematic of the overall system and control algorithm	106
6.2.	Illustration of a generic state-space model with a feedback controller	108
6.3.	Schematic of the implemented full-state observer	113
6.4.	Schematic of the integral controller	114
6.5.	Step responses with varying K_I values	115
6.6.	Measurement algorithm vs optical results for runs 6.4-6.6 . . .	117
6.7.	Measurement algorithm vs optical results for runs 6.7-6.9 . . .	118
6.8.	Desired vs measured location and error results for runs 6.10-6.12	120
6.9.	Controlled vs measured ramp angle and error results for runs 6.10-6.12	121
6.10.	Run 6.12 x_{Des} and ϕ_{Meas} with the time zoomed-in at two places	122
6.11.	Measured vs estimated shock train location for runs 6.10-6.12 .	124
6.12.	Measured vs estimated ramp angle for runs 6.10-6.12	125

Figure		Page
6.13.	PSDs of measured values and observer residuals for runs 6.10-6.12	126
6.14.	PSDs with varied number of samples per a set	127
6.15.	Disturbance response ramp angle, pressure ratio, and LE location for low Reynolds number settings	130
6.16.	Disturbance response ramp angle, pressure ratio, and LE location for high Reynolds number settings	131
6.17.	Plot showing effect on x_{Meas} for a decrease in P_0 with and without controller implemented	133
B.1.	Illustration of pressure ratio measurement method	140
C.1.	General linear parameter model [5]	145
C.2.	Schematic of an ARX model	146
D.1.	The five-level APRBS time-based and autocorrelation plots . .	149
E.1.	A shadowgraph image of the shock train and the leading edge location	150
E.2.	A drawing of the grid drawn on the wall of the test section for shadowgraph calibration	151
E.3.	A drawing of a schlieren image with grid overlay	152
F.1.	Illustration of test facility	153
F.2.	Picture of test facility	154
F.3.	Ingersoll Rand rotary screw compressor	154
F.4.	Donaldson desiccant dryer	155
F.5.	High pressure and vacuum chambers	156
F.6.	Kimray pressure regulator	156
F.7.	Air filter	157
F.8.	High pressure ball valve and controller	158
F.9.	NI PXI computer and BNC boards	159
F.10.	Leslie air-loaded pressure reducing valve	159
F.11.	Stagnation chamber	160
F.12.	Nozzle, test section, and hydraulic actuator	161

Figure		Page
F.13.	Test section illustration	161
F.14.	Endevco Model 136 DC amplifiers, hydraulic control computer, and shadowgraph control computer	162
F.15.	FASTCAM 1280 PCI shadowgraph camera	162
F.16.	MTS hydraulic actuator compressor	163
F.17.	Wind tunnel diffuser	163
F.18.	Vacuum chamber solenoid valve and controller	164
F.19.	Stokes Microvac vacuum pump	164
G.1.	Calibration data plots for amplifier 1	167
G.2.	Calibration data plots for amplifier 2	167
G.3.	Calibration data plots for amplifier 3	167
G.4.	Calibration data plots for amplifier 4	168
G.5.	Calibration data plots for amplifier 5	168

List of Tables

Table		Page
4.1.	Test section operating runs	38
4.2.	Measurement results for the various measurement techniques .	59
4.3.	Measurement results from real-time implementation	64
5.1.	Test section operating runs	72
5.2.	The RMS of the errors from the three continuous linear models	79
5.3.	The RMS of the errors for the simulation	79
5.4.	NARX simulation error RMS values	83
5.5.	The RMS of the differences between the measured and predicted LE location	89
5.6.	Back pressure input real-time recorded results	90
5.7.	Non-dimensionalized pressure ratio results	94
5.8.	ARX modeling errors, transducers at 95% of D	95
5.9.	ARX modeling errors, transducers at 47.6% of D	95
5.10.	Ramp input simulation results	102
5.11.	Ramp input real-time recorded results	103
6.1.	Test section operating configurations	114
6.2.	Optical measurement versus measurement algorithm results . .	116
6.3.	x_{Des} vs x_{Meas} results throughout the test section	119
6.4.	x_{Meas} vs x_{Est} results throughout the test section at three Reynolds numbers	123
6.5.	ϕ_{Meas} vs ϕ_{Est} results throughout the test section at three Reynolds numbers	124
6.6.	ϕ_{Meas} vs ϕ_{Est} results throughout the test section at three Reynolds numbers	126
6.7.	Test section hole run conditions	129
C.1.	Common black-box SISO models [5]	145

Table		Page
G.1.	Pressure transducer calibration values	165
G.2.	Calibration raw data	166

List of Symbols

Symbol		Page
P_{BP}	Back pressure	2
x_{Des}	Desired shock train location	6
x_{Meas}	Measured shock train location	6
e	Error	6
u_I	Integral controller output	6
ϕ_I	Integral control commanded angle	6
ϕ_{DB}	Deadbeat controlled ramp angle	6
ϕ_{Ctl}	Commanded ramp angle	6
ϕ_{Meas}	Measured ramp angle	6
\mathbf{P}_s	Vector of static pressures	6
$\hat{\mathbf{x}}_s$	Vector of estimated position states	6
$\hat{\Phi}_r$	Vector of estimated ramp states	6
u_{DB}	Output from deadbeat controller	6
\mathbf{K}_{DB}	Deadbeat controller gains	6
z^-	Backwards shift operator	6
t	Time	6
k	Sample number	6
Δt	Time between samples	6
x_s	Actual shock train LE location	7
x_{Optic}	Shock train location from shadowgraph photography . . .	7
\mathbf{e}	Vector of the measurement errors	7
e_{RMS}	RMS of \mathbf{e}	7
u_{NL}	Input to dynamic model	8
x_{Model}	Dynamic model output	8
x_{Des}	Desired shock train location	9

Symbol		Page
Δp_2	Disturbance in static pressure just downstream of shock	11
Δx_d	Disturbance in location of a normal shock in a duct	11
s	Laplace transform complex operator	11
a	Speed of sound	11
a_{t_0}	Speed of sound in the stagnation chamber	11
A_1	Duct cross-sectional area entering the shock	11
ΔA_1	Change in duct cross-sectional area entering the shock	12
$\left(\frac{\Delta A_1}{\Delta x_d}\right)_{ss}$	Change in cross-sectional area per a change in shock location at steady-state	12
γ	Ratio of specific heats	12
p_1	Static pressure entering shock	12
M_1	Mach number entering shock	12
S_t	Shock train length	13
M_0	Mach number at isolator entrance	13
Re_θ	Reynolds number based on the boundary-layer momentum thickness	13
D_r	Diameter of a round duct	13
θ	Boundary-layer momentum thickness	13
$P_{s,e}$	Static pressure at the end of the shock train	13
$P_{s,0}$	Static pressure at isolator entrance	13
$P_L(x, t)$	Pressure correlation per AFRL research [6]	13
ξ_L	Continuous measurement along isolator wall	13
P_0	Total pressure	13
P_s	Static pressure	13
P'_s	Static pressure at the shock train LE	13
P_1	Static pressure at the most upstream transducer	13
$\Delta\phi$	Change in ϕ	26
n_t	Number of transducers	28

Symbol		Page
ζ	Transducer label symbol	28
A_T	Test section cross-sectional area	31
A^*	Cross-sectional area of a M=1 throat	32
P_0	Total pressure	33
z	z-Transform operator	34
T_0	Total temperature	37
R	Rankine	37
P_0	Total pressure	37
n_s	Number of samples in a run	38
\mathbf{x}_{Meas}	Vector of n_s x_{Meas} measurements	38
\mathbf{x}_{Optic}	Vector of n_s optical LE measurements	38
$x_{PR}(k)$	Result of the pressure ratio method	39
P_{Tare,ζ_i}	Average tare pressure measurement for transducer ζ_i	39
$\mathbf{PR}(k)$	Vector of pressure ratios	39
\mathbf{x}_{Trans}	Vector of transducer mounting locations	39
PR_{Des}	Desired pressure ratio	39
ξ_{Des}	Desired percent increase for the detection methods	40
$x_P(k)$	Result of the pressure increase method	42
$P_{s,max}$	Maximum test section static pressure	42
$P_{s,Des}$	Desired pressure for interpolation	43
$x_\sigma(k)$	Result of the standard deviation method	45
σ	Standard deviation	45
σ_{Des}	Desired interpolation standard deviation	46
σ_1	Maximum standard deviation	46
x_1	x location associated with σ_1	46
σ_0	Standard deviation in the transducer just upstream to σ_1 .	46
x_0	Mounting location for the transducer measuring σ_0	46

Symbol		Page
σ_2	Standard deviation in the transducer just downstream to the transducer measuring σ_1	46
x_2	Mounting location for the transducer measuring σ_2	46
σ	Vector of standard deviations	48
$x_\Psi(k)$	Result of the PSD method	49
ψ_{ζ_i}	Power spectral density measurement	50
$\psi_{RMS,i}$	RMS of the PSD measurement from transducer ζ_i	51
Ψ_{RMS}	Vector of ψ_{RMS} measurements	51
$x_{Sum}(k)$	Result of summation method	54
$P_{Sum}(k)$	Sum of pressure transducer measurements at k	54
$x_{BP}(k)$	Result of back pressure method	56
$[a_1 \dots a_{n_a}]$	Regression parameters associated with previous measurements	69
$[b_1 \dots b_{n_b}]$	Regression parameters associated with previous inputs	69
n_a	Number of measurement parameters	69
n_b	Number of input parameters	69
x_{Model}	Output from a generic model	69
Θ_{Cont}	Vector of continuous model regression values	70
Θ_{ARX}	Vector of ARX model regression values	70
Θ_{NARX}	Vector of NARX model regression values	70
N_r	Number of samples for a run	73
Θ_{NL}	Vector of regression parameters for a non-labeled model	73
\mathbf{x}_{Meas}	Vector of shock train locations	73
\mathbf{x}_{Des}	Vector of desired shock train LE locations	105
K_I	Integral controller gain	109
K_{DB}	Deadbeat controller gain	111
$P[\cdot]$	Nonlinearity operating on a ramp measure	113
M_p	Maximum overshoot percentage	114

Symbol		Page
x_{Resid}	Residual related to x	123
ϕ_{Resid}	Residual related to ϕ	123
$P_{0,Ave}$	Average total pressure	138
$T_{0,Ave}$	Average total temperature	138
$P_{s,Ave}$	Time-average static pressure at the most upstream transducer	138
M_{Ave}	Average stream Mach number	138
γ	Ratio of specific heats	138
a_{Ave}	Average stream speed of sound	138
V_{Ave}	Average stream velocity	138
R	Specific gas constant	139
ρ_{Ave}	Average flow density	139
μ_{Ave}	Average viscosity	139
$T_{0,Ref}$	Reference total temperature	139
$\mu_{0,Ref}$	Reference total viscosity	139
k_{DFT}	Slice in DFT	141
*	Complex conjugate	142
\times_{ew}	Element-wise multiplication	142
y	System response	143
g	Impulse response function	143
ν	System identification noise	143
h	Coloring function	143
u	System input	143
\otimes_5	Modulo base five multiplication	148
\oplus_5	Modulo base five addition	148
\mathbf{x}_G	Vector of grid x positions in laboratory space	150
\mathbf{y}_G	Vector of grid y positions in laboratory space	150
\mathbf{u}_G	Vector of grid u positions in image space	151

Symbol		Page
\mathbf{v}_G	Vector of grid v positions in image space	151
T	x Component of transformation from image to wall space .	151
u_{LE}	Image space LE u location	152
v_{LE}	Image space LE v location	152

List of Abbreviations

Abbreviation		Page
M	Mach	3
Re	Reynolds	4
AFIT	Air Force Institute of Technology	6
RMS	Root Mean Square	7
PSC	Propulsion System Controller	10
AFRL	Air Force Research Laboratory	13
NACA	National Advisory Committee of Aeronautics	14
IPD	Instantaneous Pressure Distribution	15
TIA	Turbulence Intensity Amplification	15
STD	Search-Tone Detection	15
PSD	Power Spectral Density	16
PSC	Propulsion System Controller	20
PI	Proportional-Integral	21
PD	Proportional-Derivative	21
NI	National Instruments	25
PXI	Peripheral Component Interconnect eXtensions for Instru- mentation	25
LabVIEW™	Laboratory Virtual Instrumentation Engineering Workbench	26
PID	Proportional-Integral-Differential	27
PFV	Photron Fastcam Viewer	29
FPS	Frames per Second	29
avi	Audio Video Interleave	29
APRBS	Amplitude-Modulated PseudoRandom Binary Sequence .	37
PSD	Power Spectral Density	49
ARX	Auto-Regression with eXogenous variables	68

Abbreviation		Page
NARX	Nonlinear ARX	69
DFT	Discrete Fourier Transform	141
LTI	Linear Time-Invariant	143
SISO	Single-Input Single-Output	143
AR	AutoRegressive	144
X	eXogenous	144
MA	Moving Average	144
FIR	Finite Impulse Response	145
ARX	AutoRegressive with eXternal input	145
ARMAX	AutoRegressive Moving Average with eXternal input . . .	145
ARMA	AutoRegressive Moving Average	145
OE	Output-Error	145
BJ	Box-Jenkins	145
NARX	Nonlinear ARX	146
APRBS	Amplitude-modulated Pseudo-Random Binary Sequence .	148
PRBS	Pseudo-Random Binary Sequence	148
I/O	Input/Output	158
PC	Personal Computer	160

SCRAMJET ISOLATOR MODELING AND CONTROL

I. Introduction

The scramjet is a promising technology that has been researched for over 40 years and is capable of providing hypersonic air-breathing propulsion for air vehicles. The overall system is deceptively simple in that, much like a ramjet, it has no moving parts. The reality, though, is that the components are quite complex in their design and operation. This chapter will begin with a discussion of the scramjet components with a particular focus on the isolator, the primary component of interest for this research. Next, the hypothesis and the research motivation will be discussed. The chapter will conclude with an outline of the research that was accomplished to validate the hypothesis.

1.1 Major Scramjet Components

A dual-mode scramjet is an engine that can operate in both a scramjet and a ramjet mode and was the engine of interest for this research. The dual-mode scramjet is composed of four major components: the inlet, the isolator, the combustor, and the exhaust nozzle which can be seen in Figure 1.1. In the inlet, the flow is initially slowed across a series of shocks prior to entering the isolator. The isolator allows the flow pressure to increase to that of the combustor. This pressure increase is accomplished across a series of shocks, named a shock train, within the isolator. Engine unstart occurs when the shock train is disgorged from the isolator and the inlet. This can happen either when the pressure in the combustor, labeled the back pressure, is too large in relation to the inlet pressure or from combustor and/or inlet pressure perturbations. Finally, to conclude the scramjet flowpath, energy is added to the flow in the combustor, developing the back pressure, and the flow is expanded through the exhaust nozzle.

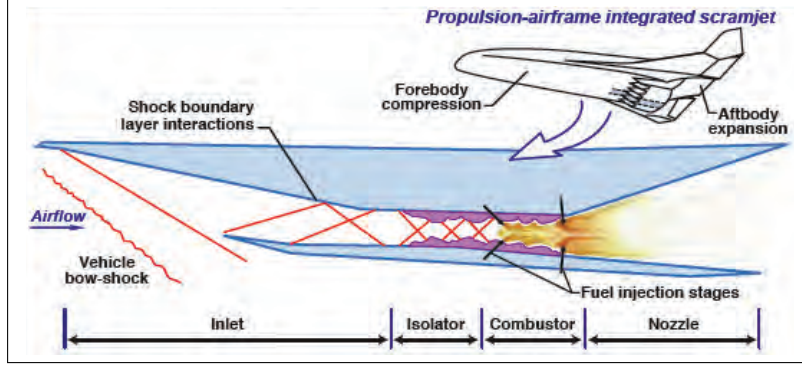


Figure 1.1: Scramjet major components [1]

1.2 The Scramjet Isolator

Traditionally, studies into scramjet inlets, to include the isolator, have started with the study of the diffuser within a ramjet inlet. Common to these studies is the assumption that there is a standing normal shock just inside the diffuser [7–10]. However, a single normal shock rarely exists within a ramjet or scramjet compression system [2]. Rather, a multiple shock formation, called a “pseudoshock” or a “shock train” often forms which is contained within an isolator. The isolator serves two purposes, the first is to isolate the inlet from disturbances in the combustor and the second is to provide the shock train with enough duct length to develop and allow as much pressure increase as possible, given the isolator length, between the inlet and the combustor. The maximum amount of pressure increase in the isolator is equal to that across a normal shock, but this increase is, instead, spread across the length of a shock train, the composition of which is either a series of lambda shocks or oblique shocks [2].

The flow within an isolator is similar to that within a supersonic tunnel, but with a significant amount of back pressure, P_{BP} , from the combustion process in the burner. This Fanno flow can be modeled with the assumptions of one-dimensional, adiabatic flow with no external work along with the existence of skin friction. Boundary layers form on the duct surfaces and grow along the length of the flowpath, causing the

effective cross-sectional area available for full velocity flow to decrease. This decrease in the area acts as a nozzle that will increase the flow Mach, M , number toward one for a subsonic flow and decrease the flow Mach number toward one for a supersonic flow [11]. When P_{BP} is increased, a shock forms in the flow. For lower Mach numbers ($M \lesssim 1.5$) a single normal shock generally forms. For mid-range Mach numbers ($1.5 \lesssim M \lesssim 1.7$) the flow will appear as a series of normal shocks, called lambda shocks, as described in the following paragraph. Finally, for higher Mach numbers ($M \gtrsim 1.7$), the flow will appear as a series of oblique shocks [12,13]. Diagrams of the normal and the oblique shock trains are presented in Figure 1.2. In this figure, as well as in all figures showing the flow, the flow is from left to right.

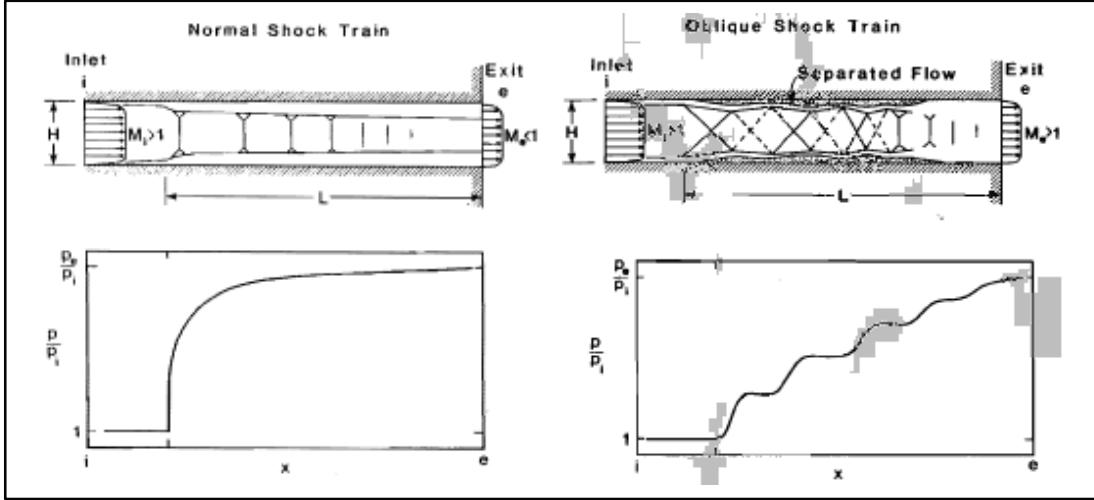


Figure 1.2: Normal and oblique shock trains [2]

The reason for these interesting flows is the interaction between the boundary layer and the shock (or series of shocks) itself. As the strength of the shock increases, the shock will form what is called a lambda shock. This shock, shown in Figure 1.3, actually bifurcates near the boundary layer. Additionally, the shock will cause boundary layer separation and flow reversal (within the boundary layer) [14]. This separation will increase the boundary layer size within the flow, increasing the Mach number of the subsonic flow behind the shock to potentially develop a supersonic zone behind

the shock. This supersonic region was termed a “supersonic tongue” [14] and has been detected both by simulation and by experimentation for a number of different Mach and Reynolds (Re) numbers [15, 16]. This supersonic region then decreases to subsonic speeds with another shock due to the increased size of the boundary layer and the process repeats itself until there is not enough energy in the flow to develop a supersonic zone downstream of a shock and the flow remains completely subsonic, which marks the end of the shock train. With increases in Mach or Reynolds number values, the size of the embedded supersonic region decreases [3]. Further, as the value of Mach is increased, separation becomes more pronounced and a series of oblique shocks form a shock train as the flow goes from supersonic to subsonic [2].

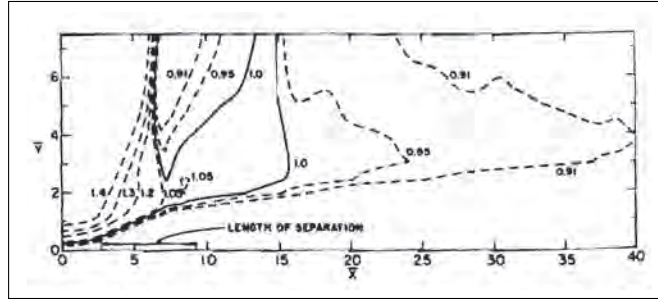


Figure 1.3: Supersonic tongue after a bifurcated normal shock [3]

1.3 Hypothesis

The hypothesis of this research was that the location of a shock train developed within a cold-flow blow-down wind tunnel could be sensed, modeled, and controlled using pressure transducers and an adjustable ramp mounted in the downstream portion of the wind tunnel. Control in this case implies that the controller can place and hold the steady-state shock train leading edge location to within \pm one duct away from the desired shock train leading edge location.

The various chapters in this dissertation demonstrate that the hypothesis was validated; the shock train location can be controlled within a cold-flow blow-down wind tunnel to within \pm one duct height. This was accomplished first by developing a method to locate the shock train leading edge location using the pressure increase

in the test section. Next, a dynamic model was developed and validated to model the location of the shock train leading edge with inputs from either the back pressure or a ramp assembly mounted in the test section. Finally, the measurement algorithm and dynamic model were used to develop a control algorithm using the ramp assembly. The hypothesis was validated by demonstrating positive control of the shock train leading edge location using the developed measurement and feedback control algorithms.

1.4 Motivation

The motivation for this effort is to lay the groundwork for the implementation of a closed-loop feedback control algorithm for a scramjet engine. As discussed earlier in the chapter, inlet unstart occurs in a scramjet when the shock train becomes disgorged from the inlet [2]. This can happen for a number of reasons, one of which is a change in the angle of attack of the air vehicle which effects the flow into the isolator [17, 18]. Another potential unstart cause comes from fueling the scramjet combustor. Fuel increases can be used for air vehicle acceleration, but these increases produce a large back pressure that can fall out of balance with the pressure of the flow entering the isolator. An example of when the fuel was changed and unstart occurred is what happened on the second X-51A flight. After the initial boost, when the engine was changing from ethylene to JP-7, the program manager believes more thrust was produced than was anticipated and the inlet unstated [19]. The engine could not be restarted and the air vehicle flew into the ocean [20]. This is an example of what happens when the back pressure to inlet flow pressure ratio is too large. When this happens the shock train will become disgorged from the isolator. If the shock train LE could be actively controlled, the LE could be placed at a predetermined location in anticipation of positive or negative changes in angle of attack or velocity. Additionally, active control of the LE could negate the need for a long isolator, thus decreasing the overall size and weight of the scramjet, potentially increasing range and/or payload.

1.5 Test Apparatus

All runs accomplished in this research were completed on a cold-flow high-speed wind-tunnel located at the Air Force Institute of Technology (AFIT). A test section consisting of a 24 in. duct with an adjustable ramp was mounted along the flowpath of the wind tunnel. The test section has a 2.5 in. \times 2.5 in. square cross-section. Taps used to mount high-frequency pressure transducers were drilled into the ceiling and floor of the test section to measure wall static pressures throughout a run. Additionally, data was collected using high-speed shadowgraph photography to verify the final shock train LE measurements. The entire assembly was controlled using a computer utilizing LabVIEWTM software.

1.6 Accomplished Research

The research accomplished to address the hypothesis was completed in three parts: validate a shock train LE measurement algorithm, develop a dynamic model for the shock train LE location, and develop a feedback controller. Each of the three parts is considered in a separate chapter within this document. The overall control algorithm implemented as a part of this research is presented in Figure 1.4 where x_{Des} is the desired shock train LE location, x_{Meas} is the measured shock train LE location using the developed measurement algorithm, e is the difference between x_{Des} and x_{Meas} , u_I is the output from the integral controller, ϕ_I is the integral control commanded angle, ϕ_{DB} is the ramp angle commanded by the deadbeat controller, ϕ_{Ctl} is the commanded ramp angle, ϕ_{Meas} is the measured ramp angle, \mathbf{P}_s is a vector of static pressures, $\hat{\mathbf{x}}_s$ is a vector of the estimated location states, $\hat{\Phi}_r$ is a vector of the estimated ramp states, u_{DB} is the deadbeat controller output, \mathbf{K}_{DB} is the deadbeat controller gains, z^{-1} is the backwards shift operator, t is time, k is a sample number, and Δt is the time between samples.

1.6.1 Validate a Shock Train Location Measurement Algorithm. The first task accomplished was to develop and validate an algorithm to locate the shock train

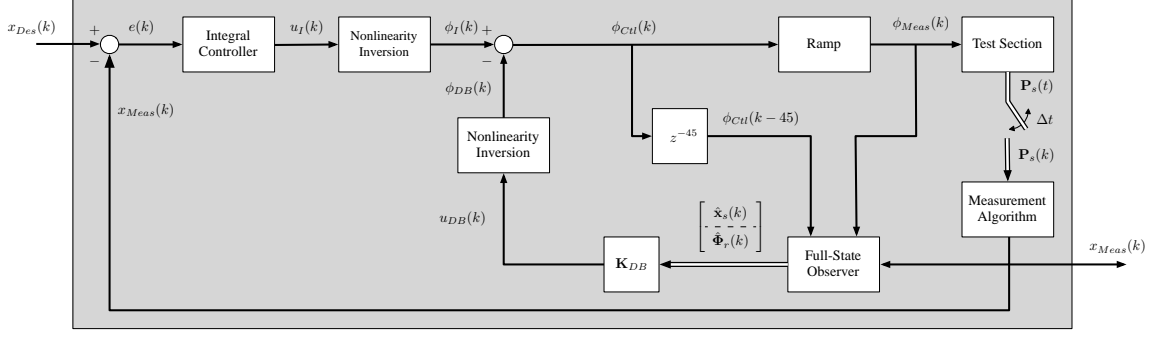


Figure 1.4: Schematic of the overall controller

LE within the AFIT wind-tunnel test section. In Figure 1.4, this task is captured in the block labeled “Measurement Algorithm.” The importance of this block was to develop a way to measure x_s , the actual shock train location, for use in a closed-loop feedback control algorithm. The approach taken was to use the vector of static pressures collected at sample k , $\mathbf{P}_s(k)$, in an algorithm to calculate the shock train location and return the “measured” shock train location at sample k , $x_{Meas}(k)$. Six different approaches were considered to use as the measurement algorithm. Previous methods [21–23] used to locate the LE location using wall-mounted pressure transducers had accuracies no better than the distance between two pressure transducers. Contemporary methods [24–26] used to locate the LE did not include a correlation to shadowgraph measurements at a rate greater than 30 frames per sec. The contribution of this portion of the research is that, not only is the calculated x_{Meas} correlated with the measured shock train location using the high-speed (500 frames per sec) shadowgraph photography, labeled x_{Optic} , but the accuracy is significantly better than the distance between pressure transducers. The error metric used was the root mean square, RMS, of the vector of measurement errors where the vector is composed of the error for each k throughout a run, labeled \mathbf{e} , and the measurement error was defined as the difference between x_{Meas} and x_{Optic} . The RMS of \mathbf{e} was given the symbol e_{RMS} .

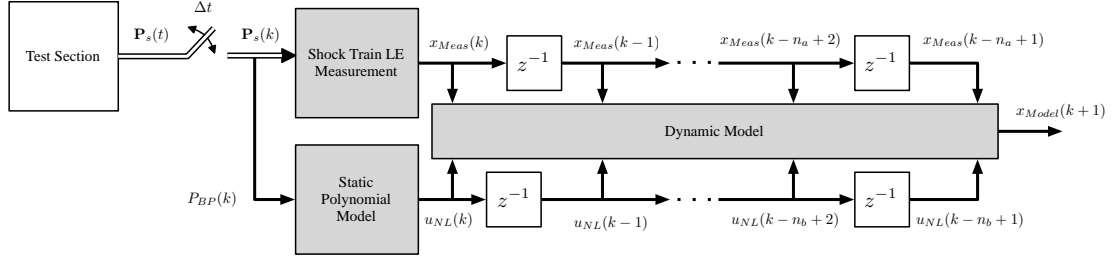


Figure 1.5: Schematic of dynamic modeling

1.6.2 Develop a Dynamic Model of x_s Within a Duct. The next step in the research was to develop two shock train LE location dynamic models for a shock train within a duct. Two different types of models were developed as a part of the research:

1. a dynamic model relating P_{BP} to x_s
2. a dynamic model relating the measured ramp angle, ϕ_{Meas} , to x_s .

The intention of the first model type was to demonstrate that the relationship between the shock train LE location and the back pressure could be modeled in a fashion that was useful to develop an automatic control algorithm to control x_s . A general schematic inclusive of the P_{BP} to x_s models developed in Chapter V is presented in Figure 1.5 where u_{NL} is the dynamic model input and x_{Model} is the dynamic model output. All of the models developed included a static model and a dynamic model and relied on the measurement algorithm developed earlier in the research. In the second model type, the same static nonlinear/dynamic model structure was used to develop a model that was then implemented in a control algorithm. The dynamic model developed for the second portion of the modeling effort represents the blocks labeled “Test Section” and “Nonlinearity Inversion” in Figure 1.4.

The dynamic modeling approach taken as a part of this research was to adopt a system identification “black box” approach. Using this approach, several input signals are provided to the system and the output is recorded. The input signals were changes in P_{BP} for the first model and ϕ_{Meas} for the second model. The output signal for both dynamic model types was labeled x_{Model} when implemented in the

LabVIEWTM algorithm. Several model structures were then assumed and evaluated by comparing the experimentally collected data to simulation data. The simulation was accomplished using the same experimental inputs collected in a test run and compared the output from the model simulation to the output measured in the test section. The model structure chosen was a Hammerstein model structure. The Hammerstein model is composed of a static nonlinear model followed by a dynamic model. A static nonlinear model is a model that accepts an input and returns an output in the same sample set, k , whereas a dynamic model is one that accepts inputs from several sample sets (e.g. $k, k-1, k-2$) and returns an expected output at a different time (e.g., $k+1$). The Hammerstein model and the system identification approach are discussed more thoroughly in Appendix C.

1.6.3 Develop and Validate an Automatic Feedback Controller for x_s . The final portion of this research was to develop and validate an automatic controller for the shock train LE location, x_s . The controller that was developed utilized the shock train measurement algorithm and the ϕ_{Meas} to x_s model that were both developed and validated as a part of this research. The different parts of the controller are presented in Figure 1.4 and are labeled “Integral Controller,” “Full-State Observer,” and \mathbf{K}_{DB} . The control algorithm used was a dead beat controller along with integral control and a full-state observer. The controller was implemented on a computer with LabVIEWTM and the values for the desired shock train location, x_{Des} , were compared to x_{Optic} to calculate e_{RMS} . The controller was developed to operate throughout the Reynolds number range achievable in the test section.

1.7 Contributions of This Research

As a part of this research, first a measurement algorithm was developed to locate the shock train LE within a duct using pressure transducer measurements. The first contribution was to provide an algorithm, validated using high-speed shadowgraph imagery, capable of providing a continuous (in terms of x) shock train location mea-

surement applicable throughout the available test section Reynolds number range. The next contribution was to develop a dynamic model relating P_{BP} to x_s . Previous scramjet models have either not included the shock train dynamics [27–31], have been based on perturbation models which have suffered from a limited input space of available pressure changes [7–10, 32], or regarded the dynamics as noise [18, 33, 34]. The model structure and/or modeling approach developed in this research could, potentially, be exported to another isolator for use in a control algorithm. The model was validated to predict the shock train location to within the distance between pressure transducers (less than 47.6% of D) and the dynamic model input space included pressures that could place the shock train throughout the test section. Finally, a controller was developed and validated to actually control the location of the shock train LE. To date, few controllers have been implemented with the objective of controlling the shock train location throughout the isolator in mind. The closest may be the propulsion system controller (PSC) from the X-43A, which used the fuel flow and inlet cowl as actuators in a proportional-integral feed-forward controller [35] used to prevent unstart. Specifically, in regards to fuel flow, the controller decreased the amount of fuel provided to the combustor if potential unstart conditions were noted. The controller did not command the shock train location throughout a run. The controller developed and validated as a part of this research provides the capability to place the shock train LE at a desired location within the isolator which, among other things, enables an enhanced margin of safety for air vehicle turns and changes of angle of attack.

Having motivated and previewed the results, the dissertation is arranged as follows. Chapter II covers the current literature on the topics of LE detection, scramjet isolator modeling, and scramjet control in more detail. Chapter III covers the test apparatus and procedures that were used as a part of this research. Chapter IV covers the research accomplished for location measurement. Chapter V covers the modeling research and the control research is presented in Chapter VI. Finally, the conclusions are presented in Chapter VII.

II. Literature Review

The focus of this research is shock train LE location measurement, modeling, and control within the isolator of a scramjet. This chapter will summarize the research to date on LE detection, shock train LE location modeling, and shock train LE location control. To build a foundation for this discussion, this chapter will begin with a discussion of the shock train dynamics and pressure distribution. It will then highlight the areas of contribution of this research, including LE detection, scramjet modeling, and scramjet propulsion controls.

2.1 System Dynamics

Study into the dynamics of a shock train in a scramjet began with normal shocks in a duct and/or a supersonic inlet. Beginning in the 1950s [32] the reaction of a normal shock in a duct with varying cross-sectional area to downstream pressure changes was studied. Results of the initial study show that, for small downstream disturbances in the pressure Δp_2 , there is a first-order lag relationship to changes in the location of a normal shock, Δx_d . This system is described by the transfer function in Equation (2.1) [32]

$$\frac{\Delta x_d(s)}{\Delta p_2(s)} = k_H \frac{1}{a + \sigma_H s} \quad (2.1)$$

where:

$$\sigma_H = \frac{1}{a_{t_0}} \frac{A_1}{\left(\frac{\Delta A_1}{\Delta x_d}\right)_{ss}} \sigma'_H \quad (2.2)$$

$$k_H = -\frac{\gamma + 1}{4\gamma} \frac{1}{p_1} \frac{1}{M_1} \frac{a_1}{a_{t_0}} \frac{A_1}{\left(\frac{\Delta A_1}{\Delta x_d}\right)_{ss}} \sigma'_H \quad (2.3)$$

$$\sigma'_H = \frac{\frac{2(\gamma+1)}{\gamma-1} M_1 \left(1 + \frac{\gamma-1}{2} M_1^2\right)^{\frac{1}{2}}}{1 + \frac{\gamma^2+1}{\gamma-1} M_1^2} \quad (2.4)$$

where the subscript “H” is from the author who developed the model, H. G. Hurrell, s is the complex operator associated with the Laplace transform, a is the speed of sound, a_{t_0} is the speed of sound in the stagnation chamber, A_1 is the duct cross-

sectional area entering the shock, ΔA_1 is the change in the duct cross-sectional area due to the duct design, $\left(\frac{\Delta A_1}{\Delta x_d}\right)_{ss}$ is the change in cross-sectional area per a change in shock location at steady-state, γ is the ratio of specific heats, p_1 is the static pressure entering the shock, and M_1 is the Mach number of the flow entering the shock.

Subsequent researchers [9] took a different approach, although also based on a perturbation theory approach, the work considered an admittance function describing the strength of a reflected acoustic wave from a normal shock in a diffuser. They too arrived at the conclusion that isolator dynamics can be modeled with a first-order lag transfer function. Using the acoustic wave approach, it was shown [9] that a thin normal shock in a diffuser is stable (under most conditions) when in a diverging duct and unstable when in a converging duct.

2.2 *Pressure Rise*

In the 1950s one of the first attempts to develop a dynamic pressure model for the pressure rise within a shock train was made [36]. The historic model, called the “shockless model”, was based on one-dimensional analysis of the flow and the consideration that the entropy increase from multiple oblique shocks is less than that from a single normal shock. As a result, the assumption was made that dissipative phenomenon within the shock train occurred primarily in the turbulent dissipative regions of the boundary layer and downstream of the shock train as opposed to within the shocks [36]. Later, the “shockless model” was modified [13] to better accommodate the flow boundary conditions at the end of the shock train as well as to allow for the calculation of the pressure on walls surrounding the shock train. This model, called the “diffusion model” proved adequate to calculate the length of the shock train, and could be used to calculate the static pressure for a high Mach number flow (M=2.79 was tested), but was inadequate for static pressure distribution calculations at lower Mach numbers. Additionally, while dynamic capabilities of the model were considered, only time-averaged results were provided.

Other researchers in the 1970s [37] were also studying the pressure distribution in scramjet engines. Specifically, they developed a heuristic relationship describing the pressure profile within an isolator based on time-averaged isolator wall static pressure distributions. This relationship is presented in Equation (2.5)

$$\frac{S_t (M_0^2 - 1) Re_\theta^{1/4}}{D_r^{1/2} \theta^{1/2}} = 50 \left(\frac{P_{s,e}}{P_{s,0}} - 1 \right) + 170 \left(\frac{P_{s,e}}{P_{s,0}} - 1 \right)^2 \quad (2.5)$$

where S_t is the shock train length, M_0 is the Mach number at the entrance to the isolator, Re_θ is the Reynolds number based on the boundary-layer momentum thickness, D_r is the diameter of the round duct, θ is the boundary-layer momentum thickness, $P_{s,e}$ is the pressure at the end of the shock train, and $P_{s,0}$ is the static pressure at the inlet to the isolator. Unfortunately, the correlation presented in Equation (2.5) requires knowledge of the boundary-layer momentum thickness, which either requires significant assumptions, computer simulations, or pitot tubes inserted within the flow. The boundary layer thickness was later measured [38] using a pitot rake to determine the steady-state boundary-layer thickness at two Mach numbers within an isolator.

Recently, the Air Force Research Laboratory (AFRL) [6] has attempted to improve upon the correlation presented in Equation (2.5) to provide a mathematical model for the wall pressure distribution that does not include the boundary-layer momentum thickness. The flow was considered at two Mach numbers while using different isolators with different surface finishes and led to the correlation presented in Equation (2.6)

$$P_L(\xi, t) = M_0(t)^2 \frac{[(P_s(\xi, t) - P'_s(t)) / P_0(t)]}{P_{BP}(t) / P_1(t)} \quad (2.6)$$

where $P_L(x, t)$ is the pressure per the AFRL-developed correlation at every point in time, t , location along the isolator wall, ξ_L , P_0 is the total pressure, P_s is the static pressure, P'_s is the static pressure at the shock train LE, P_1 is the static pressure at the most upstream transducer, and P_{BP} is the back pressure.

There are no first-principles-based models for the static pressure distribution within the isolator. Since these models are based off heuristics and/or assumptions, they all have significant error bands on their results. In addition, these models do not model the transient pressure behavior due to changes in back pressure. These models validate that a significant pressure rise is incident with the shock train LE location; a consideration that was used in the shock train location measurement algorithm of this research.

2.3 Leading Edge Detection

In order to control the shock train LE location within a scramjet isolator, one must be able to realize or measure the LE location. This concept was noted in the X-43A engine control research which provided a feedback controller based on increases in unstart probability [35]. The majority of the research into locating the shock train LE is based on the static pressure increase within the boundary layer due to the shocks impinging upon the isolator walls from the shock train [2]. This pressure is then measured with wall-mounted pressure transducers and the LE is located through some algorithm with varying accuracy. Recent research has expanded this raw pressure rise technique to include considerations of pressure standard deviations, pressure measurement spectral content [24, 25] and pressure summation correlations [39].

Starting in the mid-1950s, the National Advisory Committee of Aeronautics (NACA) began studies on the control of the shock train within a ramjet diffuser [40]. Successive early studies, which also assumed a single normal shock, studied techniques for sensing the location of the shock [21–23, 26]. The authors in these studies considered the entire wall pressure profile within the inlet and assumed the LE location of the shock train was at the large initial pressure increase which is in agreement with the pressure correlations discussed in Section 2.2. Due to computing limitations, the accuracy of the shock train position could only be as accurate as the spacing between pressure transducers in the wall of the inlet [21–23]. Ultimately, a

technique based on the sum of wall pressure measurements that originated from this method of research, was successfully used on the YF - 12 [26].

This ramjet research was expanded [24] to include shocks of increased strength at higher Mach numbers ($M \approx 3$) and their accompanying shock trains. Additionally, in this research, 30 frames per second shadowgraph imaging recorded the shock train LE location. Multiple ways to locate the LE were considered, including the instantaneous pressure distribution (IPD) method, the turbulence intensity amplification (TIA) method, and the search-tone detection (STD) method. The first method is very similar to the previous NACA and NASA studies and measured the wall pressure to determine the shock train location based on the increased static pressure from a shock. The second technique is based on the amplification of the boundary layer turbulence after passage of the shock. Due to the motion of the shock train LE and its interaction with the boundary layer, high-frequency spectral content is created within the boundary layer which can then be measured with pressure transducers. The TIA method measures the RMS value of the pressure fluctuations at each sensor and assumes the LE is at the transducer with an increase in high-frequency content. Unfortunately, this method is also limited in accuracy to the distance between the pressure transducers. In the STD method, a tone of a known frequency was added to the flow. The assumption was that the tone (acoustic wave) would excite the LE and this excitation would be observable in the pressure readings. Unfortunately, the STD technique did not work, the TIA method was rejected as being noisy and the IPD method was recommended [24].

In a patent [41], the task of locating the shock train LE was considered again. Utilization of an estimation routine was specifically rejected due to the assumption that an estimation routine would require too much flow characterization using previous knowledge for implementation. The technique utilized for this patent involved taking a least-squares curve-fit of the pressure distribution. The resulting equation was then adjusted using tuning parameters to fit the curve to a predetermined shape. After fitting, the shock train LE was determined to be the point in the curve where

the pressure increases significantly [41]. While this technique provides a way to determine the location of the shock within the distance between the pressure transducers, it is still based on wall pressure measurements and is essentially an extension of the wall pressure measurements already discussed.

Contemporary LE detection research [25, 42] built on these previous efforts using a direct-connect wind-tunnel connected to a combustor. First [42] several historic techniques were validated while the need for an isolator was also validated. Next [25] research into different ways to locate the shock train LE with the isolator for potential use in a feedback controller was accomplished. Three LE detection techniques were considered. The first technique was to consider the location where the normalized (static pressure normalized by total pressure) wall pressure increased 150%. This technique permitted interpolation between pressure transducers and is very fast to compute. The second technique included finding the location where the standard deviation of the pressure increased by 150%. The pressure standard deviation technique proved not to be as effective at determining the LE location as the pressure rise technique [25]. The final LE detection technique implemented was to locate the high frequency content of the flow [24, 42]. In the research it was determined that the frequency content of the pressure measurement power spectral density (PSD) from a pressure transducer downstream of the shock train was primarily less than 0.2 kHz. When the shock train was upstream relative to the same transducer, more power was concentrated in the higher frequencies of the PSD (measured up to 4 kHz). As a result of these frequency findings, a technique in which the shock train LE was located by using an increase in the PSD was proposed [25]. While this technique was considered, the authors argued that calculating the PSD at each transducer and then finding the LE is too cumbersome as opposed to the previous simple pressure rise techniques [25]. The shock train LE detection methods were not validated using optical measurements in these contemporary studies [25, 42].

Several researchers have considered how to detect the location of a shock train LE. Historical studies were hampered by accuracy issues, primarily due to a lack of

computing power, while contemporary studies were hampered by a lack of validation by high-speed optical measurements (i.e., shadowgraph measurements greater than 30 frames per second). This research bridges the gap by considering a shock train LE detection technique that is accurate to distances between transducers and is validated using optical measurements taken at 500 frames per second.

2.4 *Current Modeling*

After validating a method to locate the shock train LE, the next step was to develop a dynamic model of the system. Some models exist for the scramjet, but generally either neglect the shock train or are limited in input space to not including the entire isolator. In this section, the current state of research into scramjet isolator modeling is discussed.

2.4.1 Linearized Models. Several researchers [7–10] attempted to derive the dynamics of a normal shock using first principles. In these theories, pressure perturbations were assumed to act like acoustic waves in the flow and a model for the system dynamics was developed by applying a perturbation theory approach to the normal shock relations. One of the best known models [7] assumed acoustic disturbances from both the inlet and the combustor would travel through the boundary layer to perturb a normal shock. Unfortunately, this analysis was based on a thin normal shock as opposed to a shock train. Additionally, since perturbation theory, which is a linearization technique based on small perturbations from a selected point, was used, the model produced is only valid for small perturbations from any point rather than the entire isolator length. Later [43], a piecewise linear method was used to enlarge the input space for the control of a normal shock by creating a series of linear models around an equilibrium manifold. The analysis accomplished [43] was also built on the assumption of a normal shock, so would, potentially, have limited applicability to a shock train.

2.4.2 *Engine Models Developed to Support Hypersonic Vehicle Models.* The next major focus of study that resulted in scramjet models dealt with the study of the simulation and control of the total hypersonic vehicle, primarily for pitch control [4, 30, 44]. In these studies, the scramjet was typically treated as an actuator. Only later modeling efforts [29, 31] included significant details of the scramjet interior operation. Additionally, these studies were used to optimize flight profiles for single-stage to orbit missions using various techniques [45]. These studies were typically based on a X-30-type airframe with an integrated airframe/propulsion flowpath as displayed in Figure 2.1. In this configuration, the forebody compresses the flow and

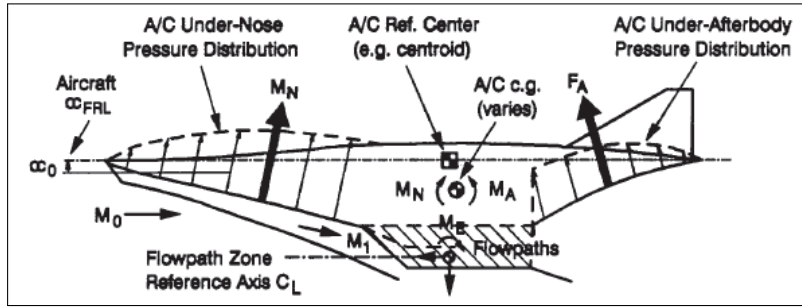


Figure 2.1: Integrated hypersonic engine flowpath [4]

the flow is expanded along the aft-body, creating significant forces on the fore and aft of the air vehicle. As a result, there is a strong coupling between the propulsion, aerodynamic pitch control, and the vehicle's elastic body [44, 46]. An extension of this initial research was on the optimal configuration for a hypersonic launch vehicle. This research revealed that the maximum achievable mass fraction for these air vehicles is a strong function of the propulsion system efficiency [47].

In an effort to improve hypersonic air vehicle modeling efforts, AFRL sponsored research that included the shock train [29, 31]. This research did provide for a higher fidelity model of the propulsion flow by first considering fuel burn time based on individual fuel species and, second, considering the strength of the pre-combustion shock train using impulse functions. In regards to the isolator portion of the model, although a more refined model than previous attempts, it still did not relate the LE location to the P_{BP} from the combustor. Rather, the model, which included fuel

ratio and fuel burn rate, modeled the static pressure increase across the whole shock train, not the location of the shock train LE. As a result, the model would not be able to predict the location of the shock train, only that there would be a shock train somewhere within the isolator. Additionally, the authors commented that the model is too complex to be used for real-time, model-based control due to the computation time needed to calculate solutions with the model. While those modeling hypersonic air vehicles are refining their propulsion model, they have not created a model relating the back pressure to the LE location.

The current models have several inadequacies for application to an automatic control algorithm for controlling the shock train LE location throughout the length of the isolator. First, the linearized normal shock equation models are based on a normal shock assumption. Applying perturbation theory to the normal shock equations limits the applicability of these models in regards to the isolator length range for which they are valid. Models designed for hypersonic vehicles are inadequate for an automatic controller since they either completely neglect the shock train or do not predict the location of the shock train LE. The contribution of this research was the development of a model, applicable throughout the isolator, that is specific to the shock train LE location.

2.5 Controls

The final portion of this research included designing a feedback controller capable of controlling the LE to a desired location without unstating the isolator. The control of a scramjet has been shown to be a challenging hurdle to overcome [35]. Additionally, there are few open-source papers that discuss scramjet control algorithms as implemented on current vehicles. As a result, the state of the art for the control of scramjets is still in its formative stages and there is still a great deal of discussion as to the best “actuator” to be used to control the scramjet flow. The primary goal of most scramjet controllers is to prevent unstart while allowing the largest pressure increase possible in the isolator. The maximum pressure increase expected in an isolator is that

caused by a normal shock [48]. The previously proposed published control algorithms are based on proportional, proportional-integral, or quadratic control [7, 35, 49–53]. Additionally, there have been some more contemporary authors that have considered nonlinear controllers in the form of a “smoothed” controller or gain scheduling [18, 54].

2.5.1 Proportional Controllers. One of the first applicable controllers [7] was designed to prevent unstart of a normal shock within a diffuser and was based on a model developed using the perturbation approach described in Subsection 2.4.1. While the assumption when creating this model was that there was a single normal shock in the inlet, the analysis is still useful for scramjet research. The analysis was based on an acoustic wave approach for shock motion as well as acoustic reflection and transmission where flow disturbances were modeled as either acoustic or entropy waves propagating through the flow. As a result of this propagation time and the delays resulting from that propagation time, it was noted that the control bandwidth would be limited. Although the assumption that there is a single shock is not applicable to a typical isolator, there will likely be a time delay in an isolator as well due to the time needed for pressure waves to travel through the boundary layer to the shock train leading edge. To control the shock train location, a proportional controller was used based on the perturbation-theory based model. The proportional gain was calculated based on the effects of acoustic waves traveling through the system in order to compensate for the aforementioned time delays. Using the proportional controller on bleed air to decrease the boundary layer size, the normal shock was able to track to the desired location through flow disturbances in simulation [7]. Additionally, proportional control and simple on/off control have been considered [7, 49], for use in bleed air controllers to regulate the amount of mass removal from the flow [50, 55] to minimize the impact on thrust.

An example of a fielded system utilizing a proportional fuel-flow controller is the X-43A. The X-43A propulsion system controller (PSC) was used to prevent unstart by changing the fuel flow using a proportional-integral with feedforward controller.

Additionally, the X-43A PSC commanded the inlet cowl to either full-open or closed. The X-43A PSC decreased the amount of fuel when an unstart became probable in the course of a flight [35]. Finally, NASA and Russia tested a scramjet in 1998 that opened and closed fuel valves to prevent unstart based on the shock train LE reaching a certain location [51]. Neither of these controllers offer the capability to actively direct the shock train LE to a desired location.

2.5.2 Optimal Controllers. As discussed in the modeling section, researchers attempting to model and control a hypersonic air vehicle considered scramjet models of varying detail. These models typically consider the scramjet as an actuator in the control scheme and the actual control algorithm for the engine itself is neglected. While these controllers are, generally, highly optimized based on the pre-planned flight profiles, several will also have another controller (e.g., linear quadratic controller [52], proportional-integral (PI) and proportional-derivative (PD) [53]) to handle perturbations from the optimized route. The controllers use the cowl and diffuser cross-sectional areas as well as the fuel equivalence ratio as actuators to maintain air-vehicle attitude. While these techniques have shown promise in controlling the air vehicle, these control techniques have neglected the shock train LE location within the engine itself.

2.5.3 “Smooth” Controller. In a recent paper [54], three controllers were considered to control the location of the shock train LE to prevent unstart: a proportional controller, a PI controller, and a “smooth” controller. The smooth controller adds a ‘smoothing’ term, in the form of a hyperbolic tangent scaled off the maximum measured disturbance, to the proportional controller. The results were that the proportional controller was not able to track to the desired shock location after a disturbance whereas the PI controller was able to accomplish this task. The actuator used in this research was the change in the inlet cross-sectional area. When restrictions on control authority were placed on the controller, the PI controller was unable to accurately track the desired shock location, whereas the “smooth” controller was

able to track the desired shock train location and handle control bandwidth limitations [54].

2.5.4 Gain Scheduling. Others have developed a control algorithm using gain scheduling [18]. In this approach, the shock train dynamics are modeled as noise and the gains in a PI controller are based on the location of the shock train LE within the isolator. Through simulations, the authors validated a gain scheduling approach to controlling the location of the shock train within the isolator. No experimental results were presented in the research.

2.6 Literature Review Conclusion

The purpose of the literature review was to describe the state of the art in scramjet LE detection, modeling, and control. While multiple authors have developed methods to measure the location of a shock train LE, either the methods were validated with lower frequency (30 frames per sec) shadowgraph photography or the shock train LE locations were not validated at all. The measurement portion of this research builds upon the previous research by validating the detected (by the measurement algorithm) shock train LE location on a frame-by-frame basis using high-speed (500 frames per sec) shadowgraph photography. Next, current dynamic models range from those developed using perturbation theory, which limit the input space of the model to small pressure perturbations, to models that disregard the shock train LE location altogether. This research initially builds upon the perturbation theory models by introducing a nonlinearity to increase the input space for the perturbation models to include large pressure increases. After increasing the input space with a nonlinearity, the first-order-lag model was reconsidered with different model types to develop a model that can accurately predict the shock train LE location throughout the test section. Finally, there are no controllers in the open literature capable of placing the shock train LE location at desired locations throughout the test section that have published experimental results. In this research, a control algorithm was

developed and validated that provides control authority throughout the test section. In the next chapter, the methodology and test apparatus used in this research will be described.

III. Methodology

In this chapter, the test apparatus, test conditions, and laboratory procedures used to collect data are presented. The test apparatus, located at the AFIT aeronautical engineering laboratories, included a cold-flow supersonic wind tunnel along with computers for data collection. Section 3.2 includes a discussion on the test conditions and procedures as well as a discussion of shock waves that form within the test section. The dynamics of the ramp assembly are discussed in Section 3.3.

3.1 Test Apparatus

The primary test components were a vacuum pump and reservoir, a stagnation chamber and a high-pressure compressor (up to approximately 180 psi) and reservoir to provide the airflow for the test section. Additionally, there are several valves, both manual and automatic, to provide control of the air flow. A drawing of the test setup is presented in Figure 3.1 and pictures of the test facility components are presented in Appendix F. The actual test section is 24 in. long and has square cross-sectional dimensions of 2.5×2.5 in. An illustration of the test section with the transducer mounting locations noted on the illustration is presented in Figure 3.2. For all runs conducted, a M=1.8 nozzle was attached to the test section. A drawing of the Mach 1.8 nozzle, drawn to scale, is presented in Figure 3.3.

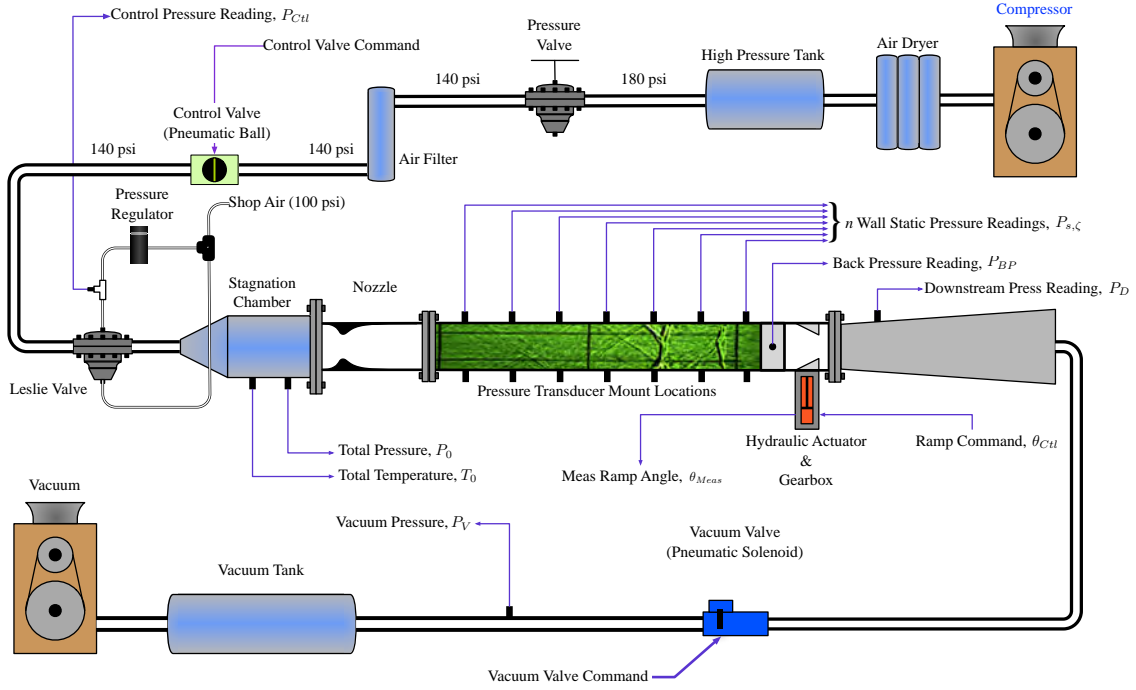


Figure 3.1: A drawing of the air flow path (not to scale)

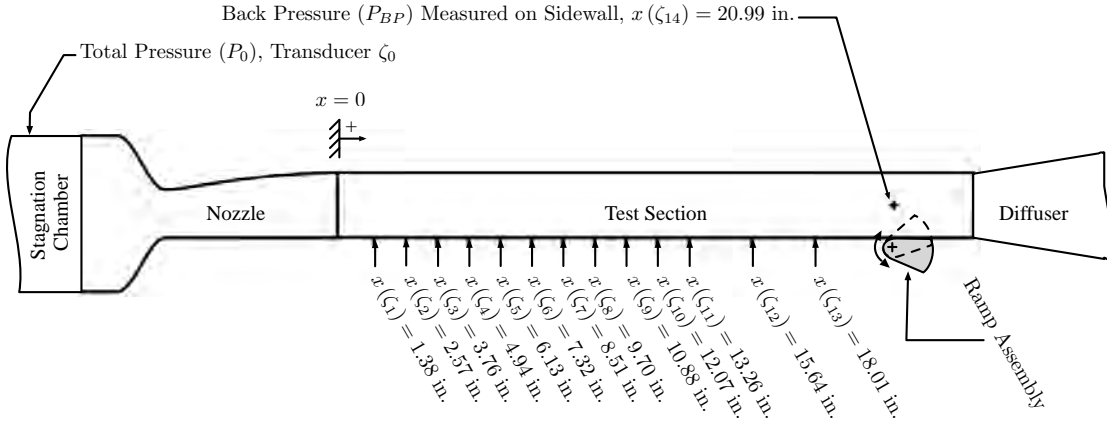


Figure 3.2: A drawing of the test section and transducer mounting locations (not to scale)

The computer system used in this research was a National Instruments (NI) Peripheral Component Interconnect eXtensions for Instrumentation (PXI) chassis computer system. This system, which used Windows XP as an operating system, allowed

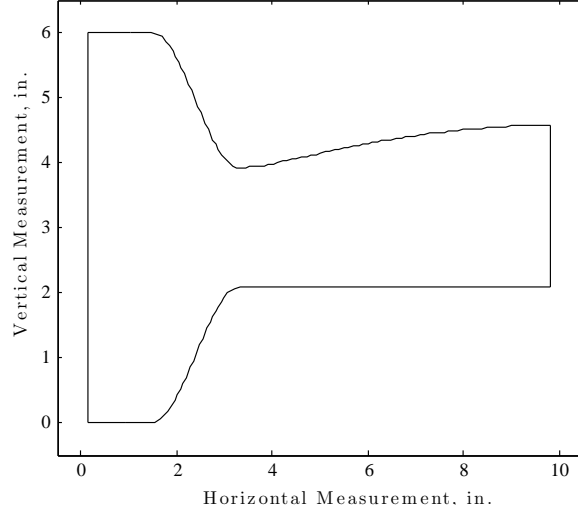


Figure 3.3: A drawing of the Mach 1.8 nozzle used throughout this research

inputs and outputs for data collection and control signals through several removable cards. The NI PXI unit used for this research operated a NI Laboratory Virtual Instrumentation Engineering Workbench (LabVIEWTM) program that started, analyzed (when applicable), and stopped each run.

Prior to the commencement of the research detailed in this dissertation, the AFIT supersonic wind tunnel was modified to incorporate a ramp assembly in the test section and mounting points for pressure transducers along the test section floor and ceiling as a part of a Masters thesis [56]. The wind tunnel has two nozzles, one for Mach 2.94 flow and one for Mach 1.80 flow. A lambda shock train was produced in the Mach 1.80 flow and an oblique shock train was produced in the Mach 2.94 flow, consistent with anticipated results [2]. Both shock train types were observed using shadowgraph photography. Having both nozzles allows for research on both types of shock trains utilizing the same wind tunnel and test section. There is a very limited ramp angle range between shock train formation and unstart (average of $\Delta\phi = 0.377$ deg. where $\Delta\phi$ is the difference between the ϕ_{Meas} at shock formation and the ϕ_{Meas} at unstart in this instance) for the Mach 2.94 nozzle [56]. The commanded accuracy of the ramp assembly is only accurate to ± 0.2 deg., though. As a result, the range for active control using the Mach 2.94 nozzle in this test configuration is

negligible. For the Mach 1.80 nozzle, the range between shock formation and unstart is larger ($\Delta\phi \approx 4$ deg.) using both the top and bottom ramps. The available ramp deflection is then increased to approximately $\Delta\phi \approx 6$ deg. when only the bottom ramp is used in the Mach 1.80 flow. In addition to the increased ramp deflection range from removing the ceiling-mounted ramp, removal of the ramp also decreases the rotating mass, thus increasing (marginally) the bandwidth of the ramp assembly. The ramp bandwidth will be discussed in Section 3.3. As a result of the control authority, increased ramp bandwidth, and the experimental necessity, only the Mach 1.80 nozzle with a single ramp was considered in this research.

After removal of the ceiling-mounted ramp, the test section ramp assembly consisted of a single ramp mounted in the floor in the downstream portion of the test section. The location of the ramp is indicated in Figure 3.1 and a picture of both of the ramps (before the upper ramp was removed) is presented in Figure 3.4. The ramp was connected to a hydraulic actuator controlled with an MTS[®] proportional-integral-differential (PID) controller with inputs from the LabVIEW[™] system. The PID gains were set prior to the collection of any data and were not changed during data collection. The MTS[®] controller accepted external commands from the LabVIEW[™] controller via analog voltages for the desired hydraulic extension and provided feedback on the hydraulic extension via analog voltages. The digital-to-analog and analog-to-digital conversions were accomplished by the LabVIEW[™] computer.

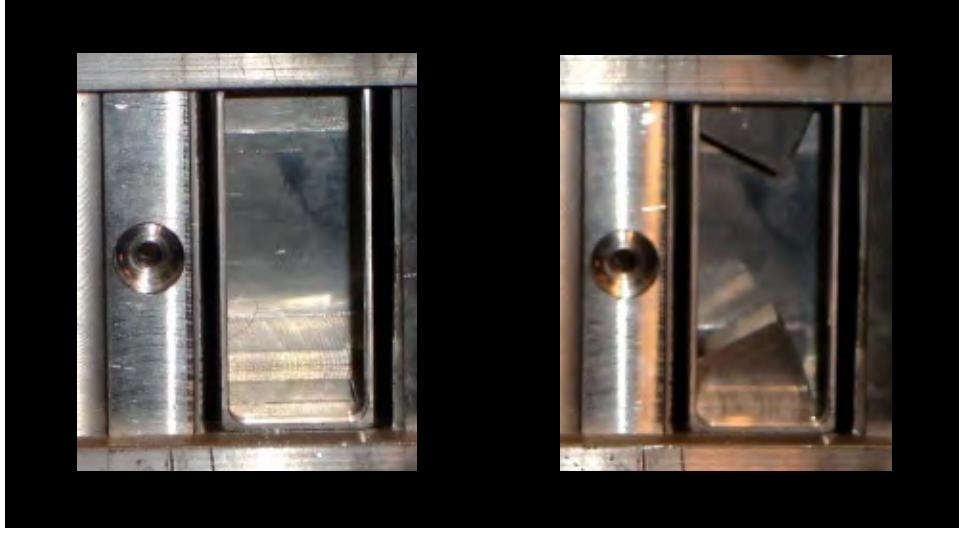


Figure 3.4: A picture of the ramps contracted and extended

Pressure transducers were placed along the top and bottom of the test section to measure the wall static pressure and deduce the shock train LE location using the detection algorithm validated in Chapter IV. There are n_t transducers used in each run. They are labeled with the symbol ζ and mounted with the most upstream transducer at station one. Therefore, for example, the most upstream transducer was ζ_1 , which was mounted at x_{ζ_1} and collected pressure data $P_{s,1}$. The pressure transducer numbers increased as they were mounted further downstream with the most downstream transducer measuring P_{BP} . The pressure transducers selected for this research were Endevco 8530c-50 pressure transducers. These piezoresistive units provided high frequency capabilities (up to 320 kHz) as well as the ability to measure pressures up to 100 psia. These 15 transducers were then connected to five Endevco Model 136 three-channel DC amplifiers which provided a voltage to the NI PXI computer and the LabVIEWTM software which accomplished the analog-to-digital conversion. The transducers were calibrated prior to the collection of any data at the AFRL Propulsion Directorate and the calibration data is presented in Appendix G.

Finally, in addition to the LabVIEWTM collected data, data was also collected using a high-speed camera configured to collect shadowgraph images. The camera

was a Photron FASTCAM-X 1280PCI camera attached to a PC running Photron Fastcam Viewer (PFV) version 2.4.3.8 software. The camera recorded 500 frames per second (FPS) at a full resolution of 1280×1024 pixels [57]. Additionally, due to the mirrors used, the camera had a limited field-of-view of approximately 9 in. of the test section so tests over the entire test section required multiple runs along with camera moves. The camera was activated with a signal from the LabVIEWTM software to the PFV software, which activated the camera, added a time stamp to each image, converted to an audio video interleave (avi) file and saved the video. The avi format allowed the video to be viewed as a video for frame-by-frame for analysis.

3.2 Operating Conditions and Experimental Procedure

All tests were run in a room that is heated and cooled for the winter and summer, respectively. Additionally, the room barometric pressure was recorded on each day of testing using a separate barometer located in the lab. Finally, following precedent [56], the wind tunnel was always started prior to deployment of the ramp. This technique ensured a started tunnel prior to any experimental effort, allowing a common starting point for all experiments.

3.2.1 Test Procedure. A typical run lasted for 15 seconds and can be divided into four data collection phases. The first two phases involved taking ambient measurements from each transducer and the thermocouple and then opening the vacuum chamber valve. The third phase included opening the high-pressure tank valve and starting the wind-tunnel. During this third phase, labeled the tare phase, the ramp is not deployed. The tare pressures from each transducer, P_{Tare, ζ_i} , are the time-average of the static pressure readings from each transducer over this phase after the pressures have steadied. Typical tare flow is for approximately two seconds on each run. The final phase, in which data was recorded, started when the ramp was deployed to cause changes in P_{BP} and the individual static pressures, P_{s, ζ_i} . After data collection had ended, the run concluded when the high-pressure valve and the vacuum chamber

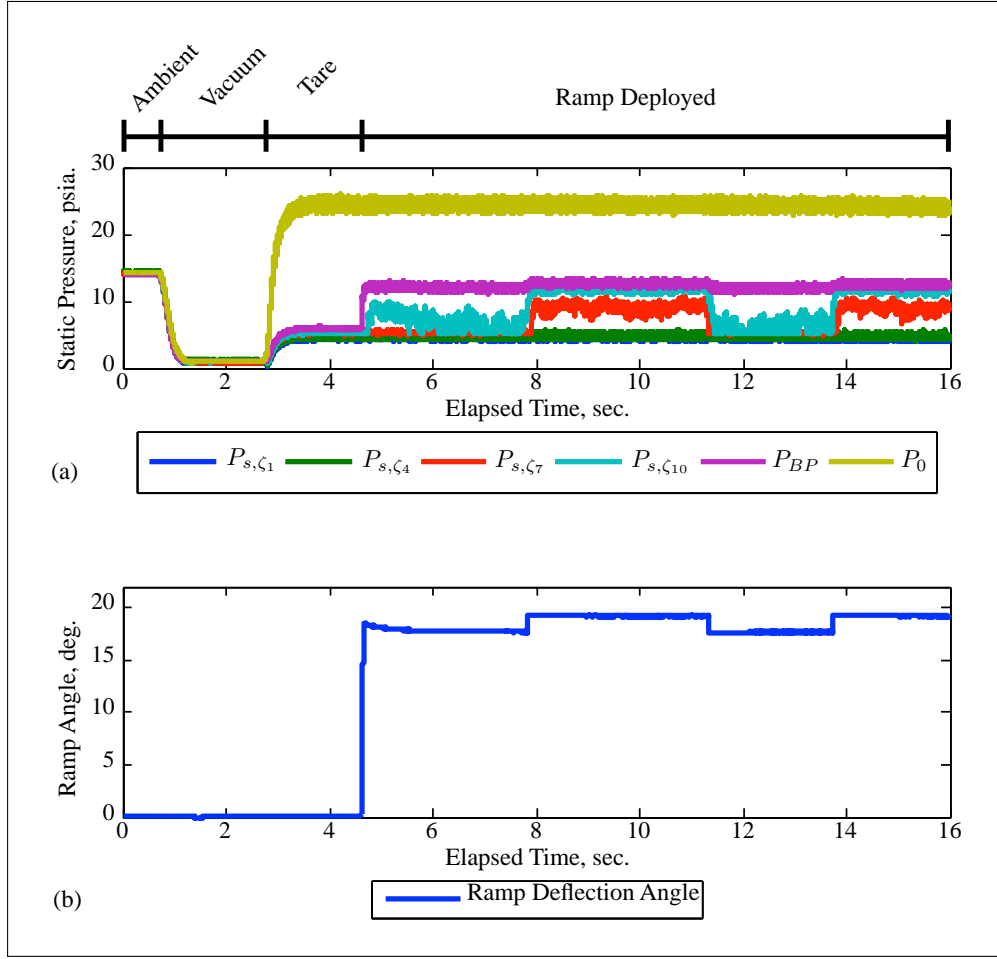


Figure 3.5: (a) Data collection phases and high-frequency pressure measurements (b) Ramp deployment angles

valve were closed. A plot of the measurements from six pressure transducers as well as the ramp deflection angle for run 4.9, to be discussed in Chapter IV, is presented in Fig. 3.5.

3.2.2 Test Section Shock Waves. A plot of the static pressure along the test section floor and ceiling prior to ramp deployment is presented in Figure 3.6 for $Re=4.9 \times 10^6/ft.$ and Figure 3.7 for $Re=7.3 \times 10^6/ft.$ In each of the figures, the pressure plot is presented in the (a) plot and a shadowgraph image of the entire test section (created by pasting three images together to get the full test section) is presented in each (b) plot. As can be seen in the pressure plots, the pressure generally increases

along the test section, which would be expected in typical Fanno flow without a shock. The flow in the initial portion of the test section does not follow this assumption, though, and exhibits a significant pressure fluctuation in the 3-5 in. region primarily along the top of the test section. Potential sources of this increase are the nozzle asymmetry and the interface between the nozzle and the test section which has a 0.011 in. lip that could cause the shocks that are obvious in the shadowgraph images. The cause of the step between the nozzle entrance and the test section entrance is the slight difference in dimensions between the two as presented in Figure 3.8. In addition to the vertical dimension, there is also a dimensional difference in the horizontal plane, but there is no way to experimentally measure the horizontal plane effects since, other than the single P_{BP} transducer, there are no transducers mounted on the wall and the shadowgraph can not be placed to record vertically. There does seem to be a correlation, particularly in the low Reynolds number flow, between a shock impinging on the ceiling or floor and an increase in the static pressure. Additional research would be needed to discern the source of the pressure increase but it could be due to the nozzle asymmetry across the horizontal axis. A drawing of the nozzle contour is presented in Figure 3.3 and it can be seen that the nozzle top and bottom contours are not the same. This most likely results in asymmetric flow from the nozzle into the test section and potentially results in the pressure gradients noticed. For the purposes of the control and measurement algorithm, this pressure increase can cause an error in the calculated shock train location using pressure measurements. This error is evident when pressures are measured near the nozzle exit and will be discussed in Section 6.4.

3.2.3 Choke Points. In addition to the shocks that travel down the test section, the flow control was also degraded by a choke point upstream of the stagnation chamber. Throughout the testing a $M=1.80$ nozzle was used as shown in Figure 3.3. Assuming $M=1.80$, and isentropic flow, then $A^*/A_T = 0.6949$ and, since the test section has a 2.5 in. \times 2.5 in. square cross-section, $A_T=6.25 \text{ in.}^2$ where A_T is the test

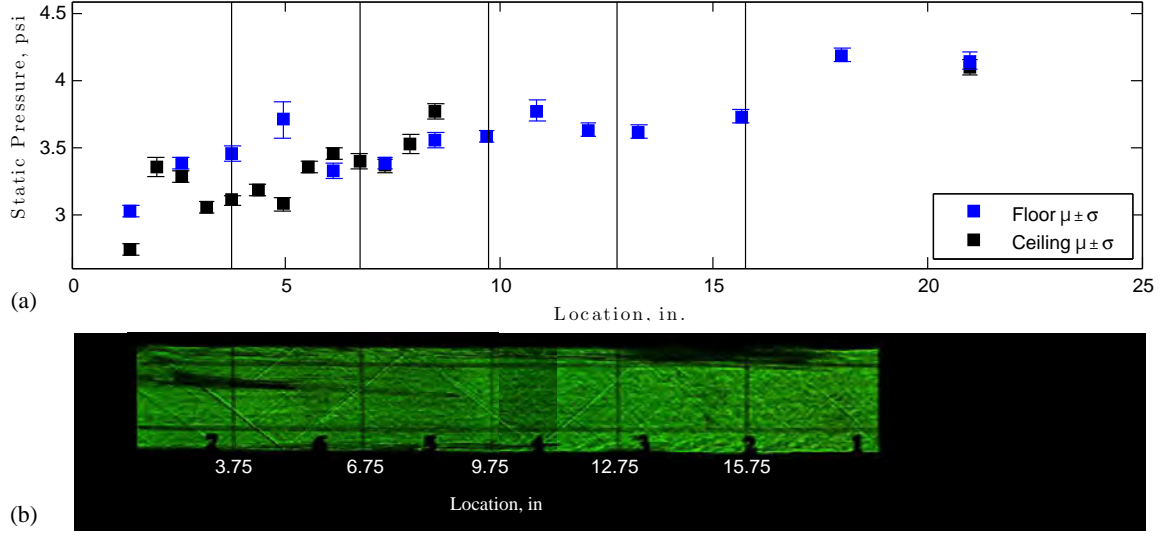


Figure 3.6: (a) The test section static pressures on the floor and ceiling (b) A shadowgraph of the entire test section ($Re = 4.9 \times 10^6/\text{ft.}$)

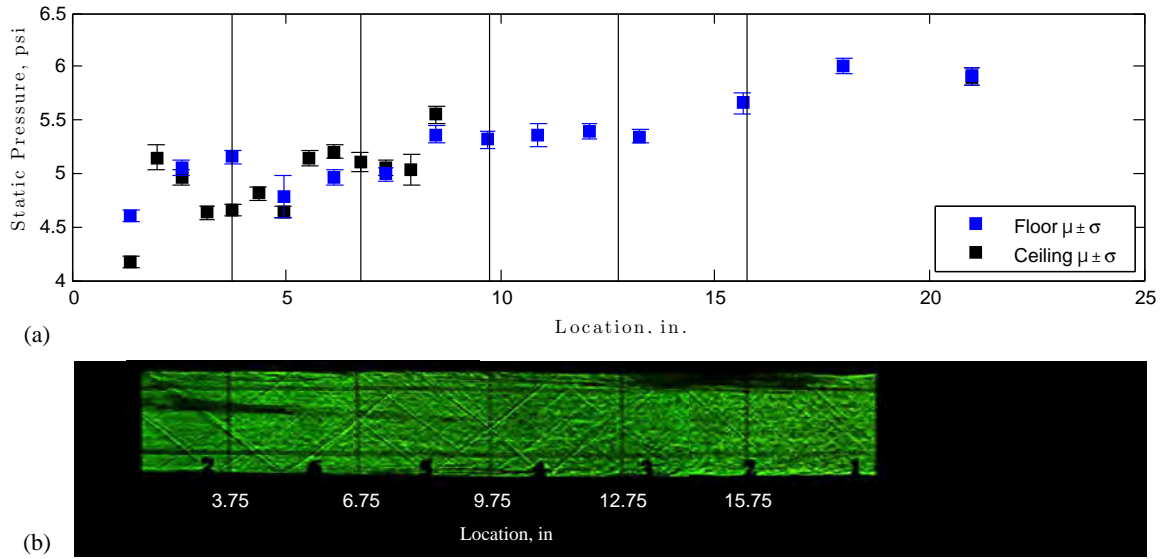


Figure 3.7: (a) The test section static pressures on the floor and ceiling (b) A shadowgraph of the entire test section ($Re = 7.3 \times 10^6/\text{ft.}$)

section cross-sectional area and A^* is the cross-sectional area of a $M=1$ throat. As a result, the flow will potentially choke where the cross-sectional area is less than 4.34 in.². Potential choke points include the piping downstream from the air filter which has an internal cross-sectional area of approximately 2³/₄ in.², the pneumatic control ball valve with an internal cross-sectional area of approximately 1¹/₂ in.², any potential

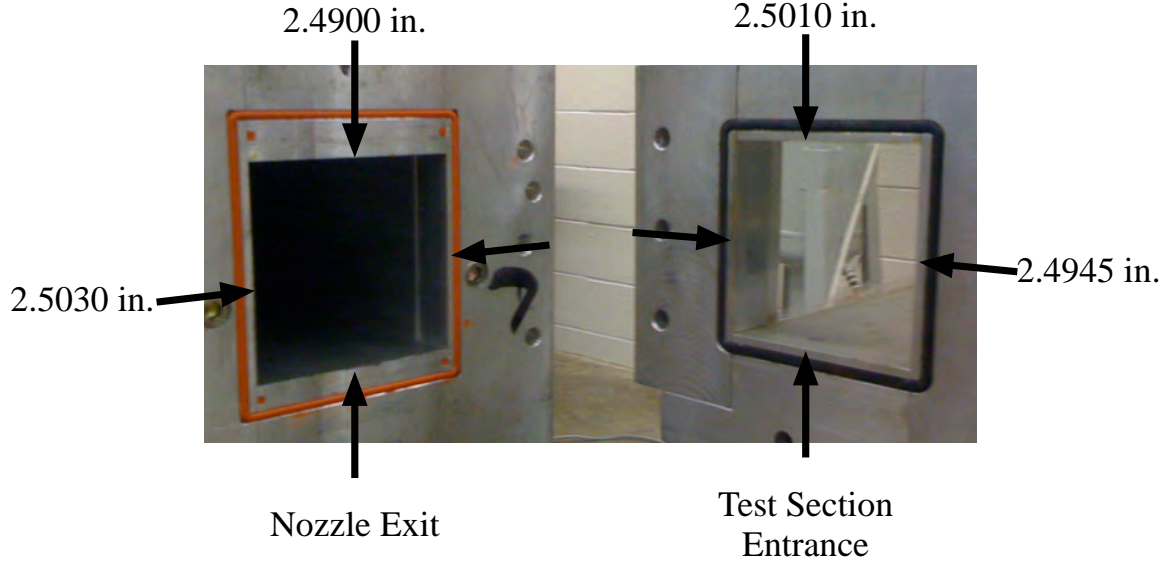


Figure 3.8: A photo of the nozzle exit and test section entrance

openings/fittings within the air filter, and the pressure valves in the flow. The result of the choke point was evidenced in a decrease in the available total pressure, P_0 , range for testing. The maximum total pressure achievable in the stagnation chamber using the $M=1.80$ nozzle is approximately 24.5 psia with a resultant Reynolds number of $7.6 \times 10^6/\text{ft}$.

3.3 Ramp Actuator Dynamics

The ramp dynamics were considered in order to develop a more complete model of the system for use in the control algorithm to be discussed in Chapter VI. The approach taken to model the ramp was to provide sinusoidal inputs to the ramp from 0.5 Hz to 50 Hz. The commands were generated using the pre-packaged LabVIEWTM signal generator code. The commanded ramp angle, ϕ_{Cu} and the measured ramp angle, ϕ_{Meas} , were recorded throughout the run. In order to increase the LabVIEWTM cycle rate, no other calculations were accomplished in the run. Additionally, no air was applied, so all the frequencies were tested in a single run. The sample rate for the ramp actuator study was 1 kHz.

The data was post processed and a Bode plot using ϕ_{Ctl} as the input and ϕ_{Meas} as the output was created as presented in Figures 3.9a and 3.9b. First, notice the actuator only has a 10 Hz bandwidth although the ramp assembly mass was reduced by removing the ceiling-mounted ramp sub-assembly. As a result, the ramp assembly is not able to control around any disturbances with a frequency greater than 10 Hz. The magnitude plot reveals that a two-pole transfer function with both poles at approximately 10 Hz adequately models the ramp at these lower frequencies. As can be seen by the significant phase drop in the phase plot, there is a significant transport lag. The transfer function that best fits the data in these lower frequencies is presented in Equation (3.1) and, in z-space, with $\Delta t = 0.001$ sec., in Equation (3.2) where z is the z-transform operator. The full ramp transfer function was used to develop the control algorithm to be discussed in Chapter VI.

$$G_{Ramp}(s) = \frac{27225}{(s + 164.9)^2} e^{-0.018s} \quad (3.1)$$

$$G_{Ramp}(z) = \frac{0.012204(z + 0.8959)}{(z - 0.8479)^2} z^{-18} \quad (3.2)$$

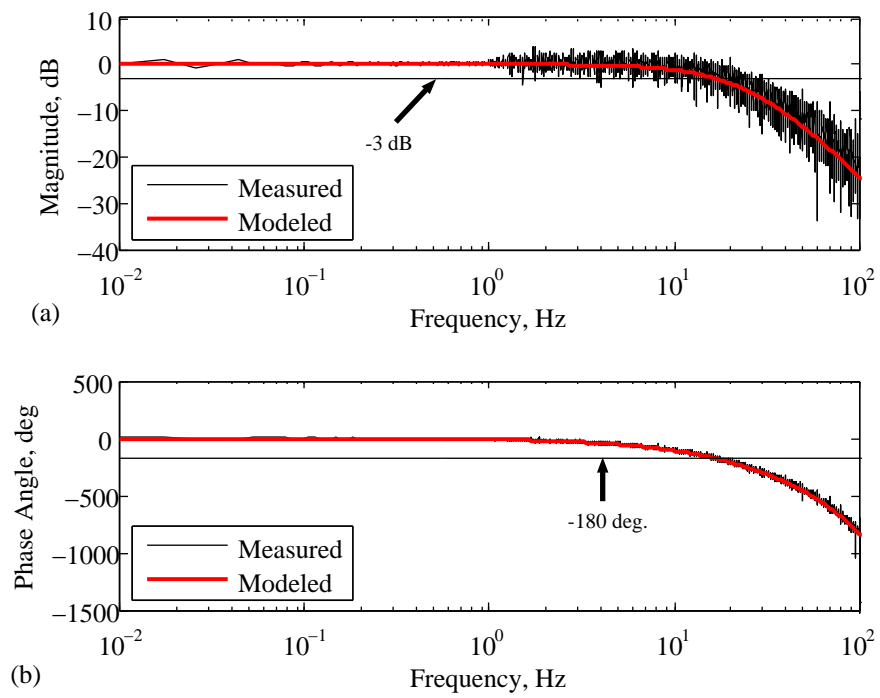


Figure 3.9: Transfer function of ramp input/measured output angle

IV. Shock Train Leading Edge Location Measurement Techniques

In order to control the location of the shock train LE, one must be able to measure the shock train LE location. The objective of this portion of the research was to develop and validate an algorithm capable of locating the shock train LE with the set of pressure transducers mounted along the test section floor. Six algorithms were compared to one another using the shadowgraph shock train location data as the “truth” data. Since previous studies [21–23] have shown accuracy equal to the distance between transducers, a goal of the research was to provide a validated algorithm to provide shock train LE location measurements with errors less than the distance between pressure transducers.

The research considered six previously demonstrated [23–25] shock train location measurement techniques. The first technique considered located the shock train leading edge using the ratio of the static pressure measurement at each transducer to the time average static pressure measurement at the same transducer taken during the tare portion of the run. In the second technique, the shock train LE location was calculated using the increase in static pressure along the test section with each set of pressure measurements. The increase in the pressure measurement standard deviation was used for the third technique. The fourth technique used the increase in the pressure measurement frequency content coincident with the shock train LE to determine the LE location. In the final two techniques, a correlation was developed between the shock train LE location measured using the shadowgraph imagery and either the sum of the static pressures or the back pressure. The shock train LE location could then be calculated using the correlation. For those utilizing pressure or frequency increase, different percent increases were also considered. The accuracy of each technique was then assessed against the high-speed shadowgraph LE measurements in post-processing. The most accurate techniques were then implemented in the LabVIEWTM system and run real-time to investigate their suitability for real-time control. The contribution of this portion of research is that, unlike previous research,

the shock train LE location from the six methods, x_{Meas} , was compared to the experimentally derived truth data, in this case the 500 frames per sec. shadowgraph-measured shock train location, x_{Optic} .

Fourteen runs were studied for this portion of the research, as presented in Table 4.1 where T_0 is the total pressure in Rankine, R , and P_0 is the total pressure (psia). In each run, the downstream-mounted ramp was quickly (approximately 20 ms) raised to the ramp angle indicated in Table 4.1, Column 2 to approximate a step input. In run 4.9, the ramp was raised to four different angles, $\phi_{CU} = [17.5, 19, 17.5, 19]$ so measurements could be made in both transient and long steady-state conditions. In runs 4.10-4.14 the ramp angle followed a five-level Amplitude-Modulated Pseudo-Random Binary Sequence (APRBS) [58] after the wind tunnel was started. The APRBS routine was selected to validate the measurement algorithm with significant dynamic inputs since APRBS inputs were chose for use as the input for the system identification techniques presented in Chapter V. The APRBS routine is described in further detail in Appendix D and the ramp angles are noted as “APRBS” in Table 4.1. Finally, the developed measurement algorithm was implemented for real-time shock train location recording and tested at different Reynolds number settings in runs 4.12-4.14.

4.1 Method Descriptions Along with Results and Analysis

Six methods were considered for calculating the shock train LE location. These methods include the pressure ratio method presented in Subsection 4.1.1, the pressure rise method presented in Subsection 4.1.2, the standard deviation method in Subsection 4.1.3, the frequency content method in Subsection 4.1.4, the pressure summation method in Subsection 4.1.5, and the back pressure method in Subsection 4.1.6.

The analysis of each technique includes a plot of the detected shock train location from run 4.9. Run 4.9 was chosen for algorithm development since it incorporates both significant ramp changes and long periods with no control inputs. The analysis for each technique will also include a plot of error in the detected shock train

Table 4.1: Test section operating runs

Run	Ramp Angle, deg	P_0 , psia	T_0 , R	Re Number
4.1	15	24.46	521	$7.58 \times 10^6/\text{ft.}$
4.2	16	24.43	521	$7.57 \times 10^6/\text{ft.}$
4.3	17	24.42	520	$7.57 \times 10^6/\text{ft.}$
4.4	17.5	24.41	519	$7.57 \times 10^6/\text{ft.}$
4.5	18.5	24.42	520	$7.57 \times 10^6/\text{ft.}$
4.6	19	24.44	521	$7.57 \times 10^6/\text{ft.}$
4.7	19.25	24.44	520	$7.58 \times 10^6/\text{ft.}$
4.8	19.5	24.43	520	$7.57 \times 10^6/\text{ft.}$
4.9	17.5, 19, 17.5, 19	24.45	520	$7.58 \times 10^6/\text{ft.}$
4.10	APRBS	24.45	520	$7.58 \times 10^6/\text{ft.}$
4.11	APRBS	24.42	521	$7.57 \times 10^6/\text{ft.}$
4.12	APRBS	23.82	525	$7.20 \times 10^6/\text{ft}$
4.13	APRBS	19.88	529	$6.04 \times 10^6/\text{ft}$
4.14	APRBS	15.84	530	$4.78 \times 10^6/\text{ft}$

location. The vector of errors, \mathbf{e} is defined as the difference between the vector of detected LE locations for all n_s time samples in a run, \mathbf{x}_{Meas} , and the vector of the LE locations from the shadowgraph, \mathbf{x}_{Optic} , according to Equation (4.1). Note that \mathbf{x}_{Meas} is down-sampled from 10,000 Hz to 500 Hz for the so it is the the same length as \mathbf{x}_{Optic} . Further, the optical and measurement data were synchronized by aligning the initial large motion of the shock train LE. The runs presented in Chapter V and Chapter VI were sampled at 1000Hz. The 500 Hz results are used for all location and error plots for clarity. The root mean square (RMS) of the error is then the RMS of \mathbf{e} as defined in Equation (4.2). After comparing the results of each technique on run 4.9 where the ramp was changed four times between 17.5 and 19 deg., run 4.10 was considered to compare the most accurate techniques using several ramp input changes throughout the run. The final measurement algorithm was selected using the data from run 4.10. Run 4.11 was used to validate the dynamic models developed in Chapter V after they were developed using the data from run 4.10. The measurement

algorithm was then validated at different Reynolds numbers using the data from runs 4.12-4.14 in Section 4.3.

$$\mathbf{e} = \mathbf{x}_{Meas} - \mathbf{x}_{Optic} \quad (4.1)$$

$$e_{RMS} = \sqrt{\frac{e^2(1) + e^2(2) \dots e^2(n_s)}{n_s}} \quad (4.2)$$

4.1.1 Pressure Ratio Method. The first of the six considered methods was labeled the pressure ratio method. The result of the pressure ratio method was labeled $x_{PR}(k)$ and was based on the ratio between the static pressure at each transducer with the ramp deployed and the tare pressure for the same transducer. The tare pressure is defined as the static pressure in the test section when there is flow, but prior to ramp deployment. P_{Tare,ζ_i} was the time-average of approximately two seconds of data at transducer i . Note, that, for simplicity, the term Δt will be assumed throughout the remainder of this research, so $x_{PR}(k)$ implies $x_{PR}(k\Delta t)$. To implement the pressure ratio method, the average tare pressure readings for each transducer in the test section, P_{Tare,ζ_i} , was compared to the static pressure at each sample, k , for the same set of transducers, $P_{s,\zeta_i}(k)$. A vector of the transducer pressure ratios as shown in Equation (4.3) was then created.

$$\mathbf{PR}(k) = \begin{bmatrix} \frac{P_{s,\zeta_1}(k)}{P_{Tare,\zeta_1}} & \frac{P_{s,\zeta_2}(k)}{P_{Tare,\zeta_2}} & \dots & \frac{P_{s,\zeta_{14}}(k)}{P_{Tare,\zeta_{14}}} \end{bmatrix} \quad (4.3)$$

The shock train location is then calculated for each k , by linear interpolation, using the vector of pressure ratios $\mathbf{PR}(k)$, a vector of the transducer mounting locations, \mathbf{x}_{Trans} , and the desired pressure ratio, PR_{Des} as in Equation (4.4) where *interp* implies linear interpolation. The linear interpolation method is detailed in Appendix B. PR_{Des} is the pressure ratio defined to be indicative of the shock train LE location.

$$x_{PR}(k) = \text{interp}(\mathbf{PR}(k), \mathbf{x}_{Trans}, PR_{Des}) \quad (4.4)$$

The pressure ratio for each transducer along with the mounting location for each transducer is displayed in Figure 4.1 with an example $PR_{Des} = 1.50$. The PR_{Des} points are based off the desired percent increase, ξ_{Des} , in the pressure ratio. The PR_{Des} points considered in this research were $PR_{Des} = 1.25, 1.50$, and 1.75 representing $\xi_{Des} = 25\%, 50\%$, and 75% static pressure increase in comparison to the tare pressures. The LE locations using this method at different ξ levels are presented in

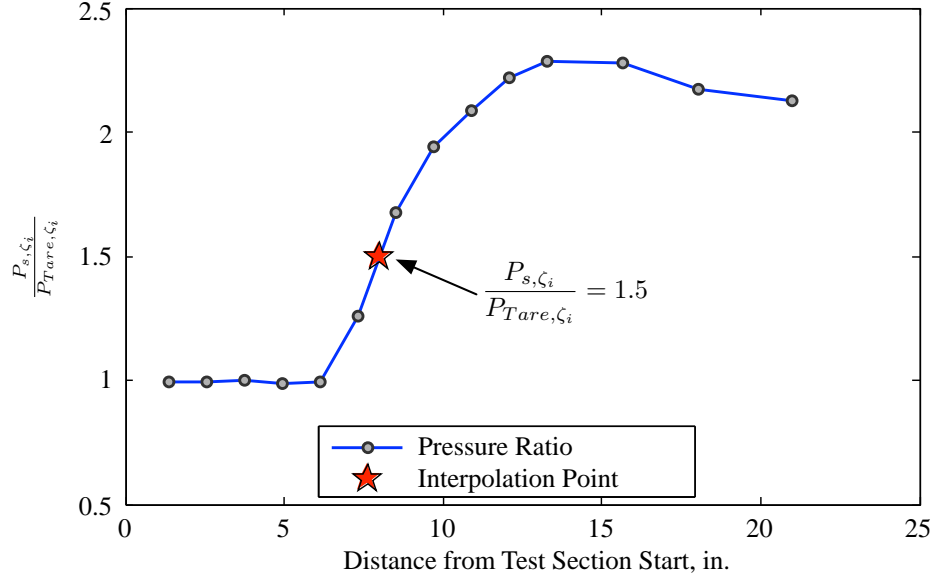


Figure 4.1: Illustration of pressure ratio measurement method

Figures 4.2a - 4.2c and the error is presented in Figures 4.2d - 4.2f. As can be seen, the 50% pressure increase criterion closely matches the location of the shock train LE throughout the run. This result confirms, based on shadowgraph shock train location measurements, previous research [24, 25] that the desired percent increase in the pressure is roughly 50% although the previous research was not confirmed with shadowgraph imagery taken at 500 frames/sec nor did it vary the percent increase level. The e_{RMS} result from this run is 0.3 in. (12% of D) and is also presented in Table 4.2 in the summary, Section 4.4.

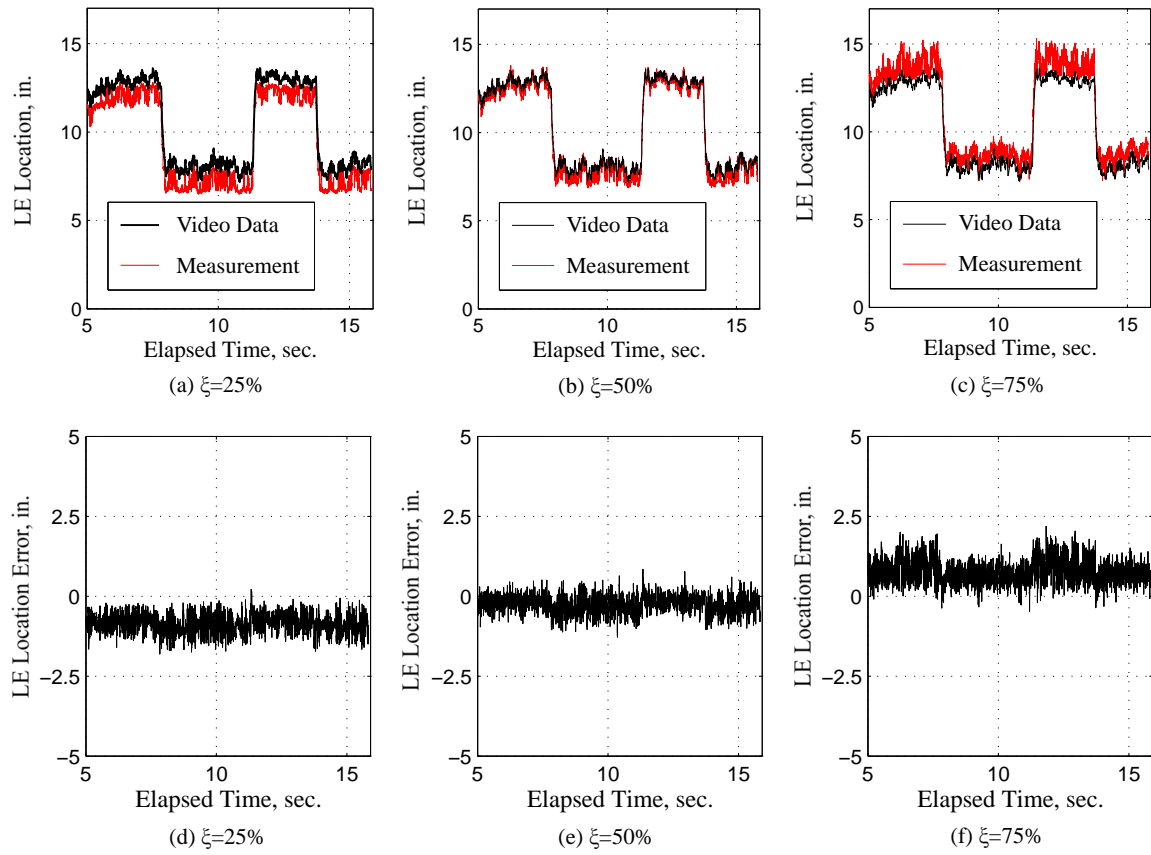


Figure 4.2: Pressure ratio method measurement and error plots

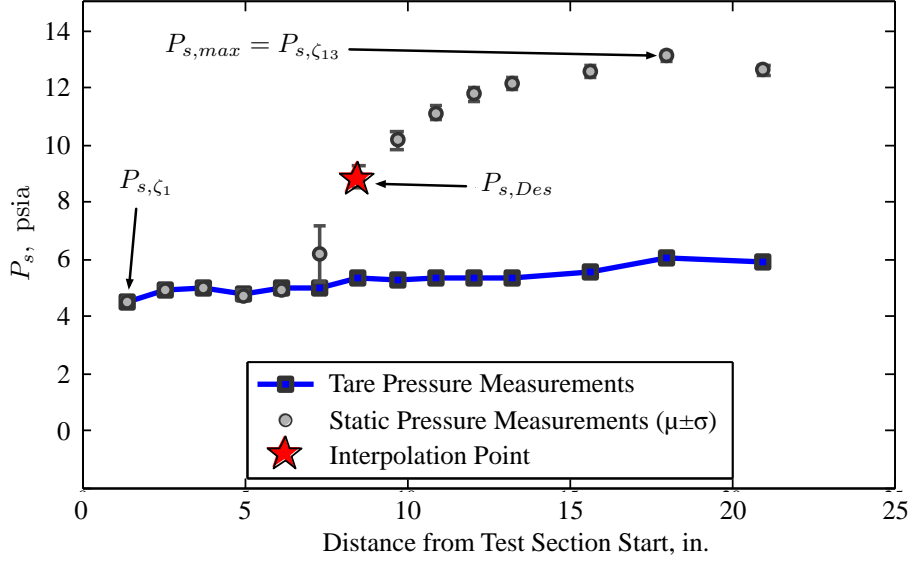


Figure 4.3: Illustration of pressure increase method

4.1.2 Pressure Increase Method. The second method, labeled the pressure increase method with the result labeled $x_P(k)$, was based on the increase in static pressure along the test section with the ramp deployed. The method relied on the pressure increase from the first transducer, ζ_1 , to the maximum test section static pressure measurement, $P_{s,max}$. An illustration to help clarify this method is presented in Figure 4.3. In this figure, the average tare measurement is provided as the blue line along the bottom to show the static pressure measurements before ramp deployment. The circle plots with the vertical lines are the average pressure measurements along with the pressure standard deviation from 300 data points taken when the shock train was in steady-state with a mean at approximately 7 in. Finally, the red star is the interpolation point that is used to locate the shock train LE location. The use of the pressure increase across the test section is similar to previous research [38] in which a percentage of the entire static pressure increase is used as an indication of the shock train location. In this method, first a vector of the static pressures along the test

section at each sample, k , was created as seen in Equation (4.5).

$$\mathbf{P}_s(k) = [P_{s,\zeta_1}(k) \ P_{s,\zeta_2}(k) \ \dots \ P_{s,\zeta_{14}}(k)] \quad (4.5)$$

The desired interpolation pressure was calculated using an equation similar to one from previous research [38] and a desired percent increase, ξ_{Des} as presented in Equation (4.6)

$$P_{s,Des}(k) = P_{s,\zeta_1}(k) + \xi_{Des}(P_{s,max}(k) - P_{s,\zeta_1}(k)) \quad (4.6)$$

where $P_{s,Des}$ is the desired pressure for interpolation. Finally, the shock train LE location was calculated for each sample, k , by interpolation using the vectors, $\mathbf{P}_s(k)$ and the transducer locations \mathbf{x}_{Trans} along with the calculated $P_{s,Des}(k)$ according to Equation (4.7). In Equation (4.7) *interp* implies using linear interpolation as it did in the previous section and the linear interpolation method is detailed in Appendix B..

$$x_P(k) = \text{interp}(\mathbf{P}_s(k), \mathbf{x}_{Trans}, P_{s,Des}(k)) \quad (4.7)$$

Unlike the previous method, this method requires no prior knowledge of a tare state and is, therefore, more operationally feasible. Inherent in this method is a fairly smooth increase in the static pressure, though. As was noted in Chapter III, the static pressure increases in the first five inches of the test section so location measurements using this method in the first five inches of the test section were problematic (this will be discussed in Section 6.4). This upstream inaccuracy is not inherent in the pressure ratio method since the pressure rise is in the tare pressure, which is then divided to create the pressure ratio vector. Since the pressure rise is in both the tare and the ramp-deployed pressure readings, it divides to a ratio of 1 unless the shock is over an upstream transducer. The shock train LE location as predicted using this method and different percent increases is presented in Figures 4.4a-4.4c and the error for each of the percent increases is presented in Figures 4.4d-4.4f. As was noticed in the previous method, the $\xi_{Des} = 50\%$ increase criterion was the closest to the shadowgraph results,

reaffirming previous research [25, 38]. The e_{RMS} result from this run is 0.3 in. (12% of D) and is also presented in Table 4.2.

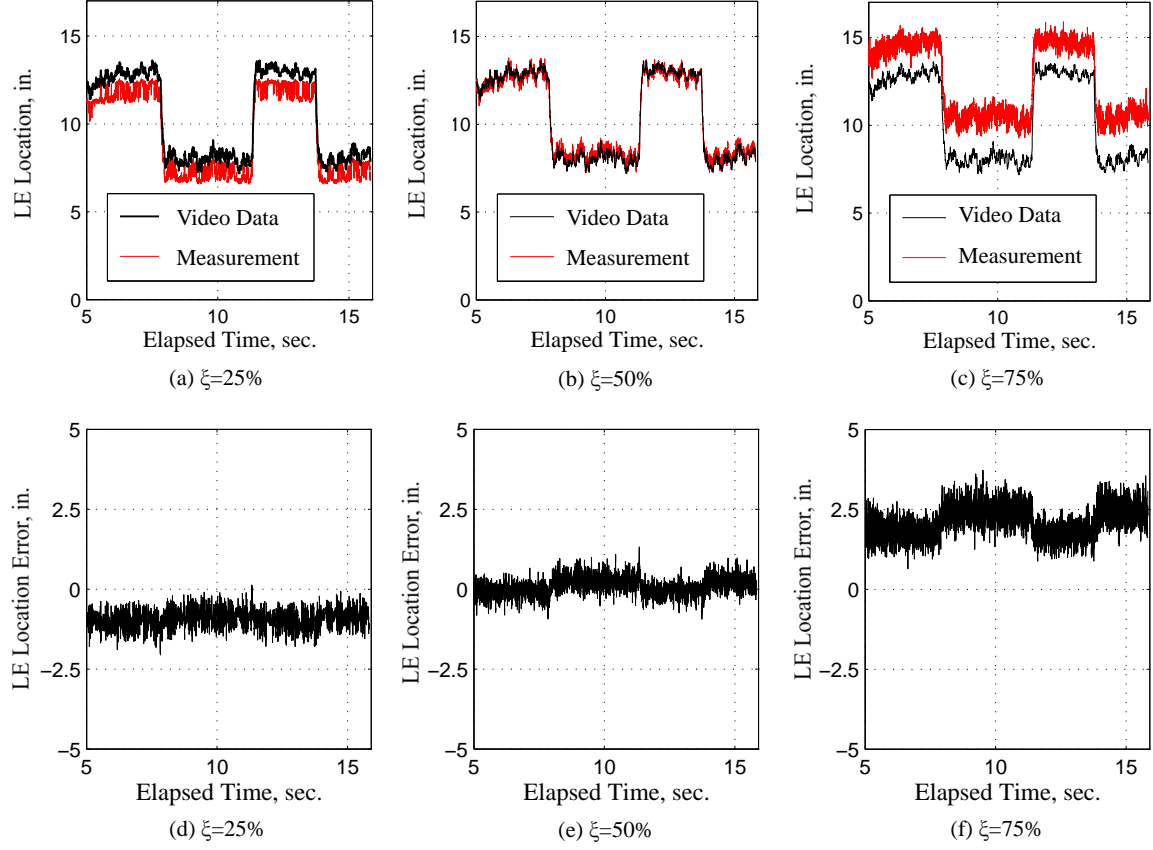


Figure 4.4: Pressure increase method measurement and error plots

4.1.3 Standard Deviation Method. The third method, labeled the standard deviation method with the results labeled $x_\sigma(k)$, was based on the increase in standard deviation, σ , of the static pressure measurements. The method relied on increases in the pressure σ when a shock train LE oscillates over or is upstream to a transducer as noted in previous research [25]. The increase in standard deviation was also noted in this research. Specifically, it was noted that the pressure standard deviation is lower when the LE is downstream relative to the measuring transducer and the standard deviation increases when the LE is upstream of a transducer. Finally, there is a significant increase in the pressure standard deviation when the shock train LE oscillates directly over the transducer. A plot of the pressure standard deviation measurements throughout run 4.9 for a transducer mounted at 9.7 in. is presented in Figure 4.5. The increases when the LE traverses the transducer as well as the two standard deviation levels when the LE is upstream and downstream relative to the transducer are noticeable on this plot. A very thin spike that is three to four times higher than the downstream standard deviation can also be seen in Figure 4.5 when the shock train LE crosses over the transducer.

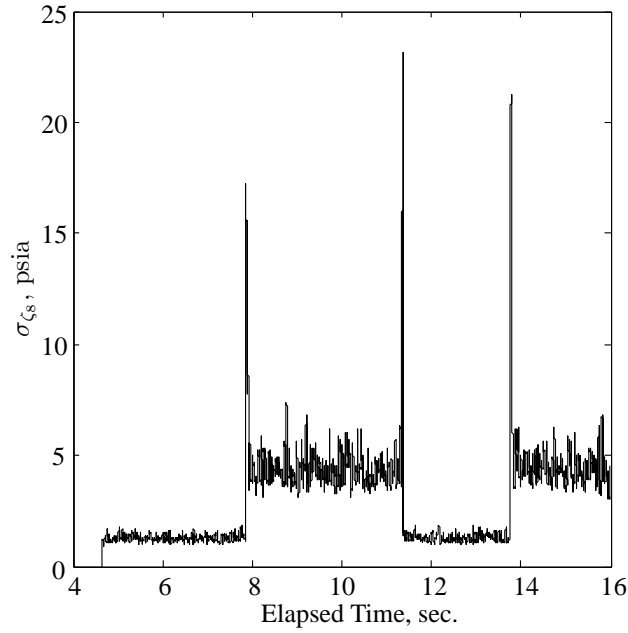


Figure 4.5: Standard deviation measurement throughout run 4.9 measured at 9.7 in.

A plot of the standard deviation measured along the test section at the different transducers is presented in Figure 4.6. In Figure 4.6 the predicted shock train LE standard deviation is displayed as σ_{Des} , σ_1 is the maximum σ in the test section and is located at x_1 . Also, σ_0 is the standard deviation in the transducer just upstream to the transducer measuring σ_1 and x_0 is mounting location for that transducer. Finally, σ_2 is the standard deviation in the transducer mounted just downstream to the transducer measuring σ_1 which is located at x_2 . These standard deviation and location measurements are used to locate the shock train LE using three assumptions with the assumed standard deviations valid at the tested Reynolds number:

1. When the standard deviation is measured to be greater than 18 psia at any transducer, the shock train LE is assumed to be over that transducer
2. When the $5 < \sigma_1 < 18$, the shock train oscillations span two transducers, as in Figure 4.6. In this case, the shock train LE standard deviation (σ_{Des}) is assumed and the LE location is projected with a straight line
3. When there is no measurement greater than 5 psia, the shock train LE oscillations over the previous 250 samples were assumed to be predominantly between two transducers. The shock train LE is then assumed to be midway between the maximum and downstream transducers used in the previous shock train location calculation.

The first assumption was made by studying Figure 4.5. When the LE crosses the transducer, the standard deviation jumps above 18 psia at this Reynolds number. The differences in the absolute values are most likely due to timing differences between when the shock train LE is atop a transducer and the time a pressure is sampled. Assumption two arises from Figure 4.6 in which the LE location is oscillating primarily between sixth (x_1) and seventh (x_2) transducers. This can be noticed by the significant standard deviation increase at transducer six (x_1) and the slight increase at transducer seven (x_2). This indicates that the majority of the increased pressure readings are over transducer six at x_1 , but a few increased pressure readings (over the

nominal downstream pressure reading) are over transducer seven at x_2 . A straight line assumption is then made to the desired standard deviation to locate the shock train LE. The final assumption arises from the handful of times when the standard deviation did not spike at any transducer. In this case, it was assumed that the LE was oscillating between two transducers and the LE location was just assumed to be the midpoint between the transducers used in the previous sample set calculation.

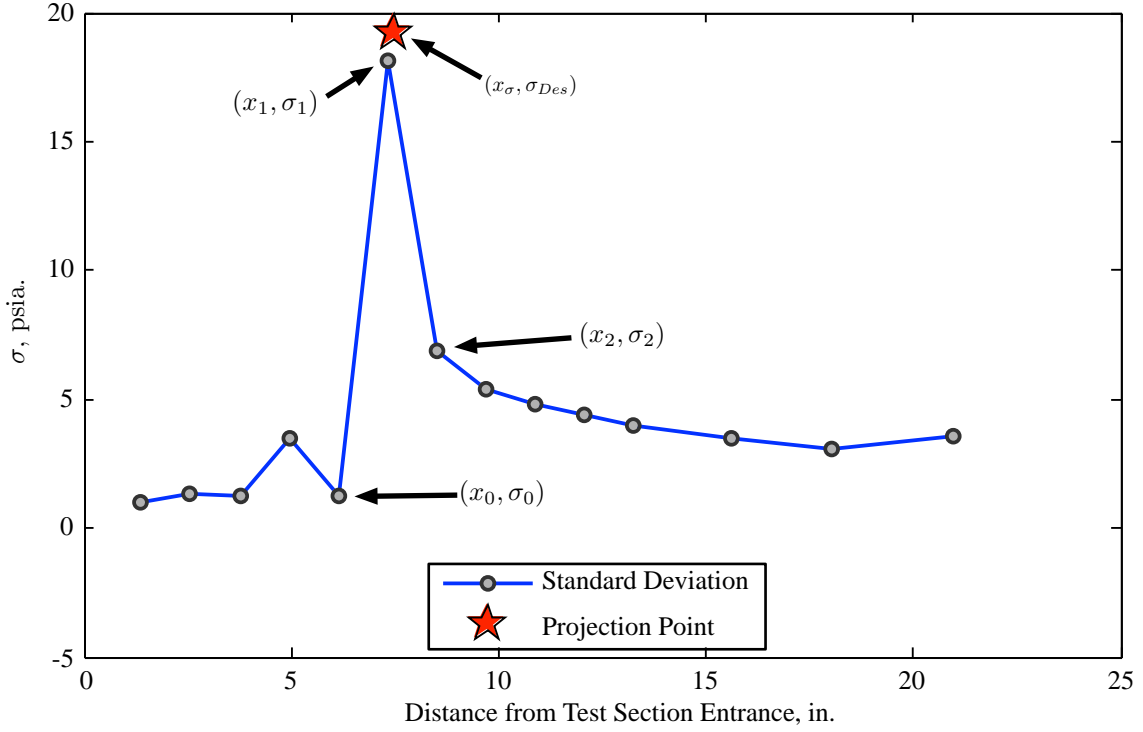


Figure 4.6: Diagram of the standard deviation method implementation

The σ used for each sample, k , was based on the previous 250 samples (i.e. $\sigma((k - 250) : k)$) with a 10 kHz sampling frequency. The procedure for this technique was to first collect a vector of standard deviations, as seen in Equation (4.8)

$$\boldsymbol{\sigma}(k) = [\sigma_{\zeta_1}(k) \quad \sigma_{\zeta_2}(k) \quad \dots \quad \sigma_{\zeta_{14}}(k)] \quad (4.8)$$

where

$$\sigma_{\zeta_i}(k) \equiv \sigma(P_{s,\zeta_i}(k)). \quad (4.9)$$

and σ is a vector of the test section σ measurements. The projection point σ_{Des} , assuming $5 < \sigma_1 < 18$, was then defined and x_σ was calculated using a linear projection assuming a continuation of the slope from (x_0, σ_0) and (x_1, σ_1) as presented in Equations (4.10)-(4.12)

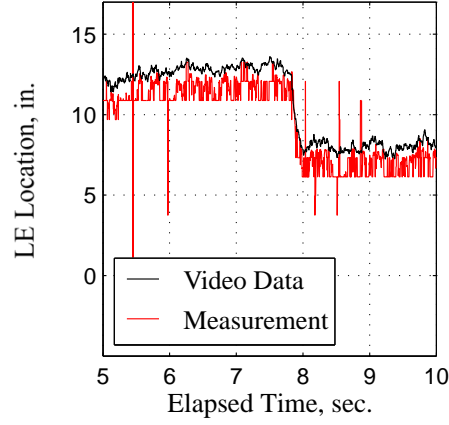
$$Slope = \frac{\sigma_1 - \sigma_0}{x_1 - x_0} \quad (4.10)$$

$$\sigma_{Int} = \sigma_1 - Slope \cdot x_1 \quad (4.11)$$

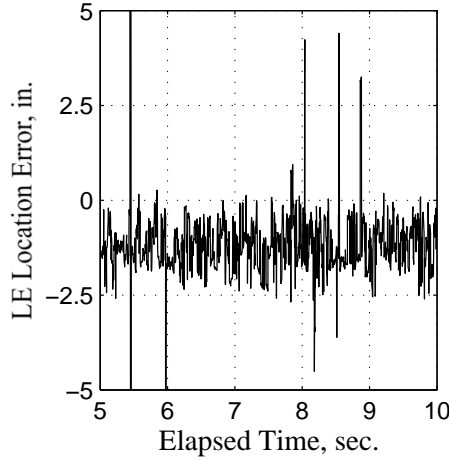
$$x_\sigma = \frac{\sigma_{Des} - \sigma_{Int}}{Slope} \quad (4.12)$$

The σ_{Des} values considered in this research were $\sigma_{Des} \in [12, 14, 16, 18]$. The calculated shock train location for each sample set is presented in Figure 4.7a and the error in the shock train location is presented in Figure 4.7b for the case when $\sigma_{Des} = 18$ in. For each of the σ_{Des} values, $e_{RMS} = 1.10$ in. or 44% of a duct height, D , so, due to the similarity of the plots, they are not presented.

While the standard deviation was able to predict the shock train LE location to within the distance between transducers, the method, using these assumptions, was barely able to do so. The primary reason for this is that the algorithm is looking for a thin standard deviation spike that is often between transducers. To gain additional accuracy, additional transducers are required, which is not the case with the other methods. It will also be seen that the standard deviation is less accurate than any of the other methods to be discussed. Additionally, the method is (marginally) more computationally expensive than using the pressure increase methods. Finally, due to the consideration of the previous 250 samples, there is an inherent latency in the algorithm. As a result of these considerations, the standard deviation is not an



(a) $\sigma_{Des} = 18$ in



(b) $\sigma_{Des} = 18$ in

Figure 4.7: Shock train LE location and error using standard deviation method

optimal method for locating the shock train LE and will not be considered further. The e_{RMS} result from this run was 1.10 in. (44% of D) and is presented in Table 4.2 for comparison to other methods.

4.1.4 Shock Train Location from Frequency Content. The fourth method was based on the increase in the power spectral density (PSD) of the pressure measurements on the wall at the shock train LE. The results of the PSD method are labeled $x_{\Psi}(k)$. When the shock train LE is downstream of a particular pressure transducer, there is less power in the higher frequency portion of the PSD, labeled with the sym-

bol ψ_{ζ_i} [24, 25, 39, 59]. Conversely, when the shock train LE is upstream to a pressure transducer, there is an increase in the high frequency portion of the particular ψ_{ζ_i} . This can be noted in Figure 4.8 in which the PSD is plotted for two transducers, one located at $x = 10.9$ in. and the other located at $x = 15.6$ in. while the LE is oscillating between 12.5 in. and 13.5 in. Specifically, PSDs were taken at the seven second point in run 4.9 according to the procedure explained in this section. As can be noticed, the transducer (at $x = 10.9$ in.) upstream to the LE location has a lower overall PSD measurement in relation to the transducer (at $x = 15.6$ in.) mounted downstream to the LE.

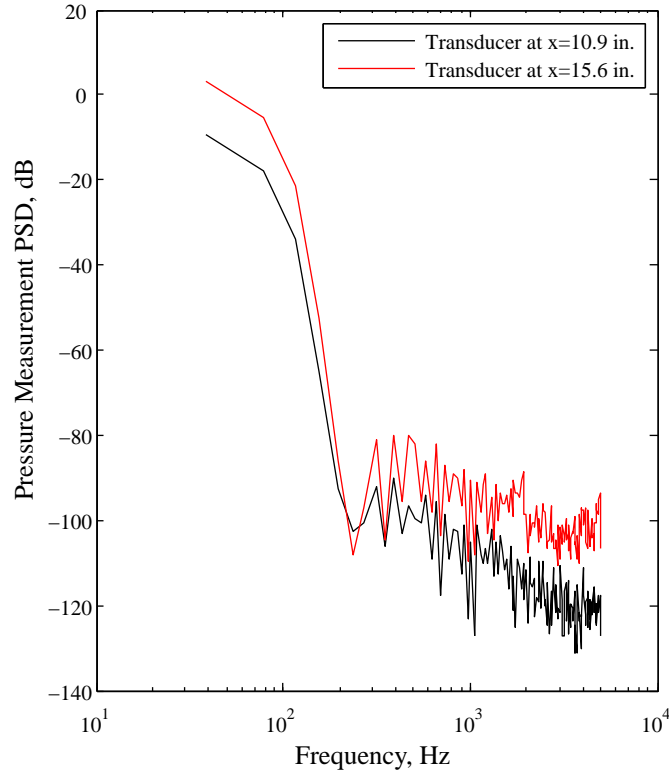


Figure 4.8: PSD for two transducers with LE between them

The method that was used to locate the shock train using the frequency content first involved taking the one-sided PSD of the previous 512 samples for all test section transducers as in Equation (4.13). To calculate the PSD, the **Matlab**[®]

pwelch.m command was used. A PSD calculation method is detailed in Appendix B. The output of the *pwelch.m* command was a vector of the power per frequency, $[\psi_{P_s, \zeta_i}(f_1) \ \psi_{P_s, \zeta_i}(f_2) \ \dots \ \psi_{P_s, \zeta_i}(f_m)]$, which was then used in the RMS calculation.

$$\psi_{P_s, \zeta_i}(k) = PSD(P_{s, \zeta_i}((k - 512) : k)) \quad (4.13)$$

The RMS value of the one-sided ψ_{ζ_i} was then calculated according to Equation (4.14). The $\psi_{RMS, i}$ values were then concatenated to form the vector, Ψ_{RMS} according to Equation (4.15). The vector Ψ_{RMS} was then split into values greater than and less than 0.1, representing values upstream and downstream relative to the shock train LE location. It was determined after several runs that the value of $\Psi_{RMS} = 0.1$ was the limit for transducer Ψ_{RMS} values when the shock train LE was downstream relative to the transducer. This value would need to be reevaluated if used on a different test section or flow conditions. The mean of the upstream transducer Ψ_{RMS} values was then calculated and used for percent increase calculations. The shock train location was then calculated using linear interpolation based on a desired percent increase, ξ_{Des} , in the Ψ_{RMS} vector along with the transducer locations as presented in Figure 4.9.

$$\psi_{RMS, i} = \sqrt{\frac{\psi_{s, \zeta_i}^2(f_1) + \psi_{s, \zeta_i}^2(f_2) + \dots + \psi_{s, \zeta_i}^2(f_m)}{m}} \quad (4.14)$$

$$\Psi_{RMS} = [\psi_{RMS, 1} \ \psi_{RMS, 2} \ \dots \ \psi_{RMS, 14}] \quad (4.15)$$

The results from using the PSD to locate the shock train LE at various ξ settings are presented in Figures 4.10a-4.10c and the error, as calculated using Eqn. (4.1), is presented in Figures 4.10d-4.10f. These results indicate that the PSD using the 25% increase interpolation point can be used as an accurate indication of the shock train LE location. Further, using the PSD requires little to no prior knowledge to calculate the shock train LE location. The method is the most computationally expensive of the ones considered in this research, though. Due to the accuracy of the method

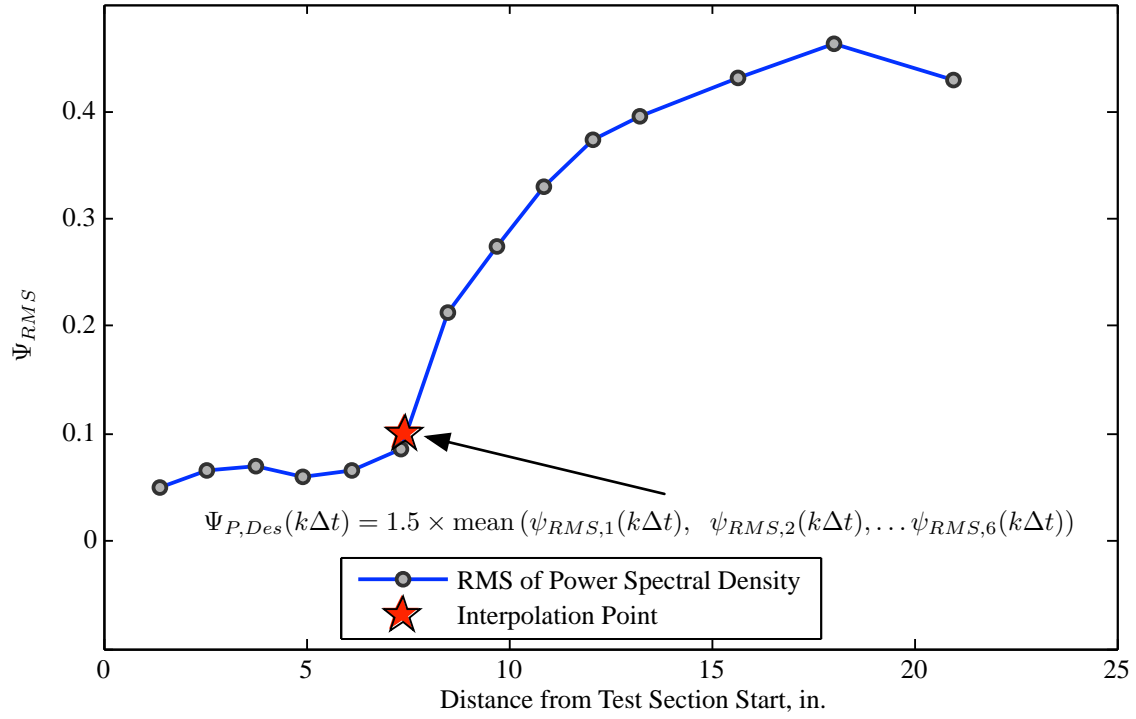


Figure 4.9: Illustration of the PSD method

and the potential for operational and laboratory use, assuming fast computation, the method was reconsidered using the data from run 4.10. The e_{RMS} result from this run is 0.46 in. (18.4% of D) and is also presented in Table 4.2.

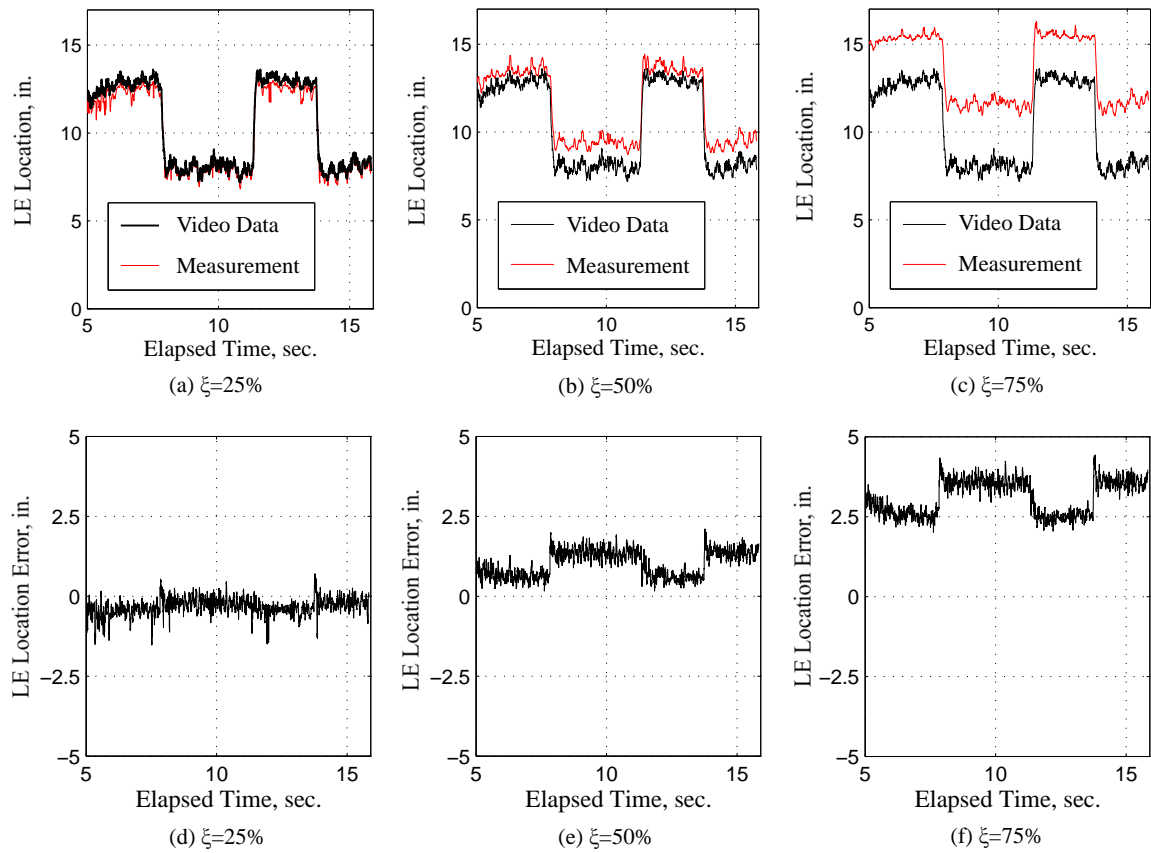


Figure 4.10: Frequency content method measurement and error plots

4.1.5 Static Pressure Summation Method. The next LE detection technique considered was based on a technique used by NASA in the 1970s [26] as well as in contemporary research [39]. The method involved creating a static model relating the sum of the wall pressures to the shock train LE location. The static model accepted the sum of the static pressure measurements as the input and returned the LE location, labeled $x_{Sum}(k)$ as the output. The relationship can be seen in a plot displaying x_{Optic} and the sum of the pressure transducer readings at k , $P_{Sum}(k)$, in Figure 4.11. The data used to create Figure 4.11 was from runs 4.1-4.8. As can be seen, there is a predictable relationship between the sum of static pressures and the shock train location for a given Reynolds number. The sum of the pressure transducers from each sample was then used in a least squares regression to provide the static polynomial model provided in Equation (4.16).

$$x_{Sum}(k) = 104.08 - 1.96P_{Sum}(k) + 1.39 \times 10^{-2}P_{Sum}^2(k) - 3.47 \times 10^{-5}P_{Sum}^3(k) \quad (4.16)$$

After creation of the static model, the sum of the static pressures was then run through Equation (4.16) to locate x_{Sum} at each k for the data collected from run 4.9. The location results from this analysis is presented in Figure 4.12a and the error is presented in Figure 4.12b. As can be seen, there is a very good correlation between the LE location as a result of the sum of the pressures and the LE location from the shadowgraph photography. Unfortunately, this method requires a significant amount of preliminary research into the pressure relationships within the isolator test section. Additionally, a correlation developed at one Reynolds number may not be relevant at another Reynolds number, depending on how different the flows are. As a result, while these results indicate the method can be very accurate in the laboratory, it is probably not the best option for operational use. Due to the accuracy, although a significant amount of prior knowledge is necessary for the method, the method was considered in the real-time implementation study. The e_{RMS} result from this run is

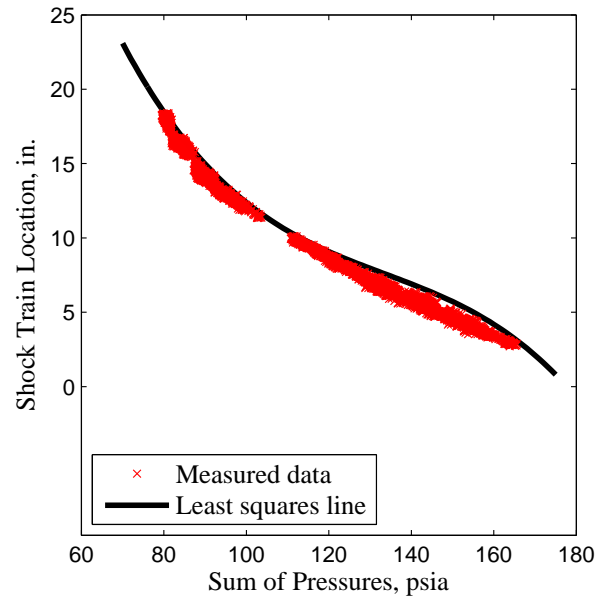


Figure 4.11: Illustration of the pressure sum method data and static model

0.27 in. (10.8% of D) and is also presented in Table 4.2 for a comparison to other methods.

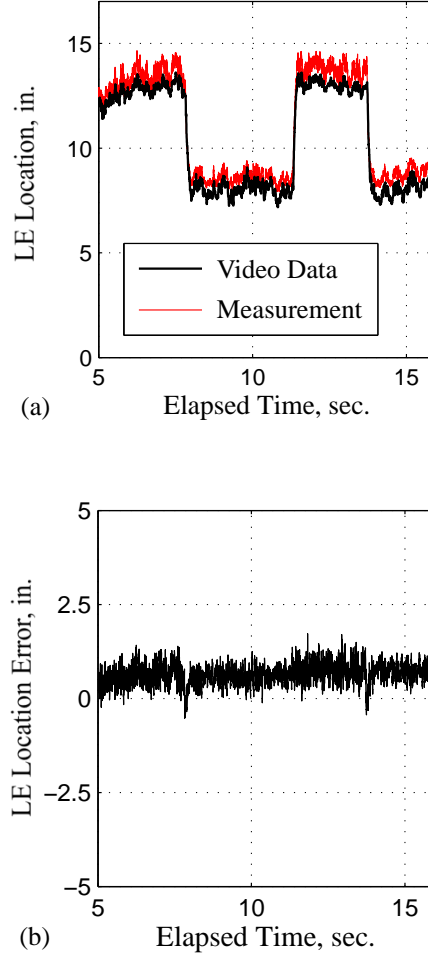


Figure 4.12: Sum of pressures correlation method measurement and error plots

4.1.6 Back Pressure Method. The final method considered for locating a shock train LE within the isolator used the back pressure, P_{BP} , as the input and returned the LE location, labeled $x_{BP}(k)$. In this method, similar to the sum of pressures method, a static polynomial model was developed using a least squares regression. The data used to develop the model, presented in Equation (4.17), was from runs 4.1-4.8.

$$x_{BP}(k) = -218.53 + 45.14P_{BP}(k) - 2.16P_{BP}^2(k) \quad (4.17)$$

A plot of the data used in the least squares procedure to create the static polynomial model relating P_{BP} to x_{Optic} along with a line created using the polynomial is presented

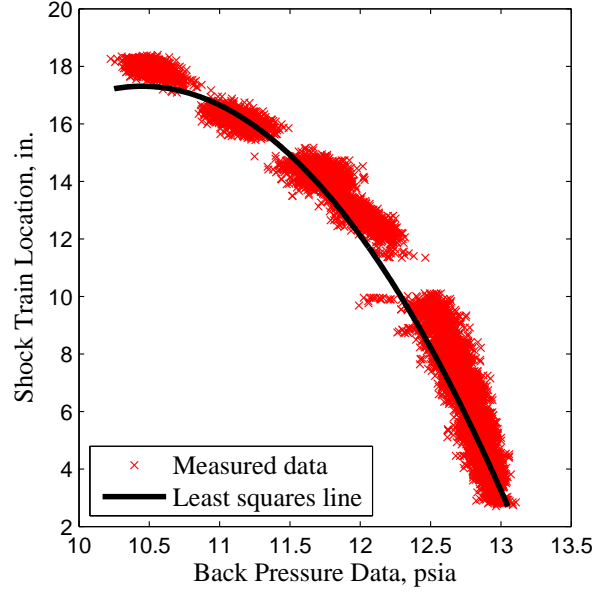


Figure 4.13: Diagram of the back pressure method data and static model

in Figure 4.13. The results of running the measured back pressure at each sample from run 4.9 into the back pressure polynomial model is then displayed in Figure 4.14a and the error is displayed in Figure 4.14b. The back pressure method, while able to predict the shock train LE location, resulted in noisy measurements. Additionally, a significant amount of prior knowledge about the back pressure to shock train LE location was necessary to develop the static polynomial model used in the method. As a result of the previous considerations, the method will not be considered further for locating the shock train LE but, with the addition of a dynamic model, can be used to model the shock train LE location as will be presented in Chapter V. The e_{RMS} result from this run is 0.79 in. (31.6% of D) and is also presented in Table 4.2.

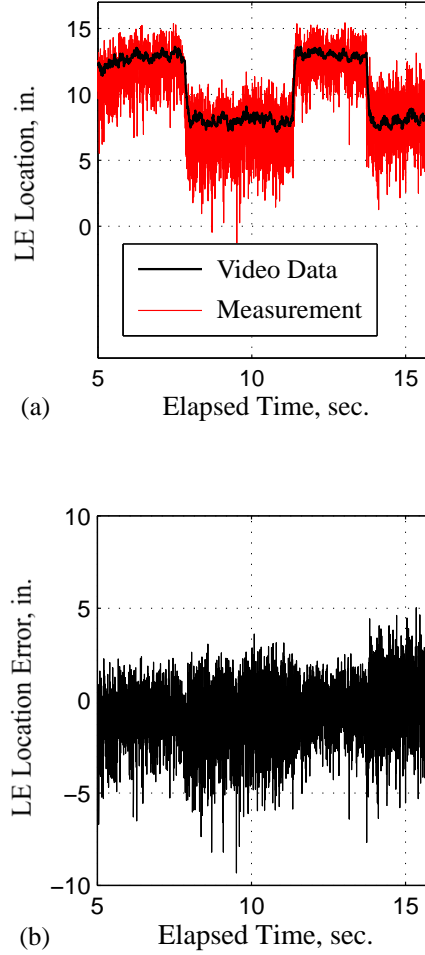


Figure 4.14: Back pressure correlation method measurement and error plots

4.2 Complex Input Run

The previous analysis included consideration of the ability of each method to detect the shock train LE location on run 4.9, a run with only four changes in ramp angle. A final test, prior to control algorithm development, for the most accurate techniques as measured by the e_{RMS} metric, is to consider a run with additional ramp changes, referred to as a ‘complex input’. The run chosen for the final post-processing comparison was run 4.10 and the ramp inputs after initially rising from the floor are presented in Figure 4.15. The ramp inputs used were from a five-level APRBS [60] and the APRBS algorithm is detailed in Appendix D. The use of an APRBS excitation signal allowed later system dynamic modeling research using

system identification which will be presented in Chapter V. The methods chosen for this run were the PSD method, the P_{Sum} static model method, the pressure rise method, and the pressure ratio method. The location, as predicted by each method, is presented in Figures 4.16a-4.16b and Figures 4.17a-4.17b. The error is presented in Figures 4.16c-4.16d and Figures 4.17c-4.17d. As can be seen, each of the detection methods were able to detect the shock train location within 40% of a duct height, D , whereas the transducers were separated by 47.6% of D , so they all met the desired accuracy. The e_{RMS} results from this run are presented in Table 4.2. While the pressure increase method returned the best result for this run, the results indicate they are all potentially useful for an automatic control algorithm. The pressure rise method was determined to exhibit the best trade-off between accuracy, computational speed, and minimal required previous knowledge and was used for model development in Chapter V and control algorithm development in Chapter VI.

Table 4.2: Measurement results for the various measurement techniques

Method	Interpolation Percent	Run 4.9 e_{RMS} , in.	Run 4.9 e_{RMS} , % of D	Run 4.10 e_{RMS} , in.	Run 4.9 e_{RMS} , % of D
P_{Sum}	N/A	0.27	10.8	0.34	13.6
Pressure Rise	50%	0.30	12.0	0.23	9.2
Pressure Ratio	50%	0.30	12.0	0.48	19.2
Ψ_{RMS}	125%	0.46	18.4	0.38	15.2
P_{BP}	N/A	0.79	31.6	N/A	N/A
σ_{ζ_i}	N/A	1.10	44.0	N/A	N/A

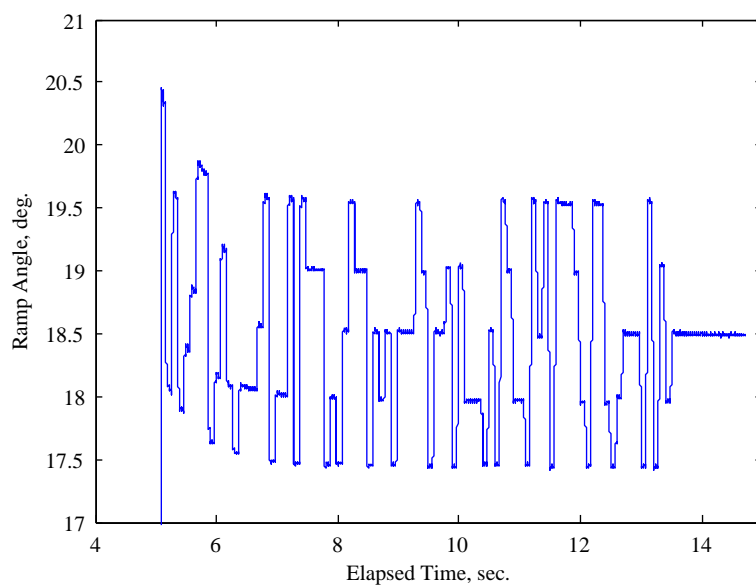


Figure 4.15: A plot of the ramp angle for run 4.10

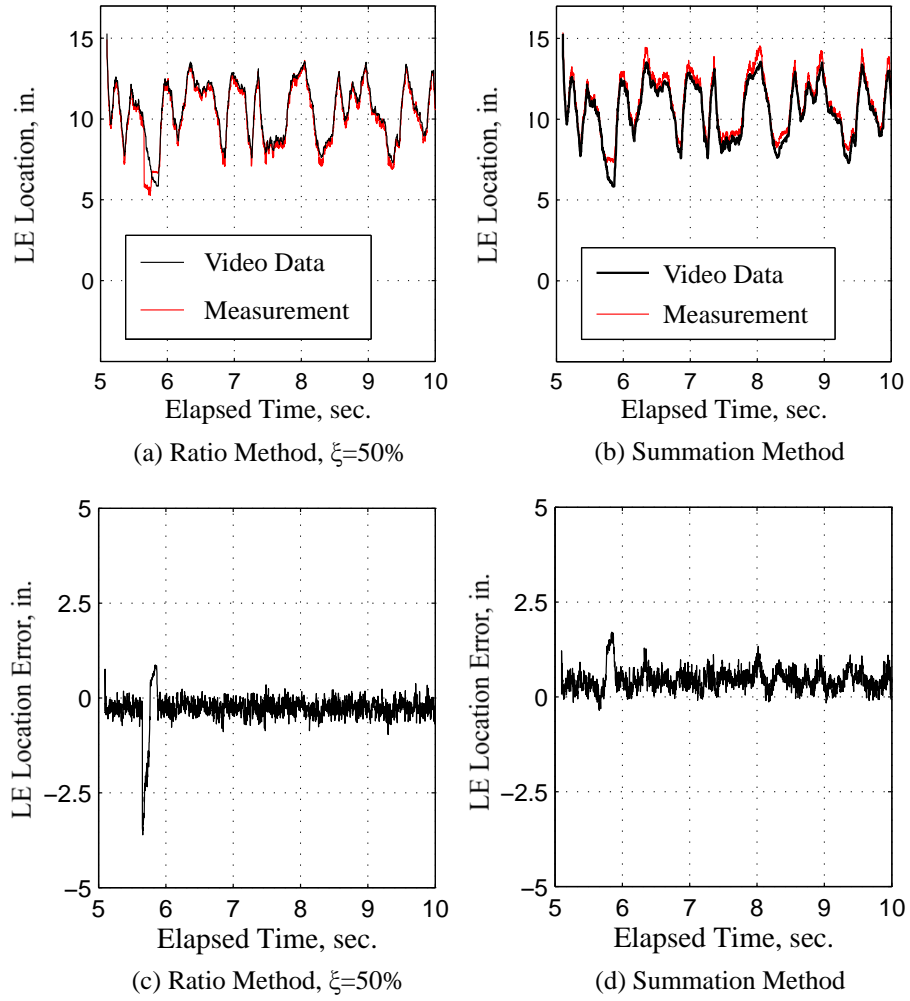


Figure 4.16: Complex input stream run results for ratio and summation methods

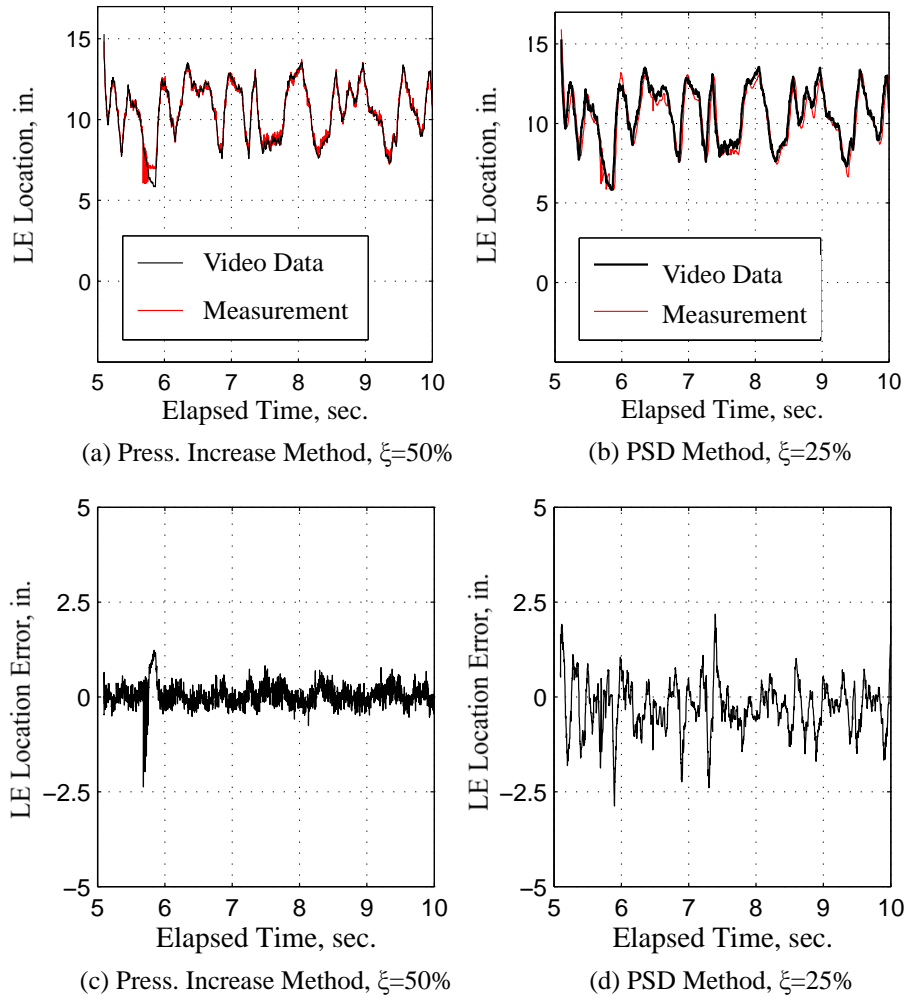


Figure 4.17: Complex input stream run results for ratio and PSD methods

In order to further consider the robustness of the pressure increase method, run 4.10 was reanalyzed with the assumption that half of the transducers were removed. As a result of this assumption, the transducers were separated by 2.3760 in. (transducer center to center) or 95% of D . The result is an increase in the e_{RMS} value to $e_{RMS} = 0.40$ in. or 16% of D . The $e_{RMS} = 0.23$ in. when the transducers were positioned at 47.6% of D using this technique. Additional study with different transducer separation values is necessary to determine if there is a constant relationship between the transducer spacing and the measurement e_{RMS} value. A plot of the location and the error when the transducers were separated by 95% of D is presented in Figure 4.18.

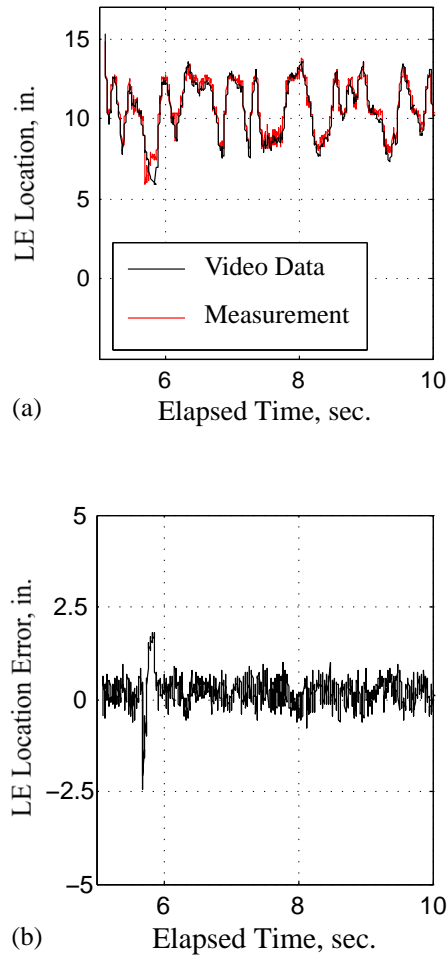


Figure 4.18: 50% pressure rise method measurement and error plots with transducers separated by 95% of D

4.3 Real-Time Implementation

After post-processing analysis of the various algorithms, the pressure increase method was implemented into a LabVIEWTM routine. The shock train LE location x_P was calculated at each step, k , throughout runs 4.12-4.14 to validate the method at different Reynolds numbers. The shock train LE location using the shadowgraph was then measured after each run was accomplished. In this, and for the remainder of the research, the LE location, x_{Meas} , will always imply the pressure rise method at 50% pressure increase indicated shock train LE location, $x_{Meas} \equiv x_P$. The shock train LE location from runs 4.12-4.14 is presented in Figures 4.19a-4.19c and the error is presented in Figure 4.19d-4.19f. The RMS values from the real-time implementation were all less than 40% of D whereas the spacing between the transducers was 47.6% of D . The e_{RMS} values for runs 4.12-4.14 are presented in Table 4.3

Table 4.3: Measurement results from real-time implementation

Run	Re Number, $/ft$	e_{RMS} , in.	e_{RMS} , % of D
4.12	7.20×10^6	0.23	9.2
4.13	6.04×10^6	0.43	17.2
4.14	4.94×10^6	0.39	15.6

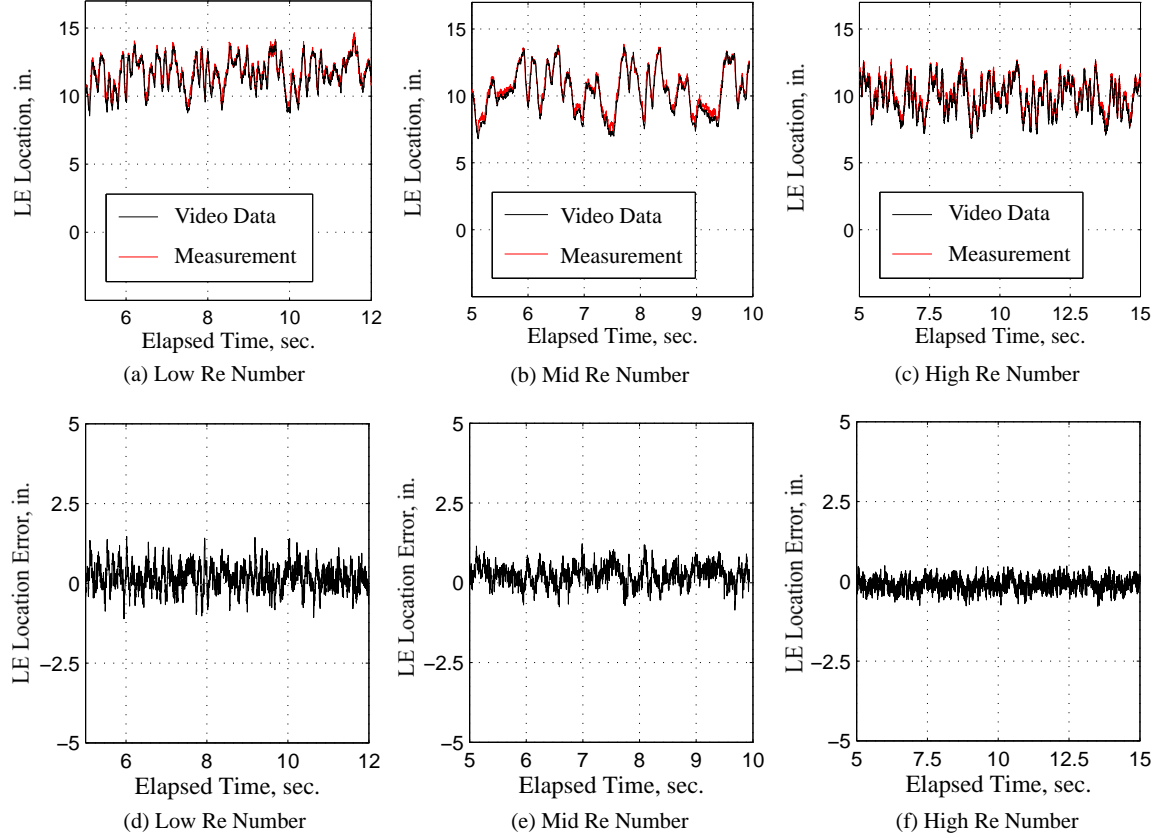


Figure 4.19: Real time pressure increase method location and error plots across Reynolds numbers ($\xi = 50\%$)

4.4 Summary and Conclusion

Six methods for locating the LE of a shock train were investigated using post-processing in this chapter. After post-processing consideration, one method was selected and was implemented in LabVIEWTM to collect shock train measurement data throughout a run. The methods considered included the pressure ratio method, the pressure increase method, the standard deviation method, the PSD method, the summation static model method, and the back pressure static model method. All of the detection methods used an array of pressure transducers mounted along the centerline of the floor of the test section and/or a single transducer mounted in the side wall. Back pressure was varied using the ramp assembly in the far downstream portion of the test section.

The detected shock train LE locations from each of the methods were calculated and compared to measured results using high-speed shadowgraph photography, x_{Optic} . The shadowgraph videos were analyzed on a frame-by-frame basis to locate the shock train LE for the entirety of each run. The shadowgraph data collection method is detailed in Appendix E. The measured e_{RMS} values for the two post-processed runs under study are presented in Table 4.2. This table included results from runs 4.9 and 4.10 and revealed that the pressure increase method was one of the more accurate methods. The pressure increase method was then implemented in the LabVIEWTM routine for real-time testing. The e_{RMS} results for the three real-time implemented runs are presented in Table 4.3. After implementation into the LabVIEWTM routine, the method was able to measure the shock train LE location to within 18% of D .

The pressure ratio method was chosen for implementation as a part of this research for three reasons. First, the method was computationally one of the most simple in comparison to the other methods compared since it only requires a single calculation for the interpolation point and linear interpolation. Second, the method required no previous knowledge prior to detecting the shock train LE. Finally, the pressure rise method was one of the most accurate methods in comparison to the shadowgraph results.

V. Shock Train Location Modeling

The purpose of this chapter is to discuss the dynamic shock train leading edge (LE) location modeling efforts and results achieved as a part of this research. A dynamic model of the engine was used to develop and implement an automatic control algorithm for positioning the shock train LE location within the AFIT cold-flow blow-down wind tunnel. In this research, a set of dynamic models were initially developed relating the back pressure, P_{BP} , to the shock train LE location, x_{Meas} . The intention of this initial set of dynamic models was to develop a model structure that could be adapted to different test sections. After the development and the comparison of these initial dynamic models and the decision to use a particular structure, that model structure was used to develop a model that related the measured ramp angle, ϕ_{Meas} , to x_{Meas} . The ϕ_{Meas} to x_{Meas} model, along with the ramp assembly transfer function presented in Equation (3.2) were then used to develop and validate the control algorithm presented in Chapter VI. All dynamic models were developed using a black-box system identification approach.

The modeling efforts accomplished as a part of this research have roots in historical [7, 32] perturbation theory-based efforts. In these studies, a perturbation-theory approach was used to develop dynamic models relating flow pressure disturbances to the normal shock location in a duct using the normal shock relations. The downside to the models developed using a perturbation theory approach to linearize the nonlinear normal shock relations was that the input space of pressure distributions over which the equations were developed was limited. In order to control the shock train LE, the input space for the model must include back pressures capable of changing the shock train LE location throughout the entire test section. As a result of the desire to use models that were developed for small pressure perturbations, but have them apply throughout the applicable pressure range, nonlinear static models were used to provide the input to any of the dynamic models. The use of the static models had the effect of increasing the input space of potential pressures to the overall model. This structure of a static nonlinearity followed by a dynamic model is labeled a Hammer-

stein structure which is noted as one of the best choices when the nonlinearity in a system is primarily assumed in the input space [61]. Each of the models considered as a part of this research was composed of a static nonlinear model as well as a dynamic model to approximate a Hammerstein model.

As has been shown previously [62, 63], the shock train LE will oscillate up to an equivalent diameter, D_e , about its mean position where $D_e = 4 \times \text{Area}/\text{Perimeter}$ and area and perimeter are cross-sectional measurements. Since the AFIT test section has a square cross-section, the equivalent diameter is the same as the duct height, D , which is 2.5 in. and the goal was to develop a dynamic model capable of predicting the shock train LE location to within D . The metric for comparison to the duct height criteria was the root-mean-square of the model error vector, e_{RMS} , as calculated using Equation (4.1) and Equation (4.2).

The first type of dynamic model considered was based on simple continuous models. From the 1950s [32] through the 2000s [7], theoretical modeling of the shock train LE location has been based on a perturbation analysis applied to the normal shock equations. The resultant models indicated a first-order lag filter can be used to model the back pressure to shock train LE location relationship. As a result, the first continuous model considered was a first-order lag. Additional models incorporated a zero and a pole at the origin on the Laplace-transform, s , plane. Each of these models is presented in the first column of Table 5.2 in Section 5.2.

After considering the continuous models, an Auto-Regression with eXogenous variables (ARX) model structure was then considered for the dynamic model. The intention of using the ARX model structure was to increase the complexity of the model from the simple continuous models while remaining linear (in the dynamic model). The basic structure of the ARX models considered in this research is presented in Equation (5.1) [5]

$$x_s(k+1) = -a_1x_s(k) - \dots - a_{n_a}x_s(k-n_a) + b_1u_{NL}(k) + \dots + b_{n_b}u_{NL}(k-n_b) + e(k) \quad (5.1)$$

where e is the error, u_{NL} is the input to the dynamic model (the output from the static model), $[a_1 \dots a_{n_a}]$ and $[b_1 \dots b_{n_b}]$ are the regression parameters and n_a and n_b are the number of parameters applied to the input and the output measurements. The ARX model is discussed in detail in Appendix C. The parameters are optimized using a least squares regression on the input and output measurements. Further, the e term was not modeled in this research. Twenty-five different ARX models were considered by varying the number of regression parameters, n_a and n_b between one and five parameters. It was found there no improvement in the modeling accuracy if the number of regression parameters was increased beyond five parameters for either the measurement or the input. The ARX modeling e_{RMS} values are provided in Table 5.3 in Section 5.3.

The final model structures considered were Nonlinear ARX (NARX) models. In order to keep the number of models limited, only polynomial nonlinearities were considered and the maximum number of regression parameters considered were five. As a result of these considerations, fifty-four NARX models were developed and validated. These models are presented in Table 5.4 in Section 5.4. NARX models differ from ARX models, in the implementation for this research, in that the input and output measurements can be raised to varying powers and can be multiples of each other. All NARX models were linear in the parameters and the regression parameters for each were calculated using a least-squares regression. The NARX model is also discussed in Appendix C.

Finally, two different types of results are presented in this research, simulation and real-time results. The results presented in the continuous, ARX, and NARX modeling subsections are the results of simulations. In these sections, a model was developed first using data from run 4.10 in Table 4.1 and then a simulation was run using the P_{BP} measurements from run 4.11 in Table 4.1. In the simulation routine, the output from the model, x_{Model} , was used for the shock train LE location in each successive calculation. As a result of using x_{Model} , any previous modeling errors

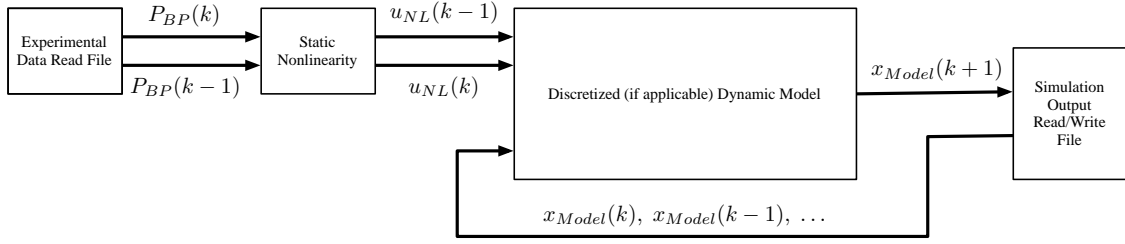


Figure 5.1: A schematic of the data flowing into the static and dynamic model for simulation

were propagated through the simulation. The results from the simulation are then compared to the actual measured outputs from run 4.11.

A schematic of the simulation process is presented in Figure 5.1. The process began by opening the data file for the run under study. The algorithm stepped through each k in the data set by first running $P_{BP}(k)$ and $P_{BP}(k-1)$, the current and previous back pressure measurements through the static nonlinearity to calculate $u_{NL}(k)$ and $u_{NL}(k-1)$. The assumption is that no additional previous measurements are needed and the algorithm would be changed for higher order discrete linear models. The outputs from the static nonlinearity calculations were then used by the discrete dynamic model along with previous dynamic model outputs. In the case that no model outputs had been calculated, actual measured shock train locations were used as the inputs to the discrete dynamic model.

In the real-time algorithm, the three models (a discretized continuous, an ARX, and a NARX model) were implemented in LabVIEWTM along with the pressure rise measurement algorithm developed in Chapter IV. The values for x_{Meas} and P_{BP} were measured for each sample, k and then used in the implemented models to predict the shock train location at the next step, $x_{Model}(k+1)$. As a result of using x_{Meas} instead of x_{Model} , modeling errors were not propagated through to the next prediction to the same level as in the simulation, and the one-step prediction was more accurate than the simulated response. The real-time results and a schematic of the real-time process is provided in Figure 5.2 where Θ_{Cont} is the vector of continuous model regression values, Θ_{ARX} is the vector of ARX model regression values, and Θ_{NARX} is

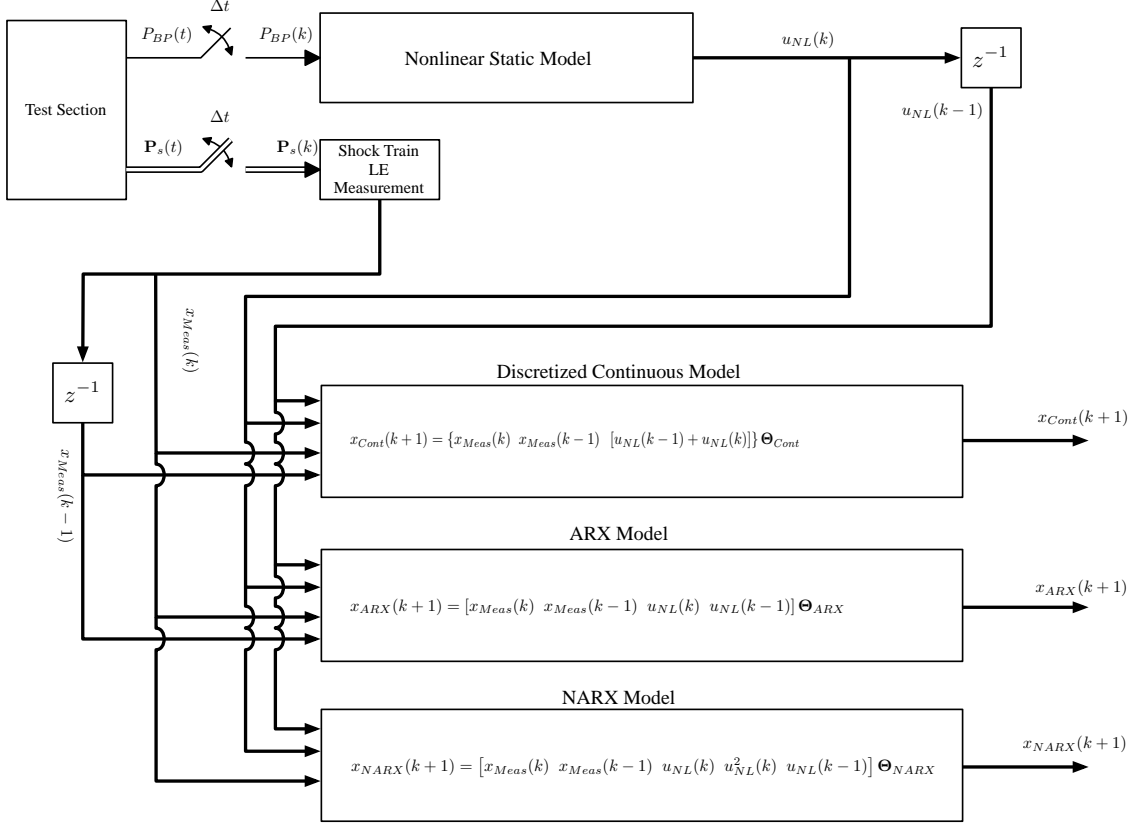


Figure 5.2: A schematic of the data flowing into the static and dynamic model for real-time shock train location prediction

the vector of NARX model regression values. In Figure 5.2, first the static pressures are measured and the shock train LE location is calculated using the pressure rise method discussed in Chapter IV. Additionally, the back pressure is measured and fed through the static nonlinearity to calculate the dynamic model input, $u_{NL}(k)$. Next, a pair of LabVIEWTM z^{-1} blocks were used to record the $u_{NL}(k)$ and $x_{Meas}(k)$ for use as $u_{NL}(k-1)$ and $x_{Meas}(k-1)$. The values of $u_{NL}(k)$, $x_{Meas}(k)$, $u_{NL}(k-1)$, and $x_{Meas}(k-1)$ were then used in each of the different model algorithms, running in parallel, to calculate the one-step predicted shock locations.

In addition to the runs detailed in Chapter IV, an additional set of runs were accomplished. The list of runs accomplished are presented in Table 5.1. In runs 5.1-5.8, the ramp was raised from 9 to 20 degrees in $1/2$ deg. increments. The results from

those runs were combined to develop static models at two other Reynolds number settings, as well as to refine the static models at the high Reynolds number setting. In runs 5.9-5.20, additional APRBS runs were accomplished to refine the dynamic models at the high, medium, and low Reynolds number settings. Finally, in runs 5.21-5.23, the refined models were implemented in LabVIEWTM and tested in real-time runs at various Reynolds number settings.

Table 5.1: Test section operating runs

Run	Ramp Angle, deg	P_0 , psia	T_0 , R	Re Number
5.1	Step Inputs	21.54	525	$6.61 \times 10^6/\text{ft}$
5.2	Step Inputs	16.31	526	$4.97 \times 10^6/\text{ft}$
5.3	Step Inputs	14.85	512	$4.48 \times 10^6/\text{ft}$
5.4	Step Inputs	14.86	513	$4.48 \times 10^6/\text{ft}$
5.5	Step Inputs	19.63	511	$5.97 \times 10^6/\text{ft}$
5.6	Step Inputs	19.63	511	$5.97 \times 10^6/\text{ft}$
5.7	Step Inputs	23.60	511	$7.25 \times 10^6/\text{ft}$
5.8	Step Inputs	23.68	512	$7.27 \times 10^6/\text{ft}$
5.9	APRBS	14.91	513	$4.49 \times 10^6/\text{ft}$
5.10	APRBS	14.92	513	$4.49 \times 10^6/\text{ft}$
5.11	APRBS	14.92	513	$4.49 \times 10^6/\text{ft}$
5.12	APRBS	14.92	513	$4.49 \times 10^6/\text{ft}$
5.13	APRBS	23.40	512	$7.10 \times 10^6/\text{ft}$
5.14	APRBS	23.41	512	$7.12 \times 10^6/\text{ft}$
5.15	APRBS	23.42	512	$7.11 \times 10^6/\text{ft}$
5.16	APRBS	23.41	512	$7.11 \times 10^6/\text{ft}$
5.17	APRBS	19.25	512	$5.84 \times 10^6/\text{ft}$
5.18	APRBS	19.27	512	$5.85 \times 10^6/\text{ft}$
5.19	APRBS	19.27	512	$5.85 \times 10^6/\text{ft}$
5.20	APRBS	19.28	512	$5.85 \times 10^6/\text{ft}$
5.21	APRBS	14.93	513	$4.49 \times 10^6/\text{ft}$
5.22	APRBS	18.80	513	$5.67 \times 10^6/\text{ft}$
5.23	APRBS	23.46	514	$7.08 \times 10^6/\text{ft}$

5.1 Static Polynomial Model

Each model presented in this dissertation is composed of both a static nonlinear model and a dynamic model as required in the Hammerstein model structure. These models combine to relate n_a back pressure or ramp angle measurements along with n_b shock train LE location measurements to a predicted shock location labeled $x_{Model}(k + 1)$. The initial nonlinear static models were developed by combining the P_{BP} or ϕ_{Meas} and x_{Meas} measurements from runs 4.1 through 4.8, assuming a static model structure (i.e. a polynomial of a certain order), and then using a least squares regression to calculate the regression parameters. The regression matrix used in the least squares calculation for the P_{BP} to x_{Meas} model is presented in Equation (5.2) and the calculation for the regression polynomials is presented in Equation (5.3)

$$X_{NL} = \begin{bmatrix} 1 & P_{BP,1}(1) & P_{BP,1}^2(1) \\ 1 & P_{BP,1}(2) & P_{BP,1}^2(2) \\ \vdots & \vdots & \vdots \\ 1 & P_{BP,1}(N_1) & P_{BP,1}^2(N_1) \\ 1 & P_{BP,2}(1) & P_{BP,2}^2(1) \\ \vdots & \vdots & \vdots \\ 1 & P_{BP,7}(N_7) & P_{BP,7}^2(N_7) \\ 1 & P_{BP,8}(1) & P_{BP,8}^2(1) \\ 1 & P_{BP,8}(2) & P_{BP,8}^2(2) \\ \vdots & \vdots & \vdots \\ 1 & P_{BP,8}(N_8) & P_{BP,8}^2(N_8) \end{bmatrix} \quad (5.2)$$

$$\Theta_{NL} = (X_{NL}^T X_{NL})^{-1} X_{NL}^T \mathbf{x}_{Meas} \quad (5.3)$$

where N_r is the number of samples in run r such that the number of samples in run seven is labeled N_7 , Θ_{NL} is a vector of the regression parameters for the nonlinear static model and \mathbf{x}_{Meas} is a vector of the measured shock train LE locations for the

runs under consideration. A similar regression matrix was developed for the ϕ_{Meas} to x_{Meas} model with P_{BP} replaced by ϕ_{Meas} . After calculating the regression parameters, the preliminary nonlinear static model for high Reynolds numbers is presented in Equation (5.4). The data used in the least squares regression for the high Reynolds number setting is the same data as used to develop the P_{BP} measurement model presented Chapter IV as Figure 4.13, so, for a high Reynolds number, the static nonlinearity is the same as well.

$$u_{NL}(k) = -2.16P_{BP}^2(k) + 45.14P_{BP}(k) - 218.53 \quad (5.4)$$

The preliminary study (based on the runs from Chapter IV) was only accomplished at the upper Reynolds number level ($Re > 7 \times 10^6/\text{ft}$). Using the data collected in runs 5.1-5.2, additional Reynolds numbers were considered as well. The additional set of static polynomials calculated using the least squares regression detailed in the previous paragraph are presented as Equation (5.5) for $Re \approx 6.5 \times 10^6/\text{ft}$ and Equation (5.6) for $Re \approx 5 \times 10^6/\text{ft}$. Plots of the data versus least squares regression plots are presented in Figure 5.3a for the data from runs 4.1-4.8 from Chapter IV as well as Equation (5.4), Figure 5.3b for the data run 5.1 as well as Equation (5.5), and Figure 5.3c for the data from run 5.2 as well as Equation (5.6).

$$u_{NL}(k) = -1.13P_{BP}^2(k) + 18.42P_{BP}(k) - 56.25 \quad (5.5)$$

$$u_{NL}(k) = -2.19P_{BP}^2(k) + 27.12P_{BP}(k) - 65.47 \quad (5.6)$$

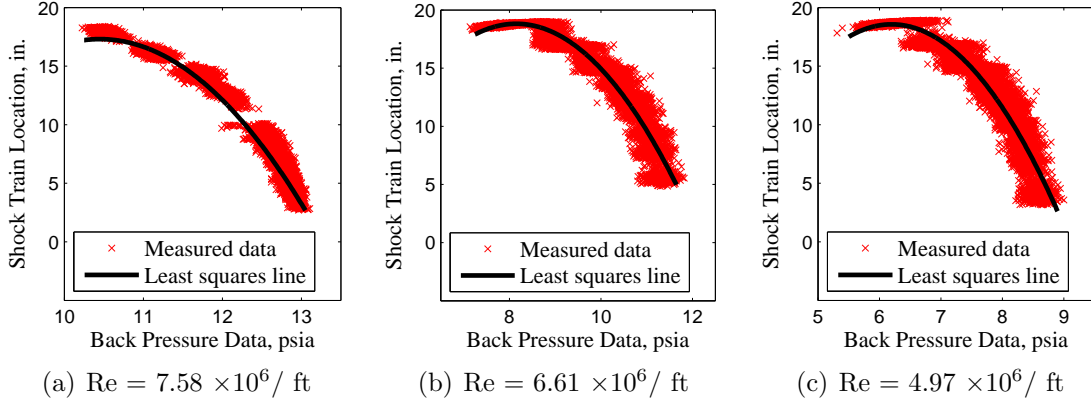


Figure 5.3: P_{BP} to u_{NL} static models at three Reynolds numbers

5.2 Continuous Linear Model with Static Polynomial Input

The output of the static model is the input to the dynamic model. The first dynamic model attempted was a continuous one. The first dynamic models considered were developed at the high Reynolds number setting and included the appropriate static nonlinear model for the Reynolds number as discussed in Section 5.1 and a continuous model. The continuous models considered are presented in the first column of Table 5.2. Initially, continuous model structures were chosen to consider the ability of a first-order lag filter to model the shock train LE dynamics with the addition of a nonlinearity (the static model). The overall structure is presented in Figure 5.4. In this figure, an array of back pressures (or ramp angles depending on the model) is provided to the static nonlinearity which then is used to calculate an array of u_{NL} values. The array of u_{NL} values along with an array of x_{Meas} values is provided to the dynamic model which is then used to calculate the one-step predicted shock train LE location. This overall structure is similar to a Hammerstein model and is common to all the models presented in this dissertation. Additional continuous models built on that first-order lag filter. The **Matlab**[®] system identification toolbox was used to calculate the continuous model parameters (pole, zero, and gain, as applicable) in each model with the array of u_{NL} values from run 4.10 as the input and the array of x_{Meas} values from run 4.10 as the output. The run 4.10 u_{NL} values were calculated by operating on the vector of all the P_{BP} values from the run using the

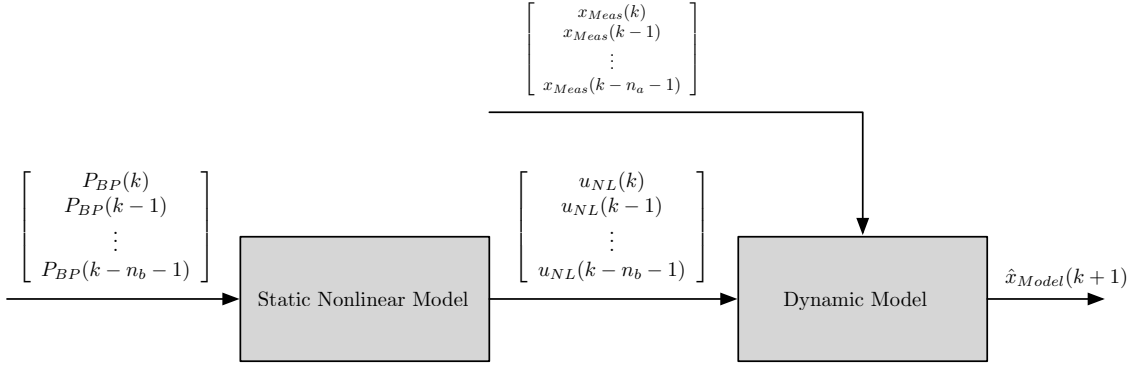


Figure 5.4: The Hammerstein model as implemented in this research

static nonlinearity. The toolbox process model optimization algorithm, set to the simulation mode, was used to develop each model [64]. The e_{RMS} from simulated results for each model, with the bias offset, are displayed in Table 5.2. The bias noticed in the simulations is due to two factors: 1) differences between the Reynolds number the nonlinear model was developed at and the Reynolds number of the run under study and, 2) steady-state error from the developed dynamic model. A step input was applied to each of the three models and there was no steady-state error in the first two models, there was a significant steady-state error in the third model, though. The step input response for shock train LE commanded to 10 in. is presented in Figure 5.5. The 10 in. command was used since the dynamic model command, u_{NL} , was, on average, around 10 in. for run 4.11 as is presented in Figure 5.6. As can be seen in Figure 5.5, there is approximately a 1 in. steady-state error from the pole-integrator-zero transfer function. This error was not evident in the other two transfer functions. The other models did exhibit approximately a $1/4$ in. bias, though, which was due to a slight mismatch between the Reynolds number used to develop the static nonlinearity and the Reynolds number of run 4.11. The combination of the bias from the Reynolds number mismatch and the steady-state error contribute to the bias that was exhibited in the simulation for the third model presented in Table 5.2. Since this bias is predictable, and does not show in the real-time results due to consistent x_{Meas} updates, it was subtracted from the e_{RMS} results presented in Table 5.2. Each model

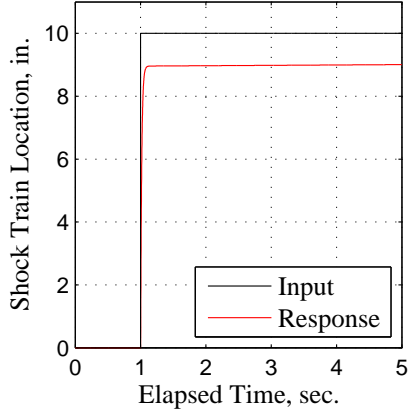


Figure 5.5: Step response for model three from Table 5.2

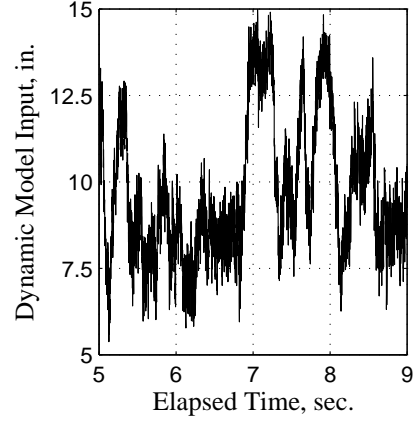


Figure 5.6: u_{NL} commands for model three from Table 5.2

presented was developed using the u_{NL} and x_{Meas} data from run 4.10 and validated using u_{NL} and x_{Meas} data from run 4.11. By adding a zero and an integrator (pole at the origin on the s plane) to a first-order lag filter, the shock train LE location can be modeled with an e_{RMS} of nearly 20% of a duct height which is particularly significant considering the transducers were mounted with a separation of 47.6% of D . As can be seen in Figure 5.7b, there are several times where the error spikes to values greater than the distance between transducers, however the maximum error remains less than D throughout the run. These results confirm the theoretical, perturbation-theory based work [7, 32] for a shock train with the addition of a simple nonlinear model and slight changes to the dynamic model. Since the perturbation-theory based dynamic models had a limited input space composed of small perturbations in back pressure, the static nonlinear model effectively increased that input space to include significant changes in back pressure. The results of the measured and the simulated shock train LE locations are presented in Figure 5.7a and the error is presented in Figure 5.7b for the third model from Table 5.2.

These results imply that, while a first-order lag model (first two entries in Table 5.2) along with a static nonlinearity can be used to model the relationship between P_{BP} and x_s , the modeling errors are on the order of D . In order to more accurately model the system dynamics, the model order must be increased above the pertur-

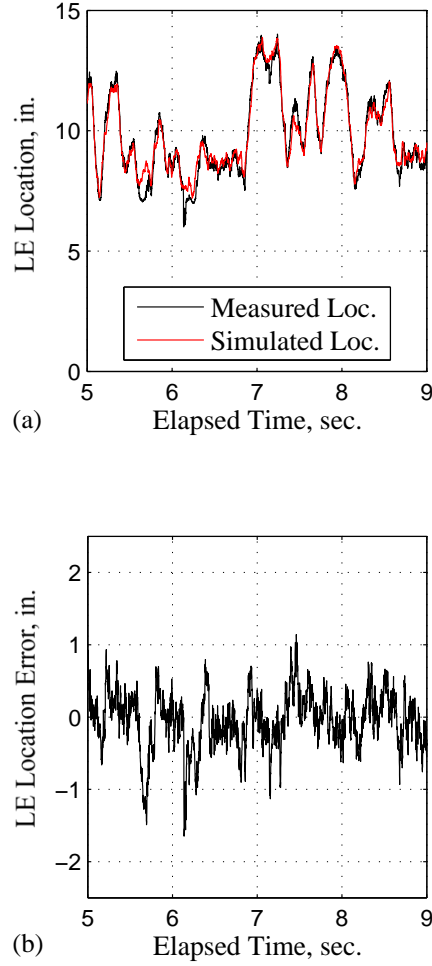


Figure 5.7: Continuous model simulation location and error plot for run 4.11 validation

bation theory indicated single-pole model. An increase to two poles significantly decreased the model error. Of particular interest, the two-pole system is moderately more complex than the theoretical first-order lag filter indicating that the static non-linearity can be used to enable the use of a simple linear model by enlarging the range of P_{BP} values in the dynamic model input range from those of small perturbations. In the next subsection, consideration is given to increasing the order of the system further while staying with a linear model for the dynamic portion of the assumed Hammerstein structure.

Table 5.2: The RMS of the errors from the three continuous linear models

Model	zero	pole	K (gain)	Bias, in.	e_{RMS} , in.
$G = \frac{K}{s+pole}$	N/A	55.89	56.1	0.18	2.69
$G = \frac{K(s+zero)}{s+pole}$	774.0	51.67	6.7×10^{-2}	0.19	2.38
$G = \frac{K(s+zero)}{s(s+pole)}$	1.31×10^{-3}	[0 61.15]	54.79	1.19	0.55

5.3 ARX Models with Static Polynomial Input

The next set of dynamic models considered were based on the ARX structure presented in Equation (5.1). This structure was chosen to examine the advantages of additional complexity over the continuous models while remaining linear for the dynamic portion of the Hammerstein model. Twenty-five different ARX models were developed by varying the number of input regression parameters, n_a , and output regression parameters, n_b in Equation (5.1). Of note, the bias experienced in the previous subsection was also evidenced in the ARX modeling. The bias for each of the different models was 0.26 in., which is comparable to the error from the Reynolds number static model mismatch. Although predictable, the bias was not removed in Table 5.3 although it was removed in Table 5.2. The modeling e_{RMS} values are presented in Table 5.3.

Table 5.3: The RMS of the errors for the simulation

	$n_b = 1$	$n_b = 2$	$n_b = 3$	$n_b = 4$	$n_b = 5$
$n_a = 1$	0.56	0.52	0.52	0.54	0.55
$n_a = 2$	0.56	0.52	0.53	0.54	0.56
$n_a = 3$	0.62	0.57	0.55	0.57	0.58
$n_a = 4$	0.61	0.56	0.55	0.55	0.56
$n_a = 5$	0.64	0.59	0.58	0.58	0.58

A probable cause for the homogeneity of the results in Table 5.3 is the large number of the samples collected to construct the ARX models. The error due to variation in the parameters from the optimal parameter values, or “variance error” [61] increases with the number of parameters in a model and can be estimated according to Equation (5.7).

$$\text{variance error} \sim \sigma^2 \cdot \frac{n_a + n_b}{N} \quad (5.7)$$

An estimate of the variance for a linear model can be calculated from the error vector, \mathbf{e} , the number of regressors, $n_a + n_b$, and the number of samples, N , according to Equation (5.8) [61].

$$\hat{\sigma}^2 = \frac{\mathbf{e}^T \mathbf{e}}{N - (n_a + n_b)} \quad (5.8)$$

In the presented models, the estimated noise variance ranges from 0.13 – 0.17 in. and $n_a + n_b \in [2, 10]$ whereas approximately 10,000 samples were used for each model. As a result, increases in the order of the model can be predicted to result in negligible changes in the variance error which explains why the e_{RMS} values are approximately the same as in Table 5.3. The primary concern is then to overcome any error due to inflexibility of the model structure as a result of not having enough parameters. This type of error is labeled “bias error” [61]. When choosing the number of parameters in a model using black-box techniques, one is attempting to balance the bias and the variance error. Assuming the same number of samples, an increase in the number of parameters decreases the bias error, but increases the variance errors. As a result of the desire to decrease the variance error, the number of parameters were kept limited. This topic is discussed in greater detail in Appendix C.

The e_{RMS} calculations for the $n_a = n_b = 2$ run show a slight improvement over the best continuous model calculation, approximately 21% of a duct height versus 22% of D for the continuous model. Additionally, the $n_a = n_b = 2$ model is one of the models with the lowest number of parameters. As a result of the previous considerations, the $n_a = n_b = 2$ model will be considered in the real-time analysis section. The $n_a = n_b = 2$ model equation is presented in Equation (5.9). The

simulated location results are presented in Figure 5.8a, and the ARX simulation error is presented in Figure 5.8b for the $n_a = n_b = 2$ model. As was seen when considering the continuous models, a simple linear model is capable of accurately modeling the P_{BP} to x_s dynamics when used in conjunction with the static nonlinear model discussed in Section 5.1. In the next subsection, along with the static nonlinear model, nonlinear dynamic models will also be considered.

$$x_s(k+1) = 0.9644x_s(k) - 0.0012x_s(k-1) + 0.0049u_{NL}(k) + 0.0316u_{NL}(k-1) \quad (5.9)$$

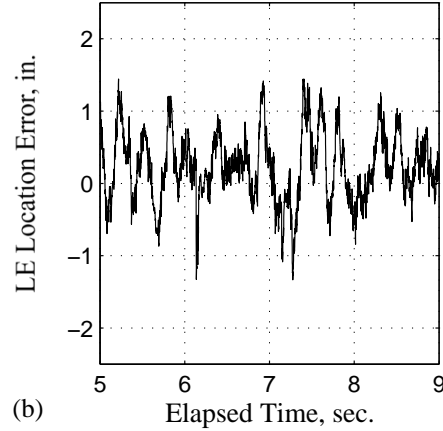
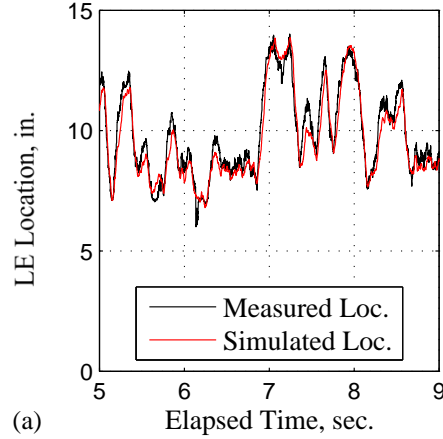


Figure 5.8: ARX model simulation location and error plot

5.4 NARX Models with Static Polynomial Input

The next set of combined models considered in the Hammerstein construct included the static polynomial developed in Section 5.1, along with a series of NARX models used for the dynamic model. The NARX model structure is discussed in Appendix C. The NARX models chosen were all polynomial-based and, therefore, were linear in the parameters to enable regression parameter optimization using a least squares regression. The terms considered included $x_s(k)$, $x_s(k-1)$, $u_{NL}(k)$, $u_{NL}(k-1)$, $x_s^2(k)$, $x_s^2(k-1)$, $u_{NL}^2(k)$, $u_{NL}^2(k-1)$, $x_s(k)x_s(k-1)$, $u_{NL}(k)u_{NL}(k-1)$, $x_s(k)u_{NL}(k)$, $x_s(k-1)u_{NL}(k-1)$, $x_s(k)u_{NL}(k-1)$, and $x_s(k-1)u_{NL}(k)$ where x_s is the shock train location when not associated with a measurement technique. One of the downsides to using a polynomial-based NARX model is that the dimensionality grows exponentially with the consideration of additional parameters if all the potential parameters are used. To keep the modeling task tractable, only a limited number of models were constructed by adding a nonlinear term and/or the removing a linear term to the $n_a = n_b = 2$ ARX model already chosen in the previous section. As a result, 54 different model configurations were considered. As in the prior two model sets (the continuous and the ARX modeling sets), run 4.10 was used to develop each of the models and run 4.11 was used to validate each model. The simulation was accomplished by stepping the model forward using actual P_{BP} measurements and previous simulation measurements (x_{Model}) according to the schematic presented in Figure 5.1. The NARX models developed and validated, along with the e_{RMS} values, are presented in Table 5.4. The bias for model 43, the model that was chosen, was also approximately $1/4$ in., in agreement with the previous biases from the Reynolds number mismatch for the static nonlinearity. As in Table 5.3, the bias is not corrected for in any of the models presented in Table 5.4.

One of the general principles of system identification, called the “parsimony principle” [5], is that the simplest model that accurately describes the system dynamics should be chosen. The model chosen for further consideration due to its accuracy and relative simplicity is model 43 in Table 5.4. The first reason this model was

selected was the model's similarity to the chosen ARX model; the only difference between the $n_a = n_b = 2$ ARX model and NARX model 43 was a square term which increases the simulation accuracy by 0.1 in. Secondly, model 43 is one of the more accurate models amongst the fairly homogenous error values associated with the five-parameter models. As in the continuous modeling and the ARX modeling subsections, the P_{BP} to x_s dynamics can, again, be fairly accurately modeled by a simple model when the static nonlinearity is utilized. The results of running a simulation with the P_{BP} measurements from run 4.11 are presented in Figure 5.9a and the error plot is presented in Figure 5.9b. The equation for this model, with the regression parameters included, is presented as Equation (5.10). NARX model 43 was considered, along with the third continuous model and the $n_a = n_b = 2$ ARX models in the real-time implementation subsection.

$$x_s(k+1) = 0.9631x_s(k) - 0.0021x_s(k-1) + 0.0096u_{NL}(k) - 0.0002u_{NL}^2(k) + 0.0317u_{NL}(k-1) \quad (5.10)$$

Table 5.4: The RMS of NARX simulation errors

Numb.	Model Structure	e_{RMS} , in.
1	$x_s(k+1) = ax_s(k) + bu_{NL}(k) + cx_s(k-1)$	0.5321
2	$x_s(k+1) = ax_s(k) + bu_{NL}(k) + cu_{NL}(k-1)$	0.4934
3	$x_s(k+1) = ax_s(k) + bu_{NL}(k) + cx_s^2(k)$	0.4845
4	$x_s(k+1) = ax_s(k) + bu_{NL}(k) + cu_{NL}^2(k)$	0.4795
5	$x_s(k+1) = ax_s(k) + bu_{NL}(k) + cx_s^2(k-1)$	0.4755
6	$x_s(k+1) = ax_s(k) + bu_{NL}(k) + cu_{NL}^2(k-1)$	0.6933
7	$x_s(k+1) = ax_s(k) + bu_{NL}(k) + cx_s(k)u_{NL}(k)$	0.4826
8	$x_s(k+1) = ax_s(k) + bu_{NL}(k) + cx_s(k)u_{NL}(k-1)$	0.5987
9	$x_s(k+1) = ax_s(k) + bu_{NL}(k) + cx_s^2(k)u_{NL}(k)$	0.4806
10	$x_s(k+1) = ax_s(k) + bu_{NL}(k) + cx_s^2(k)u_{NL}(k-1)$	0.5332

Continued on the next page ...

Table 5.4 – Continued

Numb.	Model Structure	e_{RMS} , in.
11	$x_s(k+1) = a x_s(k) + b u_{NL}(k) + c x_s(k) u_{NL}^2(k)$	0.4784
12	$x_s(k+1) = a x_s(k) + b u_{NL}(k) + c x_s(k-1) u_{NL}^2(k)$	0.4756
13	$x_s(k+1) = a x_s(k) + b u_{NL}(k) + c x_s(k) u_{NL}^2(k-1)$	0.5925
14	$x_s(k+1) = a x_s(k) + b u_{NL}(k) + c x_s(k-1) u_{NL}^2(k-1)$	0.5877
15	$x_s(k+1) = a x_s(k) + b u_{NL}(k) + c x_s^2(k-1) u_{NL}^2(k-1)$	0.5420
16	$x_s(k+1) = a x_s(k) + b u_{NL}(k) + c x_s(k-1) + d x_s^2(k)$	0.4761
17	$x_s(k+1) = a x_s(k) + b u_{NL}(k) + c x_s(k-1) + d u_{NL}^2(k)$	0.4711
18	$x_s(k+1) = a x_s(k) + b u_{NL}(k) + c x_s(k-1) + d x_s^2(k-1)$	0.4722
19	$x_s(k+1) = a x_s(k) + b u_{NL}(k) + c x_s(k-1) + d u_{NL}^2(k-1)$	0.6830
20	$x_s(k+1) = a x_s(k) + b u_{NL}(k) + c x_s(k-1) + d x_s(k) u_{NL}(k)$	0.4741
21	$x_s(k+1) = a x_s(k) + b u_{NL}(k) + c x_s(k-1) + d x_s(k) u_{NL}(k-1)$	0.5874
22	$x_s(k+1) = a x_s(k) + b u_{NL}(k) + c x_s(k-1) + d x_s(k)^2 u_{NL}(k)$	0.4721
23	$x_s(k+1) = a x_s(k) + b u_{NL}(k) + c x_s(k-1) + d x_s(k)^2 u_{NL}(k-1)$	0.5231
24	$x_s(k+1) = a x_s(k) + b u_{NL}(k) + c x_s(k-1) + d x_s(k) u_{NL}(k)^2$	0.4701
25	$x_s(k+1) = a x_s(k) + b u_{NL}(k) + c x_s(k-1) + d x_s(k-1) u_{NL}(k)^2$	0.4687
26	$x_s(k+1) = a x_s(k) + b u_{NL}(k) + c x_s(k-1) + d x_s(k) u_{NL}(k-1)^2$	0.5814
27	$x_s(k+1) = a x_s(k) + b u_{NL}(k) + c x_s(k-1) + d x_s(k-1) u_{NL}(k-1)^2$	0.5784
28	$x_s(k+1) = a x_s(k) + b u_{NL}(k) + c x_s(k-1) + d x_s(k-1)^2 u_{NL}(k-1)^2$	0.5341
29	$x_s(k+1) = a x_s(k) + b u_{NL}(k) + c u_{NL}(k-1) + d x_s^2(k)$	0.4412

Continued on the next page ...

Table 5.4 – Continued

Numb.	Model Structure	e_{RMS} , in.
30	$x_s(k+1) = a x_s(k) + b u_{NL}(k) + c u_{NL}(k-1) + d u_{NL}^2(k)$	0.4374
31	$x_s(k+1) = a x_s(k) + b u_{NL}(k) + c u_{NL}(k-1) + d x_s^2(k-1)$	0.4374
32	$x_s(k+1) = a x_s(k) + b u_{NL}(k) + c u_{NL}(k-1) + d u_{NL}^2(k-1)$	0.4537
33	$x_s(k+1) = a x_s(k) + b u_{NL}(k) + c u_{NL}(k-1) + dx_s(k)u_{NL}(k)$	0.4401
34	$x_s(k+1) = a x_s(k) + b u_{NL}(k) + c u_{NL}(k-1) + dx_s(k)u_{NL}(k-1)$	0.4420
35	$x_s(k+1) = a x_s(k) + b u_{NL}(k) + c u_{NL}(k-1) + dx_s(k)^2 u_{NL}(k)$	0.4378
36	$x_s(k+1) = a x_s(k) + b u_{NL}(k) + c u_{NL}(k-1) + dx_s(k)^2 u_{NL}(k-1)$	0.4397
37	$x_s(k+1) = a x_s(k) + b u_{NL}(k) + c u_{NL}(k-1) + dx_s(k)u_{NL}(k)^2$	0.4363
38	$x_s(k+1) = a x_s(k) + b u_{NL}(k) + c u_{NL}(k-1) + dx_s(k-1)u_{NL}(k)^2$	0.4348
39	$x_s(k+1) = a x_s(k) + b u_{NL}(k) + c u_{NL}(k-1) + dx_s(k)u_{NL}(k-1)^2$	0.4405
40	$x_s(k+1) = a x_s(k) + b u_{NL}(k) + c u_{NL}(k-1) + dx_s(k-1)u_{NL}(k-1)^2$	0.4389
41	$x_s(k+1) = a x_s(k) + b u_{NL}(k) + c u_{NL}(k-1) + dx_s(k-1)^2 u_{NL}(k-1)^2$	0.4361
42	$x_s(k+1) = a x_s(k) + b u_{NL}(k) + c x_s(k-1) + d u_{NL}(k-1) + e x_s^2(k)$	0.4409
43	$x_s(k+1) = a x_s(k) + b u_{NL}(k) + c x_s(k-1) + d u_{NL}(k-1) + e u_{NL}^2(k)$	0.4370

Continued on the next page ...

Table 5.4 – Continued

Numb.	Model Structure	e_{RMS} , in.
44	$x_s(k+1) = a x_s(k) + b u_{NL}(k) + c x_s(k-1) + d u_{NL}(k-1) + e x_s^2(k-1)$	0.4374
45	$x_s(k+1) = a x_s(k) + b u_{NL}(k) + c x_s(k-1) + d u_{NL}(k-1) + e u_{NL}^2(k-1)$	0.4417
46	$x_s(k+1) = a x_s(k) + b u_{NL}(k) + c x_s(k-1) + d u_{NL}(k-1) + e x_s(k) u_{NL}(k)$	0.4397
47	$x_s(k+1) = a x_s(k) + b u_{NL}(k) + c x_s(k-1) + d u_{NL}(k-1) + e x_s(k) u_{NL}(k-1)$	0.4417
48	$x_s(k+1) = a x_s(k) + b u_{NL}(k) + c x_s(k-1) + d u_{NL}(k-1) + e x_s(k)^2 u_{NL}(k)$	0.4375
49	$x_s(k+1) = a x_s(k) + b u_{NL}(k) + c x_s(k-1) + d u_{NL}(k-1) + e x_s(k)^2 u_{NL}(k-1)$	0.4394
50	$x_s(k+1) = a x_s(k) + b u_{NL}(k) + c x_s(k-1) + d u_{NL}(k-1) + e x_s(k) u_{NL}(k)^2$	0.4360
51	$x_s(k+1) = a x_s(k) + b u_{NL}(k) + c x_s(k-1) + d u_{NL}(k-1) + e x_s(k-1) u_{NL}(k)^2$	0.4347
52	$x_s(k+1) = a x_s(k) + b u_{NL}(k) + c x_s(k-1) + d u_{NL}(k-1) + e x_s(k) u_{NL}(k-1)^2$	0.4402
53	$x_s(k+1) = a x_s(k) + b u_{NL}(k) + c x_s(k-1) + d u_{NL}(k-1) + e x_s(k-1) u_{NL}(k-1)^2$	0.4387
54	$x_s(k+1) = a x_s(k) + b u_{NL}(k) + c x_s(k-1) + d u_{NL}(k-1) + e x_s(k-1)^2 u_{NL}(k-1)^2$	0.4360

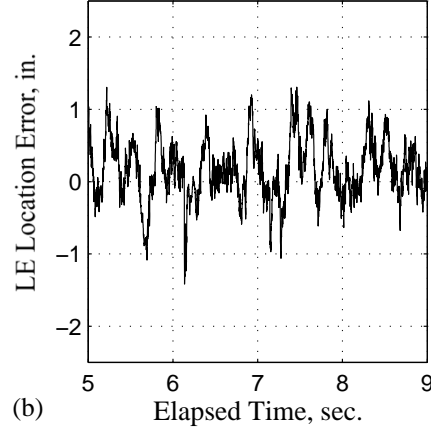
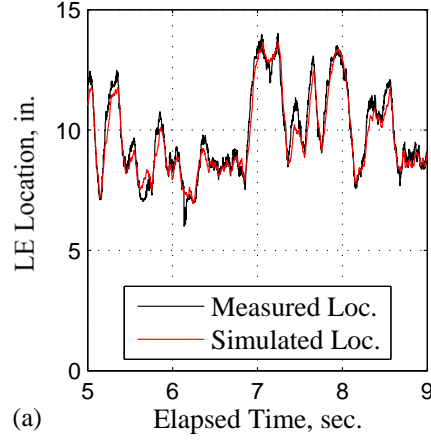


Figure 5.9: NARX model simulation location and error plot

5.4.1 Real-Time Experimental Results. Finally, the one-step prediction from the continuous, the ARX, and the NARX models were calculated for each set of pressure samples collected throughout run 4.12 in Table 4.1. The first step to implementing the models was to discretize the continuous model. The zero-pole-integrator continuous model from Table 5.2, was discretized then reformatted to a one-step format as presented in Equation (5.14). The original continuous transfer function was

$$G_{Cont}(s) = \frac{54.79(s + 1.31 \times 10^{-3})}{s(s + 61.15)} = \frac{54.79s + 0.07177}{s^2 + 61.15s} \quad (5.11)$$

which was then converted to discrete form using the `Matlab® c2d.m` command, which is a `Matlab®` routine that converts a continuous transfer function into a discrete transfer function. A 1 kHz sample rate was used in the conversion and discretized transfer function presented in Equation (5.12) was returned by the routine.

$$G_{Disc}(z) = \frac{x_s(z)}{u(z)} = \frac{0.05315z - 0.05315}{z^2 - 1.941z + 0.9407} \quad (5.12)$$

Equation 5.12 was cross-multiplied to get

$$x_s(k+2) - 1.94x(k+1) + 0.094x(k) = 0.053u(k+1) - 0.053u(k) \quad (5.13)$$

which was then rearranged and shifted one time step to gain the one-step format as presented in Equation (5.14)

$$x_s(k+1) = 1.94x_s(k) - 0.94x_s(k-1) + 0.053[u(k-1) - u(k)]. \quad (5.14)$$

The ARX and NARX models were already in discrete form and were used as is.

The ARX and the NARX equations presented as Equation (5.9) and Equation (5.10), respectively, the pressure increase shock location measurement algorithm from Chapter IV, the static nonlinear models from Section 5.1, and the discretized continuous equation were integrated into the LabVIEWTM routine and tested in run 4.12. Each model produced a predicted shock train LE location for the next sample based on the appropriate inputs for each model. The real-time recorded shock train LE location from the measurement, the discretized continuous model, the ARX model, and the NARX model predicted locations are presented in Figure 5.10a, Figure 5.10b, and Figure 5.10c, respectively, and the error between the measured location and the predicted locations from the three models are shown in Figure 5.10d, Figure 5.10e, and Figure 5.10f, respectively. The e_{RMS} values are presented in Table 5.5.

The real-time results confirm the accuracy of the models constructed in the continuous, ARX, and NARX modeling subsections. In addition, the real-time results

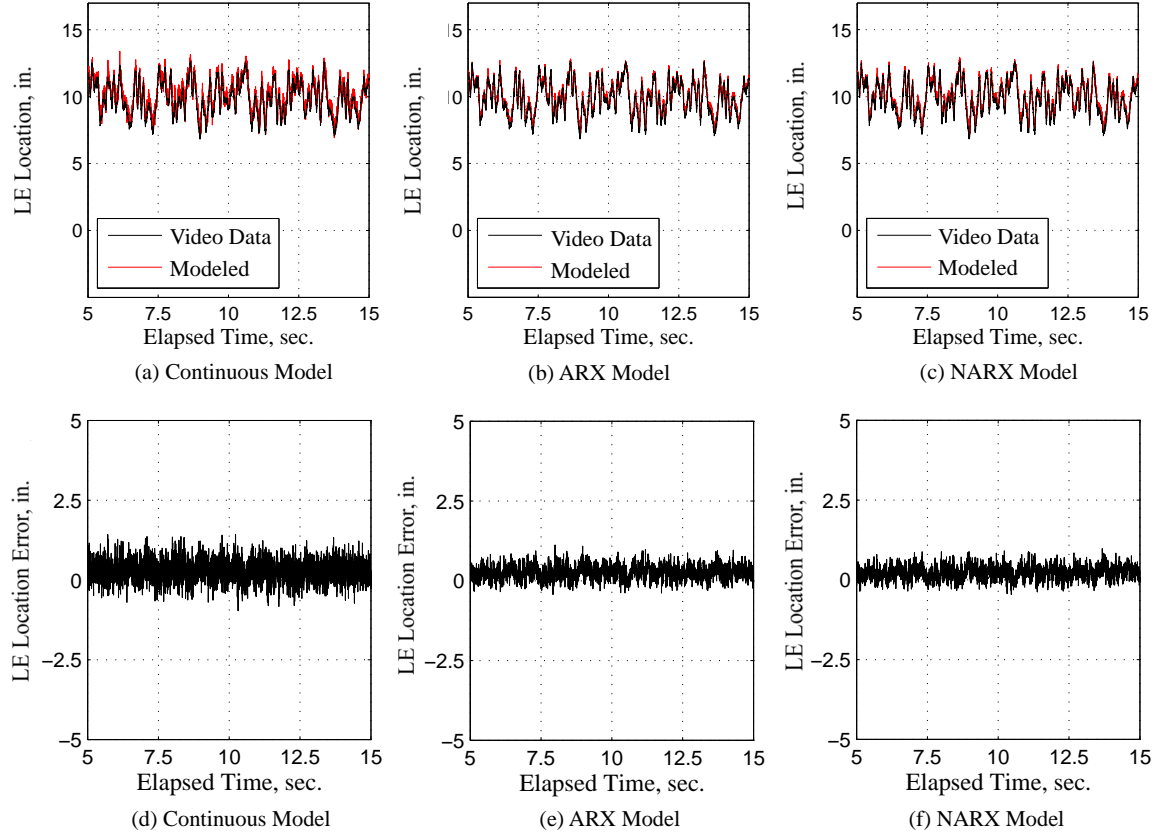


Figure 5.10: Continuous, ARX, and NARX modeling real-time results

confirm that the tested ARX and NARX models are more accurate than the continuous models. Also, there was no bias in the real-time runs due to the consistent x_{Meas} updates. These results demonstrate that there is minimal advantage to including the square term included in the NARX model. Finally, the real-time results demonstrate that, when a static nonlinearity is used, a simple, linear model can be used to model the dynamics of the P_{BP} to x_s relationship within an isolator.

Table 5.5: The RMS of the differences between the measured and predicted LE location

Model	e_{RMS} , in.	e_{RMS} , % of D
Discretized Continuous	0.420	16.8%
ARX	0.338	13.5%
NARX	0.309	12.4%

Finally, a comparison was made to determine the accuracy of the P_{BP} -based Hammerstein models using the pressure rise shock train location measurement algorithm against the optical measurement. A comparison was accomplished in runs 4.12-4.14 which were first introduced in Chapter IV and spanned the available Reynolds numbers. In these runs, the P_{BP} -based Hammerstein model, composed of a static nonlinear model and an ARX model, for each Reynolds number was implemented in the LabVIEWTM routine to predict the shock train location, x_{Model} at the next step, $k+1$, for each sample set, k . The ARX model was selected for the real-time modeling across Reynolds numbers due to its low e_{RMS} measure as seen in Table 5.5 and that the model remained linear. The model-predicted shock train locations along with the optically measured shock train locations are presented in Figures 5.11a-5.11c and the errors are presented in Figures 5.11d-5.11f. Additionally, a table of the e_{RMS} values are presented in Table 5.6 for the three runs under consideration. The average of the e_{RMS} values from the three runs is 0.45 in., or 18% of D , which is significantly lower than the distance between transducers of 47.6% of D .

Table 5.6: Back pressure input real-time recorded results

Run	Re	e_{RMS} , in.	e_{RMS} , % of D
4.12	7.20×10^6 /ft	0.438	17.52%
4.13	6.04×10^6 /ft	0.577	23.06%
4.14	4.78×10^6 /ft	0.338	13.52%

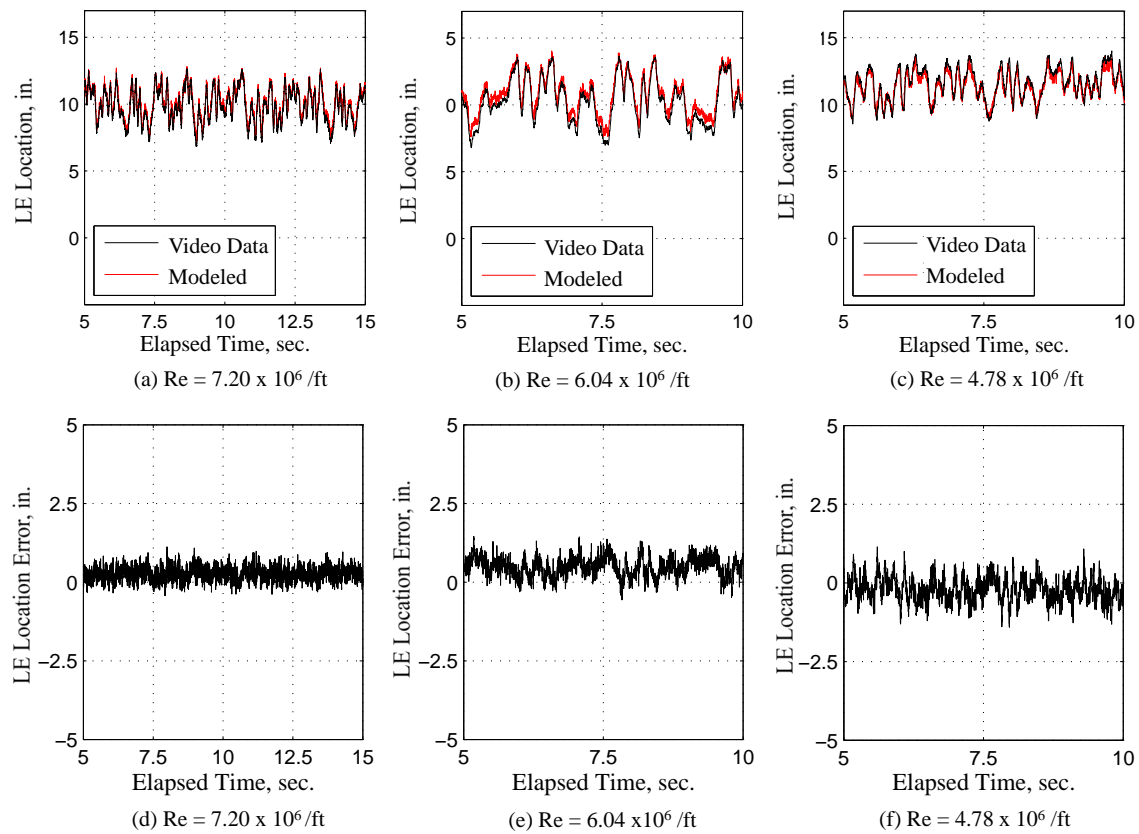


Figure 5.11: Real-time results for static nonlinear and ARX models

5.4.2 Non-Dimensionalized Model. Finally, the P_{BP} -based model was converted to a model based on the back-pressure to total pressure ratio, P_{BP}/P_0 . The non-dimensional model used a new static nonlinearity and the same ARX model presented as Equation (5.9). As in Section 5.1, a second-order polynomial was used as the static nonlinear model portion of a Hammerstein-model. The parameters in the static nonlinear model polynomial were calculated using data from runs 4.1-4.8 and runs 5.1-5.2. As opposed to what was accomplished in Section 5.1, in this case, the P_{BP}/P_0 data from all of the runs were combined for one regression matrix. Additionally, a single vector of the x_{Meas}/D values from the runs was used in the regression calculation. The non-dimensional static model developed is presented in Equation (5.15) and data along with a plot of the correlation are presented in Figure 5.12.

$$u_{NL}(k) = -213.477 \left(\frac{P_{BP}(k)}{P_0(k)} \right)^2 + 161.196 \frac{P_{BP}(k)}{P_0(k)} - 22.972 \quad (5.15)$$

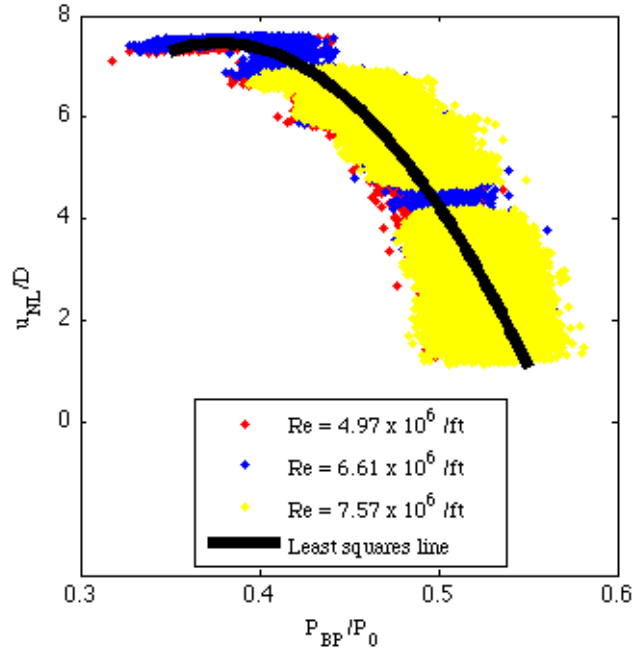


Figure 5.12: P_{BP}/P_0 to u_{NL}/D static model and data at three different Reynolds numbers

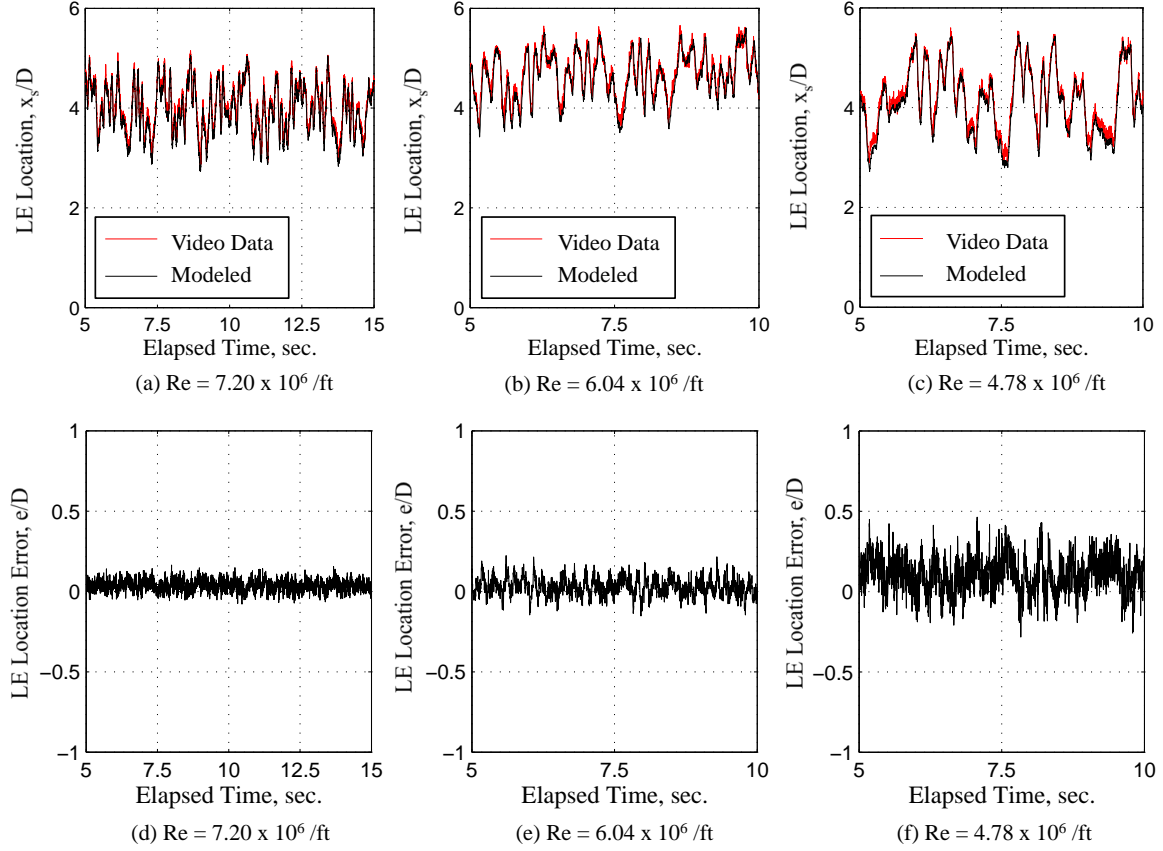


Figure 5.13: Location and error results using the non-dimensionalized model

The non-dimensionalized Hammerstein model using the static nonlinear model presented as Equation (5.15) and the ARX model presented as Equation (5.9) was validated with simulations of runs 4.12-4.14. In these simulations, actual pressure ratio and shock train LE location measurements were used as the inputs and the model outputs were compared to optical measurements for the error plots. The shock train locations as predicted by the non-dimensionalized Hammerstein model are presented in Figures 5.13a-5.13c and the errors are presented in Figures 5.13d-5.13f. Additionally, the e_{RMS} values from the runs are presented in Table 5.7. As can be seen by comparing Table 5.6 to Table 5.7, using the pressure ratio as the input to the Hammerstein model can be more accurate across Reynolds numbers. This is a result of slightly different Reynolds numbers in the evaluation runs in comparison to those from the runs used to develop the individual, Reynolds number tuned, static models.

Table 5.7: Non-dimensionalized pressure ratio results

Run	Re	e_{RMS} , in.	e_{RMS} , % of D
4.12	7.20×10^6 /ft	0.308	12.30%
4.13	6.04×10^6 /ft	0.389	15.55%
4.14	4.78×10^6 /ft	0.380	15.20%

Since the primary way to change the Reynolds number in the AFIT test section is to change the total pressure, differences in the Reynolds number are corrected for by using P_{BP}/P_0 in the static model.

5.4.3 Increased Transducer Spacing. The next consideration made was to consider the effect of using fewer transducers to develop the model and measure the shock train LE location. Three simulations were accomplished to compare ARX results developed with fewer transducers to optical data from runs 5.21-5.23. The same previously developed static nonlinearities (Equations (5.4)-(5.6)) were used in the simulation along with a new ARX model developed with the data from runs 5.13-5.16. The ARX model was developed by first calculating the shock train LE location using the decreased set of transducers and then including the new location measurements, along with the u_{NL} measurements from the static nonlinearity in a linear regression. The new model was then used to simulate the one-step prediction as if it had been implemented in the LabVIEWTM routine. The one-step prediction e_{RMS} values with the 95% of D transducer spacing is presented in Table 5.8 and the results when the transducers are mounted at 47.6% of D are presented in Table 5.9. As could be expected, the error increases as the distance between the transducers is increased. The reason for this increase is that the measurement algorithm is less accurate because the measurement algorithm is based on interpolation between transducers as is presented in Figure 4.3. When the distance between the transducers is increased, the accuracy of the LE location estimate is decreased due to the difference between the assumed linear relationship between pressure measurements amongst transducers used in interpolation and the actual curved increase in pressure measurement. The e_{RMS} values

were less than 23% of D when the transducers were mounted with a spacing of 95% of D and 17% of D with a 47.6% of D spacing indicating that the ARX model could be implemented with increased transducer spacing. Plots of the location predictions from the ARX model and the shadowgraph measured location are presented in Figures 5.14a-5.14c and the errors are presented in Figures 5.14d-5.14f for the increase transducer spacing simulations.

Table 5.8: ARX modeling errors, transducers at 95% of D

Run	e_{RMS} , in.	e_{RMS} , % of D
5.21	0.485	19.38%
5.22	0.564	22.54%
5.23	0.347	13.87%

Table 5.9: ARX modeling errors, transducers at 47.6% of D

Run	e_{RMS} , in.	e_{RMS} , % of D
5.21	0.317	14.33%
5.22	0.310	16.88%
5.23	0.330	12.87%

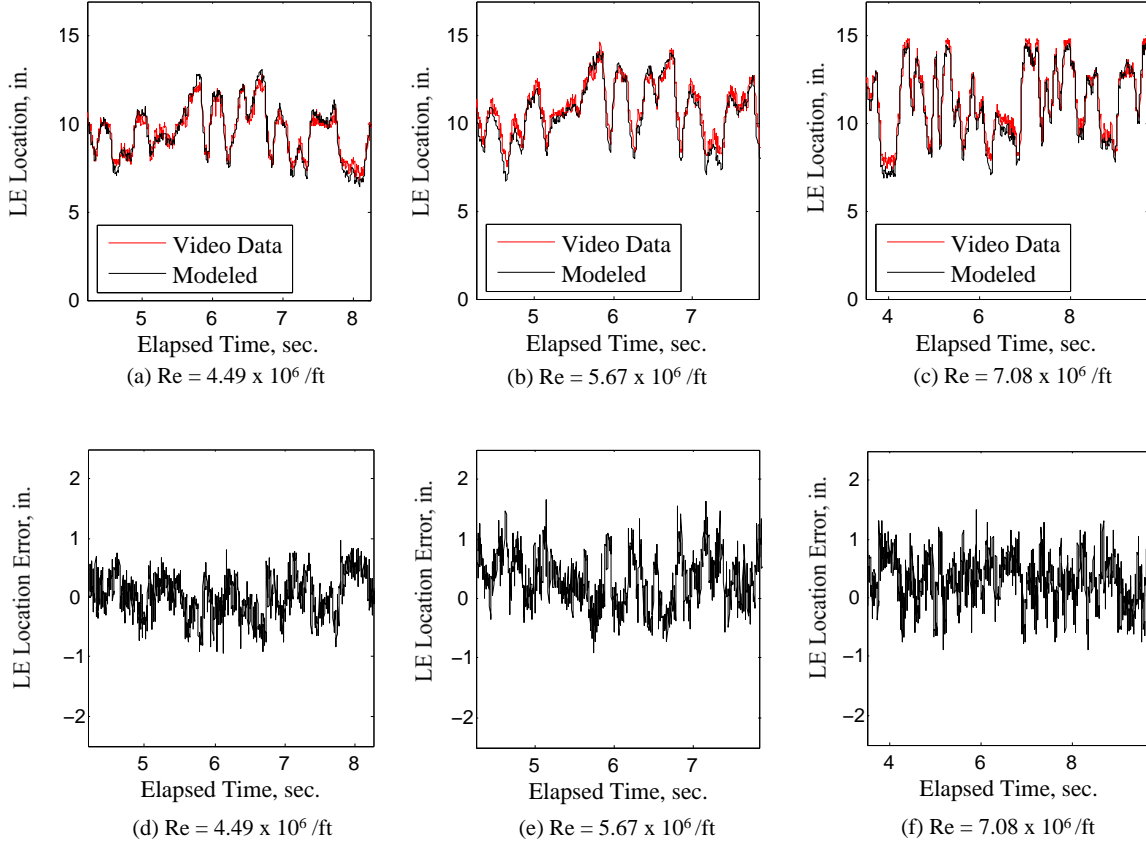


Figure 5.14: ARX modeling simulation location and error plots with increased transducer spacing

5.5 Ramp Angle to Location Modeling

After the conclusion of the P_{BP} to x_s modeling, efforts were applied to developing a dynamic model to relate the ramp angle, ϕ_{Meas} , to the shock train LE location, x_s . The same Hammerstein-like structure with an $n_a = n_b = 2$ ARX model was assumed for the ϕ_{Meas} to x_s dynamic model with the one change being that the three-parameter static nonlinear model was replaced by a four-parameter polynomial due to a better fit to experimental data. The modeling efforts for this portion of the research followed the same procedure of developing the static models first and then developing the dynamic models.

5.5.1 Static Nonlinear Models. The modeling started by accomplishing six different runs (runs 5.3-5.8) in which the ramp was raised from 9 to 20 degrees in

increments of $1/2$ deg. twice in the same run. A plot of the ramp input (ϕ_{Meas}) and the shock train location (x_{Meas}) for run 5.3 is presented in Figure 5.15a and Figure 5.15b, respectively. The average measured shock train locations using x_{Meas} , after the shock

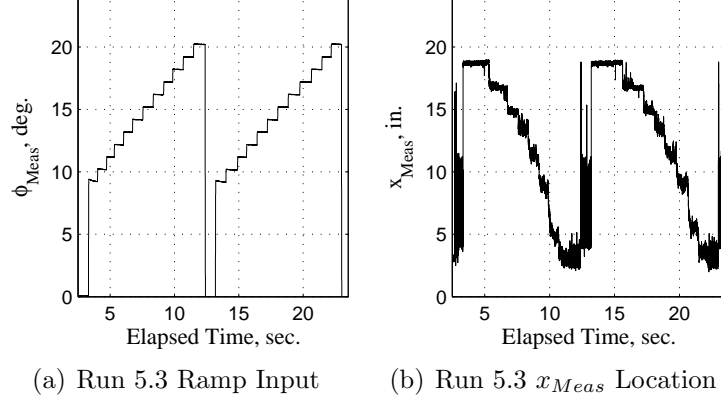


Figure 5.15: Multiple step input and x_{Meas} output plots for run 5.3

had started oscillating around its mean position at that ramp level, were then noted for each $1/2$ deg. ramp location. As a result, data was collected to relate ϕ_{Meas} to x_{Meas} at distinct ϕ_{Meas} settings and at three Reynolds number settings. The sets of ϕ_{Meas} vs x_{Meas} data were then used, in a similar manner to the P_{BP} to x_{Meas} data in Section 5.1 to develop a static polynomial model for a single Reynolds number setting. The static polynomial models developed for the three different Reynolds number settings are presented in Equations (5.16)-(5.18) and are plotted, along with the data used to generate the static models in Figures 5.16a-5.16c.

$$Re = 4.47 \times 10^6 / ft :$$

$$u_{NL}(k) = -0.0021\phi_{Meas}^3(k) - 0.0613\phi_{Meas}^2(k) + 1.4294\phi_{Meas}(k) + 13.067 \quad (5.16)$$

$$Re = 5.97 \times 10^6 / ft :$$

$$u_{NL}(k) = 0.0129\phi_{Meas}^3(k) - 0.8111\phi_{Meas}^2(k) + 13.8224\phi_{Meas}(k) - 52.6362 \quad (5.17)$$

$$Re = 7.24 \times 10^6 / ft :$$

$$u_{NL}(k) = -0.0031\phi_{Meas}^3(k) - 0.0762\phi_{Meas}^2(k) + 2.9557\phi_{Meas}(k) + 0.1990 \quad (5.18)$$

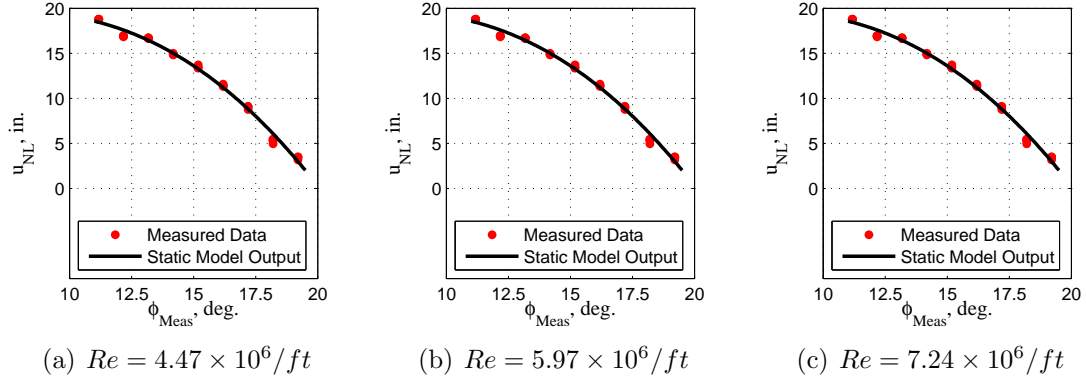


Figure 5.16: Real-time results for static nonlinear and ARX models

Additionally, the data from all the runs were combined to develop a single static model that, after testing, was shown to span the entire range of Reynolds numbers with a trade-off in accuracy that could be overcome with the control algorithm. The results of the control algorithm will be presented in Chapter VI. The combined static nonlinearity is presented in Equation (5.19) and all static ramp-based polynomial models are presented together in Figure 5.17. The combined model is listed as the “Control Nonlinearity” in Figure 5.17 since this was the polynomial used in the control algorithm developed in Chapter VI.

$$u_{NL}(k) = 0.0152\phi_{Meas}^3(k) - 0.8990\phi_{Meas}^2(k) + 14.9685\phi_{Meas}(k) - 58.0210 \quad (5.19)$$

5.5.2 Static Nonlinearity Inversion. In addition to the static nonlinearity, the inverse of the static nonlinearity was also needed for implementation in the control algorithm. The inversion was developed using the same ϕ_{RA} and x_{Meas} data as was used to develop the static nonlinearities presented in Subsection 5.5.1, except in this case, the x_{Meas} data was used as the inputs and the ϕ_{RA} data was used as the output. The polynomial equations developed as the inverse of the Hammerstein model static nonlinear model are presented in Equations (5.20)-(5.22). Additionally, as in the previous subsection, an inverse static nonlinearity was developed by combining the

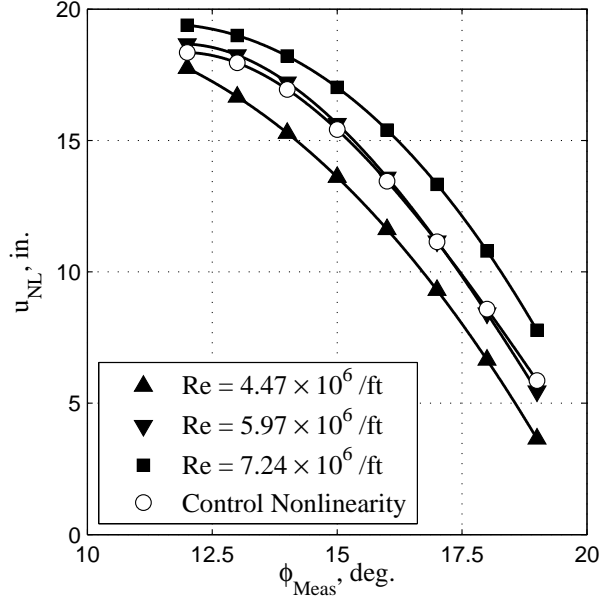


Figure 5.17: Plot of the measured ramp angle to dynamic model input nonlinearities data from runs 5.3-5.8. This inverse nonlinearity was used in the control algorithm at all Reynolds numbers available in the test section. The equation for the combined static nonlinearity inversion is presented in Equation (5.23) and a plot of all the inversions is presented in Figure 5.18.

$Re = 4.47 \times 10^6 / ft :$

$$\phi_{Meas}(k) = -0.0013u_{NL}^3(k)0.0230u_{NL}^2(k) - 0.4683u_{NL}(k)20.4456 \quad (5.20)$$

$Re = 5.97 \times 10^6 / ft :$

$$\phi_{Meas}(k) = -0.0019u_{NL}^3(k)0.0426u_{NL}^2(k) - 0.5902u_{NL}(k) + 21.1414 \quad (5.21)$$

$Re = 7.24 \times 10^6 / ft :$

$$\phi_{Meas}(k) = -0.0019u_{NL}^3(k) + 0.0426u_{NL}^2(k) - 0.5993u_{NL}(k)21.8838 \quad (5.22)$$

Combined inversion:

$$\phi_{Meas}(k) = -0.0010u_{NL}^3(k) + 0.0150u_{NL}^2(k) - 0.3667u_{NL}(k) + 20.6700 \quad (5.23)$$

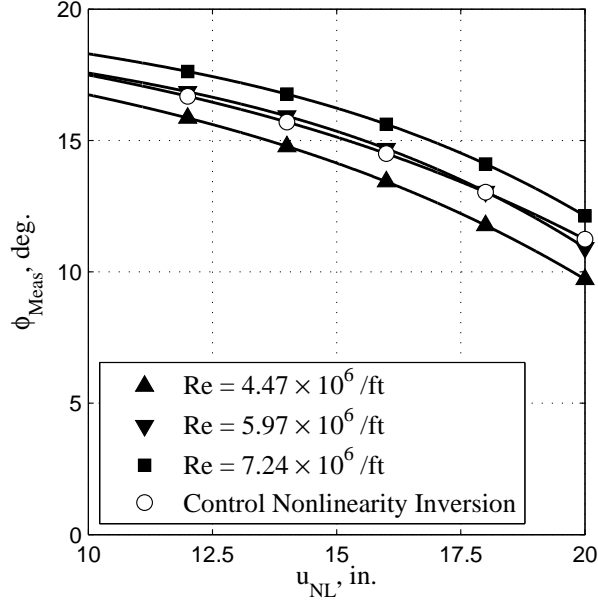


Figure 5.18: Plot of the dynamic model input to measured ramp angle nonlinearity inversions

5.5.3 Dynamic Model Development. Following the development of the static model, a dynamic model was developed for the relationship between u_{NL} , which was the static nonlinearity output from the ramp angle in this case, and x_{Model} . The same $n_a = n_b = 2$ ARX model structure was assumed for the dynamics in this portion of the research. Runs 5.9-5.20 were used to develop and validate the various models at different Reynolds numbers. As an example, for the Low Reynolds number, the data for runs 5.9-5.11 was combined for times when the ramp was deployed and then the model was validated using the data from run 5.12. Similar groupings of development versus evaluation data sets were accomplished to develop mid-range and a high-range models. As a consideration of the input ramp angles used to develop the data, a five-level APRBS algorithm was used. Ramp angle PSDs for the different Reynolds number sets of runs are presented in Figures 5.19a-5.19c. As can be noted, there is a significant drop at 10 Hz due to the ramp bandwidth and the repeating nature of the APRBS algorithm. As detailed in Appendix D, the APRBS algorithm is built on clock math, thus repeating itself. This repeating nature is evidenced in the PSDs by the repeated drops and rises in the plots.

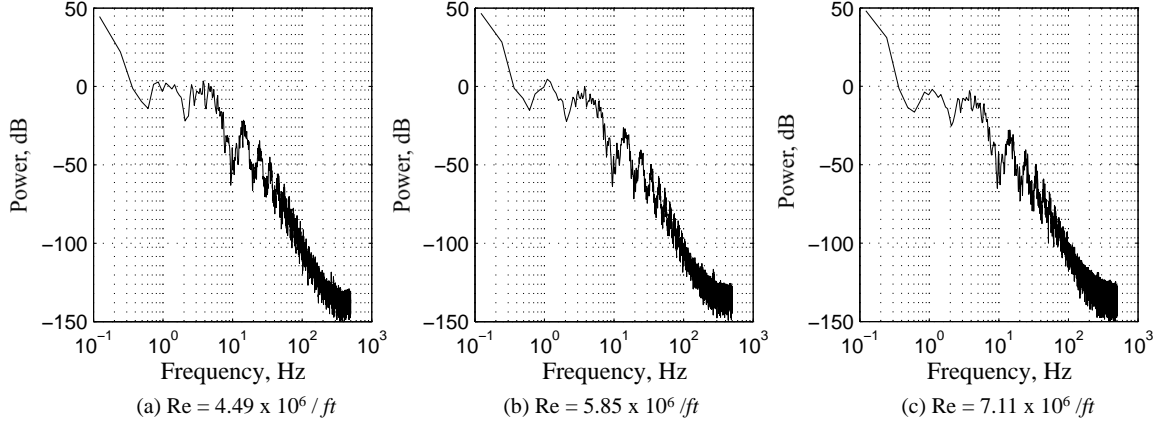


Figure 5.19: Ramp input PSD plots for runs 5.9-5.20

The $u_{NL}(k)$ calculations from the outputs of the static polynomials operating on each $\phi_{Meas}(k)$ were then used as the inputs and the $x_{Meas}(k)$ values as the outputs in another linear regression algorithm to calculate the dynamic models at each Reynolds number setting. The developed models are presented in Equations (5.24)-(5.26).

$$Re = 4.49 \times 10^6 / ft$$

$$x_{Model}(k+1) = 0.6264x_{Model}(k) + 0.3461x_{Model}(k-1) + 0.2073u_{NL}(k) - 0.1804u_{NL}(k-1) \quad (5.24)$$

$$Re = 5.67 \times 10^6 / ft$$

$$x_{Model}(k+1) = 0.6261x_{Model}(k) + 0.3469x_{Model}(k-1) + 0.1609u_{NL}(k) - 0.1335u_{NL}(k-1) \quad (5.25)$$

$$Re = 7.08 \times 10^6 / ft$$

$$x_{Model}(k+1) = 0.6725x_{Model}(k) + 0.3018x_{Model}(k-1) + 0.2623u_{NL}(k) - 0.2361u_{NL}(k-1) \quad (5.26)$$

Simulations were accomplished using the combined static nonlinearity, Equation (5.23), and the dynamic model appropriate to the evaluation run's Reynolds number. The runs that were simulated for comparison were runs 5.12, 5.16, and 5.20 to span the available Reynolds number range. Plots of the recorded and simulated location data

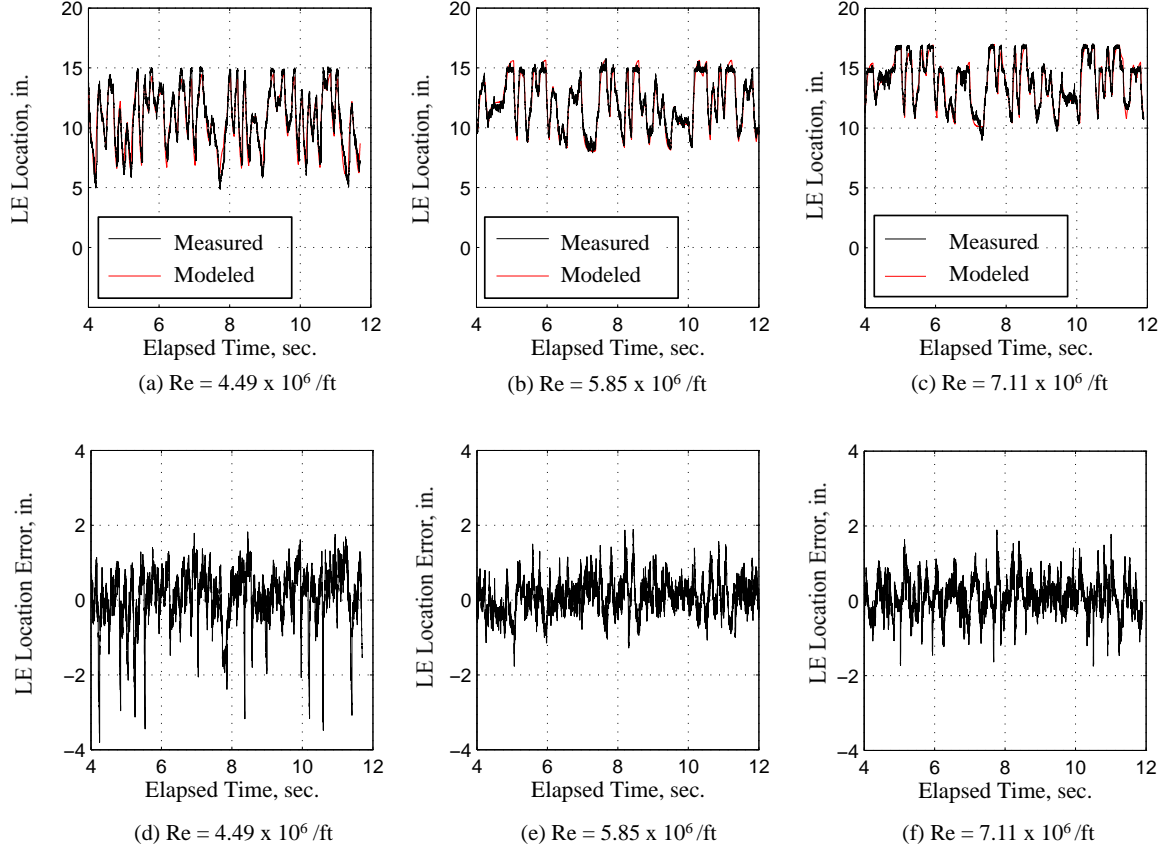


Figure 5.20: ϕ_{Meas} -based Hammerstein model simulation results

are presented in Figures 5.20a-5.20c and the errors are presented in Figures 5.20d-5.20f. Finally, a table of the simulation results is presented in Table 5.10. As can be noted, although the run errors increase as the Reynolds number decreases, even at the worst case, the modeling error is still less than the 47.6% of D distance between the pressure transducers.

Table 5.10: Ramp input simulation results

Run	Re	e_{RMS} , in.	e_{RMS} , % of D
5.12	4.49×10^6 /ft	0.8263	33.05
5.20	5.85×10^6 /ft	0.7874	31.50
5.16	7.11×10^6 /ft	0.7543	30.17

Next, each of the Reynolds number-specific Hammerstein models were implemented in the LabVIEWTM routine. The shock train LE location from the model,

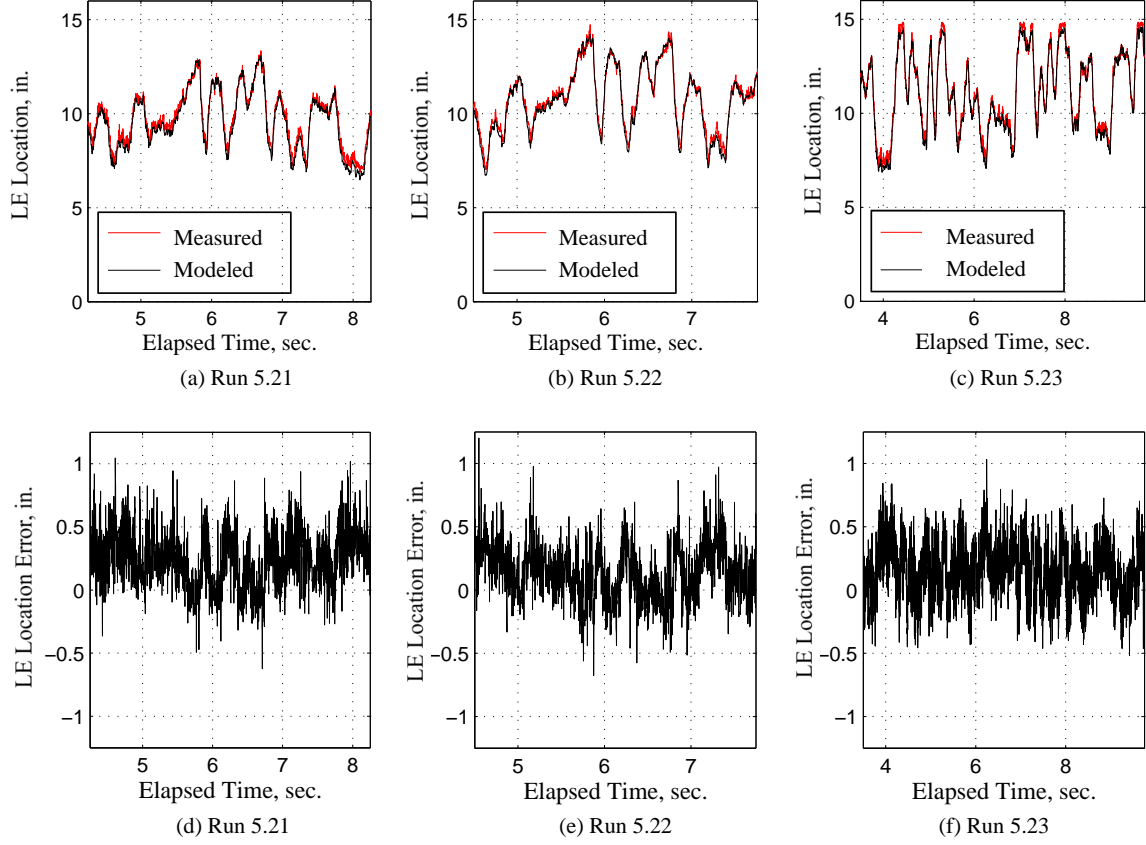


Figure 5.21: ϕ_{Meas} -based Hammerstein model real-time results

x_{Model} was calculated and recorded with each sample set, k , and compared to optical data, x_{Optic} . The x_{Model} and x_{Optic} comparison plots are presented in Figures 5.21a-5.21c and the error plots are presented in Figures 5.21d-5.21f. The accuracy comparison using the e_{RMS} value, as before, is presented in Table 5.11.

Table 5.11: Ramp input real-time recorded results

Run	Re	e_{RMS} , in.	e_{RMS} , % of D
5.21	$4.49 \times 10^6/\text{ft}$	0.3076	12.30
5.22	$5.67 \times 10^6/\text{ft}$	0.2521	10.09
5.23	$7.08 \times 10^6/\text{ft}$	0.2529	10.11

5.6 Modeling Conclusion

In order to model the shock train LE location within the test section, two Hammerstein models were developed. The models developed proved to be significantly more accurate than was the goal with e_{RMS} values significantly less than D . The first set of Hammerstein models used the back pressure, P_{BP} , as the input and were tailored to the appropriate Reynolds number for a run. The second set of Hammerstein models used the ramp angle, ϕ_{Meas} , as the input and were also tailored to the appropriate Reynolds number for a run. Each set of Hammerstein models were validated by comparing the one-step predicted shock train location, x_{Model} , against the optically measured shock train location, x_{Optic} . The results demonstrated accuracies less than 24% of D for the P_{BP} -based models (less than 16% for P_{BP}/P_0 -based models) and less than 13% for the ϕ_{Meas} -based models. Each final dynamic model successfully predicted the shock train LE location to within the distance between transducers, 47.6% of D .

VI. Control

After completing the development of a shock train measurement algorithm and a dynamic model of the system, the research then focused on the development of an automatic controller to place the shock train leading edge (LE) at a desired location, x_{Des} , within the test section. As noted in Chapter I, the shock train in a scramjet isolator tends to oscillate up to a duct height, D , on its own, so the goal of this research is to develop a controller that can place the shock train LE with a steady-state error of less than D . Since the shock train does not reach a steady-state where it no longer oscillates, the term steady-state is used to mean the state of the system after the initial transients from a commanded change in ramp angle have settled. The steady-state goal was for the e_{RMS} , as defined by Equation. (6.1) and Equation. (6.2) to be less than D

$$\mathbf{e} = \mathbf{x}_{Des} - \mathbf{x}_{Meas} \quad (6.1)$$

$$e_{RMS} = \sqrt{\frac{\mathbf{e}^T \mathbf{e}}{N}} \quad (6.2)$$

where N is the number of samples, \mathbf{x}_{Des} is a N sample vector of the desired shock train locations and the other variables are previously defined.

A schematic of the overall system with the controller is presented in Figure 6.1. The command to change the shock train LE location is originated by the user in a change to the x_{Des} position. This x_{Des} value is then compared to the measured shock train location, x_{Meas} to generate an error term, e which is then fed into an integral controller which will be discussed in Section 6.3. The output from the integral controller, u_I , is then converted to an angle, ϕ_I , using the inverse static nonlinearity developed in Chapter V (z^{-18}) and compared to the input from the deadbeat controller discussed in Section 6.1, ϕ_{DB} for the ramp command, ϕ_{Cu} . ϕ_{Cu} is then fed into the ramp and a 45 cycle lag block, z^{-45} before being processed by the observer. The z^{-45} operation was used to accommodate the transport lag noticed in the ramp bode plot from Chapter III as well as LabVIEWTM processing time. The 45 cycle lag was

developed after noting the lag between ϕ_{Ctl} and ϕ_{Meas} changes was approximately 0.045 sec. and considering that the sampling frequency used was 1000 Hz, so there was 0.001 sec. between samples. The ϕ_{Meas} value then fed into the test section where the ramp changed the flow within the test section. The vector of static pressures, \mathbf{P}_s , is then sampled and the measured shock train location, x_{Meas} is calculated. Additionally, since there is no observability into the states, a full-state observer was implemented. This observer design will be discussed in Section 6.2. The four-state (two-states for the shock train location and two-states for the ramp angle) output from the observer was then operated on by the deadbeat gain, \mathbf{K}_{DB} , to produce the deadbeat ramp angle, ϕ_{DB} .

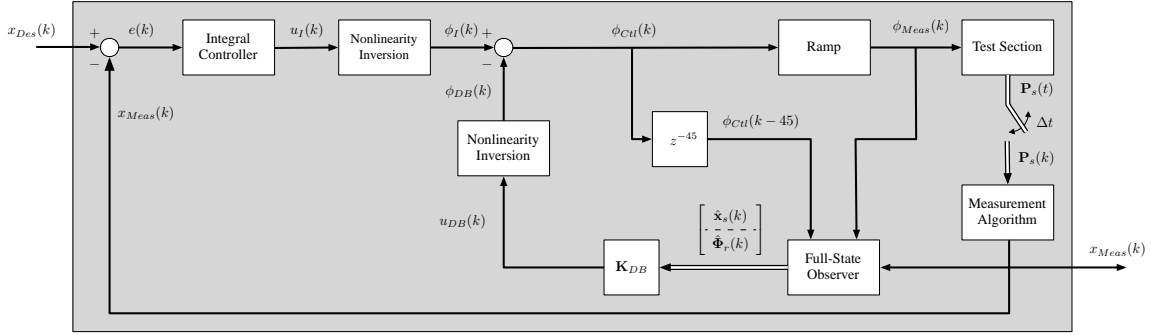


Figure 6.1: Schematic of the overall system and control algorithm

6.1 Deadbeat Controller Design

The desire for this controller is to move the shock train to the desired location as quickly as possible without an excessive (more than 20% of commanded change in location) amount of overshoot. As a result, a deadbeat controller was chosen for the inner loop in the control algorithm and an integral controller was used to attenuate the overshoot endemic to a deadbeat controller. Proportional and LQR controllers were also considered, but a significant amount of steady-state error was noted in the proportional controller and the LQR reaction times were slower than desired. In a deadbeat controller, the deadbeat response is commanded by changing K so that all the eigenvalues of the $[A - BK]$ closed-loop plant matrix are zero [65]. The $[A - BK]$ matrix is the matrix created by adding a feedback controller to the standard state-space form dynamics and measurement equations presented in Equation (6.3) and Equation (6.4), respectively, where A , B , and C are matrices of the appropriate size, \mathbf{x} is a vector of states, and y is the output. Additionally, a schematic of the state-space form transfer function is presented in Figure 6.2a.

$$\mathbf{x}(k + 1) = A\mathbf{x}(k) + Bu(k) \quad (6.3)$$

$$y(k) = C\mathbf{x}(k) \quad (6.4)$$

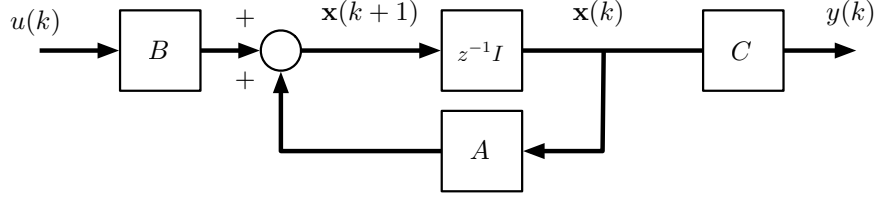
Next, a feedback controller is wrapped around the system as is displayed in Figure 6.2b and the terms are combined as is shown in Figure 6.2c. The result is that the original “ A ” matrix is now composed of “ $[A - BK]$ ” as is presented in Equation 6.5, so, the controller is now changing the dynamics of the system by changing the eigenvalues of the “ A ” matrix to those of “ $[A - BK]$ ”.

$$\mathbf{x}(k + 1) = (A - BK)\mathbf{x}(k) + Bu(k) \quad (6.5)$$

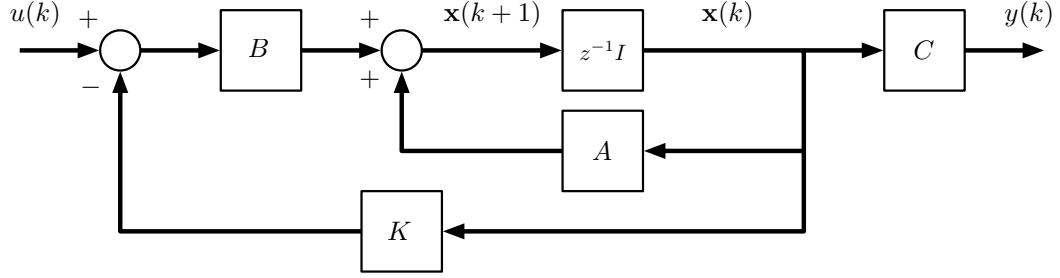
$$y(k) = C\mathbf{x}(k) \quad (6.6)$$

As a result of placing all the $[A - BK]$ eigenvalues at zero, disturbances are driven to

(a) Start with a state-space form transfer function:



(b) Add a feedback control loop:



(c) Combine terms:

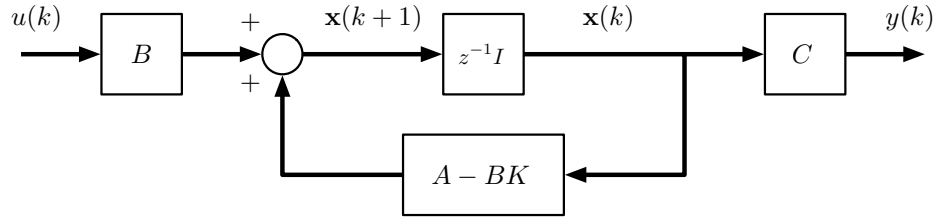


Figure 6.2: Illustration of a generic state-space model with a feedback controller

the plant null space in a finite number of samples and the system will have a minimal settling time [66].

The deadbeat controller gains were calculated by first placing the ramp transfer function and the ARX portion of the system Hammerstein model into state-space form. The ramp transfer function, developed from the ramp Bode plot in Chapter III is presented in Equation (6.7).

$$G_{Ramp} = \frac{0.012204(z + 0.8959)}{(z - 0.8479)^2} z^{-18} = \frac{0.012204z + 0.0109}{z^2 - 1.6958z + 0.7189} z^{-18} \quad (6.7)$$

G_{Ramp} can then be placed into a controllable canonical state-space form without the delay term, z^{-18} , as is presented in Equation (6.8) and the ramp measurement

equation is presented in Equation (6.9).

$$\Phi_r(k+1) = \begin{bmatrix} 0 & 1 \\ -0.7189 & 1.6958 \end{bmatrix} \Phi_r(k) + \begin{bmatrix} 0 \\ 1 \end{bmatrix} \phi_{Ctl}(k) \quad (6.8)$$

$$\phi_{Meas}(k) = \begin{bmatrix} 0.0109 & 0.012204 \end{bmatrix} \Phi_r(k) \quad (6.9)$$

The matrices from the ramp state-space and measurement equations are then labeled according to Equations (6.10-6.12).

$$A_r \triangleq \begin{bmatrix} 0 & 1 \\ -0.7189 & 1.6958 \end{bmatrix} \quad (6.10)$$

$$B_r \triangleq \begin{bmatrix} 0 \\ 1 \end{bmatrix} \quad (6.11)$$

$$C_r \triangleq \begin{bmatrix} 0.0109 & 0.012204 \end{bmatrix} \quad (6.12)$$

The state-space and measurement equations for the ARX model, developed in Chapter V, are then presented in Equation (6.13) and Equation (6.14), respectively. Since the nonlinearity inversion adequately inverts the nonlinear model for ϕ_{Meas} and u_{NL} values in which the shock train LE remains within the test section, the nonlinearity is not considered during the deadbeat control gain calculation. The nonlinear model will be included when considering the integral gain, K_I .

$$\mathbf{x}_s(k+1) = \begin{bmatrix} 0 & 1 \\ 0.3018 & 0.6725 \end{bmatrix} \mathbf{x}_s(k) + \begin{bmatrix} 0 \\ 1 \end{bmatrix} \phi_{Meas}(k) \quad (6.13)$$

$$x_{Meas}(k) = \begin{bmatrix} -0.2361 & 0.2623 \end{bmatrix} \mathbf{x}_s(k) \quad (6.14)$$

The matrices from the system state-space and measurement equations are then relabeled as presented in Equations (6.15)-(6.17).

$$A_s \triangleq \begin{bmatrix} 0 & 1 \\ 0.3018 & 0.6725 \end{bmatrix} \quad (6.15)$$

$$B_s \triangleq \begin{bmatrix} 0 \\ 1 \end{bmatrix} \quad (6.16)$$

$$C_s \triangleq \begin{bmatrix} -0.2361 & 0.2623 \end{bmatrix} \quad (6.17)$$

Now, after substituting Equation (6.9) into Equation (6.13) as well as relabeling the matrices, the ARX state-space dynamics equation is

$$\mathbf{x}_s(k+1) = A_s \mathbf{x}_s(k) + B_s C_r \Phi_r(k). \quad (6.18)$$

The ramp and ARX state-space equations can now be combined to form the open-loop system going from ϕ_{Ctl} to x_{Meas} . The open-loop state-space equation is presented in Equation (6.19) and the open-loop measurement equation is presented in Equation (6.20).

$$\begin{Bmatrix} \mathbf{x}_s(k+1) \\ \Phi_r(k+1) \end{Bmatrix} = \begin{bmatrix} A_s & B_s C_r \\ \underline{0} & A_r \end{bmatrix} \begin{Bmatrix} \mathbf{x}_s(k) \\ \Phi_r(k) \end{Bmatrix} + \begin{bmatrix} \underline{0} \\ B_r \end{bmatrix} \phi_{Ctl}(k) \quad (6.19)$$

$$x_{Meas}(k) = \begin{bmatrix} C_s & \underline{0} \end{bmatrix} \begin{Bmatrix} \mathbf{x}_s(k) \\ \Phi_r(k) \end{Bmatrix} \quad (6.20)$$

The matrices of the open-loop system are then relabeled to

$$A_{OL} \triangleq \begin{bmatrix} A_s & B_s C_r \\ \underline{0} & A_r \end{bmatrix} \quad (6.21)$$

$$B_{OL} \triangleq \begin{bmatrix} \underline{0} \\ B_r \end{bmatrix} \quad (6.22)$$

$$C_{OL} \triangleq \begin{bmatrix} C_s & \underline{0} \end{bmatrix} \quad (6.23)$$

so, the open-loop state-space dynamics and measurement equations are

$$\begin{bmatrix} \mathbf{x}_s(k+1) \\ \underline{\Phi_r(k+1)} \end{bmatrix} = A_{OL} \begin{bmatrix} \mathbf{x}_s(k) \\ \underline{\Phi_r(k)} \end{bmatrix} + B_{OL} \phi_{Cu}(k) \quad (6.24)$$

$$x_{Meas}(k) = C_{OL} \begin{bmatrix} \mathbf{x}_s(k) \\ \underline{\Phi_r(k)} \end{bmatrix}. \quad (6.25)$$

To close the loop, now consider that

$$\begin{aligned} \phi_{Cu}(k) &= \phi_I(k) + \phi_{DB}(k) \\ &= \phi_I(k) - \mathbf{K}_{DB} \begin{bmatrix} \mathbf{x}_s(k) \\ \underline{\Phi_r(k)} \end{bmatrix} \end{aligned} \quad (6.26)$$

when the observer is not considered for the controller gain determination and K_{DB} is the deadbeat controller gain where the desired controller without the nonlinearity inversion is

$$\phi_{DB} = -\mathbf{K}_{DB} \begin{bmatrix} \mathbf{x}_s(k) \\ \underline{\Phi_r(k)} \end{bmatrix}. \quad (6.27)$$

The observer was developed separately and will be presented in Section 6.2. After substituting Equation (6.27) into Equation (6.24) and collecting terms, the closed-loop

equation for the deadbeat controlled inner loop, without the observer, from Figure 6.1 is

$$\begin{Bmatrix} \mathbf{x}_s(k+1) \\ \Phi_r(k+1) \end{Bmatrix} = [A_{OL} - B_{OL}\mathbf{K}_{DB}] \begin{Bmatrix} \mathbf{x}_s(k) \\ \Phi_r(k) \end{Bmatrix} + B_{OL}\phi_I(k) \quad (6.28)$$

$$x_{Meas}(k) = C_{OL} \begin{Bmatrix} \mathbf{x}_s(k) \\ \Phi_r(k) \end{Bmatrix}. \quad (6.29)$$

Since the desired response is the deadbeat response, the eigenvalues of $A_{OL} - B_{OL}\mathbf{K}_{DB}$ were placed at the z -plane origin (i.e. $z = \begin{bmatrix} 0 & 0 & 0 & 0 \end{bmatrix}$), so the deadbeat controller gains are

$$\begin{aligned} \mathbf{K}_{DB} &= \begin{Bmatrix} K_{DB,s} & K_{DB,r} \end{Bmatrix} \\ &= \begin{bmatrix} 10.6113 & 30.3846 & -0.3357 & 2.3683 \end{bmatrix}. \end{aligned} \quad (6.30)$$

6.2 Observer Design

The only measurement available for use in the feedback controller in Equation (6.27) is the shock train LE location from the measurement algorithm, x_{Meas} and the measured ramp angle, ϕ_{Meas} . As a result, a full-state observer was implemented to provide estimates of the values of the states at each k during a run. A schematic of the observer is presented in Figure 6.3. The inputs to the observer are $\phi_{Meas}(k)$, $x_{Meas}(k)$, and the commanded ramp angle 45 cycles prior to k , $\phi_{Ch}(k - 45)$. The 45 cycle lag was integrated into the algorithm due to the transport lag noted first while considering the actuator in Section 3.3 and then when accomplishing step inputs which will be discussed in Section 6.3. The first transport lag was noted when the Bode plot of the ramp response was analyzed. The full control LabVIEWTM routine was not used to collect the data for the ramp analysis, though, so extra lags from calculations were not in the data. During step input runs using the full shock train control LabVIEWTM code, it was noticed that the transport lag was greater than

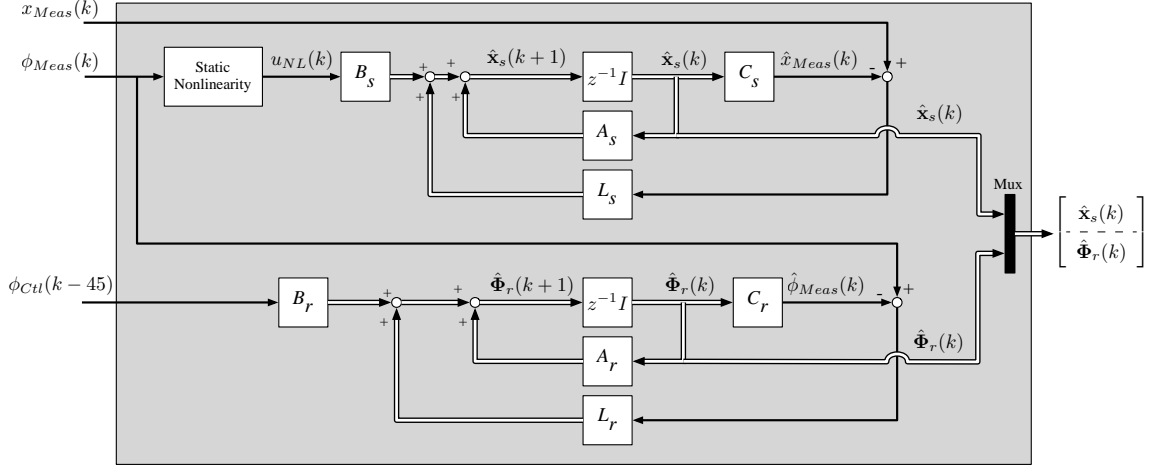


Figure 6.3: Schematic of the implemented full-state observer

just the ramp lag. As a result, the lag used for the observer was increased from 18 cycles to 45 cycles to correspond to the combined lag from both the ramp and LabVIEWTM calculation. Additionally, note that the static nonlinearity is integrated into the observer design for the estimation of the states related to the shock train location, $\hat{\mathbf{x}}_s$. Finally, since both the shock train LE location ARX model and the model of the ramp are 2-state models, the estimated states for the shock train, $\hat{\mathbf{x}}_s$ and for the ramp angle, $\hat{\Phi}_r$ have two states, so the output from the observer is all four states. A state-space equation for the observer is presented in Equation (6.31) where $P[\cdot]$ implies the nonlinearity operating on $\phi_{Meas}(k)$.

$$\begin{aligned} \begin{Bmatrix} \hat{\mathbf{x}}_s(k+1) \\ \hat{\Phi}_r(k+1) \end{Bmatrix} &= \begin{bmatrix} A_s - L_s C_s & \underline{0} \\ \underline{0} & A_r - L_r C_r \end{bmatrix} \begin{Bmatrix} \hat{\mathbf{x}}_s(k) \\ \hat{\Phi}_r(k) \end{Bmatrix} + \dots \\ &\quad \begin{bmatrix} L_s & B_s & \underline{0} \\ \underline{0} & \underline{0} & L_r \end{bmatrix} \begin{Bmatrix} x_{Meas}(k) \\ P[\phi_{Meas}(k)] \\ \phi_{Meas}(k) \end{Bmatrix} + \begin{bmatrix} \underline{0} \\ B_r \end{bmatrix} z^{-45}[\phi_{Cu}(k)] \quad (6.31) \end{aligned}$$

Finally, the deadbeat response is desired, again, in the observer, so the observer poles were placed at $z = [0000]$. The calculated observer gains are presented in

Equation (6.32)

$$\mathbf{L} = \begin{Bmatrix} L_s \\ L_r \end{Bmatrix} = \begin{bmatrix} 35.6822 \\ 34.6819 \\ 60.3764 \\ 85.0293 \end{bmatrix} \quad (6.32)$$

6.3 Integral Control

In order to account for fit errors between the Hammerstein model and the actual system as well as to slow the system (since a deadbeat controller was selected for the observer and the pole placement), an integral controller was added to the control algorithm. A schematic of the integral controller is presented in Figure 6.4. The inte-

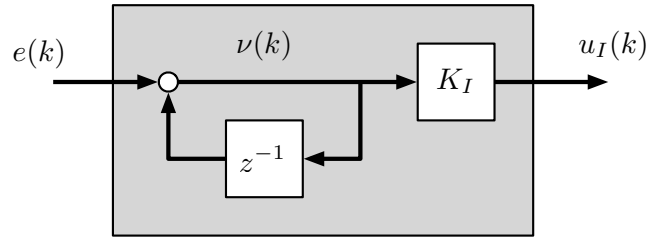


Figure 6.4: Schematic of the integral controller

gral control gain, K_I was selected through experimentation. Step inputs commanding x_{Des} from 5 to 15 in. were applied to the system while varying K_I in runs 6.1 through 6.3. The desired specification for a step response was an overshoot, M_p , less than 20%. The response at three different K_I settings is presented in Table 6.1 as well as in Figures 6.5a-6.5c. The specification was met by placing setting $K_I = 0.0075$, so this integral gain value was used for all controlled runs.

Table 6.1: Test section operating configurations

Run	Re, /ft	K_I	t_{lag} , sec.	M_p
6.1	7.04×10^6	0.0050	0.044	Overdamped
6.2	7.05×10^6	0.0075	0.044	1.89 in., 18.9%
6.3	7.05×10^6	0.0100	0.044	2.03 in., 20.3%

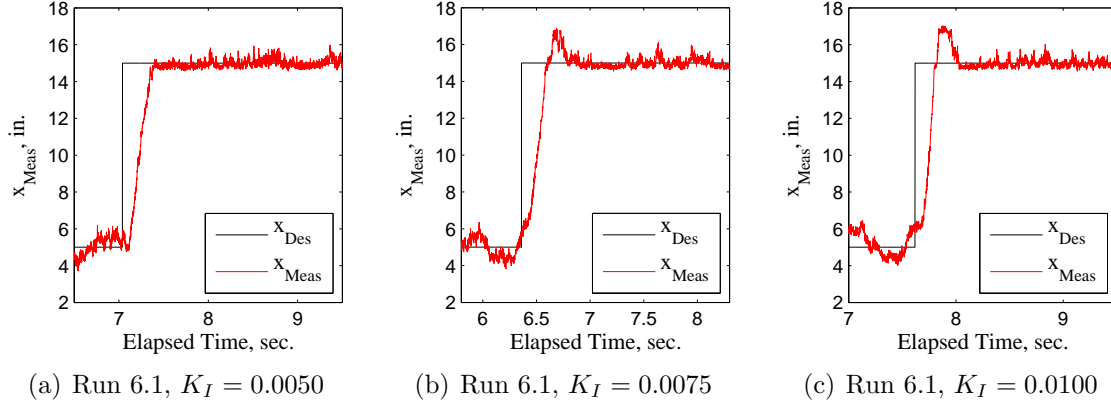


Figure 6.5: Step responses with varying K_I values

6.4 Controller Optical vs Measurement Algorithm Comparison

The measurement algorithm performance was verified with all the measurement and control algorithms implemented into the LabVIEWTM routine before the controller performance was evaluated. A comparison was made between the measured location using the measurement algorithm, x_{Meas} , to the shock train LE location from the shadowgraph, x_{Optic} , at various Reynolds numbers throughout the test section. Since x_{Optic} was compared to x_{Meas} and not x_{Des} , the measurement algorithm performance only affects control performance. Six different runs were used to collect the data for this subsection. In each run, the ramp is raised to an initial position (out of the shadowgraph field of view) to develop the shock train, and then raised to two additional positions within the shadowgraph field of view. The six runs considered include three runs at each end of the Reynolds number range available in this test section. Additionally, a range of shock train LE locations ($x_{Des} \in [3.75, 6.75, \dots, 15.75]$) was considered at each Reynolds number setting. The results from the testing are placed in Table 6.2. The x_{Meas} data was collected at 1kHz and then downsampled to the shadowgraph data rate of 500 FPS for comparison. Additionally, plots of the results are placed in Figures 6.6a-6.6f and Figures 6.7a-6.7f. In these figures, the top row of plots displays the actual measurements and the bottom row displays the error, defined as the difference between x_{Meas} and x_{Optic} .

As can be noted from the location plots, the x_{Meas} location was validated throughout the test section for the range of available Reynolds numbers to within 30% of a duct height. Additionally, when in the center portion of the test section, the measurement algorithm is more accurate. The algorithm does have difficulty in the far upstream portion of the test section, though. When commanded to $x_{Des} = 3.75$ in. there is some discrepancy between x_{Meas} and x_{Optic} . A likely reason for this discrepancy is the significant pressure increase in the test section within the first 5 in. downstream from the nozzle as discussed in Chapter III. The measurement algorithm relies on interpolation amongst the pressure transducer readings to locate x_{Meas} . The pressure increase in the upstream portion of the test section breaks the implicit assumption of this technique of a monotonically increasing static wall pressure along the test section, thus resulting in significant errors in location measurements in the far upstream portion of the test section. Throughout the remainder of the test section, the measurement algorithm is accurate to less than 20% of a duct height although the pressure transducers are separated by 47.6% of a duct height.

Table 6.2: Optical measurement versus measurement algorithm results

Run	x_{Des} , in.	Re, $/ft$	$\mu(e)$, in.	$\sigma(e)$, in	e_{RMS} , in.	e_{RMS} , % of D
6.4	3.75, 6.75	4.58×10^6	0.6452	0.3751	0.7456	29.83
6.5	9.75, 12.75	4.54×10^6	0.2285	0.2476	0.2939	11.76
6.6	12.75, 15.75	4.53×10^6	0.3914	0.4569	0.4933	19.73
6.7	3.75, 6.75	7.16×10^6	0.5787	0.2827	0.6433	25.73
6.8	9.75, 12.75	7.04×10^6	0.3214	0.3275	0.4015	16.05
6.9	12.75, 15.75	7.05×10^6	0.3517	0.4315	0.4444	17.78

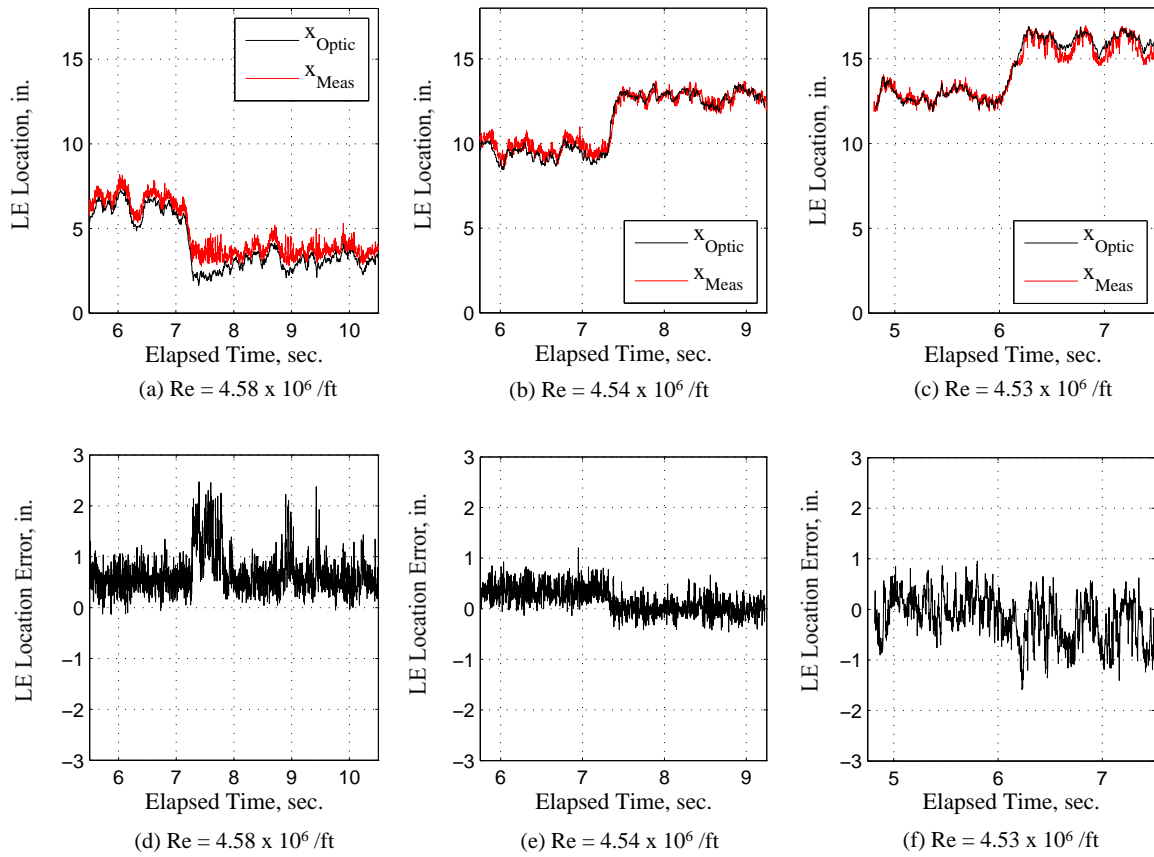


Figure 6.6: Measurement algorithm vs optical results for runs 6.4-6.6

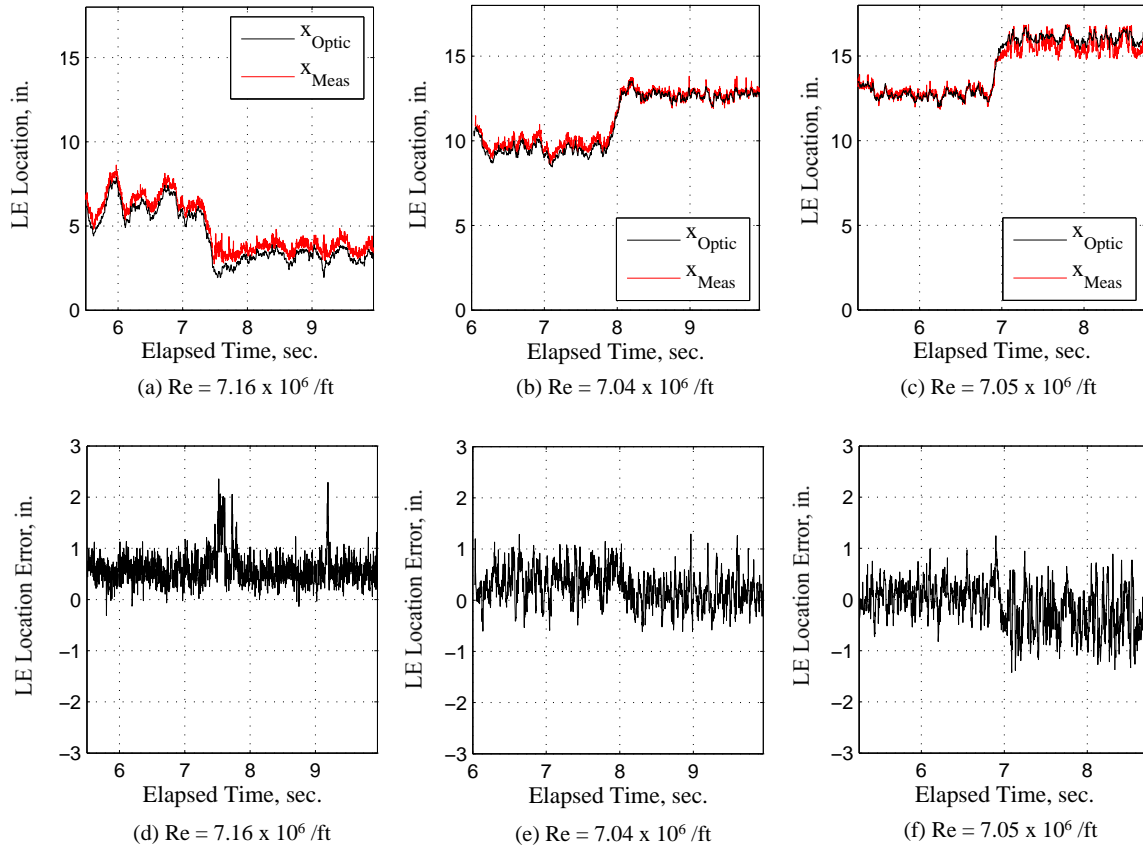


Figure 6.7: Measurement algorithm vs optical results for runs 6.7-6.9

6.5 Controller Performance

The next consideration is the ability to direct the shock train LE location throughout the test section. Three runs, presented in Table 6.3, were accomplished to display this capability. Additionally, the location plots are presented in Figures 6.8a-6.8c and the error plots are presented in Figures 6.8d-6.8f. Plots of the commanded ramp angle, ϕ_{Ctl} versus the measured ramp angle, ϕ_{Meas} are presented in Figures 6.9a-6.9c and the error, defined as $\phi_{Ctl} - \phi_{Meas}$ is presented in Figures 6.9d-6.9f. As can be seen in these ramp angle plots, there is an approximately 0.2 deg. error between the commanded and the measured ramp angle. In these runs, the shock train location was controlled by changing the x_{Des} value such that $x_{Des} = [4, 8, 6, 12, 10, 16, 14, 18]$ in. and three Reynolds numbers were considered.

As can be seen, the controller is able to place the shock train LE at a desired location throughout the test section to within $1/2$ of D at all three Reynolds number settings. The overall goal of the control efforts was to place the shock train within one D . The effects of the transport lag in the system can be observed in the delay between changes in x_{Des} and ϕ_{Meas} as presented in Figure 6.10. Although the lag is evident, due to the consideration of the transport lag in the controller design as well as the controller's robustness, the controller is still capable of holding the shock train LE at a desired location. Additionally, the controller is able to control around a approximately 0.2 deg. ramp deflection error. The controller is capable of actively controlling the shock train location to overcome temporal (transport lag) and ramp measurement errors to within $1/2$ of D .

Table 6.3: x_{Des} vs x_{Meas} results throughout the test section

Run	Re, $/ft$	$\mu(e)$, in.	$\sigma(e)$, in	e_{RMS} , in.	e_{RMS} , % of D
6.10	4.54×10^6	0.6504	1.0559	1.0604	42.41
6.11	5.77×10^6	0.5802	0.9687	0.9744	38.98
6.12	7.01×10^6	0.6845	1.1301	1.1390	45.56

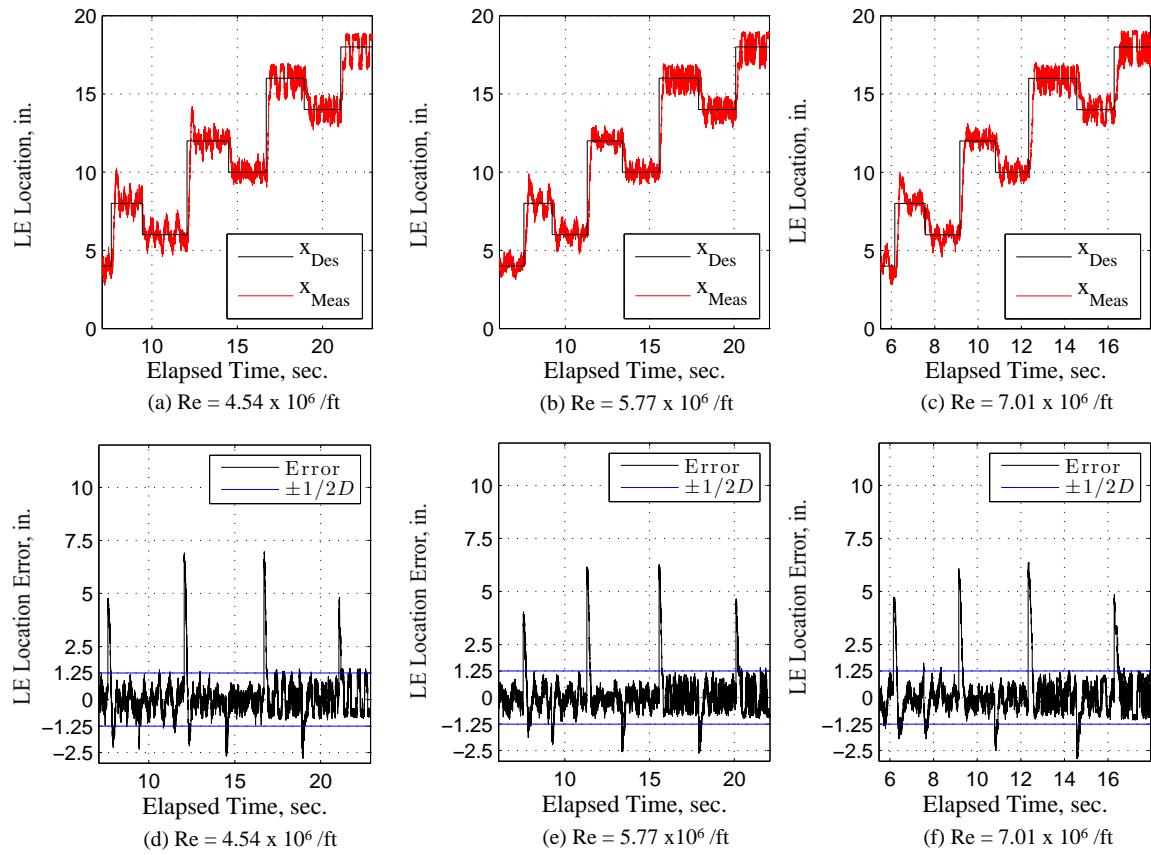


Figure 6.8: Desired vs measured location and error results for runs 6.10-6.12

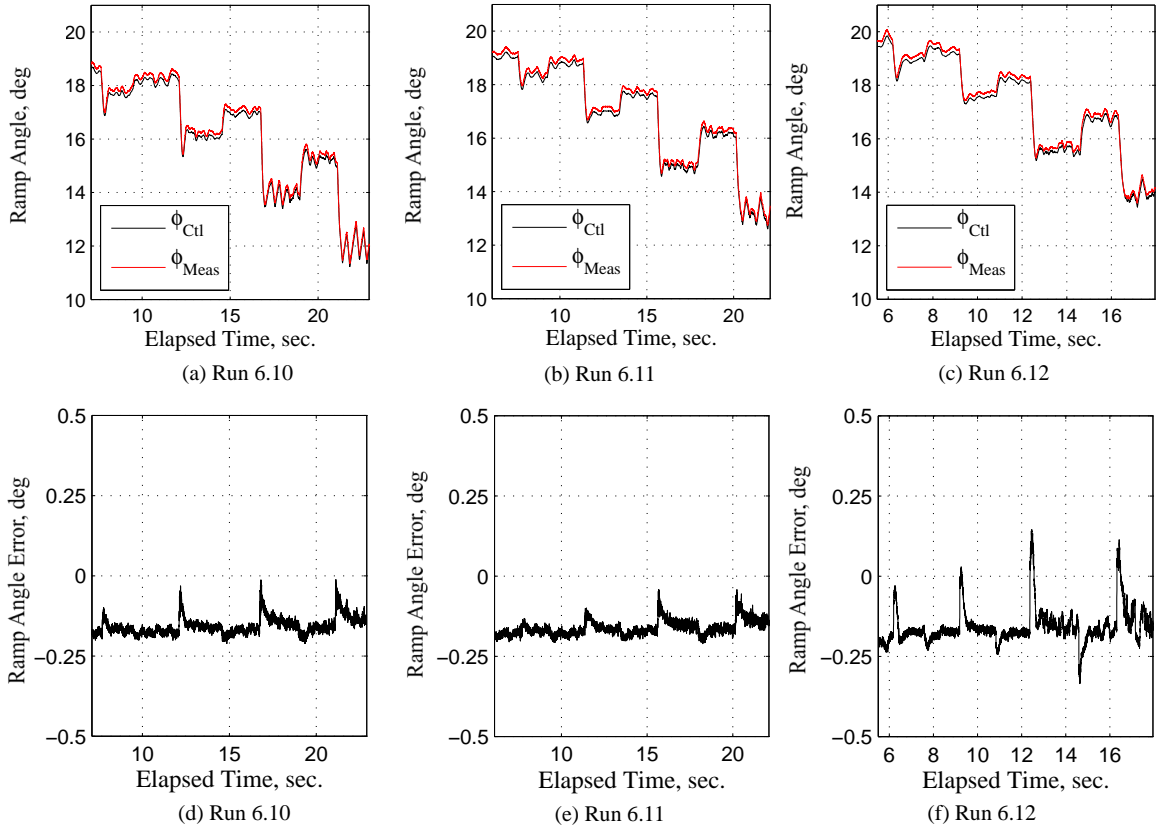
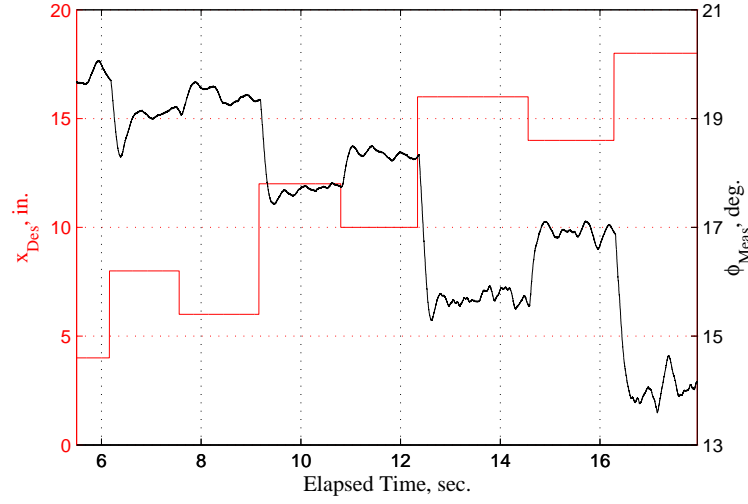
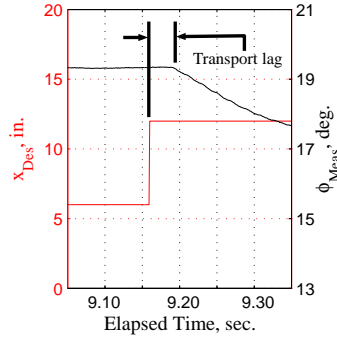


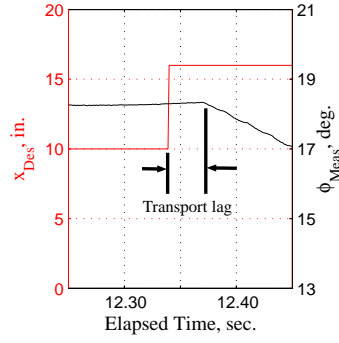
Figure 6.9: Controlled vs measured ramp angle and error results for runs 6.10-6.12



(a) Run 6.12 x_{Des} and ϕ_{Meas}



(b) Run 6.12 x_{Des} and ϕ_{Meas}



(c) Run 6.12 x_{Des} and ϕ_{Meas}

Figure 6.10: Run 6.12 x_{Des} and ϕ_{Meas} with the time zoomed-in at two places

6.6 Observer Performance

The observer is capable of accurately estimating the shock train LE location, $\hat{x}_{Meas}(k)$ and the ramp angle, $\hat{\phi}_{Meas}(k)$ throughout a run at different Reynolds numbers. The observer residuals for each run are defined as presented in Equation (6.33) and Equation (6.34)

$$x_{Resid}(k) \triangleq x_{Meas}(k) - \hat{x}_{Meas}(k) = x_{Meas}(k) - C_s \hat{\mathbf{x}}_s(k) \quad (6.33)$$

$$\phi_{Resid}(k) \triangleq \phi_{Meas}(k) - \hat{\phi}_{Meas}(k) = \phi_{Meas}(k) - C_r \hat{\Phi}_r(k) \quad (6.34)$$

where x_{Resid} is the residual related to the x measurement and ϕ_{Resid} is the residual related to the ϕ measurement. Plots of x_{Meas} versus \hat{x}_{Meas} along with the error are presented in Figures 6.11a-6.11f and ϕ_{Meas} versus $\hat{\phi}_{Meas}$ along with the ramp estimation error for runs 6.10-6.12 are presented in Figures 6.12a-6.12f. As can be seen in the plots, the observer provides location estimates within e_{RMS} values $\pm 10\%$ of D and ramp estimates well within the 0.2 deg ramp angle measurement error. Additionally, neither estimate significantly decreases in accuracy during commanded changes in the shock train LE location. Finally, PSDs of the measurement values and the residuals are presented in Figures 6.13a-6.13f. As can be seen in the LE location PSDs, the residuals are nearly white for frequencies above approximately 10 Hz. For the ramp observer PSDs, the modeling error can be seen to be quite low in frequencies less than 500 Hz. The spike at 50 Hz is due to LabVIEWTM sampling and will be discussed in the next paragraph. Since the results seen in the time-based and the frequency-based plots were so accurate, the states that led to produce the outputs must have been accurate as well.

Table 6.4: x_{Meas} vs x_{Est} results throughout the test section at three Reynolds numbers

Run	Re, /ft	$\mu(e)$, in.	$\sigma(e)$, in	e_{RMS} , in.	e_{RMS} , % of D
6.10	4.54×10^6	0.1052	0.1201	0.1541	6.166
6.11	5.77×10^6	0.1053	0.1231	0.1342	5.368
6.12	7.01×10^6	0.0938	0.1212	0.1222	4.886

Table 6.5: ϕ_{Meas} vs ϕ_{Est} results throughout the test section at three Reynolds numbers

Run	Re, /ft	$\mu(e)$, in.	$\sigma(e)$, in	e_{RMS} , deg.
6.10	4.54×10^6	0.0049	0.0048	0.0062
6.11	5.77×10^6	0.0050	0.0051	0.0064
6.12	7.01×10^6	0.0049	0.0046	0.0061

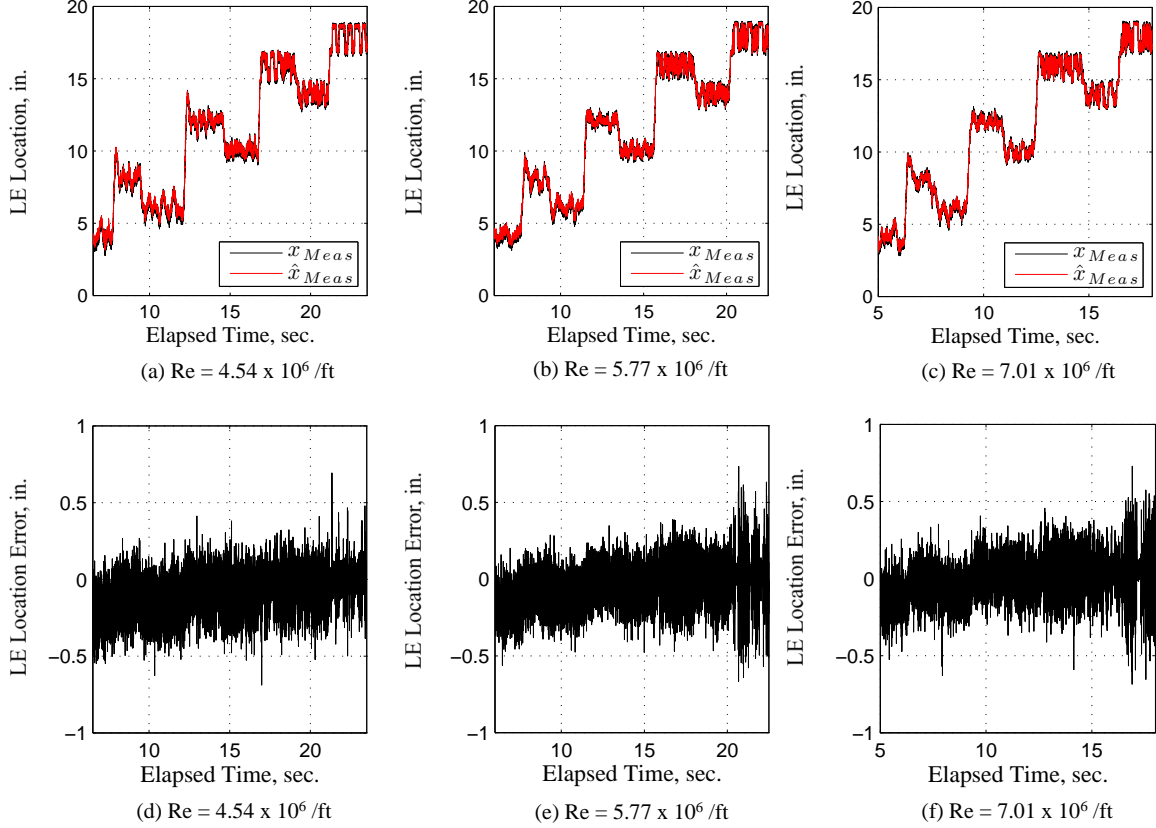


Figure 6.11: Measured vs estimated shock train location for runs 6.10-6.12

A spike can be seen at 50 Hz in the ramp angle residual PSD plots presented as Figures 6.13d-6.13f. These spikes are due to the LabVIEWTM implementation. In the LabVIEWTM routine, first, a set of samples, consisting of 20 pressure measurements, temperature measurements, and ramp measurements were collected at 1000 Hz. Then the routine calculated 20 control inputs which were sent to the ramp actuator computer. While the ramp actuator is responding to the previous 20 control inputs, the LabVIEWTM routine collects another set of samples and begins control calculations.

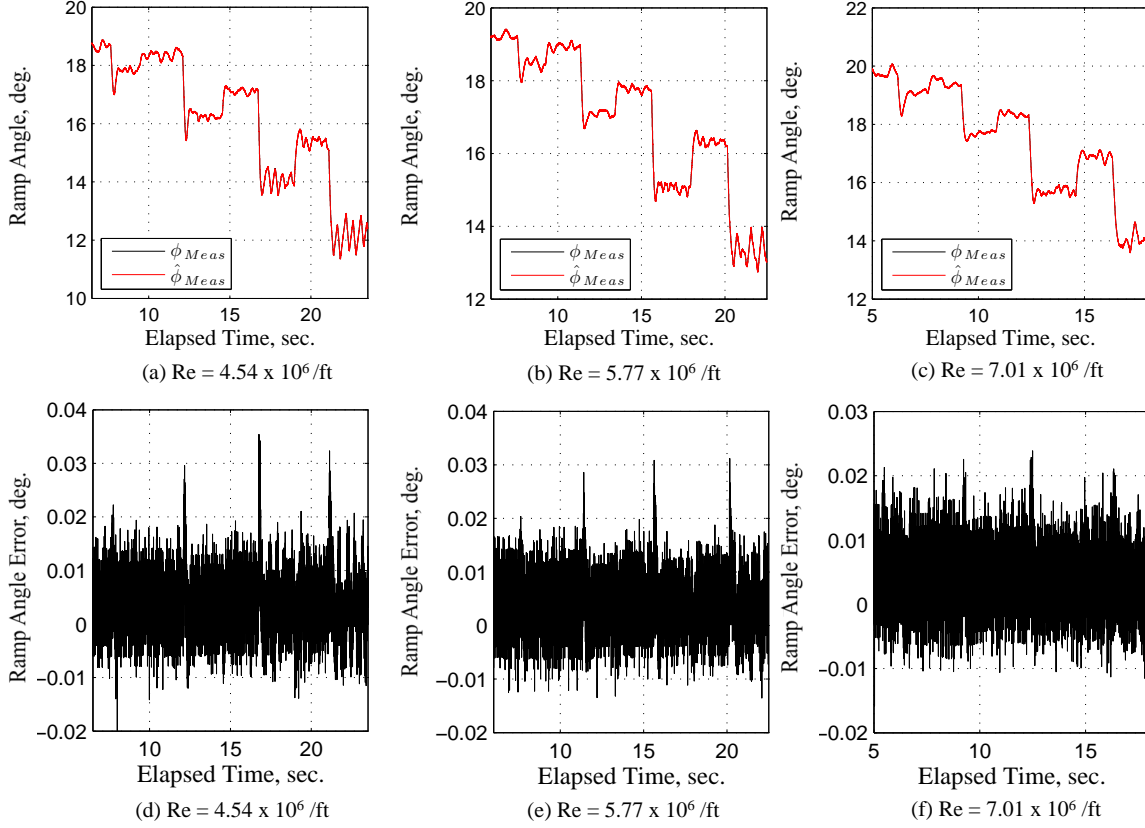


Figure 6.12: Measured vs estimated ramp angle for runs 6.10-6.12

As a result of sampling and sending control inputs in sets, the ramp command and the ramp measurement are out of synchronization. This synchronization error is then seen in the observer residuals as a spike corresponding to the frequency of a set of data being sent to the actuator. In this case, a set of commands is sent to the actuator with a frequency of 50 Hz as can be predicted using Equation (6.35).

$$\frac{1 \text{ Set}}{20 \text{ Samples}} \frac{1000 \text{ Samples}}{1 \text{ Second}} = 50 \frac{\text{Set}}{\text{Second}} = 50 \text{ Hz} \quad (6.35)$$

The number of samples can be varied by the user. Several runs, presented in Table 6.6, were accomplished in which the number of samples collected per a set were varied while the sampling frequency remained at 1000 Hz. PSD plots of the residuals for runs 6.13-6.16 are presented in Figure 6.14a and Figure 6.14b. As can be seen in

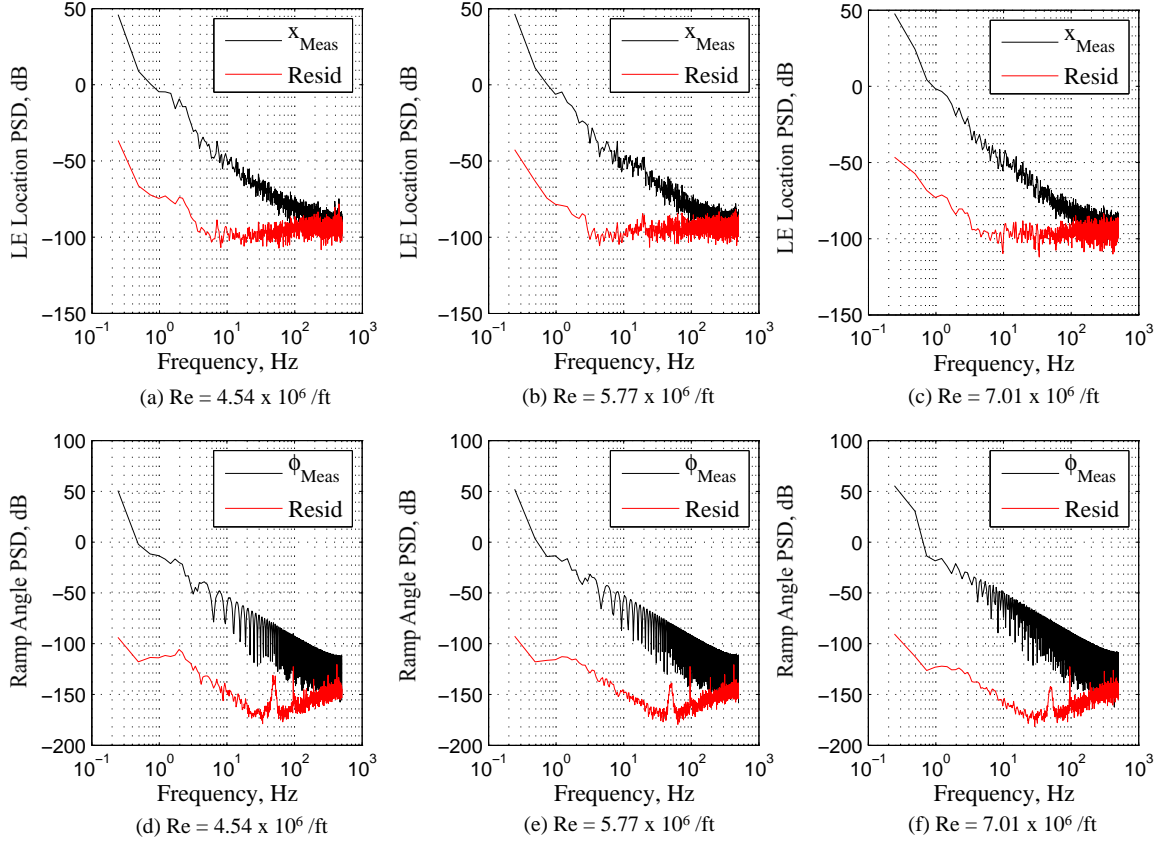
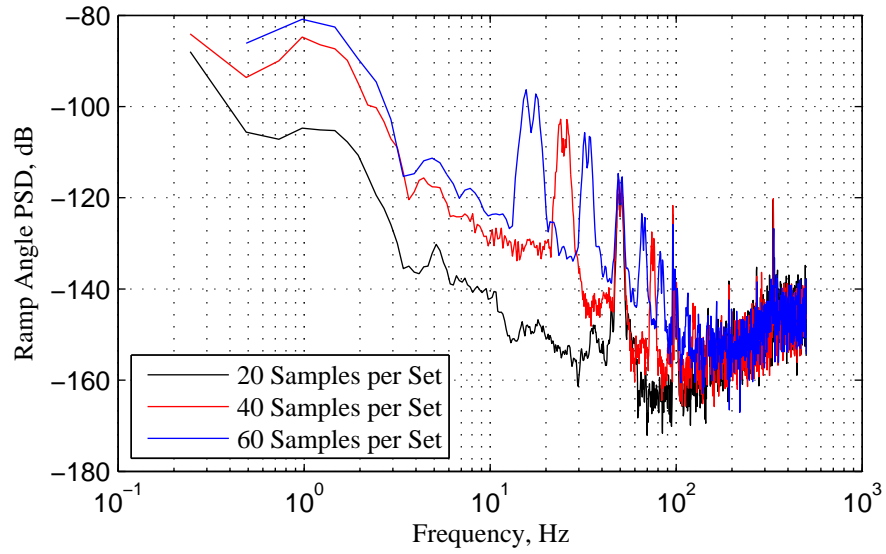


Figure 6.13: PSDs of measured values and observer residuals for runs 6.10-6.12

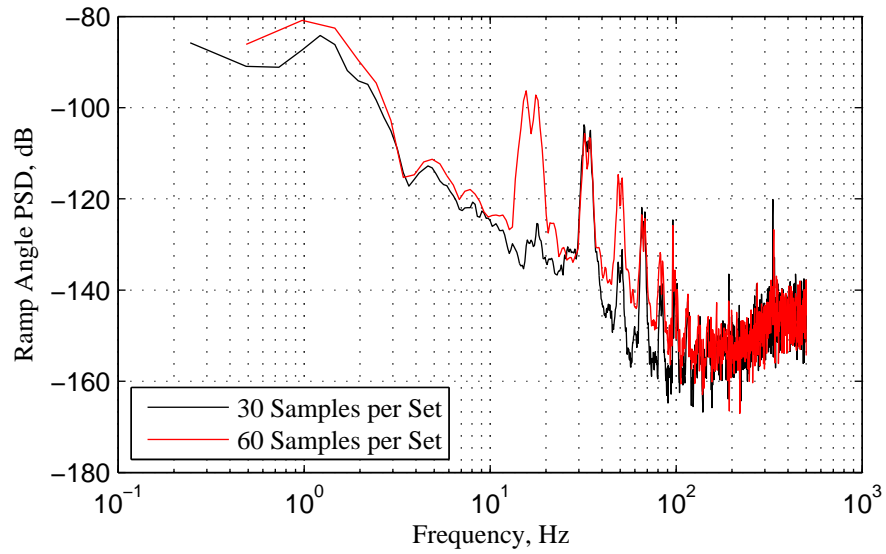
these plots, there are spikes at the expected frequency corresponding to when a set of commands is sent to the actuator and then repeated until overtaken by noise.

Table 6.6: ϕ_{Meas} vs ϕ_{Est} results throughout the test section at three Reynolds numbers

Run	Samples per Set	Sampling Frequency, Hz	Spike Frequency, Hz
6.13	20	1000	50
6.14	30	1000	33.33
6.15	40	1000	25
6.16	60	1000	16.67



(a) Runs 6.13, 6.15, and 6.16



(b) Runs 6.14 and 6.16

Figure 6.14: PSDs with varied number of samples per a set

6.7 Disturbance Rejection

The final set of tests for the control algorithm were to consider its ability to reject disturbances. Two types of disturbances were considered, in the first, a transducer hole was opened by hand in the test section during the run. The second disturbance was a decrease in the total pressure, P_0 , during a run. The controller was able to bring the shock train back to the desired location with the first disturbance and was capable of holding the shock at the desired location when P_0 was decreased.

6.7.1 Disturbance I - Test Section Hole. A means of creating the first disturbance was to manually remove the cover from an empty transducer hole in the top of the test section. The intention of this disturbance test was to approximate the effects of a sudden change in incoming flow or combustor pressure. The hole was located on the top wall at 13.258 in. and runs were accomplished in which the desired shock train was located either upstream to the hole or downstream from the hole. The controller was capable of returning the shock train to the desired location in both cases. Plots of the system response when the controller was turned on and turned off as well as the pressure ratio and the ramp angles at both high and low Reynolds number settings are presented in Figures 6.15a-6.16f. Additionally, the run conditions for runs 6.17-6.24 are listed in Table 6.7. Since the test section operated in a vacuum, the effect of opening the hole was to increase the static pressure into the section, which resulted in an increase in P_{BP} and the pressure ratio. This back pressure increase then decreased the strength of the shock from the incoming flow which resulted in a decrease in the back pressure. The back pressure decrease then translated up to the hole to increase the shock and the back pressure. This cycle continued and caused challenges for the actuator, particularly for runs 6.17, 6.18, 6.21, and 6.22, when the shock train was commanded to remain downstream relative to the hole. The effects of the pressure cycling were not as obvious when the shock train was commanded to be upstream to the hole. The exact timing of the disturbance could not be recorded by the LabVIEWTM algorithm since the cover was removed by

hand. The timing of the event is indicated by a sudden change in the x_{Meas} value greater than the normal x_{Meas} oscillations. The disturbance times were aligned for the presented disturbance plots.

Table 6.7: Test section hole run conditions

Run	Re, $/ft$	Control	$x_{Des}, in.$
6.17	4.54×10^6	On	15.75
6.18	4.55×10^6	Off	15.75
6.19	4.48×10^6	On	12.75
6.20	4.49×10^6	Off	12.75
6.21	7.04×10^6	On	15.75
6.22	7.05×10^6	Off	15.75
6.23	7.06×10^6	On	12.75
6.24	7.11×10^6	Off	12.75

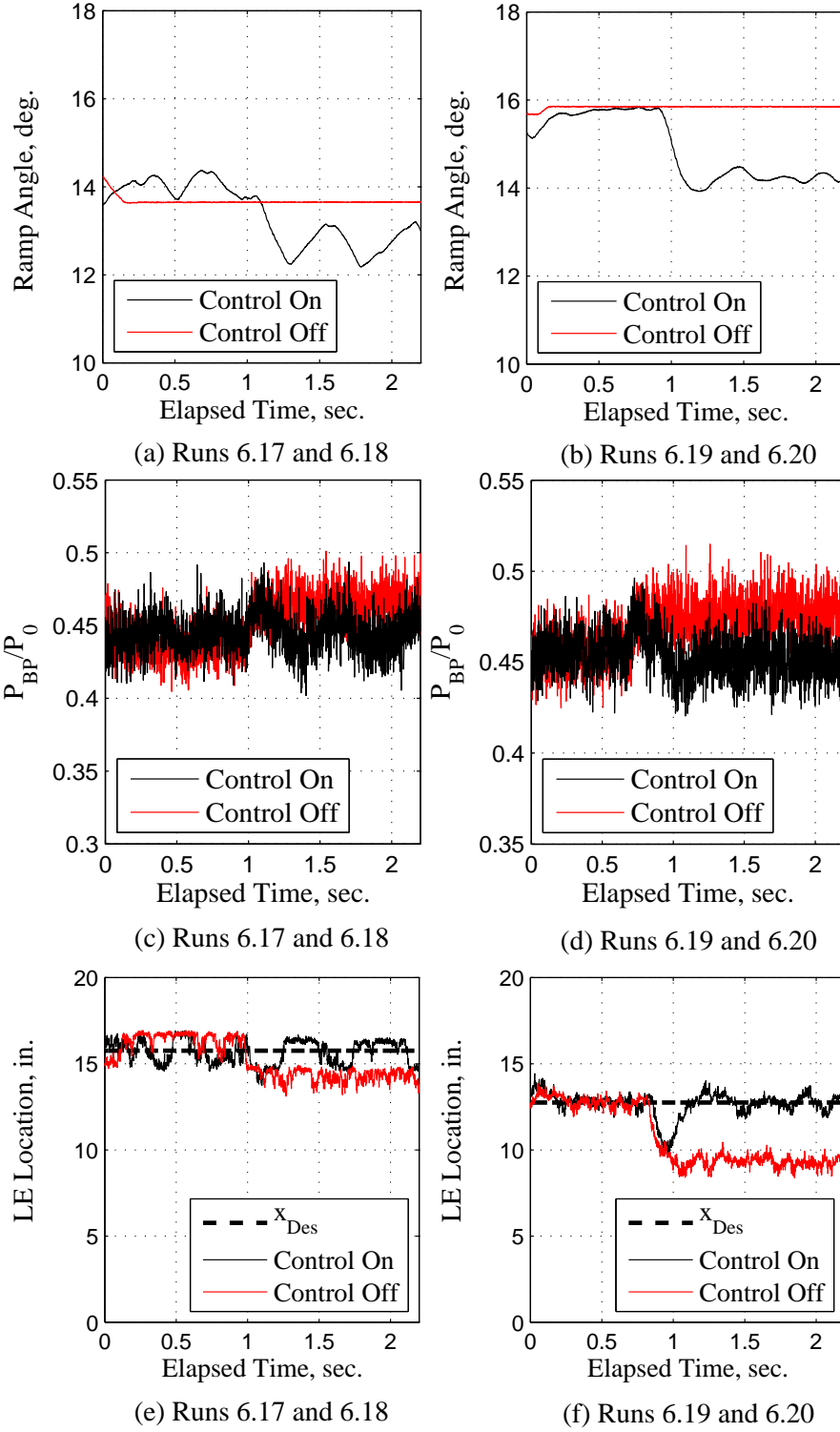


Figure 6.15: Disturbance response ramp angle, pressure ratio, and LE location for low Reynolds number settings

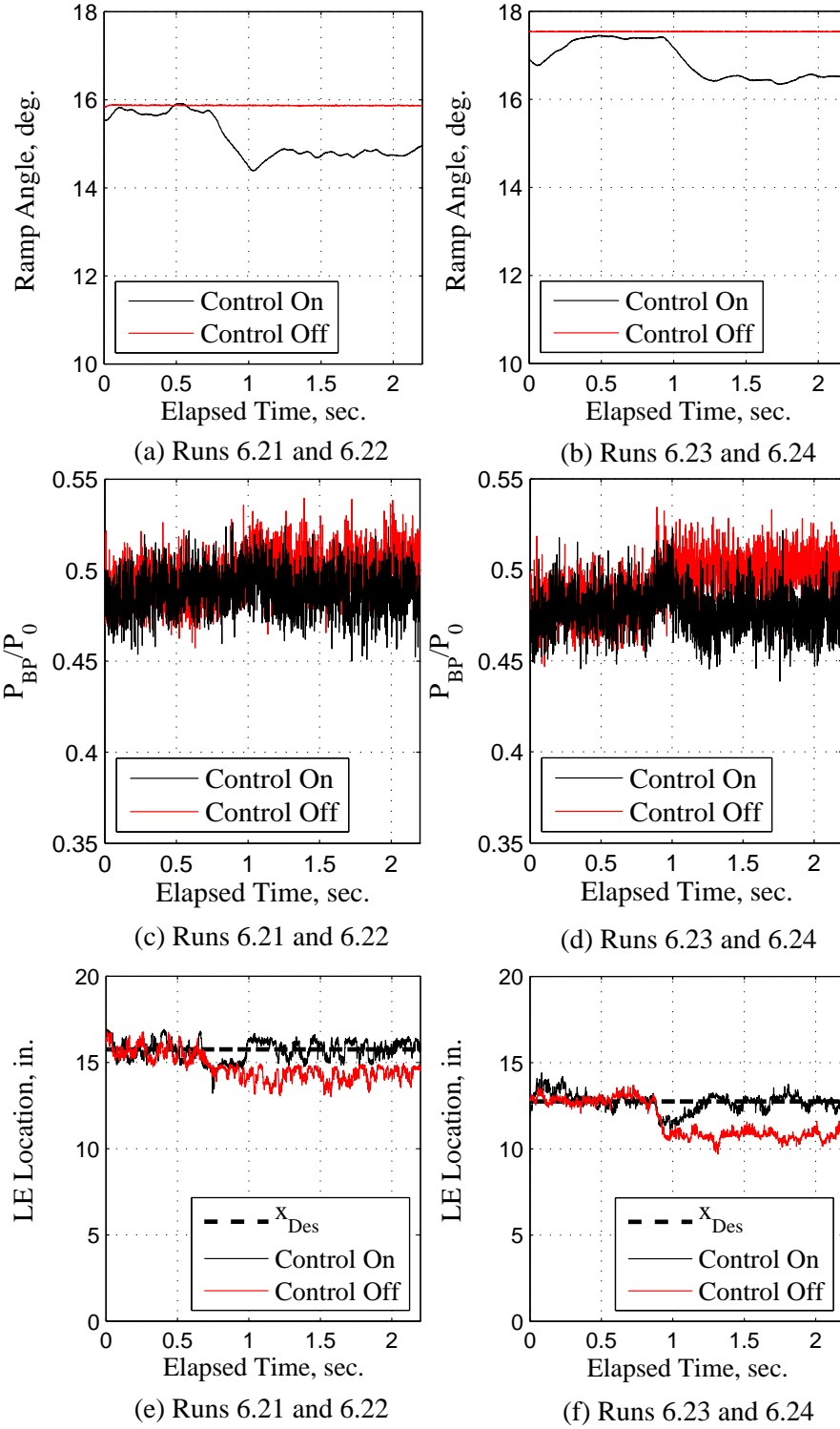


Figure 6.16: Disturbance response ramp angle, pressure ratio, and LE location for high Reynolds number settings

6.7.2 *Disturbance II - Decrease P_0 .* The second flow disturbance introduced was a decrease in P_0 throughout a run which results in an increase in the P_{BP}/P_0 pressure ratio. The intention of this type of disturbance was to mimic the gradual effects to the incoming flow due to turns or changes in angle of attack. Runs 6.23 and 6.24 were accomplished to consider the ability of the controller to compensate for this type of disturbance, both of which were started at comparable Reynolds numbers. The P_0 was decreased by manually closing the regulator for flow entering the stagnation chamber until there was not enough flow to support a shock train. In the first run, the controller was left on throughout the run and in the second, the shock was placed at the desired location, the controller was disengaged, and then P_0 was changed. The results are presented in Figure 6.17 where $x_{Des} = 15.75$ in.

When the P_0 is decreased to this test section, the P_{BP}/P_0 ratio increases and the shock train moves toward the front of the test section, as can be seen in Figure 6.17a and Figure 6.17e without any control. It is conjectured that there are local pressure effects occurring in the back pressure measurement region causing the back pressure to drop at a slower rate than the total pressure. The result of this disparity between the rate of total pressure and back pressure decrease is the increase in the pressure ratio presented as the red line presented in Figure 6.17c. When the controller remains engaged, the controller lowers the ramp angle to decrease the P_{BP}/P_0 ratio and bring the shock train back downstream. If the back pressure decreased at the same rate as the total pressure, which would be the case without the presumed local pressure effects, the pressure ratio would remain stable and the ramp would not have to rotate to keep the shock train at the desired location. The controller is capable of controlling the shock train through gradual changes in the P_0 setting in this test section.

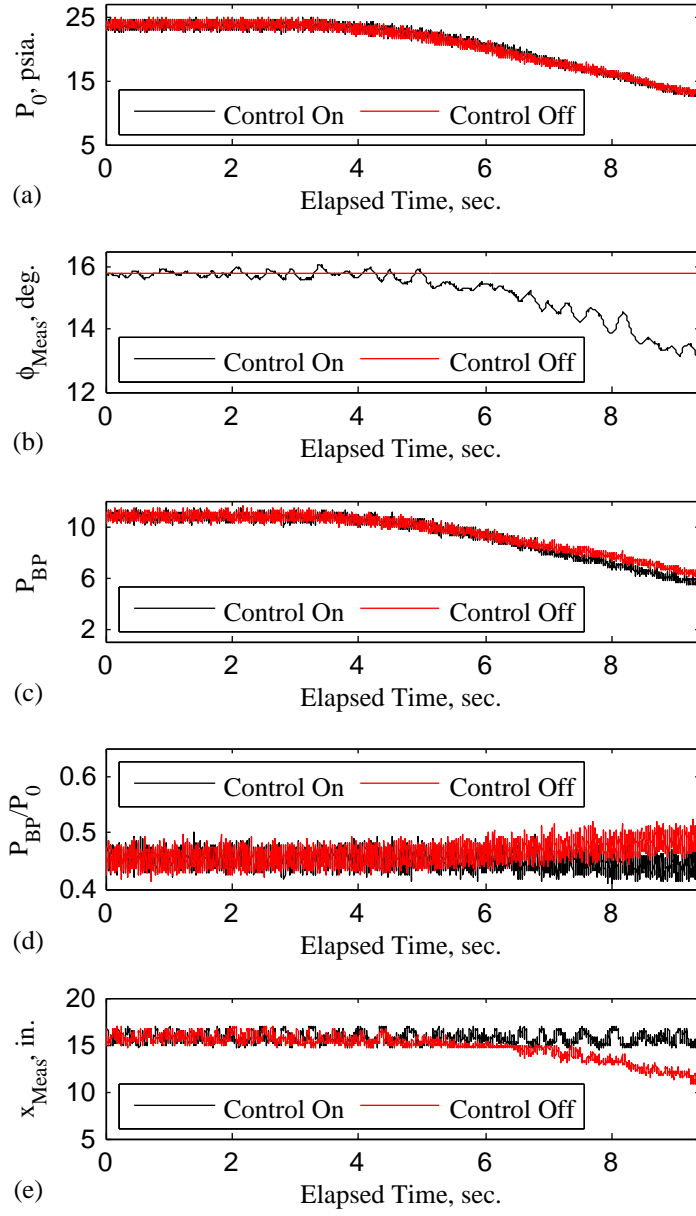


Figure 6.17: Plot showing effect on x_{Meas} for a decrease in P_0 with and without controller implemented

6.8 Control Conclusion

Although there were three main parts to this research, they all supported implementation of controlling the shock train location within an isolator. A control algorithm was developed and validated in this chapter which validated the hypothesis that the shock train LE location could be controlled using an automatic feedback controller. The closed-loop control algorithm developed and validated in this chapter was able to control the shock train LE location with a steady-state error within $\pm 50\%$ of D . Additionally, the algorithm was capable of rejecting flow perturbations. In order to perturb the flow, a hole was opened, while the shock was commanded upstream to the hole in one case and downstream from the hole in another, and the controller was able to keep the shock train LE at the desired location. A second type of perturbation was applied to the flow by decreasing the P_0 setting during the course of a run. This decrease in P_0 resulted in an increase in the P_{BP}/P_0 ratio. Again, the control algorithm was capable of controlling the shock train LE location as the pressure ratio increased throughout the run. The control algorithm developed has been shown to successfully control the shock train LE location and to do so through flow perturbations.

VII. Conclusion

The scramjet engine is a technology that can provide a significant increase in hypersonic capability for air vehicles with additional research. The technology is still in the early stages of development and a great deal of work still remains to field an operationally useful system. One of the hurdles to overcome is to develop a control system for the engine to allow significant air vehicle maneuvering without unstating the engine.

In this research, a method was developed and validated to control the shock train location within a cold-flow high-speed wind tunnel. This wind tunnel was intended as an analog for the isolator within a dual-mode scramjet. The isolator is a duct within the scramjet where pressure increases from the inlet to the combustor. Within the isolator a series of shocks, called a “shock train” form and when this shock train is expunged from the inlet, the engine is unstated which leads to a significant loss of thrust. In order to allow air vehicle maneuvers, which would result in changes to the flow path and the shock train location within the isolator, an operator must be able to control the shock train location. In this research a method for controlling that shock train location was developed and validated using an adjustable ramp located in the downstream portion of the test section. This ramp was used to adjust the back pressure to total pressure ratio, which changed the shock train location.

In order to develop the control algorithm, first a method of measuring the shock train location using test section-mounted pressure transducers was implemented and validated. This research builds on previous research in which various methods had been considered to measure the shock train location, but the measurements had either not been validated with shadowgraph photography [25,42] or only used shadowgraph photography at 30 frames per sec [24]. In this research high-speed (500 frames per sec) shadowgraph photography was used to validate the shock train location on a frame-by-frame basis. The difference between the shock train location from the measurement algorithm and the location from the shadowgraph was then calculated with every set of data samples. Finally, the RMS of the differences over an entire run was

calculated and labeled the error RMS, or e_{RMS} . The measurement algorithm validated in this research was capable of measuring the shock train leading edge location with an e_{RMS} value less than 20% of D whereas the pressure transducers were mounted with a separation of 47.6% of D indicating the algorithm was capable of accurately measuring the location between pressure transducers. This is the first research to validate an algorithm capable of measuring the shock train leading edge location with this accuracy using 500 frames per second shadowgraph imagery.

The next portion of the research was devoted to developing two dynamic models for the shock train leading edge dynamics. The back pressure, P_{BP} , and the ramp angle, ϕ_{Meas} , were used as model inputs to develop the dynamic models which related the shock train LE location to the input of interest. Previous modeling efforts did not include the shock train [4,30,44], had a much smaller input range [7–10,29,31], or treated the dynamics as noise [18]. When modeling, the e_{RMS} value was based on the difference between the model-predicted shock train LE location and the LE location measured using the shadowgraph imagery. The results were e_{RMS} values less than 24% of D with P_{BP} as the input and less than 13% of D when ϕ_{Meas} is the input while the transducers were mounted with a spacing of 47.6% of D . As an extension of the P_{BP} model, a pressure ratio, P_{BP}/P_0 , model was also developed. Simulations accomplished using this data returned e_{RMS} values less than 16% of D when compared to optical measurements. These results are particularly impressive considering that it has been shown that a steady-state shock train will oscillate around its mean location up to an entire duct height, D (i.e., the shock train will oscillate with a range from $-D$ to $+D$ around its mean location) [67]. This is the first research to develop and validate a model of the shock train LE location dynamics accurate to within a quarter of a duct height.

In the final portion of the research, a closed-loop feedback controller was developed to place the shock train leading edge at a desired location within the wind tunnel. Little research has previously been accomplished in the open literature on actively controlling the shock train location. Noting that the shock train will tend

to oscillate up to D at steady-state [67], the goal of the research was to develop an algorithm capable of controlling the shock train LE location so that the mean steady-state location and shock oscillations would remain within a range of $\pm D$ around the desired shock train LE location. The closed-loop controller surpassed the goal and was able to control the steady-state shock train LE location mean along with oscillations to a range of $\pm 50\%$ of D around the desired shock train location using an actuator with a 10 Hz bandwidth. This is the first research to develop a shock train LE control algorithm that has been tested in the laboratory and has been validated using shadowgraph photography to control the shock train location throughout the test section and at a range of Reynolds numbers.

Potential continued research includes validating the modeling and control algorithms on different test sections. The next logical step in this research would be to consider the applicability of the model structure to other test sections, particularly heated ones. If no additional test sections are available, the validity of the model structure could be investigated using the Mach 3 nozzle located at AFIT. Finally, if a first-principles physics-based model is developed, the system identification model could be compared to that physics-based model for final validation.

The components necessary for a closed-loop shock train LE location control algorithm were developed in this research. The impact of this research is the potential to decrease the needed scramjet isolator length, saving air vehicle weight and opening air vehicle interior space. An additional impact of control of the shock train LE location is a decreased chance of inlet unstart along with an increase in the operational utility of the engine to enable air vehicle maneuvers. The research lays the experimental groundwork for a closed-loop scramjet shock-train LE control algorithm.

Appendix A. Reynolds Number Calculation

The calculation used to calculate the Reynolds number, Re , is presented in this appendix. The calculations, based on isentropic relations and the ideal gas law [68], are the same as those used previously [56] on this test section. The Reynolds numbers used in plot titles are based on the time-average total pressure, $P_{0,Ave}$, the time-average total temperature, $T_{0,Ave}$, and the time-average of the static pressure at the most upstream transducer, $P_{s,Ave}$. All three of these averages are calculated based on the tare portion of a run. $T_{0,Ave}$, $P_{s,Ave}$, and $P_{0,Ave}$ are calculated by averaging each $P_0(k\Delta t)$, $P_{s,\zeta_1}(k\Delta t)$, and $T_0(k\Delta t)$, for all k samples taken during the tare portion of the run.

First, calculate the isentropic relationship, $P_{0,Ave}/P_{s,Ave}$, using the previously made measurement. Then, rearrange Equation (A.1) to get Equation (A.2) and solve for the average stream Mach number, M_{Ave} . The specific heat ratio, γ , is assumed equal to 1.4 in all equations.

$$\frac{P_{0,Ave}}{P_{s,Ave}} = \left(1 + \frac{\gamma - 1}{2} M_{Ave}^2\right)^{\frac{\gamma}{\gamma - 1}} \quad (A.1)$$

$$M_{Ave} = \left(\frac{2}{\gamma - 1} \left(\frac{P_{0,Ave}}{P_{s,Ave}}^{\frac{\gamma - 1}{\gamma}} - 1\right)\right)^{\frac{1}{2}} \quad (A.2)$$

Now, use the measured $T_{0,Ave}$ to calculate the average flow temperature, T_{Ave} . Begin by rearranging Equation (A.3) to get Equation (A.4) and then substitute.

$$\frac{T_{0,Ave}}{T_{Ave}} = 1 + \frac{\gamma - 1}{2} M_{Ave}^2 \quad (A.3)$$

$$T_{Ave} = \frac{T_{0,Ave}}{1 + \frac{\gamma - 1}{2} M_{Ave}^2} \quad (A.4)$$

The stream average speed of sound, a_{Ave} and the stream average velocity, V_{Ave} can now be found by substituting into Equation (A.5) and Equation (A.6), respectively,

where R is the specific gas constant and it is assumed that $R = 1545.31 \text{ lb}_f \cdot \text{ft} / (\text{lb}_m \cdot \text{R})$

$$a_{Ave} = \sqrt{\gamma R T_{Ave} \cdot 32.174 \text{ lb}_m \cdot \text{ft} / \text{lb}_f \cdot \text{sec}^2} \quad (\text{A.5})$$

$$V_{Ave} = M_{Ave} \cdot a_{Ave} \quad (\text{A.6})$$

Calculate the average flow density, ρ_{Ave} , by rearranging the ideal gas law to get Equation (A.7) and substituting where the $P_{s,Ave}$ is converted from the recorded units lb_f/in^2 to the units lb_f/ft^2 .

$$\rho_{Ave} = \frac{P_{s,Ave}}{R \cdot T_{Ave}} \quad (\text{A.7})$$

Use the previous results, along with Sutherland's Law, as presented in Equation (A.8) to calculate the average viscosity, μ_{Ave} . Assume reference total temperature, $T_{0,Ref}$, and total viscosity, $\mu_{0,Ref}$ to be standard sea level conditions, $T_{0,Ref} = 518.69 \text{ R}$ and $\mu_{0,Ref} = 1.2 \times 10^{-5} \text{ lb}_m / (\text{ft} \cdot \text{s})$.

$$\mu_{Ave} = \mu_{0,Ref} \left(\frac{T_{Ave}}{T_{0,Ref}} \right)^{\frac{3}{2}} \frac{T_{0,Ref} + 198.72}{T_{Ave} + 198.72} \quad (\text{A.8})$$

Finally, the Reynolds number is calculated using Equation (A.9). The result is in units of $/\text{ft}$.

$$Re = \frac{\rho_{Ave} \cdot V_{Ave}}{\mu_{Ave}} \quad (\text{A.9})$$

Appendix B. Interpolation and Power Spectral Density Calculation

The linear interpolation procedure and the power spectral density (PSD) equations are presented in this appendix.

B.1 Linear Interpolation Method

Linear interpolation was used in several of the measurement algorithms presented in Chapter IV. An example of when linear interpolation was used is in the ratio method calculation, Equation (4.4), which is represented here as Equation (B.1).

$$x_{PR}(k) = \text{interp}(\mathbf{PR}(k), \mathbf{x}_{Trans}, PR_{Des}) \quad (\text{B.1})$$

Additionally, Figure 4.1 is represented here as Figure B.1 with some pressures and locations noted on the figure. The **Matlab**[®] algorithm first finds the pressure ratio

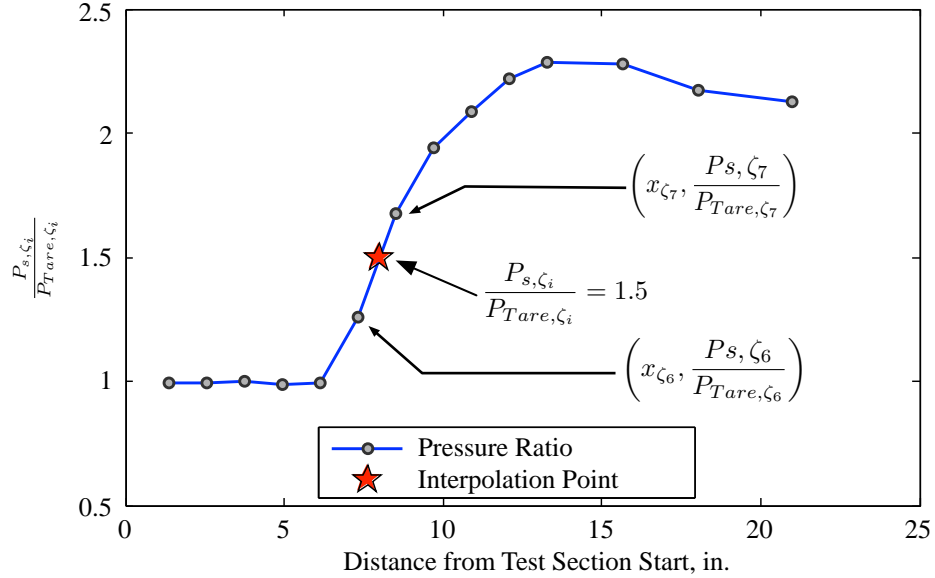


Figure B.1: Illustration of pressure ratio measurement method

immediately less than and the pressure ratio immediately greater than the desired pressure ratio, PR_{Des} , in the pressure ratio vector, $\mathbf{PR}(k)$. In this example, those

pressure ratios were measured at transducers ζ_6 and ζ_7 , respectively. The algorithm then gets the transducer mounting location from the transducer mounting vector, \mathbf{x}_{Trans} . Finally, the shock train LE location is calculated using Equation (B.2). This procedure was implied whenever *interp* was used.

$$x_{PR}(k) = m \left(PR_{Des} - \frac{P_{s,\zeta_6}}{P_{Tare,6}} \right) + x_{\zeta_6} \quad (\text{B.2})$$

where

$$m = \frac{\frac{x_{\zeta_7} - x_{\zeta_6}}{\frac{P_{s,\zeta_7}}{P_{Tare,7}} - \frac{P_{s,\zeta_6}}{P_{Tare,6}}}}{\quad} \quad (\text{B.3})$$

B.2 Power Spectral Density Calculation

The power spectral density is used in the frequency method approach which was also presented in Chapter IV. While the **Matlab**[®] *pwelch.m* routine was used in this research, the process to calculate the PSD is straightforward. The first step is to take the discrete Fourier transform (DFT) of the desired vector. In the case of the frequency method a vector of the pressures recorded over the previous 512 samples was used as originally presented in Equation (4.13) and is repeated here as Equation (B.4).

$$\psi_{P_{s,\zeta_i}}(k) = PSD(P_{s,\zeta_i}((k - 512) : k)) \quad (\text{B.4})$$

The DFT is calculated using Equation (B.5)

$$D(k_{DFT}) = \frac{1}{N} \sum_{r=0}^{N-1} x_r e^{-i \left(\frac{2\pi r k_{DFT}}{N} \right)} \quad (\text{B.5})$$

where k_{DFT} is a slice of the DFT such that the discretized frequencies are defined in Equation (B.6), N is the number of samples, Δt is the time between samples, and $x_r \equiv P_{s,\zeta_i}(k = r + 512)$.

$$\omega_{k_{DFT}} = \frac{2\pi k_{DFT}}{\Delta t N} \quad (\text{B.6})$$

The PSD is then calculated by multiplying the complex conjugate of the DFT times the DFT as presented in Equation (B.7) where $*$ means the complex conjugate, $D(1, 2, \dots N/2)$ implies a vector of the first $N/2 = 256$ $D(k_{DFT})$ calculations, and \times_{ew} implies element-wise multiplication.

$$\psi_{P_{s,\zeta_i}}(k) = D(1, 2 \dots N/2)^* \times_{ew} D(1, 2 \dots N/2) \quad (\text{B.7})$$

Appendix C. Traditional System Identification

C.1 Linear System Identification Models

While no system is completely linear, in order to understand some of the non-linear techniques, an understanding of the linear techniques is useful. Several texts have been written about both linear [5, 69–71] and nonlinear [58, 60, 61] system identification and the contents of the following discussion is common to all of them. The presented linear, time-invariant (LTI) Single-Input, Single-Output (SISO) models are based on developing an estimate for the transfer functions relating the commanded input and noise to the output. These linear transfer functions are based on the impulse response function, which characterizes a system based on the inputs and outputs for a sampled system in Equation (C.1) [5]

$$y(t) = \sum_{k=1}^{\infty} g(k)u(t-k) + \sum_{k=0}^{\infty} h(k)\nu(t-k) \quad (\text{C.1})$$

where y is the system response, g is the impulse response function, ν is white noise, h is a function to “color” the white noise to match the system noise, u is the system input, $t = k\Delta T$ for each instant, and ΔT is the time between samples. In order to simplify this notation, the q time shift operator is introduced such that $qu(t) = u(t+1)$ and $q^{-1}u(t) = u(t-1)$. Then, the following notation simplifications are made in Equations (C.2) and (C.3) [5].

$$G(q) = \sum_{k=1}^{\infty} g(k)q^{-k} \quad (\text{C.2})$$

$$H(q) = \sum_{k=0}^{\infty} h(k)q^{-k} \quad (\text{C.3})$$

With further simplification, the system can be characterized, along with a characterization of the noise, as [5]

$$y(t) = G(q)u(t) + H(q)\nu(t). \quad (\text{C.4})$$

In Equation (C.4), there are an infinite number of possible parameters in H and G to solve for so, in order to make the task of developing a model of the system more tractable, a finite number of parameters must be used. Let the number of parameters to be considered be d , then the vector $\theta \in \mathbf{R}^d$ is the vector of parameters that must be optimized to create a model of the system. Substituting this vector, we can now gain the general equation for the parameterized models as seen in Equation (C.5) [5]. Further, with some rearrangement, this can also be used to find the one-step ahead predictor equation that will be quite useful for a control algorithm as seen in Equation (C.6) [5].

$$y(t) = G(q, \theta)u(t) + H(q, \theta)\nu(t) \quad (\text{C.5})$$

$$\hat{y}(t|\theta) = H^{-1}(q, \theta)G(q, \theta)u(t) + [1 - H^{-1}(q, \theta)] y(t) \quad (\text{C.6})$$

Different models within this construct are created by choosing different polynomials for the $H(q, \theta)$ and $G(q, \theta)$ transfer functions. This general construct is presented in Figure C.1 where A , B , C , D , and F are discrete polynomials with a vector of parameters of length d , listed in the vector θ , as defined in Equations (C.8)-(C.12). In these equations, $A(q)y(t)$, $D(q)y(t)$, and the $F(q)y(t)$ are the autoregressive (AR) portions. $B(q)u(t)$ is referred to as the exogenous input (X) portion, and, $C(q)e(t)$ is referred to as the moving average part (MA) of the model [5, 70, 71].

$$A(q)y(t) = \frac{B(q)}{F(q)}u(t) + \frac{C(q)}{D(q)}\nu(t) \quad (\text{C.7})$$

where

$$A(q) = 1 + a_1q^{-1} + \cdots + a_{n_a}q^{-n_a} \quad (\text{C.8})$$

$$B(q) = b_1q^{-1} + \cdots + b_{n_b}q^{-n_b} \quad (\text{C.9})$$

$$C(q) = 1 + c_1q^{-1} + \cdots + c_{n_c}q^{-n_c} \quad (\text{C.10})$$

$$D(q) = 1 + d_1q^{-1} + \cdots + d_{n_d}q^{-n_d} \quad (\text{C.11})$$

$$F(q) = 1 + f_1q^{-1} + \cdots + f_{n_f}q^{-n_f} \quad (\text{C.12})$$

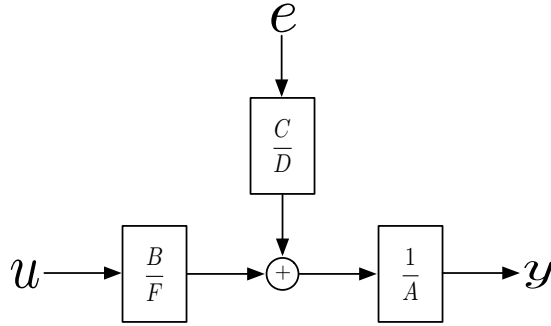


Figure C.1: General linear parameter model [5]

The different models that can be created from this construct are presented in Table C.1. In this table, the first column is the particular polynomials included in the model and the second column is the name of the model that results from that polynomial set.

Table C.1: Common black-box SISO models [5]

Polynomial	Model Structure
B	Finite Impulse Response (FIR)
AB	AutoRegressive with eXternal input (ARX)
ABC	AutoRegressive Moving Average with eXternal input (ARMAX)
AC	AutoRegressive Moving Average (ARMA)
BF	Output-Error (OE)
BFCD	Box-Jenkins (BJ)

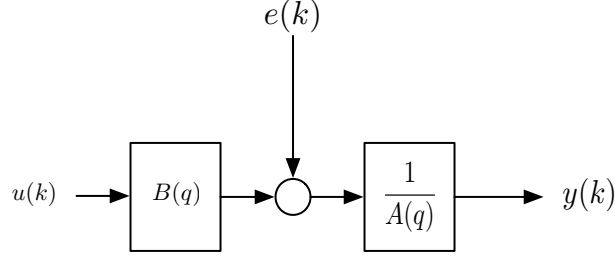


Figure C.2: Schematic of an ARX model

In particular, for this research, ARX models were used for the linear portion of a Hammerstein model. The Hammerstein model structure will be discussed in the nonlinear modeling portion of this appendix. The ARX model structure is simplified to only two polynomials, an autoregressive, and an exogenous input one, as presented in Figure C.2 [5]. The ARX model is linear in the parameters, so optimization can be accomplished using least squares. In this research, the model order was changed by changing the order of the A and/or the B polynomial.

C.2 Nonlinear System Identification Models

As an extension of the ARX model, the next model construct considered was the Nonlinear ARX (NARX) model structure. A NARX model is created by replacing the linear relationship in an ARX model such as presented in Equation (C.13) with a nonlinear relationship such as presented in Equation (C.14) by adding $f(\cdot)$ [61].

$$\hat{y}(k) = b_1 u(k-1) + \dots + b_m u(k-m) - a_1 y(k-1) - \dots - a_m y(k-m) \quad (\text{C.13})$$

$$\hat{y}(k) = f(b_1 u(k-1), \dots, b_m u(k-m), a_1 y(k-1), \dots, a_m y(k-m)) \quad (\text{C.14})$$

The nonlinear function, $f(\cdot)$, can be any nonlinear function, leading to an infinite number of possibilities. Only polynomial nonlinearities were permitted in the NARX model so that there was a limited number of possible models and each nonlinear model was linear in the parameters.

The other structure considered was the Hammerstein model structure. These models include a static nonlinearity feeding into a linear transfer function. The advantage to this configuration is that, assuming the nonlinearity is invertible, the nonlinearity can be cancelled with inversion and then a controller can be created based on the linear dynamics [60,61]. The procedure of inverting the nonlinearity was used in the control algorithm development and implementation in this research. Due to the assumption that the nonlinearity inversion was adequate for control in the local region of the nonlinearity input space, the nonlinearity was not included when considering pole-placement and observer design and the poles controller poles could be placed using linear techniques.

Once the model structure was determined, the number of parameters in the model was selected. The optimal number of parameters in a nonlinear model is a balance between two different kinds of errors; bias and variance error. Variance error is defined as the amount of change of the model parameters from the optimal parameter values [61]. This error relates to the number of parameters in that, as the number of parameters increases, assuming a static number of data points, the ability to estimate the values of the different parameters decreases. In order to decrease the variance error, one must either collect more data or decrease the number of parameters in the model. Bias error, on the other hand, is related to a decreased flexibility of the model to fit the data due to an insufficient number of parameters [61]. In order to decrease the bias error, one must increase the number of parameters in the model to allow for a more ‘flexible’ model. In order to decrease the overall error, the number of parameters considered were limited and a large number of data points were collected in the research.

Appendix D. Pseudo Random Binary Sequence Creation

One of the preliminary considerations when taking a system identification approach to modeling a system is the input signal. The only modes that can be activated for modeling are the modes that are activated by the input signal, a concept labeled “persistent excitation” [5]. As a result, it would be nice to use white noise as the input source to ensure all modes were excited. White noise is not feasible in an actual system, so a similar form of input was developed. The input used for this research was labeled an Amplitude-modulated Pseudo-Random Binary Sequence (APRBS) [61]. The advantage to using an APRBS is that the mean value and the covariance function are similar to white noise [71]. An APRBS is an extension of a Psuedo Random Binary Sequence (PRBS) which is developed using shift registers between two distinct input settings. The extension to an APRBS is to allow for multiple input settings, an extension that is necessary for a nonlinear system [60, 61].

An APRBS with five levels was used as the excitation signal in the system identification portion of this research. First, the signal was generated using Equation D.1 [60]

$$\phi_{Cu} = c_1 \otimes_5 \phi_{Cu}(k-1) \oplus_5 c_2 \otimes_5 \phi_{Cu}(k-2) \oplus_5 c_3 \otimes_5 \phi_{Cu}(k-3) \oplus_5 c_4 \otimes_5 \phi_{Cu}(k-4) \quad (\text{D.1})$$

where \otimes_5 implies modulo base five multiplication and \oplus_5 implies modulo base five addition. Further, the values for the constants for the longest period before a repeat were $c_1 = 1, c_2 = -1, c_3 = 1$, and $c_4 = 2$ which returns a period of 724 changes prior to a repeat [60]. When using Equation D.1, five levels of numbers between zero and five are generated which can be repeated with each experiment. To change the sequence one need only change the initial conditions and, to change the sequence mean, one need only add a bias. The output for a five-level PRBS is presented in Figure D.1. In Figure D.1a, a time-based plot of the commanded ramp angle is provided. The repetitive nature of a PRBS can be noted in this plot. An autocorrelation plot of the same data is then provided in Figure D.1b. The autocorrelation of white noise will have a spike at $t = 0$ and will be zero when $t \neq 0$. Although the autocorrelation

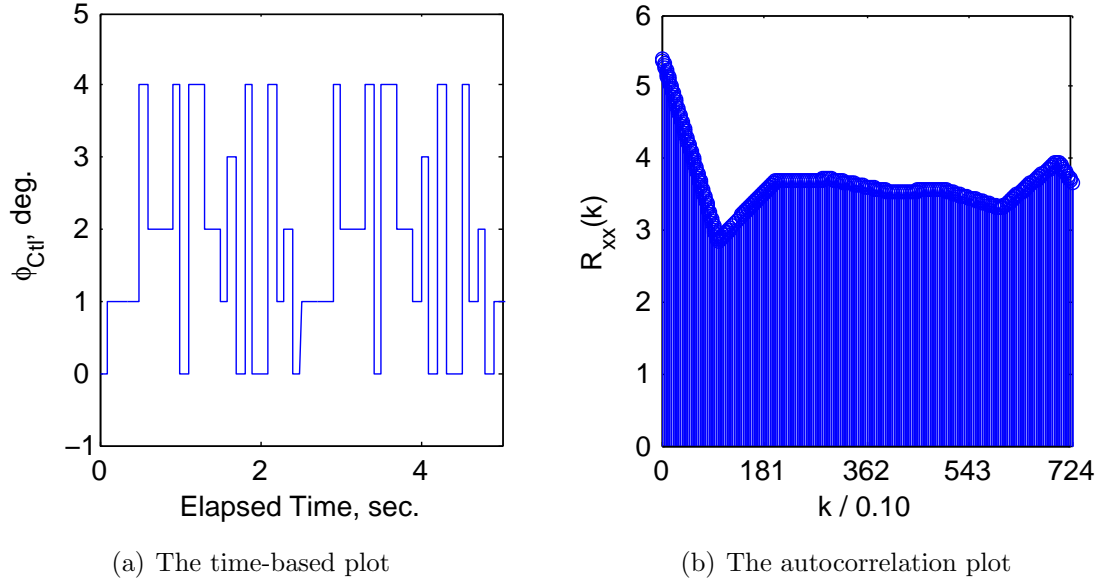


Figure D.1: The five-level APRBS time-based and autocorrelation plots

presented in Figure D.1b does not return to zero when $t \neq 0$, it does drop significantly, and remains low and relatively level until the sequence repeats after 724 ramp angle changes. This decrease and leveling off is what is meant by saying the APRBS has white noise-like statistical properties.

After initial runs to determine the ramp actuation input range between the ram/scram transition and unstart, a five-level APRBS was developed to span the range and implemented in LabVIEWTM. The time required between ramp actuation changes was 0.1 sec. since the ramp actuator had a 10 Hz bandwidth. The input and output data were then collected and used to develop the models described in Chapter V.

Appendix E. Shadowgraph Leading Edge Location Measurement Technique

The algorithm used to find the leading edge (LE) according to the shadowgraph image, x_{Optic} is explained in this appendix. The procedure is based on the assumption of an affine relationship between the image space and the laboratory space. The affine relationship assumption is then taken advantage of by creating a transform from image space to laboratory space using least squares. The technique involves manually selecting LE locations from automated frame by frame images. The streamwise location of the middle of the first lambda shock in the shock train, as presented in Fig. E.1, is defined as the shock train leading edge for this research. A fully automated algorithm was not considered.

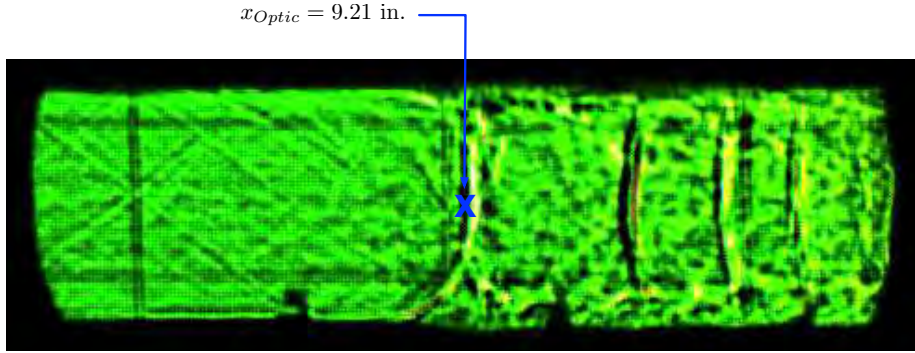


Figure E.1: A shadowgraph image of the shock train and the leading edge location

E.1 Transformation Creation

The first step is to create a grid on one of the test section acrylic walls as presented in Figure E.2. The location of $(x_A, y_A), (x_B, y_B), \dots, (x_F, y_F)$ is referenced to a zero located along the test section floor at the nozzle exit. These points are saved as a vector of grid positions (\mathbf{x}_G and \mathbf{y}_G) as shown in Equation (E.1) and Equation (E.2).

$$\mathbf{x}_G = [x_A \ x_B \ x_C \ x_D \ x_E \ x_F]^T \quad (\text{E.1})$$

$$\mathbf{y}_G = [y_A \ y_B \ y_C \ y_D \ y_E \ y_F]^T \quad (\text{E.2})$$

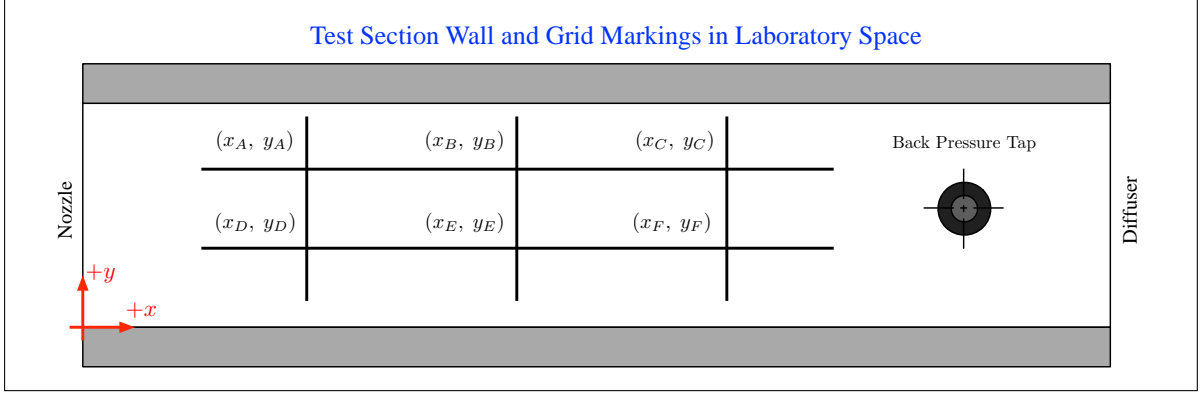


Figure E.2: A drawing of the grid drawn on the wall of the test section for shadow-graph calibration

The next step to developing the transformation from the image space to the wall space is to choose and display a frame from the recorded avi file. A drawing of a frame in image space along with the grid overlay and the set of intersections, $(u_A, v_A), (u_B, v_B), \dots, (u_F, v_F)$, is presented in Figure E.3. Then, using the **Matlab**[®] code, *ginput*(\cdot), each of the intersections is clicked on and the function returns the intersection location vectors \mathbf{u}_G and \mathbf{v}_G as shown in Equation (E.3) and Equation (E.4).

$$\mathbf{u}_G = [u_A \ u_B \ u_C \ u_D \ u_E \ u_F]^T \quad (\text{E.3})$$

$$\mathbf{v}_G = [v_A \ v_B \ v_C \ v_D \ v_E \ v_F]^T \quad (\text{E.4})$$

Using least squares, the transformation from image space to wall space can now be created. First, place \mathbf{u}_G , \mathbf{v}_G and a vector of ones into a matrix as presented in Equation (E.5) and solve for the transformation, T , according to Equation (E.6).

$$H = [\mathbf{u}_G \ \mathbf{v}_G \ \mathbf{1}_{6 \times 1}] \quad (\text{E.5})$$

$$T = (H^T H)^{-1} H^T \mathbf{x}_G \quad (\text{E.6})$$

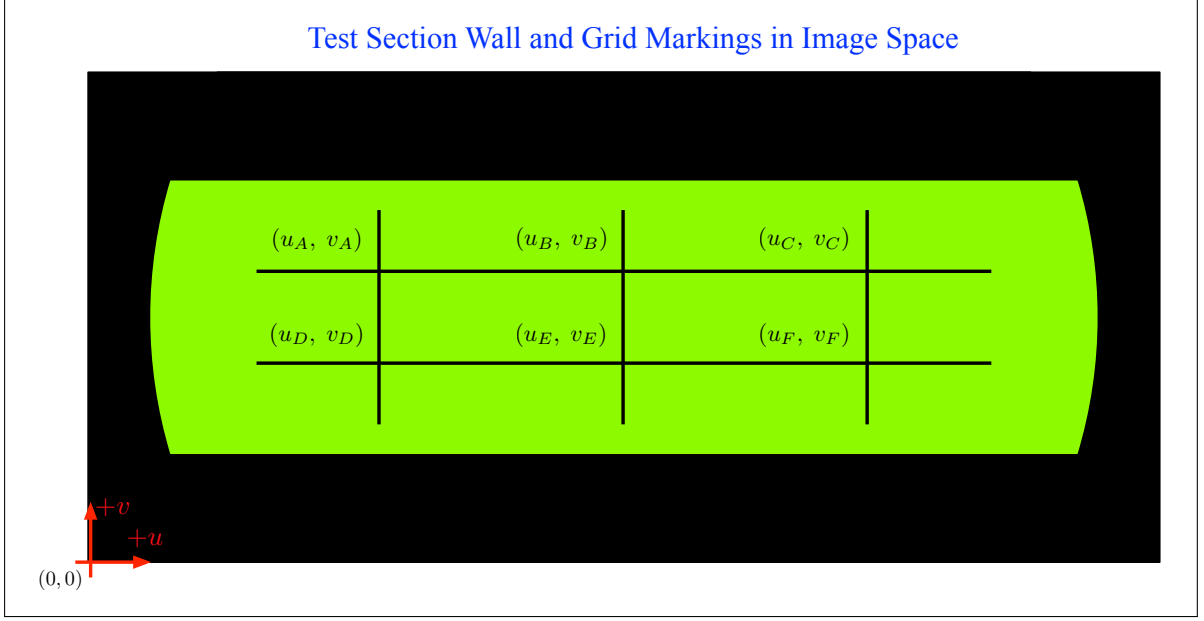


Figure E.3: A drawing of a schlieren image with grid overlay

E.2 Determining Shock Train Leading Edge Location

Now that the transformation has been created, the actual collection of the data can be started. The `Matlab`[®] code, `ginput(.)` is again used to input the location of the LE. The procedure is to open an image, click on the LE and save a u_{LE} and v_{LE} then close the image and open the next image. This is accomplished in a loop for all of the frames in the avi file. After each image space LE point at every sample time, $k\Delta t$, is collected, the transform can then be used to calculate the shadowgraph LE location measurement, x_{Optic} , according to Equation (E.7).

$$\hat{x}_{Optic}(k\Delta t) = \begin{bmatrix} u_{LE}(k\Delta t) & v_{LE}(k\Delta t) & 1 \end{bmatrix} \cdot T \quad (E.7)$$

Appendix F. Laboratory Equipment Pictures

Pictures and model numbers (where available) of the individual components introduced in Chapter III are presented in this appendix. The order of the presentation is to follow the air flow as it begins in the ambient according to Figure F.1, a reprint of Figure 3.1 from Chapter III. A picture of the test section, mounted in the AFIT wind tunnel is presented in Figure F.2.

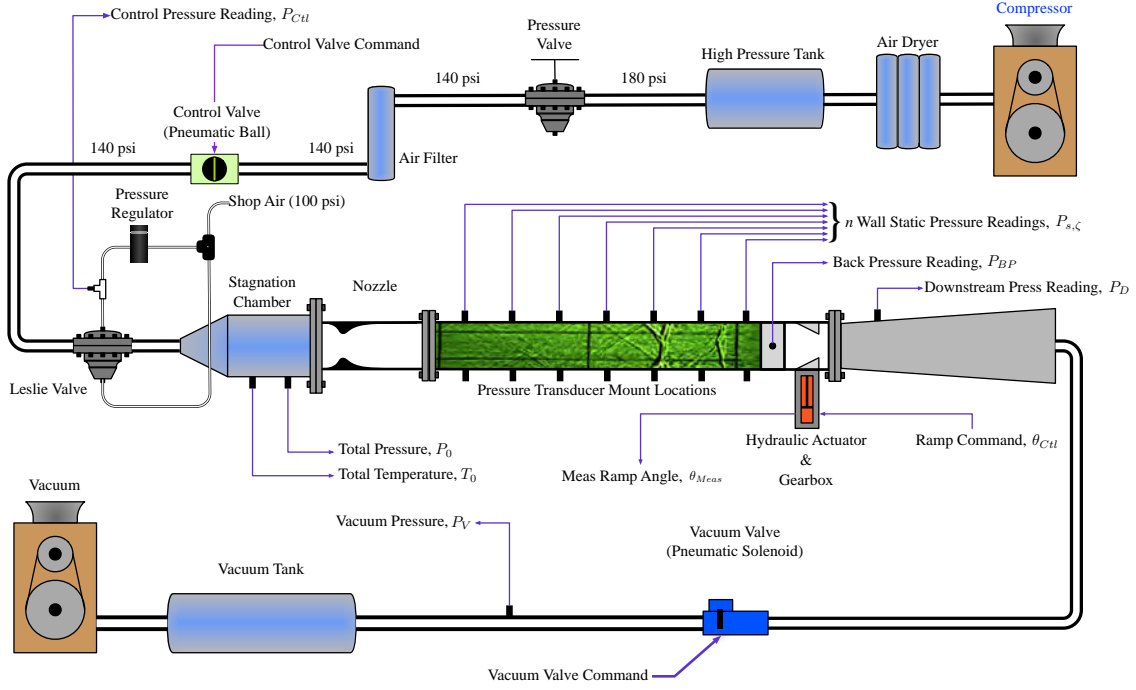


Figure F.1: Illustration of test facility



Figure F.2: Picture of test facility

The air initially starts in the ambient and is compressed by one of two Ingersoll Rand rotary screw compressors (model number UP6-50PE-200) presented in Figure F.3. The compressors are started and stopped automatically using the pressure readings in the high-pressure chamber.



Figure F.3: Ingersoll Rand rotary screw compressor

Upon leaving the compressor, the air flows through a Donaldson desiccant dryer (model AHLD-350) before being fed into a high-pressure pressure vessel. The high-pressure chamber is maintained at approximately 180 psi. A picture of the air dryer is presented in Figure F.4. The high-pressure chamber is right-hand tank in Figure F.5.



Figure F.4: Donaldson desiccant dryer



Figure F.5: High pressure and vacuum chambers

The air pressure is then reduced to 145 psi using a Kimray gas back pressure pressure regulator (model number 230 SGT PRB). A picture of the Kimray pressure regulator is presented in Figure F.6.



Figure F.6: Kimray pressure regulator

The flow then enters an air filter, presented in Figure F.7. The maximum pressure rating listed on the filters Pneumatic Products (part number PCC112001G49) housing is 150 psi, which is the reason for the Kimray pressure regulator.



Figure F.7: Air filter

The next part of the test equipment is the ball valve that opens at the beginning and closes at the end of a run. A picture of the pneumatic valve and controller is presented in Figure F.8.



Figure F.8: High pressure ball valve and controller

The ball valve, the vacuum valve presented in Figure F.18, and the hydraulic actuator presented in Figure F.12 are controlled using a National Instruments (NI) PXI computer. A picture of this computer, along with four of the five BNC boards (NI model BNC-2120) is presented in Figure F.9. The computer included a NI PXI 8196 embedded controller, a NI PXI 6070E input/output (I/O) board, three NI PXI 6120 simultaneous sampling multifunction I/O boards, and a NI PXI 6259 M series multifunction data acquisition board.

Once the ball valve has opened, the flow entered a Leslie pressure reducing valve (class GPK-1, size 2). A picture of the Leslie valve is presented in Figure F.10. The pressure on the diaphragm in the Leslie valve is controlled using the black hand control knob mounted on top of the air filter seen in Figure F.7. The total pressure entering the stagnation chamber is controlled with the Leslie valve.



Figure F.9: NI PXI computer and BNC boards



Figure F.10: Leslie air-loaded pressure reducing valve

After flowing through the Leslie valve, the air enters the stagnation chamber presented in Figure F.11 and then the test section presented in Figure F.12. The Mach 1.8 nozzle is in the left-hand portion of Figure F.12. The bolt pattern on the nozzle outlines the nozzle interior contours. The test section is in the middle of Figure F.12. In this figure, the acrylic walls that were used to enable shadowgraph photography

can be seen. Also, the hydraulic actuator is the black cylinder mounted below the right-hand portion of the test section. Finally, pressure transducer cables are aligned along the top of the test section. Throughout this research the transducers were mounted along the bottom of the test section as seen in the test section illustration presented in Figure F.13. Each of these cables are plugged into one of five Endevco DC amplifiers (Model 136) seen in Figure F.14 which then are connected via BNC cables to one of the five BNC boards connected to the NI PXI computer.

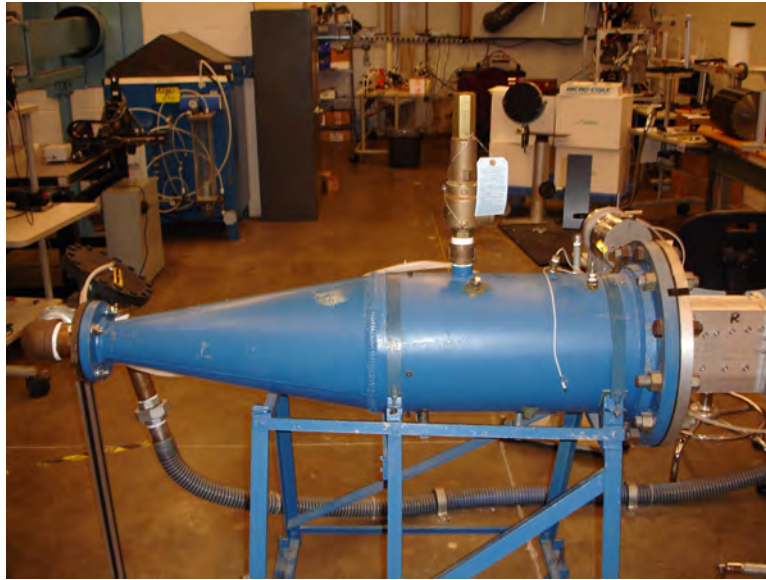


Figure F.11: Stagnation chamber

In addition to the amplifiers, the shadowgraph photography controller is the right-hand personal computer (PC) and the hydraulic controller is the left-hand PC seen in Figure F.14. Each of these computers accept commands from the NI PXI computer via BNC cables (from the BNC 2120 boards) and then control both the hydraulic actuator seen in Figure F.12 and the high-speed FASTCAM-X 1280 PCI camera presented in Figure F.15. Additionally, the hydraulic pressure is provided by the MTS 685.03 3000 psi pump presented in Figure F.16. The hydraulic pump is started at the beginning of testing for a day and continues to run throughout the day.

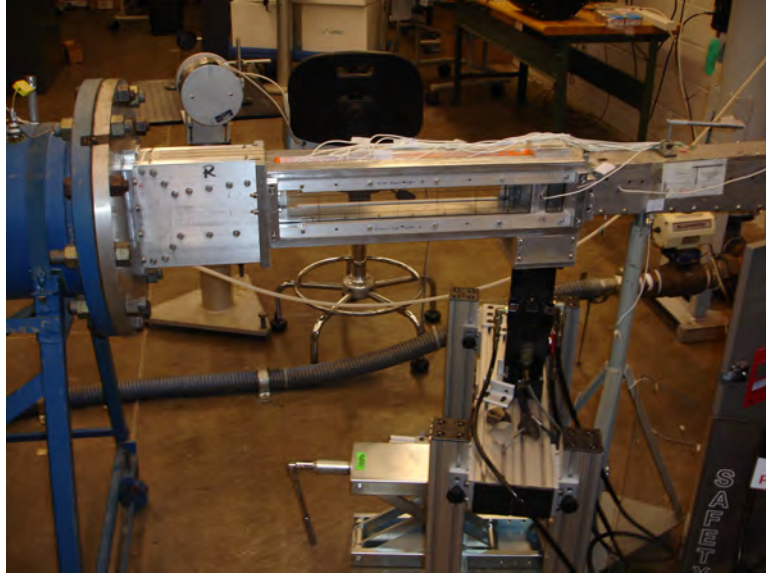


Figure F.12: Nozzle, test section, and hydraulic actuator

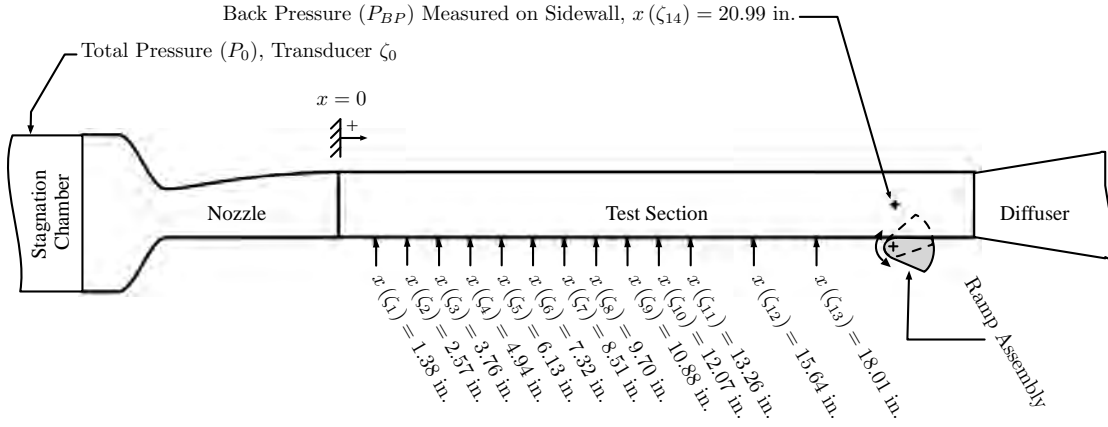


Figure F.13: Test section illustration

After the test section, the flow enters a diffuser, presented in Figure F.17 before flowing through the vacuum chamber solenoid valve presented in Figure F.18. The solenoid valve opens before and closes after the high-pressure valve in order to ensure the test section is not over-pressured. The solenoid valve is controlled by the NI PXI computer.



Figure F.14: Endeveco Model 136 DC amplifiers, hydraulic control computer, and shadowgraph control computer



Figure F.15: FASTCAM 1280 PCI shadowgraph camera

Next, the flow enters the vacuum chamber, which is the left-hand tank presented in Figure F.5. A vacuum is developed in this tank using the Stokes Microvac (Model 412-11) oil-sealed pump presented in Figure F.19.



Figure F.16: MTS hydraulic actuator compressor

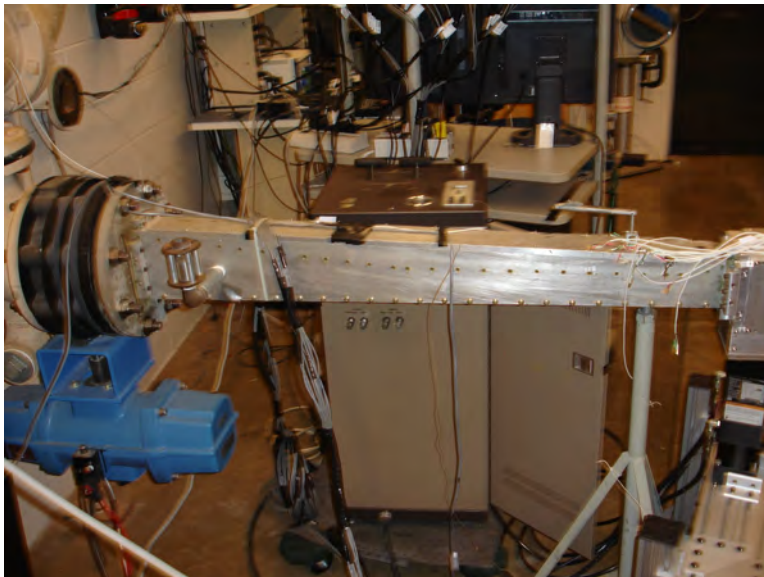


Figure F.17: Wind tunnel diffuser



Figure F.18: Vacuum chamber solenoid valve and controller



Figure F.19: Stokes Microvac vacuum pump

Appendix G. Transducer Calibrations

Each of the 15 Endevco 8530c-50 pressure transducers were calibrated at the AFRL Propulsion Directorate prior to the commencement of data collection. The calibration equations are listed in Table G.1 where the relationship between the measured voltage and the output pressure is described by Equation G.1. These values were programmed into the LabVIEWTM program and were used to convert the input voltage to the output pressure reading. The data used to develop these linear relationships is presented in Table G.2. The data was collected by pressurizing the transducers with the pressures listed in the second row. The voltage output from each amplifier/sensor combination at the input pressure is was recorded and is presented in the main body of Table G.2. Finally, the raw data along with a line for the calibration equation is presented for each amplifier/sensor combination in Figures G.1a-G.5c.

$$\text{Pressure} = \text{Slope} \times \text{Voltage} + \text{y intercept} \quad (\text{G.1})$$

Table G.1: Pressure transducer calibration values

Amplifier	Sensor	Slope	y intercept
1	1	4.7394	0.0676
1	2	4.9021	-1.1905
1	3	5.7951	1.9487
2	1	4.3487	1.2576
2	2	6.2412	-0.7847
2	3	5.1196	-0.6420
3	1	3.5097	-0.3441
3	2	3.7868	-0.3241
3	3	3.8929	0.9003
4	1	4.2829	0.2102
4	2	3.5510	0.1951
4	3	6.3234	2.7777
5	1	4.6602	0.7994
5	2	5.2613	1.9285
5	3	5.6273	-1.2128

Table G.2: Calibration raw data

		Input Pressure, psia									
Amplifier	Sensor	2	4	6	8	10	12	14	16	18	20
		Measured Voltages									
1	1	0.410	0.829	1.251	1.673	2.095	2.518	2.941	3.360	3.780	4.210
1	2	0.651	1.056	1.465	1.875	2.284	2.694	3.103	3.510	3.910	4.320
1	3	0.011	0.354	0.698	1.043	1.389	1.734	2.079	2.425	2.770	3.116
2	1	0.173	0.630	1.089	1.549	2.010	2.471	2.931	3.390	3.850	4.310
2	2	0.449	0.766	1.086	1.406	1.727	2.048	2.369	2.690	3.011	3.330
2	3	0.516	0.905	1.296	1.688	2.080	2.472	2.863	3.250	3.640	4.030
3	1	0.673	1.238	1.807	2.377	2.947	3.510	4.080	4.660	5.230	5.800
3	2	0.616	1.141	1.670	2.199	2.728	3.250	3.780	4.310	4.840	5.370
3	3	0.285	0.795	1.309	1.823	2.339	2.853	3.360	3.880	4.390	4.910
4	1	0.417	0.884	1.353	1.818	2.286	2.754	3.221	3.690	4.150	4.620
4	2	0.506	1.071	1.636	2.201	2.764	3.320	3.890	4.450	5.010	5.580
4	3	-0.126	0.195	0.512	0.825	1.142	1.459	1.775	2.091	2.407	2.723
5	1	0.257	0.687	1.117	1.543	1.974	2.405	2.836	3.260	3.690	4.120
5	2	0.012	0.393	0.773	1.155	1.535	1.916	2.296	2.676	3.056	3.430
5	3	0.570	0.926	1.282	1.637	1.993	2.349	2.705	3.061	3.410	3.770

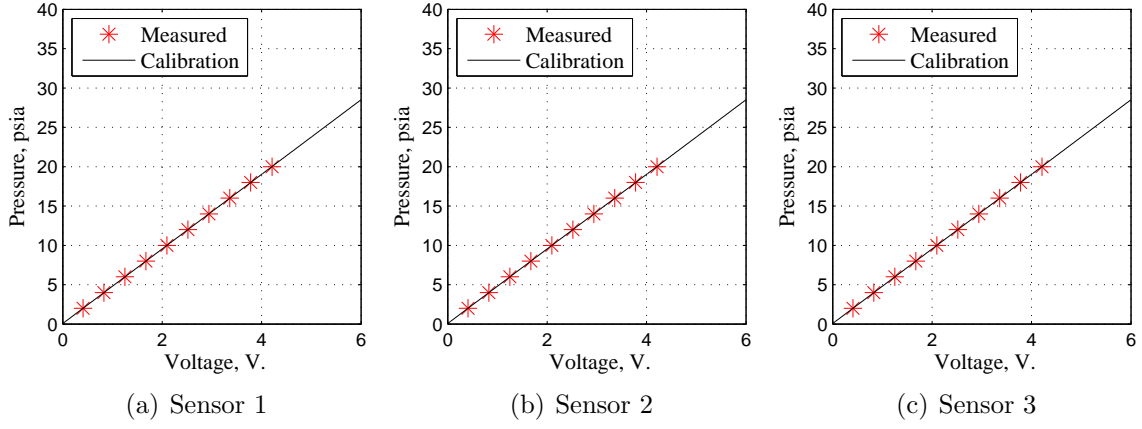


Figure G.1: Calibration data plots for amplifier 1

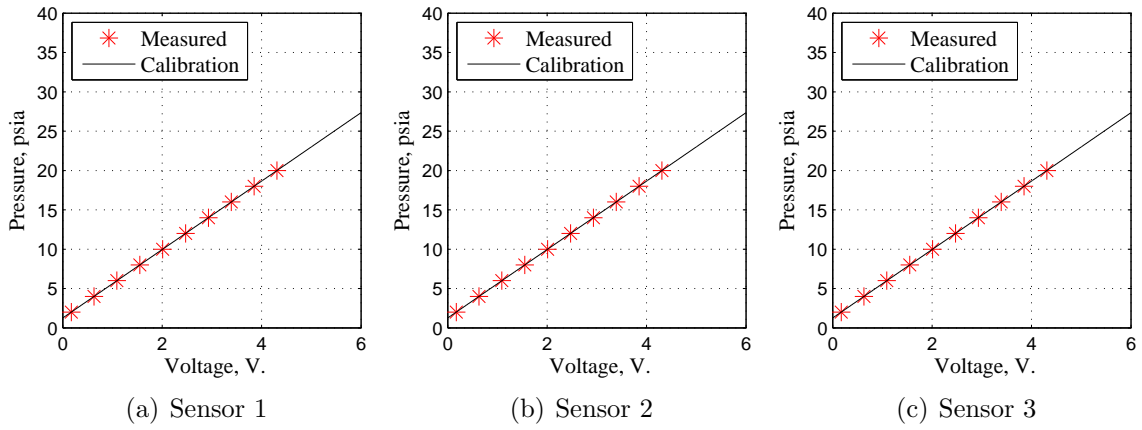


Figure G.2: Calibration data plots for amplifier 2

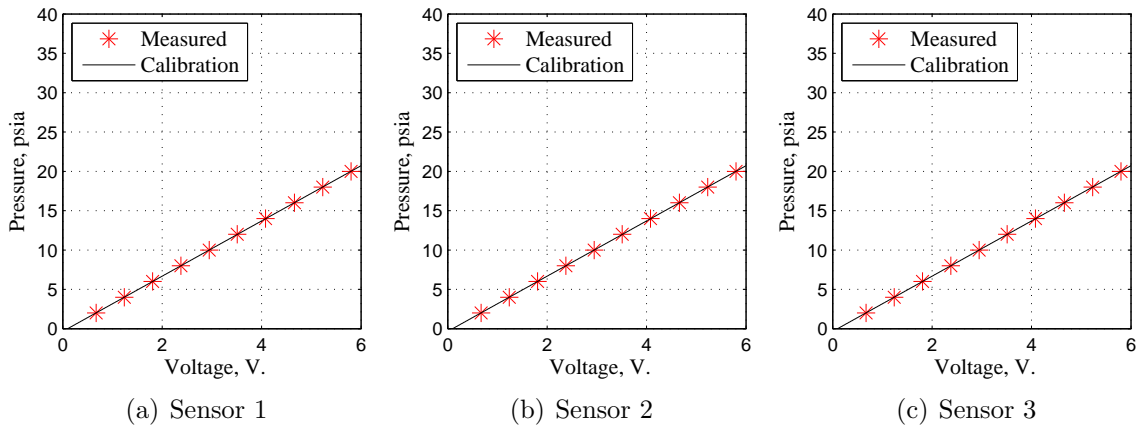


Figure G.3: Calibration data plots for amplifier 3

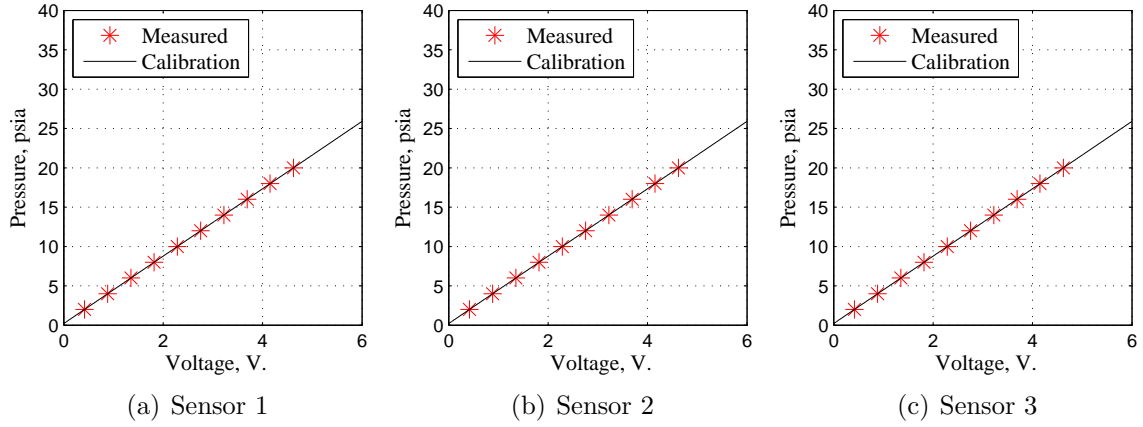


Figure G.4: Calibration data plots for amplifier 4

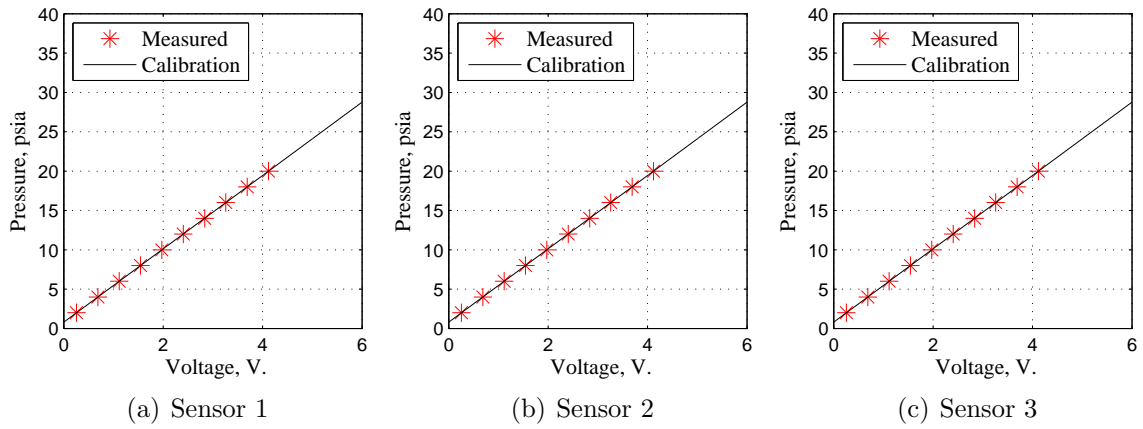


Figure G.5: Calibration data plots for amplifier 5

*Appendix H. **Matlab**[®] Analysis Codes*

The **Matlab**[®] m-codes used in the location analysis portion of Chapter IV and the modeling development and analysis portion of Chapter V are presented in this appendix. The **Matlab**[®] codes included in this appendix are the analysis codes for the pressure ratio, the pressure rise, the standard deviation, the frequency content, the summation of pressures, and the back pressure method for locating the shock train LE. Additionally, the **Matlab**[®] code for developing the ARX and NARX models along with the code for running the simulations are presented.

H.1 Pressure Ratio Method

```
function [xRatio] = RatioMethod(PressArray, LocArray)

%%%%%%%%%%%%%%%%%%%%%%%%%%%%%%%%%%%%%%%%%%%%%%%%%%%%%%%%%%%%%%%%%%%%%%%%%%%%%%
% Maj John R Hutzal
% AFIT PhD Candidate
%%%%%%%%%%%%%%%%%%%%%%%%%%%%%%%%%%%%%%%%%%%%%%%%%%%%%%%%%%%%%%%%%%%%%%%%%%%%%%
% This code accepts the following input:
%   PressArray - a (k x 14) table of the pressure measurements for each k
%   and each of the 14 transducers. The first transducer is the most
%   upstream and the 14th transducer is the BP transducer.
%   LocArray - a (14 x 1) vector of transducer mount locations.
% This code returns the following output:
%   xRatio - a struct of (k x 1) vectors of the calculated shock train LE
%   locations using the pressure ratio method.
%%%%%%%%%%%%%%%%%%%%%%%%%%%%%%%%%%%%%%%%%%%%%%%%%%%%%%%%%%%%%%%%%%%%%%%%%%%%%%
```

Create some empty arrays.

```
NS = size(PressArray,1);
RatioArray = zeros(size(PressArray));
xRatio.P25 = zeros(NS,1);
xRatio.P50 = zeros(NS,1);
xRatio.P75 = zeros(NS,1);
```

Create the tare data array.

```
p1 = plot(PressArray);
title('Click on the tare begining and ending.')
[x_tare, y_tare] = ginput(2);
clear p1
```

```

TareTimeStart = round(x_tare(1));
TareTimeEnd = round(x_tare(2));
TareArray = mean(PressArray(TareTimeStart:TareTimeEnd,:));

```

```

p1 = plot(PressArray);
title('Click on the calculation start time.')
[x_ramp, y_ramp] = ginput(1);
clear p1

```

Loop through and calculate the shock train locations.

```

for ii = round(x_ramp):NS
    RatioArray(ii,:) = PressArray(ii,:)./TareArray;
    I25 = find(RatioArray(ii,:) >= 1.25);
    I50 = find(RatioArray(ii,:) >= 1.50);
    I75 = find(RatioArray(ii,:) >= 1.75);
    if isempty(I25)
        xRatio.P25(ii,1) = 0;
    elseif (min(I25) == 1);
        xRatio.P25(ii,1) = 24;
    else
        PLess = RatioArray(ii,min(I25)-1);
        PMore = RatioArray(ii,min(I25));
        XLess = LocArray(1,min(I25)-1);
        XMore = LocArray(1,min(I25));
        xRatio.P25(ii,1) = interp1([PLess PMore], [XLess XMore], 1.25);
    end

    if isempty(I50)
        xRatio.P50(ii,1) = 0;
    end
end

```

```

elseif (min(I50) == 1);
    xRatio.P50(ii,1) = 24;
else
    PLess = RatioArray(ii,min(I50)-1);
    PMore = RatioArray(ii,min(I50));
    XLess = LocArray(1,min(I50)-1);
    XMore = LocArray(1,min(I50));
    xRatio.P50(ii,1) = interp1([PLess PMore], [XLess XMore], 1.50);
end

if isempty(I75)
    xRatio.P75(ii,1) = 0;
elseif (min(I75) == 1);
    xRatio.P75(ii,1) = 24;
else
    PLess = RatioArray(ii,min(I75)-1);
    PMore = RatioArray(ii,min(I75));
    XLess = LocArray(1,min(I75)-1);
    XMore = LocArray(1,min(I75));
    xRatio.P75(ii,1) = interp1([PLess PMore], [XLess XMore], 1.75);
end
end
end

```

H.2 Pressure Method

```
function [xPress] = PressMethod(PressArray, LocArray)

%%%%%%%%%%%%%%%%%%%%%%%%%%%%%%%%%%%%%%%%%%%%%%%%%%%%%%%%%%%%%%%%%%%%%%%%%%
% Maj John R Hutzell
% AFIT PhD Candidate
%%%%%%%%%%%%%%%%%%%%%%%%%%%%%%%%%%%%%%%%%%%%%%%%%%%%%%%%%%%%%%%%%%%%%%%%%%
% This code accepts the following input:
%   PressArray - a (k x 14) table of the pressure measurements for each k
%   and each of the 14 transducers. The first transducer is the most
%   upstream and the 14th transducer is the BP transducer.
%   LocArray - a (14 x 1) vector of transducer mount locations.
% This code returns the following output:
%   xPress - a struct of (k x 1) vectors of the calculated shock train LE
%   locations using the pressure method.
%%%%%%%%%%%%%%%%%%%%%%%%%%%%%%%%%%%%%%%%%%%%%%%%%%%%%%%%%%%%%%%%%%%%%%%%%%
```

Create some empty arrays.

```
NS = size(PressArray,1);
xPress.P25 = zeros(NS,1);
xPress.P50 = zeros(NS,1);
xPress.P75 = zeros(NS,1);

p1 = plot(PressArray);
title('Click on the calculation start time.')
[x_ramp, y_ramp] = ginput(1);
clear p1
```

Loop through and calculate the shock train locations.

```

for ii = x_ramp:NS
    % Calculate the interpolation points
    Interp25 = PressArray(ii,1) + 0.25*(max(PressArray(ii,:))-PressArray(ii,1));
    Interp50 = PressArray(ii,1) + 0.50*(max(PressArray(ii,:))-PressArray(ii,1));
    Interp75 = PressArray(ii,1) + 0.75*(max(PressArray(ii,:))-PressArray(ii,1));
    Index25 = find(PressArray(ii,:) >= Interp25);
    Index50 = find(PressArray(ii,:) >= Interp50);
    Index75 = find(PressArray(ii,:) >= Interp75);
    if isempty(Index25)
        xPress.P25(ii,1) = 0;
    elseif (min(Index25) == 1);
        xPress.P25(ii,1) = 24;
    else
        PLess = PressArray(ii,min(Index25)-1);
        PMore = PressArray(ii,min(Index25));
        XLess = LocArray(1,min(Index25)-1);
        XMore = LocArray(1,min(Index25));
        xPress.P25(ii,1) = interp1([PLess PMore], [XLess XMore], Interp25);
    end

    if isempty(Index50)
        xPress.P50(ii,1) = 0;
    elseif (min(Index50) == 1);
        xPress.P50(ii,1) = 24;
    else
        PLess = PressArray(ii,min(Index50)-1);
        PMore = PressArray(ii,min(Index50));
        XLess = LocArray(1,min(Index50)-1);
        XMore = LocArray(1,min(Index50));

```

```

        xPress.P50(ii,1) = interp1([PLess PMore], [XLess XMore], Interp50);
    end

    if isempty(Index75)
        xPress.P75(ii,1) = 0;
    elseif (min(Index75) == 1);
        xPress.P75(ii,1) = 24;
    else
        PLess = PressArray(ii,min(Index75)-1);
        PMore = PressArray(ii,min(Index75));
        XLess = LocArray(1,min(Index75)-1);
        XMore = LocArray(1,min(Index75));
        xPress.P75(ii,1) = interp1([PLess PMore], [XLess XMore], Interp75);
    end

    ii/NS*100
end

```

H.3 Standard Deviation Method

```
function [xStdDev] = StDevMethod(PressArray, LocArray)

%%%%%%%%%%%%%%%%%%%%%%%%%%%%%%%%%%%%%%%%%%%%%%%%%%%%%%%%%%%%%%%%%%%%%%%%%%%%%%
% Maj John R Hutzell
% AFIT PhD Candidate
%%%%%%%%%%%%%%%%%%%%%%%%%%%%%%%%%%%%%%%%%%%%%%%%%%%%%%%%%%%%%%%%%%%%%%%%%%%%%%
% This code accepts the following input:
%   PressArray - a (k x 14) table of the pressure measurements for each k
%   and each of the 14 transducers. The first transducer is the most
%   upstream and the 14th transducer is the BP transducer.
%   LocArray - a (14 x 1) vector of transducer mount locations.
% This code returns the following output:
%   xStdDev - a struct of (k x 1) vectors of the calculated shock train LE
%   locations using the standard deviation method.
%%%%%%%%%%%%%%%%%%%%%%%%%%%%%%%%%%%%%%%%%%%%%%%%%%%%%%%%%%%%%%%%%%%%%%%%%%%%%%
```

Create some empty arrays.

```
NS = size(PressArray,1);
xStdDev.S12 = zeros(NS,1);
xStdDev.S14 = zeros(NS,1);
xStdDev.S16 = zeros(NS,1);
xStdDev.S18 = zeros(NS,1);
x0 = zeros(NS,1);   x1 = zeros(NS,1);   x2 = zeros(NS,1);
y0 = zeros(NS,1);   y1 = zeros(NS,1);   x2 = zeros(NS,1);
```

Create the tare data array.

```
p1 = plot(PressArray);
title('Click on the tare begining and ending.')
```

```

[x_tare, y_tare] = ginput(2);
clear p1
TareTimeStart = round(x_tare(1));
TareTimeEnd = round(x_tare(2));
TareArray = mean(PressArray(TareTimeStart:TareTimeEnd,:));

p1 = plot(PressArray);
title('Click on the calculation start time.')
[x_ramp, y_ramp] = ginput(1);
clear p1

PS = PressArray;
%% %% Loop through and calculate the shock train locations
StdDevNum = 250;
for ii = round(x_ramp):NS
    % for ii = 70000:90000
    StDevArray(ii,:) = std(PressArray(ii-StdDevNum:ii,:),0,1)/...
        std(PressArray(ii-StdDevNum:ii,1));
    % Calculate the interpolation points
    [UpStd, MaxInd] = max(StDevArray(ii,:));
    % Get the maximum at each sample
    [MaxSamp, MaxInd] = max(StDevArray(ii,:));
    if MaxInd == 1
        xStdDev.S12(ii) = 0;
        xStdDev.S14(ii) = 0;
        xStdDev.S16(ii) = 0;
        xStdDev.S18(ii) = 0;
    elseif MaxInd == 14
        xStdDev.S12(ii) = 24;

```

```

xStdDev.S14(ii) = 24;
xStdDev.S16(ii) = 24;
xStdDev.S18(ii) = 24;
else
    x0(ii) = LocArray(MaxInd-1);          y0(ii) = StDevArray(ii, MaxInd-1);
    x1(ii) = LocArray(MaxInd);            y1(ii) = MaxSamp;
    x2(ii) = LocArray(MaxInd+1);          y2(ii) = StDevArray(ii, MaxInd+1);
    if MaxSamp >= 18
        xStdDev.S12(ii) = LocArray(MaxInd);
        xStdDev.S14(ii) = xStdDev.S12(ii);
        xStdDev.S16(ii) = xStdDev.S12(ii);
        xStdDev.S18(ii) = xStdDev.S12(ii);
    elseif (MaxSamp < 18) && (MaxSamp >= 5)
        Slope = (y1(ii)-y0(ii))/(x1(ii)-x0(ii));
        yInt = y1(ii)-Slope*x1(ii);
        xProjection12 = (12-yInt)/Slope;
        xProjection14 = (14-yInt)/Slope;
        xProjection16 = (16-yInt)/Slope;
        xProjection18 = (18-yInt)/Slope;
        xStdDev.S12(ii) = min([xProjection12 x2(ii)]);
        xStdDev.S14(ii) = min([xProjection14 x2(ii)]);
        xStdDev.S16(ii) = min([xProjection16 x2(ii)]);
        xStdDev.S18(ii) = min([xProjection18 x2(ii)]);
    else
        xStdDev.S12(ii) = mean([x1(ii-1) x2(ii-1)]);
        xStdDev.S14(ii) = xStdDev.S12(ii);
        xStdDev.S16(ii) = xStdDev.S12(ii);
        xStdDev.S18(ii) = xStdDev.S12(ii);
        x0(ii) = x1(ii-1);                y0(ii) = y1(ii-1);

```

```
        x1(ii) = x1(ii-1);          y1(ii) = y1(ii-1);
        x2(ii) = x2(ii-1);          y2(ii) = y2(ii-1);
    end
end
ii/NS*100
end
```

H.4 Frequency Content Method

```
function [xPSD] = PSDMethod(PArray, LocArray)

%%%%%%%%%%%%%%%%%%%%%%%%%%%%%%%%%%%%%%%%%%%%%%%%%%%%%%%%%%%%%%%%%%%%%%%%

% Maj John R Hutzell
% AFIT PhD Candidate
%%%%%%%%%%%%%%%%%%%%%%%%%%%%%%%%%%%%%%%%%%%%%%%%%%%%%%%%%%%%%%%%%%%%%%%%

% This code accepts the following input:
%   PArray - a (k x 14) table of the pressure measurements for each k
%   and each of the 14 transducers. The first transducer is the most
%   upstream and the 14th transducer is the BP transducer.
%   LocArray - a (14 x 1) vector of transducer mount locations.
% This code returns the following output:
%   xPSD - a struct of (k x 1) vectors of the calculated shock train LE
%   locations using the PSD method.
%%%%%%%%%%%%%%%%%%%%%%%%%%%%%%%%%%%%%%%%%%%%%%%%%%%%%%%%%%%%%%%%%%%%%%%%
```

Create some empty arrays to speed things up.

```
NS = size(PArray,1);
xPSD.PSD25 = zeros(NS,1);
xPSD.PSD50 = zeros(NS,1);
xPSD.PSD75 = zeros(NS,1);
RMSVector = zeros(size(PArray));

iiStart = 1000;
iiEnd = NS;

for ii = iiStart:iiEnd
```

Calculate the PSDs at each k and each transducer.

```

Samps = [ii-511:ii];

[A1S1Pxx,f1] = pwelch(PArray(Samps,7),[],[],[],10000,'onesided');
[A1S2Pxx,f2] = pwelch(PArray(Samps,8),[],[],[],10000,'onesided');
[A1S3Pxx,f3] = pwelch(PArray(Samps,9),[],[],[],10000,'onesided');
[A2S1Pxx,f4] = pwelch(PArray(Samps,10),[],[],[],10000,'onesided');
[A2S2Pxx,f5] = pwelch(PArray(Samps,11),[],[],[],10000,'onesided');
[A2S3Pxx,f6] = pwelch(PArray(Samps,12),[],[],[],10000,'onesided');
[A3S1Pxx,f7] = pwelch(PArray(Samps,1),[],[],[],10000,'onesided');
[A3S2Pxx,f8] = pwelch(PArray(Samps,2),[],[],[],10000,'onesided');
[A3S3Pxx,f9] = pwelch(PArray(Samps,3),[],[],[],10000,'onesided');
[A4S1Pxx,f10] = pwelch(PArray(Samps,4),[],[],[],10000,'onesided');
[A4S2Pxx,f11] = pwelch(PArray(Samps,5),[],[],[],10000,'onesided');
[A4S3Pxx,f12] = pwelch(PArray(Samps,6),[],[],[],10000,'onesided');
[A5S2Pxx,f14] = pwelch(PArray(Samps,13),[],[],[],10000,'onesided');
[A5S3Pxx,f15] = pwelch(PArray(Samps,14),[],[],[],10000,'onesided');

```

```

% Calculate the RMS at each k and each transducer

```

```

A1S1RMS = sqrt((A1S1Pxx'*A1S1Pxx)/numel(A1S1Pxx));
A1S2RMS = sqrt((A1S2Pxx'*A1S2Pxx)/numel(A1S2Pxx));
A1S3RMS = sqrt((A1S3Pxx'*A1S3Pxx)/numel(A1S3Pxx));
A2S1RMS = sqrt((A2S1Pxx'*A2S1Pxx)/numel(A2S1Pxx));
A2S2RMS = sqrt((A2S2Pxx'*A2S2Pxx)/numel(A2S2Pxx));
A2S3RMS = sqrt((A2S3Pxx'*A2S3Pxx)/numel(A2S3Pxx));
A3S1RMS = sqrt((A3S1Pxx'*A3S1Pxx)/numel(A3S1Pxx));
A3S2RMS = sqrt((A3S2Pxx'*A3S2Pxx)/numel(A3S2Pxx));
A3S3RMS = sqrt((A3S3Pxx'*A3S3Pxx)/numel(A3S3Pxx));
A4S1RMS = sqrt((A4S1Pxx'*A4S1Pxx)/numel(A4S1Pxx));
A4S2RMS = sqrt((A4S2Pxx'*A4S2Pxx)/numel(A4S2Pxx));
A4S3RMS = sqrt((A4S3Pxx'*A4S3Pxx)/numel(A4S3Pxx));

```

```
A5S2RMS = sqrt((A5S2Pxx'*A5S2Pxx)/numel(A5S2Pxx));
A5S3RMS = sqrt((A5S3Pxx'*A5S3Pxx)/numel(A5S3Pxx));
```

```
% Place the RMS values in an array
```

```
RMSVector(ii,:) = [A3S1RMS A3S2RMS A3S3RMS...
    A4S1RMS A4S2RMS A4S3RMS A1S1RMS A1S2RMS A1S3RMS...
    A2S1RMS A2S2RMS A2S3RMS A5S2RMS A5S3RMS];
```

Calculate the LE location from the RMS array. Determine the transducers upstream to shock

```
UpStreamTrans = find(RMSVector(ii,:) < 0.1);
% Determine the transducers downstream to shock
DownStreamTrans = find(RMSVector(ii,:) >= 0.1);
```

Linear interpolate to find the shock train location.

Use linear interp to find the shock train using the following criteria:

- 1) if DownStream is empty -> No Shock -> xs_PSD = 0
- 2) if UpStream is empty -> Unstart -> xs_PSD = 24
- 3) else interpolate

```
if isempty(DownStreamTrans)
    xs_PSD25(ii-iiStart+1,1) = 24;
    xs_PSD50(ii-iiStart+1,1) = 24;
    xs_PSD75(ii-iiStart+1,1) = 24;
elseif isempty(UpStreamTrans)
    xs_PSD25(ii-iiStart+1,1) = 0;
    xs_PSD50(ii-iiStart+1,1) = 0;
```

```

        xs_PSD75(ii-iiStart+1,1) = 0;
    else
        % Calculate the x values and the RMS values on either side of the
        % shock train LE
        x_up = LocArray(max(UpStreamTrans));
        x_down = LocArray(min(DownStreamTrans));
        RMS_up = RMSVector(ii-iiStart+1,max(UpStreamTrans));
        RMS_down = RMSVector(min(DownStreamTrans));
        % Find the interpolation value to find
        UpRMSave = mean(RMSVector(ii-iiStart+1,UpStreamTrans));
        % Assume it is at the 25%, 50%, and 75% RMS increases
        xs_PSD_RMS_25 = UpRMSave + 0.25*(max(RMSVector(ii,DownStreamTrans))-...
            UpRMSave);
        xs_PSD_RMS_50 = UpRMSave + 0.5*(max(RMSVector(ii,DownStreamTrans))-...
            UpRMSave);
        xs_PSD_RMS_75 = UpRMSave + 0.75*(max(RMSVector(ii,DownStreamTrans))-...
            UpRMSave);

        % Record estimated location and go to ii = ii+1
        % Interpolate for the shock train leading edge location
        xPSD.PSD25(ii,1) = interp1(RMSVector(ii,:), LocArray, xs_PSD_RMS_25);
        xPSD.PSD50(ii,1) = interp1(RMSVector(ii,:), LocArray, xs_PSD_RMS_50);
        xPSD.PSD75(ii,1) = interp1(RMSVector(ii,:), LocArray, xs_PSD_RMS_75);
    end
end
end

```

H.5 Static Pressure Summation Method

```
function [xSum] = PressSumMethod(PressArray)
```

```
%%%%%%%%%%%%%%%%%%%%%%%%%%%%%%%%%%%%%%%%%%%%%%%%%%%%%%%%%%%%%%%%%%%%%%%%
```

```
% Maj John R Hutzal
```

```
% AFIT PhD Candidate
```

```
%%%%%%%%%%%%%%%%%%%%%%%%%%%%%%%%%%%%%%%%%%%%%%%%%%%%%%%%%%%%%%%%%%%%%%%%
```

```
% This code accepts the following input:
```

```
% PressArray - a (k x 14) table of the pressure measurements for each k
```

```
% and each of the 14 transducers. The first transducer is the most
```

```
% upstream and the 14th transducer is the BP transducer.
```

```
% This code returns the following output:
```

```
% xSum - a (k x 1) vector of the calculated shock train LE locations using
```

```
% the summation correlation method.
```

```
%%%%%%%%%%%%%%%%%%%%%%%%%%%%%%%%%%%%%%%%%%%%%%%%%%%%%%%%%%%%%%%%%%%%%%%%
```

First, input the correlation.

```
Theta = [-3.47e-5 1.39e-2 -1.96 104.08]';
```

Calculate the sum at each k.

```
PSum = sum(PressArray,2);
```

Place the PSum array in a matrix and multiply by the Theta.

```
xSum = [PSum.^3 PSum.^2 PSum.^1 PSum.^0]*Theta;
```

H.6 Back Pressure Method

```
function [xBP] = BPMethod(PressArray)
```

```
%%%%%%%%%%%%%%%%%%%%%%%%%%%%%%%%%%%%%%%%%%%%%%%%%%%%%%%%%%%%%%%%%%%%%%%%
```

```
% Maj John R Hutzal
```

```
% AFIT PhD Candidate
```

```
%%%%%%%%%%%%%%%%%%%%%%%%%%%%%%%%%%%%%%%%%%%%%%%%%%%%%%%%%%%%%%%%%%%%%%%%
```

```
% This code accepts the following input:
```

```
% PressArray - a (k x 14) table of the pressure measurements for each k
```

```
% and each of the 14 transducers. The first transducer is the most
```

```
% upstream and the 14th transducer is the BP transducer.
```

```
% This code returns the following output:
```

```
% xBP - a (k x 1) vector of the calculated shock train LE locations using
```

```
% the back pressure correlation method.
```

```
%%%%%%%%%%%%%%%%%%%%%%%%%%%%%%%%%%%%%%%%%%%%%%%%%%%%%%%%%%%%%%%%%%%%%%%%
```

First, input the correlation.

```
Theta = [-2.16 45.14 -218.53]';
```

Grab the back pressure vector.

```
BP = PressArray(:,14);
```

Place in a matrix and multiply.

```
xBP = [BP.^2 BP BP.^0]*Theta;
```

H.7 ARX Model Maker

```
% clc; beep off;

function [theta, xs2, e, RMS, N, X, bias] = ARXMaker(na, nb, xs1, xs2, u1, u2)

%%%%%%%%%%%%%%%%%%%%%%%%%%%%%%%%%%%%%%%%%%%%%%%%%%%%%%%%%%%%%%%%%%%%%%%%%%%%%%
% Maj John R Hutzell
% AFIT PhD Candidate
%%%%%%%%%%%%%%%%%%%%%%%%%%%%%%%%%%%%%%%%%%%%%%%%%%%%%%%%%%%%%%%%%%%%%%%%%%%%%%

% This function is used to develop the ARX models and run a simulation

% This function accepts the number of desired a's and b's along with a
% time-based vector of inputs and outputs and finds the regressor vector,
% theta, using least squares

x1 = xs1.Press;
x2 = xs2.Press;

% find out which is bigger, na or nb
n = [na nb];
[val, ind] = max(n);

% Now, create the X matrix
NumSamps1 = numel(u1);
NumSamps2 = numel(u2);
NumCol = nb+na;
NumRow1 = NumSamps1-val;
NumRow2 = NumSamps2-val;
X1 = zeros(NumRow1, NumCol);
X2 = zeros(NumRow2, NumCol);
```

```

bcol = 0;   acol = 0;
for ii = 1:NumCol
    if na>nb
        if ii <= na
            X1(:,ii) = x1(na-acol:NumSamps1-(acol+1),1);
            X2(:,ii) = x2(na-acol:NumSamps2-(acol+1),1);
            acol = acol + 1;
        else
            X1(:,ii) = u1(nb-bcol+(na-nb):NumSamps1-(bcol+1),1);
            X2(:,ii) = u2(nb-bcol+(na-nb):NumSamps2-(bcol+1),1);
            bcol = bcol + 1;
        end
    else
        if ii <= na
            X1(:,ii) = x1(na-acol+(nb-na):NumSamps1-(acol+1),1);
            X2(:,ii) = x2(na-acol+(nb-na):NumSamps2-(acol+1),1);
            acol = acol + 1;
        else
            X1(:,ii) = u1(nb-bcol:NumSamps1-(bcol+1),1);
            X2(:,ii) = u2(nb-bcol:NumSamps2-(bcol+1),1);
            bcol = bcol + 1;
        end
    end
end

X = X1;

% % Calculate the condition number
% H = X'*X

```

```

% Lambdas = eig(H)
% Condition = max(Lambdas)/min(Lambdas)

% Now, create the theta vector
x1_LS = x1(val+1:NumSamps1,1);
theta = X1\x1_LS;

% Check the fits
% Non-simulation fit:
xs2.ARXOneStep = X2*theta;
NumARX = numel(xs2.ARXOneStep);
% num = theta(1:na);
% den = [1 -1*theta(nb+1:nb+na)'];
num = theta(na+1:nb+na)';
den = [1 -1*theta(1:na)'];
dsys = filt(num,den);
[z1,p1,k1] = zpkdata(dsys);
z2=cell2mat(z1);
p2=cell2mat(p1);
k1;
num./k1;
acol = 0;    bcol = 0;
for ii = 1:NumCol
    if ii <= na
        xarray(1,ii) = x2(na-acol,1);
        acol = acol + 1;
    else
        xarray(1,ii) = u2(nb-bcol,1);
        bcol = bcol + 1;
    end
end

```

```

        end
    end

    acol = 0;    bcol = 0;

    xout = x2(1:val);
    for ii = (val+1):numel(x2)-(val+1)
        xout(ii,1) = xarray*theta;
        eout(ii,1) = x2(ii-1)-xout(ii);
        for jj = 1:NumCol
            if jj <= na
                xarray(1,jj) = xout(ii-acol,1);
                acol = acol + 1;
            else
                xarray(1,jj) = u2(ii-bcol,1);
                bcol = bcol + 1;
            end
        end
    end

    acol = 0;    bcol = 0;
end

bias = mean(eout)
xs2.ARXSim = [x2(1:val+1); xout];

eSim = x2-xs2.ARXSim;
RMS = sqrt((eSim'*eSim)/NumSamps2);
N2Sim = norm(eSim,2);
NInfSim = norm(eSim,inf);
N = [N2Sim NInfSim];
e.Sim = eSim;

```

H.8 NARX Model Maker

```
% clc; beep off;

function [xs2, Pbp, eout] = NARXMaker(xs1, xs2, Pbp1, Pbp2, Ramp1, Ramp2, DV)

%%%%%%%%%%%%%%%%%%%%%%%%%%%%%%%%%%%%%%%%%%%%%%%%%%%%%%%%%%%%%%%%%%%%%%%%%%%%%%
% Maj John R Hutzell
% AFIT PhD Candidate
%%%%%%%%%%%%%%%%%%%%%%%%%%%%%%%%%%%%%%%%%%%%%%%%%%%%%%%%%%%%%%%%%%%%%%%%%%%%%%

% This function is used to develop the NARX models and run a simulation

% This function accepts the number of desired a's and b's along with a
% time-based vector of inputs and outputs and finds the regressor vector,
% theta, using least squares

% Relabel the x vector
x1 = decimate(xs1.Press,DV);
x2 = decimate(xs2.Press,DV);
u1 = decimate(Pbp1,DV);
u2 = decimate(Pbp2,DV);
r1 = decimate(Ramp1,DV);
r2 = decimate(Ramp2,DV);
NS1 = numel(x1);
NS2 = numel(x2);

% Some initial conditions
pout(1) = u1(1);
pout(2) = u1(2);
pout(3) = u1(3);
pout(4) = u1(4);
xout(1) = x2(1);
```

```

xout(2) = x2(2);
xout(3) = x2(3);
xout(4) = x2(4);
Pbp.NARX(1,:) = pout(1);
Pbp.NARX(2,:) = pout(2);
Pbp.NARX(3,:) = pout(3);
Pbp.NARX(3,:) = pout(3);
xs2.NARX(1,:) = xout(1);
xs2.NARX(2,:) = xout(2);
xs2.NARX(3,:) = xout(3);
xs2.NARX(4,:) = xout(4);
NTemp = length(x1(1:NS1-2));

% Try a poly NARX from P_BP and ramp to x_LE
xk = x1(2:NS1-1);      xkm1 = x1(1:NS1-2);
uk = u1(2:NS1-1);      ukm1 = u1(1:NS1-2);
X2 = [xk xkm1 uk uk.^2 ukm1];
theta2 = inv(X2'*X2)*X2'*x1(3:NS1,:);

% Simulate the response
% parray = [r2(2) r2(1)^2 u2(2)];
% x(k) = x2(2)          x(k-1) = x2(1)
% u(k) = u2(2)          u(k-1) = u2(1)
xarray = [xk(2) xk(1) u2(2) u2(2)^2 u2(1)];
for ii = 3:NS2
%     pout(ii) = parray*theta1;
    xout(ii) = xarray*theta2;
    eout(ii) = xout(ii)-x2(ii-1);
%     Pbp.NARX(ii,:) = pout(ii);

```

```
xs2.NARX(ii,:) = xout(ii);  
%   parray = [r2(ii) r2(ii-1)^2 Pbp.NARX(ii)];  
xarray = [xs2.NARX(ii) xs2.NARX(ii-1) u2(ii) u2(ii)^2 u2(ii-1)];  
end
```

Bibliography

1. NASA, http://www.nasa.gov/centers/langley/news/factsheets/X43A_2006_5.html.
2. Heiser, W. H. and Pratt, D. T., *Hypersonic Airbreathing Propulsion*, American Institute of Aeronautics and Astronautics, Inc., Washington D.C., 1994.
3. Om, D., Viegas, J. R., and Childs, M. E., "Transonic Shock-Wave/Turbulent Boundary-Layer Interactions in a Circular Duct," *AIAA Journal*, Vol. 23, No. 5, 1985.
4. McRuer, D., "Design and Modeling Issues for Integrated Airframe/Propulsion Control of Hypersonic Flight Vehicles," *Proceedings of the American Control Conference*, Boston, MA, June 1991, pp. 729–735.
5. Ljung, L., *System Identification, Theory for the User*, Prentice Hall, Upper Saddle River, NJ, 1999.
6. Lin, K.-C., Tam, C.-J., Jackson, K. R., Eklund, D. R., and Jackson, T. A., "Characterization of Shock Train Structures inside Constant-Area Isolators of Model Scramjet Combustors," *44th AIAA Aerospace Sciences Meeting and Exhibit*, Reno, NV, 9-12 January 2006, AIAA Paper 2006-816.
7. MacMartin, D. G., "Dynamics and Control of Shock Motion in a Near-Isentropic Inlet," *Journal of Aircraft*, Vol. 41, No. 4, 2004, pp. 846–853.
8. Willoh, R., "A Mathematics Analysis of Supersonic Inlet Dynamic," NASA Technical Note D-4969, August 1968.
9. Culick, F. and Rogers, T., "The Response of Normal Shocks in Diffusers," *AIAA Journal*, Vol. 21, No. 10, 1983.
10. Sajben, M. and Said, H., "Acoustic-Wave/Blade-Row Interactions Establish Boundary Conditions for Unsteady Inlet Flows," *Journal of Propulsion and Power*, Vol. 17, No. 5, September-October 2001, pp. 1090–1099.
11. John, J. E. and Keith, T. G., *Gas Dynamics*, Pearson Prentice Hall, Upper Saddle River, NJ, 3rd ed., 2006.
12. Waltrup, P. J. and Billig, F. S., "Structure of Shock Waves in Cylindrical Ducts," *AIAA Journal*, Vol. 11, No. 10, 1973.
13. Ikui, T., Matsuo, K., and Nagai, M., "The Mechanism of Pseudo-Shock Waves," *Bulletin of the JSME*, Vol. 17, No. 108, 1974.
14. Seddon, J., "The Flow Produced by Interaction of a Turbulent Boundary Layer with a Normal Shock Wave of a Strength to Cause Separation," British Aeronautical Research Council Reports and Technical Memoranda No. 3502, 1960.

15. Kooi, J., "Experiment on Transonic Shock-Wave Boundary Layer Interaction," (NATO) Advisory Group for Aerospace Research and Development (AGARD) Conference Proceedings (CP) Number 168, May 1975.
16. East, L., "The Application of a Laser Anemometer to the Investigation of Shock-Wave Boundary Layer Interactions," (NATO) AGARD CP 193, May 1976.
17. Cox, C., Lewis, C., Pap, R., Glover, C., Priddy, K., Edwards, J., and McCarty, D., "Prediction of Unstart Phenomena in Hypersonic Aircraft," *AIAA Sixth International Aerospace Planes and Hypersonics Technologies Conference*, Chattanooga, TN, 3-7 April 1995, AIAA Paper 1995-6018.
18. Chang, J., Fan, Y., Bao, W., Yu, D., and Shen, Y., "Unstart Margin Control of Hypersonic Inlets," *Acta Astronautica*, Vol. 66, 2010, pp. 78–87.
19. Majumdar, D., "X-51 Scramjet Test Exceeded Thrust Expectations: AFRL," *Defense News*, September 15, 2011, www.defensenews.com/story.php?i=7692206&c=AIR&s=TOP.
20. Norris, G., "X-51A Scramjet Fails on Second Attempt," *Aviation Week*, June 15, 2011, www.aviationweek.com/aw/generic/story_channel.jsp?channel=defense&id=news/awx/2011/06/15/awx_06_15_2011_p0-336299.xml.
21. Cole, G. L., Neiner, G. H., and Crosby, M. J., "Design and Performance of a Digital Electronic Normal Shock Position Sensor for Mixed-Compression Inlets," NASA Technical Note D-5606, December 1969.
22. Dustin, M. O., Cole, G. L., and Wallhagen, R. E., "Determination of Normal Shock Position in a Mixed-Compression Supersonic Inlet," NASA Technical Memorandum X-2397, November 1971.
23. Dustin, M. O. and Cole, G. L., "Performance Comparison of Three Normal-Shock Position Sensors for Mixed-Compression Inlets," NASA Technical Memorandum X-2739, March 1973.
24. Sajben, M., Donovan, J. F., and Morris, M. J., "Experimental Investigation of Terminal Shock Sensors for Mixed-Compression Inlets," *Journal of Propulsion and Power*, Vol. 8, No. 1, January-February 1992, pp. 168–174.
25. Le, D., Goyne, C., and Krauss, R., "Shock Train Leading-Edge Detection in a Dual-Mode Scramjet," *Journal of Propulsion and Power*, Vol. 24, No. 5, September-October 2008, pp. 1035–1041.
26. Dustin, M. O., Cole, G. L., and Neiner, G. H., "Continuous-Output Terminal-Shock-Position Sensor for Mixed-Compression Inlets Evaluated in Wind-Tunnel Tests of YF-12 Aircraft Inlet," NASA Technical Memorandum X-3144, December 1974.
27. Chavez, F. R. and Schmidt, D. K., "An Integrated Analytical Aeropropulsive/Aeroelastic Model for the Dynamic Analysis of Hypersonic Vehicles," *AIAA*

Atmospheric Flight Mechanics Conference, August 1992, pp. 551–563, AIAA Paper 1992-4567.

28. Chavez, F. R. and Schmidt, D. K., “Analytical Aeropropulsive/Aeroelastic Hypersonic-Vehicle Model with Dynamic Analysis,” *Journal of Guidance, Control, and Dynamics*, Vol. 17, No. 6, November-December 1994, pp. 1308–1319.
29. Torrez, S. M., Scholten, N. A., Micka, D. J., Driscoll, J. F., Bolender, M. A., Doman, D. B., and Oppenheimer, M. W., “A Scramjet Engine Model Including Effects of Precombustion Shocks and Dissociation,” *44th AIAA/ASME/SAE/ASEE Joint Propulsion Conference and Exhibit*, Hartford, CT, 21-23 July 2008, AIAA Paper 2008-4619.
30. Bolender, M. A. and Doman, D. B., “Nonlinear Longitudinal Dynamical Model of an Air-Breathing Hypersonic Vehicle,” *Journal of Spacecraft and Rockets*, Vol. 44, No. 2, March-April 2007, pp. 374–387.
31. Torrez, S. M., Driscoll, J. F., Bolender, M. A., Oppenheimer, M. W., and Doman, D. B., “Effects of Improved Propulsion Modelling on the Flight Dynamics of Hypersonic Vehicles,” *AIAA Atmospheric Flight Mechanics Conference and Exhibit*, Honolulu, HI, 18-21 August 2008, AIAA Paper 2008-6386.
32. Hurrell, H. G., “Analysis of Shock Motion in Ducts During Disturbances in Downstream Pressure,” NACA Technical Note 4090, September 1957.
33. Tao, C., Daren, Y., Juntao, C., and Wen, B., “Topological Geometry Interpretation of Supersonic Inlet Start/Unstart Based on Catastrophe Theory,” *Journal of Aircraft*, Vol. 45, No. 4, July-August 2008, pp. 1464–1468.
34. Daren, Y., Tao, C., and Wen, B., “An Idea of Distributed Parameter Control for Scramjet Engines,” *The Aeronautical Journal*, Vol. 111, No. 1126, 2007, pp. 787–796.
35. Jones, T. P. and Baumann, E., “Evaluation of the X-43A Scramjet Engine Controller Performance by Monte Carlo Technique,” *39th AIAA/ASME/SAE/ASEE Joint Propulsion Conference and Exhibit*, 2003, AIAA Paper 2003-5192.
36. Crocco, L., *Fundamentals of Gas Dynamics*, Vol. Volume III of *High Speed Aerodynamics and Jet Propulsion*, Princeton University Press, Princeton, NJ, 1958.
37. Waltrup, P. J. and Billig, F. S., “Prediction of Precombustion Wall Pressure Distributions in Scramjet Engines,” *Journal of Spacecraft*, Vol. 10, No. 9, 1973.
38. Sullins, G. and McLafferty, G., “Experimental Results of Shock Trains in Rectangular Ducts,” *AIAA 4th International Aerospace Planes Conference*, 1992, AIAA Paper 1992-5103.
39. Donbar, J. M., Linn, G. J., Srikant, S., and Akella, M. R., “High-Frequency Pressure Measurements for Unstart Detection in Scramjet Isolators,” *46th AIAA/ASME/SAE/ASEE Joint Propulsion Conference and Exhibit*, Nashville, TN, July 25-28 2010, AIAA Paper 2010-6557.

40. Hurrell, H. G., "Experimental Study of Shock-Positioning Method of Ram-Jet-Engine Control," NACA Research Memorandum E55F21, August 1955.
41. auBuchon, M. D., Caldwell, R. C., Gill, J. T., and Madden, J. P., "Ramjet/Scramjet Inlet Unstart Prevention," United States Patent, September 15 1998, Patent Number 5,806,301.
42. Le, D., Goyne, C., Krauss, R., and McDaniel, J., "Experimental Study of a Dual-Mode Scramjet Isolator," *Journal of Propulsion and Power*, Vol. 24, No. 5, September-October 2008, pp. 1050–1057.
43. Daren, Y., Tao, C., and Wen, B., "Equilibrium Manifold Linearization Model for Normal Shock Position Control Systems," *Journal of Aircraft*, Vol. 42, No. 5, September-October 2005, pp. 1344–1347.
44. Schmidt, D. K., "Integrated Control of Hypersonic Vehicles-A Necessity Not Just a Possibility," *AIAA Guidance, Navigation, and Control Conference*, August 1993, pp. 539–549, AIAA Paper 1993-3761.
45. Schmidt, D. K. and Hermann, J. A., "Use of Energy-State Analysis on a Generic Air-Breathing Hypersonic Vehicle," *Journal of Guidance, Control, and Dynamics*, Vol. 21, No. 1, 1998, pp. 71–76.
46. Schmidt, D. K., Mamich, H., and Chavez, F., "Dynamics and Control of Hypersonic Vehicles - The Integration Challenge for the 1990's," *AIAA Third International Aerospace Planes Conference*, December 1991, AIAA Paper 1991-5057.
47. Schmidt, D. K. and Lovell, T. A., "Mission Performance and Design Sensitivities of Air-Breathing Hypersonic Launch Vehicles," *Journal of Spacecraft and Rockets*, Vol. 34, No. 2, 1997, pp. 158–164.
48. Reinartz, B. U., Herrmann, C. D., Ballmann, J., and Koschel, W. W., "Aerodynamic Performance of a Hypersonic Inlet Isolator Using Computation and Experimentation," *Journal of Propulsion and Power*, Vol. 19, No. 5, 2003, pp. 868–875.
49. Mitani, T., Sakuranaka, N., Tomioka, S., and Kobayashi, K., "Boundary-Layer Control in Mach 4 and Mach 6 Scramjet Engines," *Journal of Propulsion and Power*, Vol. 21, No. 4, 2005.
50. Iannelli, J., "A Distributed Wall Mass Removal System for Improving Scramjet Isolator Performance," *46th AIAA Aerospace Sciences Meeting and Exhibit*, 2008, AIAA Paper 2008-65.
51. Volland, R. T., Auslender, A. H., Smart, M. K., Roudakov, A. S., Semenov, V. L., and Kopchenov, V., "CIAM/NASA Mach 6.5 Scramjet Flight and Ground Test," *AIAA Ninth International Aerospace Planes and Hypersonics and Technologies Conference*, Norfolk, VA, 1-5 Nov 1999, AIAA Paper 1999-4848.
52. Sigthorsson, D. O., Serrani, A., Yurkovich, S., Bolender, M. A., and Doman, D. B., "Tracking Control for an Overactuated Hypersonic Air-Breathing Vehicle with

Steady State Constraints,” *AIAA Guidance, Navigation, and Control Conference and Exhibit*, Keystone, CO, August 21-24 2006, AIAA Paper 2006-6558.

53. Rodriguez, A. A., Dickeson, J. J., Cifdaloz, O., McCullen, R., Benevides, J., Sridharan, S., Kelkar, A., Vogel, J. M., and Soloway, D., “Modeling and Control of Scramjet-Powered Hypersonic Vehicles: Challenges, Trends, and Tradeoffs,” *AIAA Guidance, Navigation, and Control Conference and Exhibit*, Honolulu, HI, 18-21 August 2008.
54. Hatlelid, J. and Akella, M., “Feedback Control Methods to Prevent Unstart in A Hypersonic Inlet,” *18th AAS/AIAA Space Flight Mechanics Meeting*, Galveston, TX, 27-31 January 2008, AAS Paper 08-114.
55. Tam, C.-J., Eklund, D., Behdadnia, R., and Jackson, T., “Investigation of Boundary Layer Bleed for Improving Scramjet Isolator Performance,” *AIAA/CIRA 13th International Space Planes and Hypersonic Systems and Technologies*, 2005, AIAA Paper 2005-3286.
56. Paek, R. I., *Back-Pressure Effect on Shock-Train Location in a Scramjet Engine Isolator*, Master’s thesis, AFIT/GAE/ENY/10-M17 Graduate School of Engineering and Management, Air Force Institute of Technology (AU), Wright-Patterson AFB OH, March 2010, (ADA517638).
57. Photron, <http://www.photron.com/index.php?cmd=products&type=legacy>.
58. Haber, R. and Keviczky, L., *Nonlinear System Identification - Input-Output Modelling Approach*, Vol. 2, Kluwer Academic Publishers, Dordrecht, The Netherlands, 1999.
59. Srikant, S., Wagner, J., Valdivia, A., M.R. A., and Clemens, N., “Unstart Detection in a Simplified-Geometry Hypersonic Inlet-Isolator Flow,” *Journal of Propulsion and Power*, Vol. 26, No. 5, September-October 2010.
60. Haber, R. and Keviczky, L., *Nonlinear System Identification - Input-Output Modelling Approach*, Vol. 1, Kluwer Academic Publishers, Dordrecht, The Netherlands, 1999.
61. Nelles, O., *Nonlinear System Identification*, Springer-Verlag, Berlin, Germany, 2001.
62. Lindstrom, C. D., Davis, D., Williams, S., and Tam, C.-J., “Shock-Train Resolved with Absorption Spectroscopy Part 2: Analysis and CFD Comparison,” *AIAA Journal*, Vol. 47, No. 10, October 2009, pp. 2379–2390.
63. Ikui, T., Matsuo, K., and Nagai, M., “The Mechanism of Pseudo-Shock Waves,” *Bulletin of the JSME*, Vol. 17, No. 108, 1974.
64. Ljung, L., *System Identification Toolbox User’s Guide*, The MathWorks, Inc., Natick, MA, 1988.

65. Elaydi, S. N., *An Introduction to Difference Equations*, Springer-Vehrlag, New York, NY, 1999.
66. Ogata, K., *Discrete-Time Control Systems*, Prentice Hall, Upper Saddle River, NJ, 1995.
67. Ikui, T., Matsuo, K., Nagai, M., and Honjo, M., "Oscillation Phenomena of Pseudo-Shock Waves," *Bulletin of the JSME*, Vol. 17, No. 112, 1974, pp. 1278–1285.
68. Anderson, J. D., *Fundamentals of Aerodynamics*, McGraw-Hill Higher Education, 3rd ed., 2001.
69. Davies, W., *System Identification for Self-Adaptive Control*, Wiley-Interscience, London, England, 1970.
70. Eykhoff, P., *System Identification, Parameter and State Estimation*, John Wiley and Sons, London, England, 1974.
71. Söderström, T. and Stoica, P., *System Identification*, Prentice Hall, New York, NY, 1989.

Vita

John Robert Hutzal was born in Sacramento, CA to LtCol Robert F. and Mrs Peggy E. Hutzal. He graduated from Marcus High School in Flower Mound, TX and received a ROTC scholarship to attend Texas A&M University. While at Texas A&M, he was a member of the Corps of Cadets in Squadron 17. He graduated from Texas A&M in 2000 with a degree in Mechanical Engineering. After graduation, he was commissioned a Second Lieutenant in the United States Air Force and began work at the B-2 System Program Office where he worked as a program manager/engineer. In 2005 he transferred to the Air Force Institute of Technology where he was a distinguished graduate and earned dual Masters degrees in Systems Engineering and Research and Development Management. After his Masters work, he was assigned to the 72D Test and Evaluation Squadron at Whiteman AFB, MO where he worked as a test engineer. John was accepted to the Aeronautical Engineering PhD program at AFIT in 2008. In addition to his engineering research, he started distance running while at AFIT and completed three half marathons and one full marathon while a student.

Permanent address: 2950 Hobson Way
Air Force Institute of Technology
Wright-Patterson AFB, OH 45433

REPORT DOCUMENTATION PAGE					<i>Form Approved</i> OMB No. 0704-0188	
The public reporting burden for this collection of information is estimated to average 1 hour per response, including the time for reviewing instructions, searching existing data sources, gathering and maintaining the data needed, and completing and reviewing the collection of information. Send comments regarding this burden estimate or any other aspect of this collection of information, including suggestions for reducing this burden to Department of Defense, Washington Headquarters Services, Directorate for Information Operations and Reports (0704-0188), 1215 Jefferson Davis Highway, Suite 1204, Arlington, VA 22202-4302. Respondents should be aware that notwithstanding any other provision of law, no person shall be subject to any penalty for failing to comply with a collection of information if it does not display a currently valid OMB control number. PLEASE DO NOT RETURN YOUR FORM TO THE ABOVE ADDRESS.						
1. REPORT DATE (DD-MM-YYYY) 15-12-2011		2. REPORT TYPE Doctoral Dissertation			3. DATES COVERED (From — To) Sep 2008 — Oct 2011	
4. TITLE AND SUBTITLE Scramjet Isolator Modeling and Control				5a. CONTRACT NUMBER 5b. GRANT NUMBER 5c. PROGRAM ELEMENT NUMBER		
6. AUTHOR(S) Hutzel, John R., Maj, USAF				5d. PROJECT NUMBER 10-247 5e. TASK NUMBER 5f. WORK UNIT NUMBER		
7. PERFORMING ORGANIZATION NAME(S) AND ADDRESS(ES) Air Force Institute of Technology Graduate School of Engineering and Management (AFIT/EN) 2950 Hobson Way WPAFB OH 45433-7765					8. PERFORMING ORGANIZATION REPORT NUMBER AFIT/DS/ENY/11-19	
9. SPONSORING / MONITORING AGENCY NAME(S) AND ADDRESS(ES) AFRL/RZAS-Bldg 18 Attn: Jeffrey M. Donbar 1950 Fifth Street WPAFB, OH 45433 (937)255-1996 Jeffrey.Donbar@wpafb.af.mil					10. SPONSOR/MONITOR'S ACRONYM(S) AFRL/RZAS 11. SPONSOR/MONITOR'S REPORT NUMBER(S)	
12. DISTRIBUTION / AVAILABILITY STATEMENT APPROVED FOR PUBLIC RELEASE; DISTRIBUTION UNLIMITED.						
13. SUPPLEMENTARY NOTES This material is declared a work of the U.S. Government and is not subject to copyright protection in the United States						
14. ABSTRACT The scramjet isolator is a duct in which pressure increases from the inlet to the combustor via a shock train. The shock train leading edge (LE) location must be controlled in an operational scramjet. A LE location measurement algorithm, dynamic model, and control algorithm were developed and validated with 500 frame per second (FPS) shadowgraph images in this research. The test apparatus consisted of a direct connect cold-flow high-speed wind tunnel with an adjustable ramp mounted in the tunnel floor. Ramp adjustments changed the tunnel cross-sectional area which changed the tunnel back pressure and LE location. Wall-mounted pressure transducers and a high-speed camera were used for data collection. The LE location measurement algorithm is the first with results validated using 500 FPS shadowgraph images to measure the LE location with root mean square (RMS) errors less than 20% of a duct height, D , although the transducers were separated by 50% of D . The developed and validated dynamic model is the first with error RMS values less than 24% of D . Finally, the first control algorithm capable of controlling the LE location within 50% of D was developed and validated.						
15. SUBJECT TERMS System Identification, Control, Modeling, Scramjet, Isolator, Hammerstein model						
16. SECURITY CLASSIFICATION OF:			17. LIMITATION OF ABSTRACT		18. NUMBER OF PAGES	
a. REPORT U	b. ABSTRACT U	c. THIS PAGE U	 UU		 224	
					19a. NAME OF RESPONSIBLE PERSON Dr. Douglas D. Decker	
					19b. TELEPHONE NUMBER (include area code) (937)522-6870; Douglas.Decker.ctr@wpafb.af.mil	